BULGARIAN CHEMICAL COMMUNICATIONS

2017 Volume 49 / Special Issue I

Selected papers of the 3rd Internatıonal Conference on New Trends in Chemıstry, Helsinki, 28 - 30 Aprıl, 2017

Journal of the Chemical Institutes
of the Bulgarian Academy of Sciences
and of the Union of Chemists in Bulgaria

BULGARIAN CHEMICAL COMMUNICATIONS

A quarterly published by

THE BULGARIAN ACADEMY OF SCIENCES

and

THE UNION OF CHEMISTS IN BULGARIA

Volume 49, Special Issue I

ИЗВЕСТИЯ ПО ХИМИЯ

Тримесечно издание на

БЪЛГАРСКА АКАДЕМИЯ НА НАУКИТЕ

и

СЪЮЗ НА ХИМИЦИТЕ В БЪЛГАРИЯ

Том 49, Специално издание I

2017

The annual subscription (for 4 issues) for vol. 49 (2017) is € 160. – including postage, handling and packaging charge.

Payments should be delivered to:

Editorial Board of Bulgarian Chemical Communications, Institute of Chemical Engineering, Unicredit Bulbank, IBAN: BG65UNCR 7630 3400 0017 48; BIC - UNCRBGSF (for Euro €).

Unicredit Bulbank, IBAN: BG18UNCR9660 3119 9033 12; SWIFT BIC - UNCRBGSF (for local currency BGN).

Selected papers presented on the 3rd International Conference on the New Trends in Chemistry, Helsinki, Finland, April 28-30, 2017

Preface

This special issue of the Bulgarian Chemical Communications is dedicated to new trends in chemistry and consists papers based on oral and posters presentations from the All in One Conferences, 3rd International Conference on New Trends in Chemistry organized in Helsinki, Finland, 28-30 April 2017. The topics are Polymer Chemistry and Applications, Pharmaceutical Chemistry, Computational Chemistry, Environmental Chemistry, Bio Chemistry, Physical Chemistry, Analytical Chemistry, Organic Chemistry, Material Chemistry and Inorganic Chemistry. In this issue, it is selected 20 manuscripts for publication.

This conference is provided a common platform for scientists and experts from various institutions to share knowledge, ideas, and achievements, to discuss impedance data analysis in a friendly environment. The symposium was dedicated to recent developments in chemistry field.

We would like to express our sincere gratitude to all the authors and reviewers of the manuscripts, and to the editorial team of the Bulgarian Chemical Communications, all of whom have critically evaluated and improved the content.

Visiting Editors,

Dr.Agnieszka KACZOR

Medical University of Lublin, Lublin, POLAND

Email*: agnieszkakaczor@umlub.pl*

Assoc.Prof.Dr.Dolunay SAKAR DASDAN

Department of Chemistry, Yildiz Technical University

Istanbul, TURKEY

Email*: dolunaykar@yahoo.com*

Bulgarian Chemical Communications, Volume 49, Issue I, (pp. 5 – 14) 2017

Molecular modelling of 2-iminothiazoles as insecticidal activity

Asiye Meriç*

[*]*Anadolu University, Faculty of Pharmacy, Department of Pharmaceutical Chemistry, Yunusemre Campus, 26470-Tepebasi/Eskisehir, Turkiye*

Submitted June 1, 2017; Accepted September 1, 2017

Insecticides are used in agriculture, medicine, industry and by consumers, indoor. Insecticides are also claimed to be a major factor behind the increase in agricultural 20th century's productivity. On the other hand, modes of their action is important in understanding whether an insecticide will be toxic to unrelated species, such as fish, birds and mammals. On the other hand, molecular docking, a new way of illuminating the effect mechanisms of biologically active chemicals offer a new green chemistry field. As provided herein, although 2-iminothiazoles are designed, synthesized and tested as protein tyrosine phosphatase 1B inhibitors, cannabinoid receptor ligands, pifithrin-α p53 inactivators, etc. there is not any remarkably record on their insecticidal docking study. Present work introduce the molecular modelling and mapping of active site of previously synthesized by us insecticidal 2-iminothiazole derivatives, by using classical docking techniques *i.e.* MOE, etc. and discuss their result.

Key words: molecular modelling; docking; insecticide; 2-iminothiazole; acetyl CoA carboxylase

1. INTRODUCTION

Insecticides are essential tools for preventing or minimizing insect damage to, and significantly increasing the quality and quantity of crops, as well as for improving the quality of life for humans, domestic animals and livestock. There are currently more than 20 different mechanisms, or modes of action, by which various commercial insecticides control insects by disrupting specific vital biological processes, but not all of these can be used against any particular pest insect. Despite the best efforts of the entire crop protection industry, a new insecticide mode of action comes to market only every 5 or 10 years, the last being in 2007 **[1]**.

Neonicotinoid insecticides, i.e. imidacloprid (IMI) and clothianidin (CTD), which act on nicotinic acetilcholine receptors (nAChRs), yet the molecular basis of such action is poorly understood. The crystal structures in complex with aceylcholine binding protein from *Lymnaea stagnalis* (Ls-AChBP) which are deposited to Protein Data Bank (PDB) suggested that the guanidine moiety of IMI and CTD stacks with Tyr185, while the nitro group of IMI but not of CTD makes a hydrogen bond with Gln55 **[2]**.

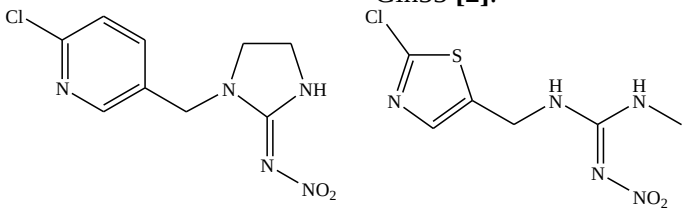

Imidacloprid (IMI) Pdb: 2ZJ**U**

Clothianidin (CTD) Pdb: 2ZJ**V**

Fig. 1. Neonicotinoid insecticides

IMI showed higher binding affinity for Ls-AChBP than that of CTD, consistent with weaker CH–p interactions in the Ls-AChBP–CTD complex than in the Ls-AChBP–IMI complex and the lack of the nitro group-Gln55 hydrogen bond in CTD. Yet, the NH at position 1 of CTD makes a hydrogen bond with the backbone carbonyl of Trp143, offering an explanation for the diverse actions of neonicotinoids on nAChRs **[2]**.

With an aim to explore the binding sites, the complementary applications of molecular docking were employed to understand the interaction between bovine serum albumin (BSA) and the organophosphate insecticides monocrotophos and phosphamidon **[3],** cf. Fig. 4.

* To whom all correspondence should be sent.
E-mail: americ@anadolu.edu.tr; asiye.meric@gmail.com

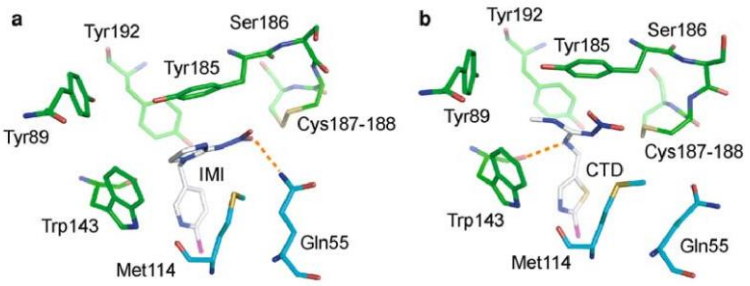

Fig. 2. Imidacloprid (IMI) and clothianidin (CTD) binding to *Lymnaea stagnalis* AChBP (Ls-AChBP). (**a)** IMI–Ls-AChBP complex. (**b)** CTD–Ls-AChBP complex **[2]**.

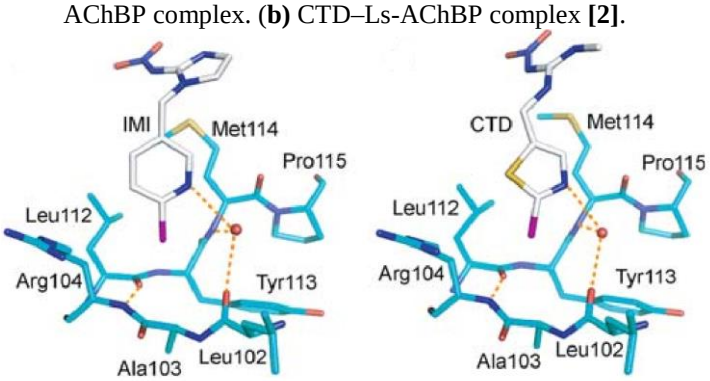

Fig. 3. Electron density maps of bound ligands and their interactions with the loop E region **[2]**.

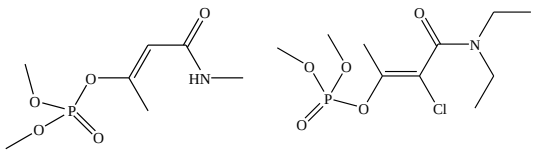

Monocrotophos Phosphamidon

Fig. 4. Organophosphate insecticides monocrotophos and phosphamidon.

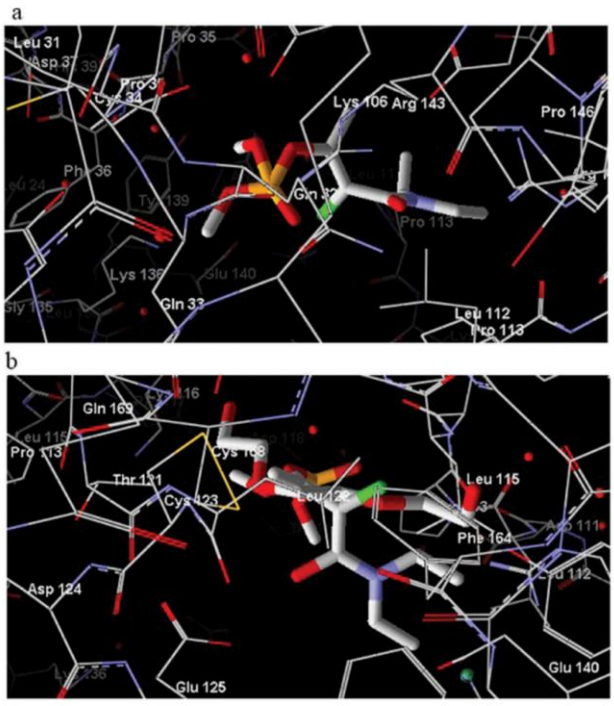

Fig. 5. The molecular docking results suggested that the insecticides bind to BSA into the hydrophobic cavity of subdomain IIA [3].

Among several classes of pesticides, carbamate compounds are widely used insecticides and acaricides. Formetanate (FMT) is one of them [4].

Laccases which are found in many plants, fungi and microorganisms are copper-containing oxidase enzymes. The latest research regarding modeling of laccase inhibition by formetanate suggested that the calculations identified Asp206 as the most relevant moiety in the interaction of FMT with the laccase enzymatic ligand binding domain. The amino acid residue Cys453 was important, because the Cys453-FMT interaction energy was not affected by the dielectric constant, although it was not a very close residue **[4]**.

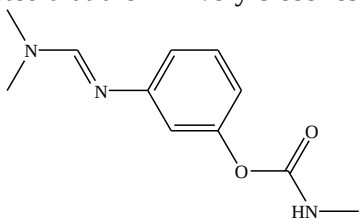

Fig. 6. Formetanate (FMT).

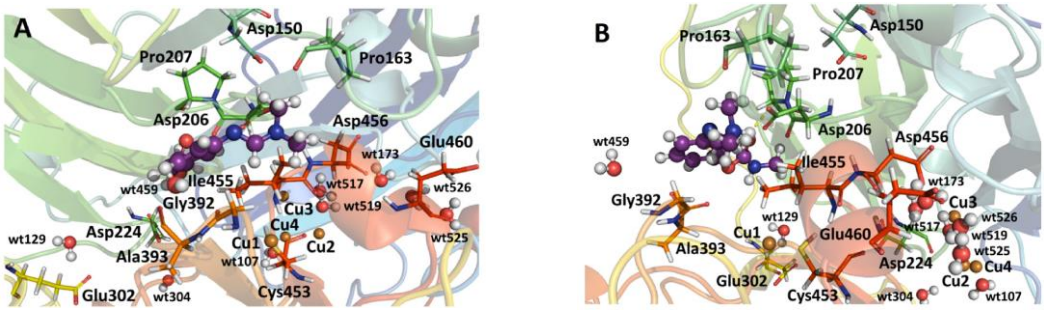

Fig. 7. Schematic representation of the binding pocket of the Lac showing the most important residues involved in the binding interaction in two different views. The only relevant residue that forms a hydrogen bond with **FMT** is **Asp206**, as shown in **B**. **Cys453** residue is important for interaction [4].

QSAR analyses of organophosphates for insecticidal activity and its *in-silico* validation using molecular docking study have been revealed that selected OP analogues from combinatorial library were docked against the generated model of AChE of *M. domestica* as receptor. The binding pockets of these ligands were observed to be very similar to that of other OPs including TCVP as reported earlier, thus hinting about the insecticidal nature of the selected OP ligands. The binding sites (**Fig. 8**) analyses reflected that four amino acid residues (Ser-235, Try-160, Trp-83, Phe-368 and His-477) were commonly present as the interacting residues with docked OP ligands. Also, the binding efficiency was elevated when other aromatic side chains (*viz*., Tyr-367, Tyr-367, *etc*.) were involved in interaction with the ligands **[5]**.

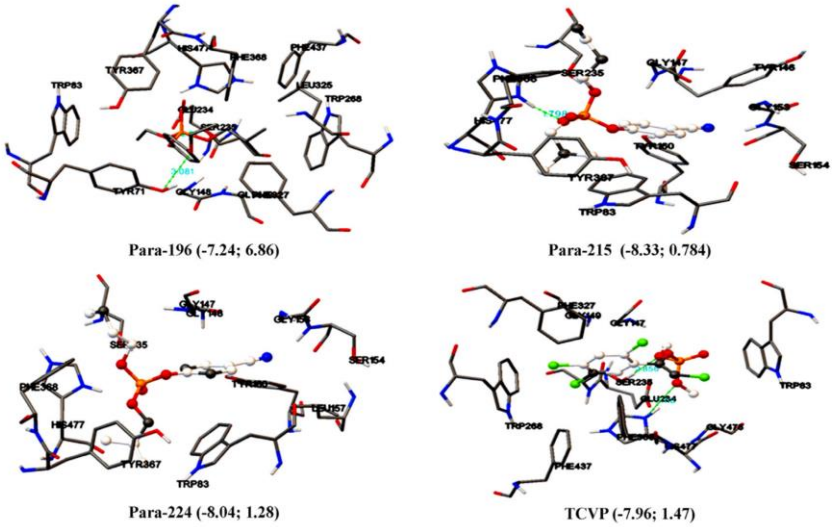

Fig. 8. The docking site of selected OP analogues of combinatorial library and Tetrachlorvinphos (**TCVP**) showing interacting residues when docked against *M. Domestica* AChE (pdb ID: **1DX4) [5]**.

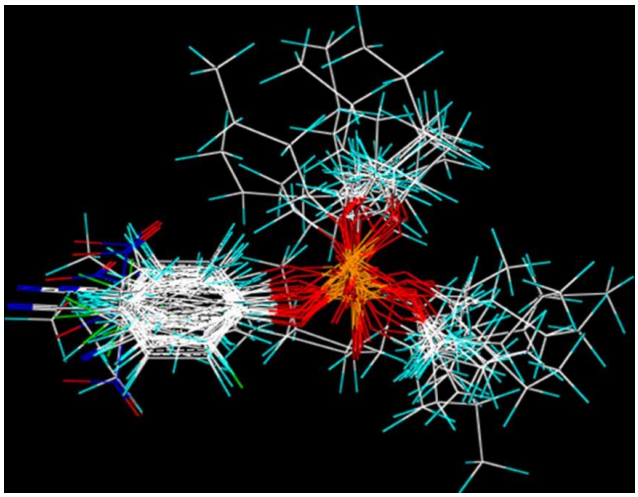

Fig. 9. Dataset compounds aligned on Molecule OP22 (maximum activity) **[5]**.

Molecular modeling of insecticides have been studied for tetronic acid derivatives via the inhibiton of acetyl-CoA carboxylase (ACCase) **[6]**.

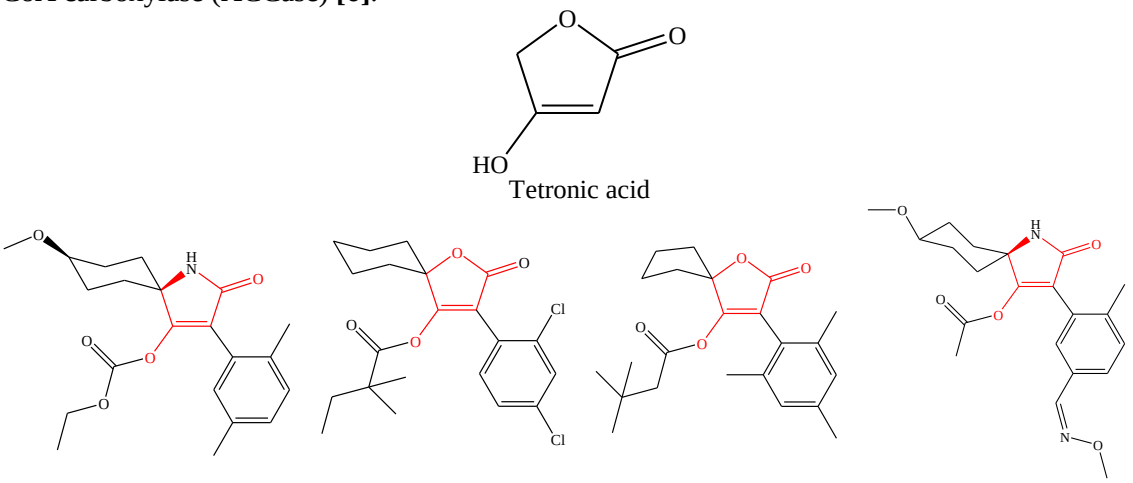

Fig. 10. The structure of representative tetronic acid derivatives and designed lead compound **[6]**.

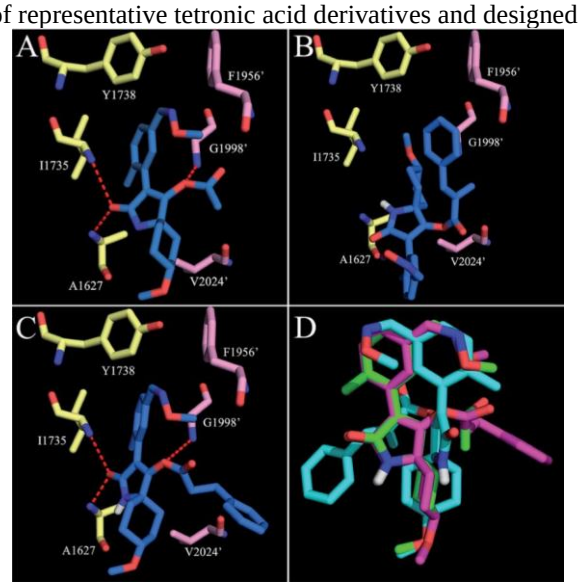

Fig. 11. Interaction mode of ACCase and active compounds 91b (**A**), 91j (**B**) and 91k (**C**) proposed by molecular docking and their molecular overlay (**D**). (pdb ID: **3PGQ) [6].**

This application relates to **thiazolylidene** containing compounds, compositions comprising such compounds, and methods of treating conditions and disorders using such compounds and compositions.

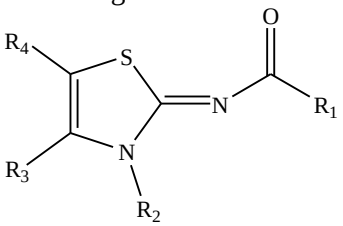

Fig. 12. Thiazolylidene compounds.

(-) – Δ^9-Tetrahydocannabinol (Δ^9-THC), the major psychoactive constituent of marijuana, exerts a broad range of effects through its interactions with two cannabinoid (CB) receptor subtypes, CB1 and CB2 **[7].**

Organophosphorus compounds (OPs) may irreversibly inhibit acetylcholinesterase (AChE), this enzyme is responsible for the hydrolysis of acetylcholine (ACh) which terminates nerve impulse transmission. A promising alternative route for OP detoxification and degradation is enzymatic catalysis. OP degrading enzymes are phosphotriesterase (PTE) (cleave different OP, breaking P-O, P-F, P-CN and Ps bonds), Human Serum Paraoxonase 1 (*Hss*PON1) (degrade substrates such as esters, lactones, oxidized phospholipids and OPs), diisopropyl fluorophosphatase (DFPase) and Human Butyrycholinesterase G117H Mutant (*Hss*BuChE) **[8]**.

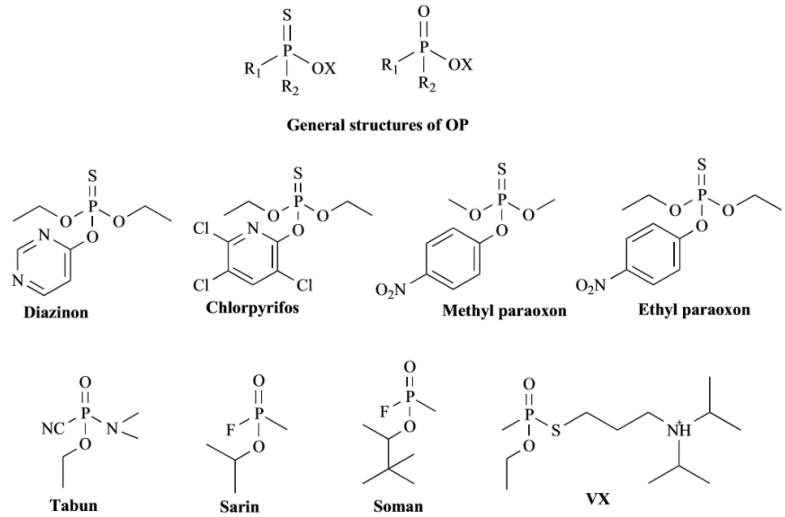

Fig. 13. General structures of organophosphorus (OPs) and common used OP compounds.

This reported knowledge point out that, at the AChE active site, the catalytic triad (Ser203-Glu334-His447) is found at the bottom of the active site gorge, surrounded by three important structural features for catalytic activity: the acyl pocket (residues Phe295, Phe297 and Phe338), the oxyanion hole (main chain nitrogen from residues Gly121, Gly122 and Ala204), and the choline-binding site (Trp86 and Tyr337) (**Fig A**). The phosphoryl oxygen of tabun adduct interacts with the amino acid residues in the oxyanion hole (distance of 2.5, 2.7 and 3.0Å from Gly121, Gly122 and Ala204, respectively). The dimethylamino group is in the acyl pocket, interacting with Trp236 and Phe338 residues (**Fig B**). The two Zn^{2+} ions (α-Zn and β-Zn) in the PTE active site are found at a distance of ~3.4Å from each other and they are linked to the enzyme structure by means of the side chains of His55, His57, His201, His230, Asp301 and Lys169. (**Fig C**).

The proposed reaction mechanism for the PTE catalyzed reaction begins with a nucleophilic attack by an activated water molecule on the P center, resulting in an inversion of configuration. That is, the reaction takes place via bimolecular nucleophilic substitution (SN2) mechanism, where the Asp301 serves as a weak base, which removes an H atom of the water molecule, activating it. Afterwards, the resulting hydroxyl ion attacks the central P. A second reaction mechanism is possible

for the OP degradation by PTE. In this case, there will be an attack to the P center directly by the carboxylic oxygen from the side chain of Asp301, promoting the expulsion of the leaving group and

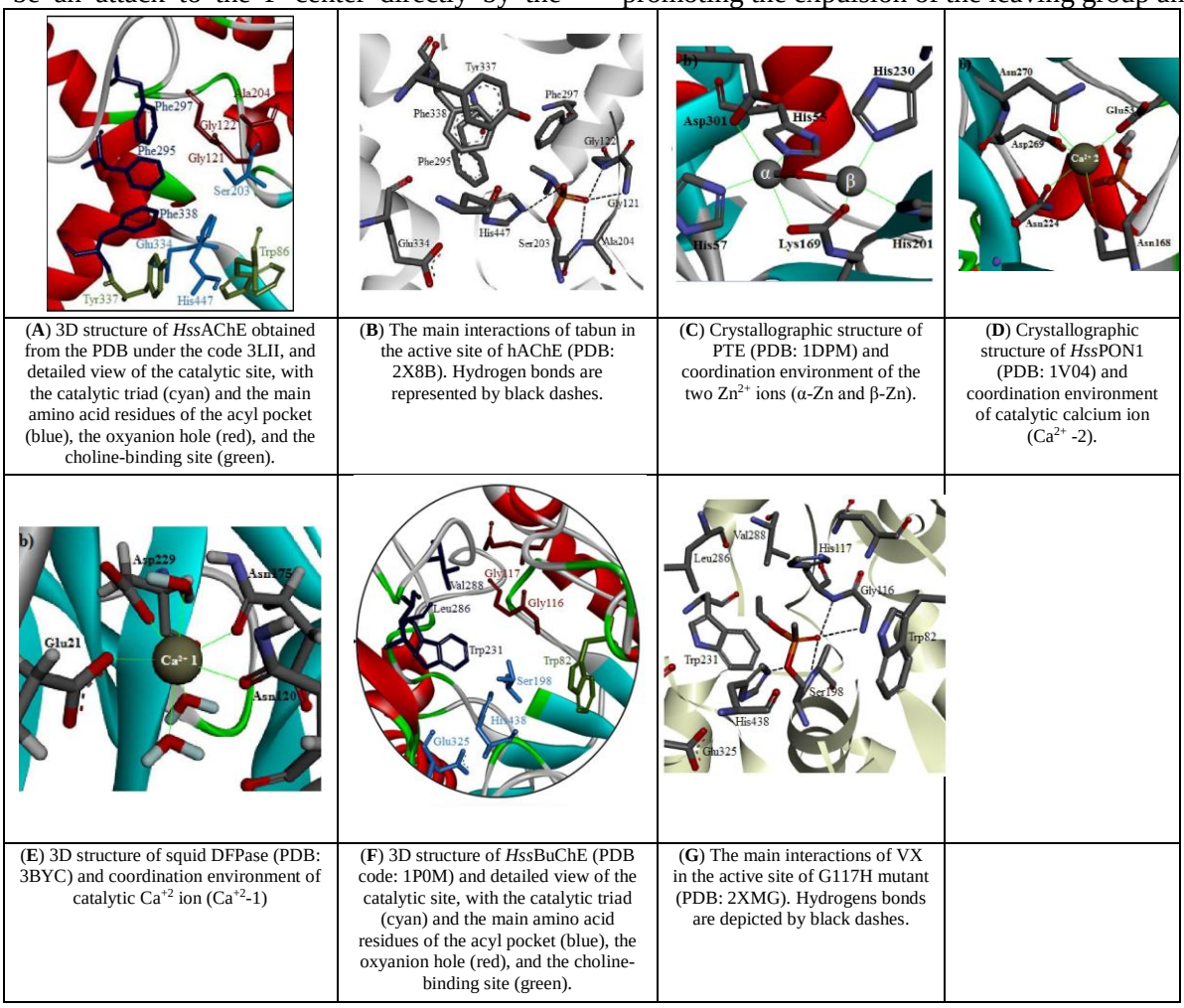

(**A**) 3D structure of *Hss*AChE obtained from the PDB under the code 3LII, and detailed view of the catalytic site, with the catalytic triad (cyan) and the main amino acid residues of the acyl pocket (blue), the oxyanion hole (red), and the choline-binding site (green).

(**B**) The main interactions of tabun in the active site of hAChE (PDB: 2X8B). Hydrogen bonds are represented by black dashes.

(**C**) Crystallographic structure of PTE (PDB: 1DPM) and coordination environment of the two Zn^{2+} ions (α-Zn and β-Zn).

(**D**) Crystallographic structure of *Hss*PON1 (PDB: 1V04) and coordination environment of catalytic calcium ion (Ca^{2+} -2).

(**E**) 3D structure of squid DFPase (PDB: 3BYC) and coordination environment of catalytic Ca^{+2} ion (Ca^{+2}-1)

(**F**) 3D structure of *Hss*BuChE (PDB code: 1P0M) and detailed view of the catalytic site, with the catalytic triad (cyan) and the main amino acid residues of the acyl pocket (blue), the oxyanion hole (red), and the choline-binding site (green).

(**G**) The main interactions of VX in the active site of G117H mutant (PDB: 2XMG). Hydrogens bonds are depicted by black dashes.

Fig. 14. Detailed view of the catalytic site of OP degrading enzymes with their ligands **[8]**.

cleavage of the OP. This reaction is assisted by Asp301 (for **Fig C**).In the active site f DFPase, the Ca^{+2}-1 is coordinated with seven ligands, three water molecules and the side chain of Glu21, Asn120, Asn175, and Asp229 (**Fig E**).

BuChE has a large active site (500 Å³) and it is normally subdivided in four parts: the acylation site, the choline-binding pocket, the acylbinding pocket and the peripheral anionic site (PAS). The acylation site is located at the bottom of the gorge and contains the catalytic triad: Ser198, Glu325 and His438 in *Hss*BuChE. The oxyanion hole is important to provide stabilization to the proposed transition states in the hydrolysis reaction through H-bonds and it consists of the side chains of residues Gly116, Gly117 and Asp199. The key residue of the choline-binding pocket is the Trp82, which is involved in cation-π interactions. The acyl-binding pocket is composed mainly by Trp231, Leu286 and Val288. And, lastly, the PAS is located at the rim of the gorge, however this is controversial because three key aromatic residues in the PAS of AChE are missing in BuChE (**Fig F**).

Proposed hydrolysis mechanism for *Hss*BuChE cover that as a first Ser198 is activated by His438 and Glu325 and then Ser198 attacks the OP center, forming a pentavalent TS, before the departure of the leaving group. The TS is stabilized by the amino acid residues in the oxyanion hole. Then, a phosphorylated enzyme intermediate is formed. This intermediate is very stable in the wild type *Hss*BuChE but unstable in the G117H mutant. The following step is the nucleophilic attack on the P atom by a water molecule, which may be activated by His438. Lastly, the product is released and the enzyme regenerated (for **Fig F**).

In (**Fig G**), the main interactions of VX in the G117H active site are represented. The VX adduct is positioned in such way that methyl group is located near His438 and the ethoxy group in the acyl-binding pocket, pointing toward Val288. The phosphoryl oxygen is interacting with the main-chain nitrogen atoms of the residues in the oxyanion hole (distance of 2.7, 2.8 and 3.2Å from His117, Gly116 and Ala199, respectively).

As pointed out at the many manuscript, bioremediation presents the most promising technology today to destroy OPs have been shown to be very efficient in detoxification of several OPs but the lack of knowledge of their mechanisms of action have limited the development of this action of these enzymes and have already contributed to important advances in the engineering of more efficient OP degrading enzymes. It is apparent that the theoretical investigations will continue reveal much more and contribute for the development of more efficient ways of detoxifying OPs **[8]**.

On the other hand, our focused on spesific functional heterocycle, 2-iminothiazoles are designed, synthesized and tested as protein tyrosine phosphatase 1B inhibitors **[9]**, cannabinoid receptor ligands **[7]**, pifithrin-α p53 inactivators **[10]**, etc. there is not any remarkably record on their insecticidal docking study.

technology. Fortunately, computational enzymology, using molecular modeling techniques like molecular docking, MD simulations, and QM/MM studies, provide the appropriate tools to improve the knowledge of the mechanisms of

The present work aimed to introduce the molecular modelling and mapping of active site of previously synthesized by us insectisidal 2-iminothiazole derivatives **[11]**, by using classical docking techniques, *i.e.* MOE, etc. **[12]**

2. MATERIAL AND METHODS

Synthesis

Synthetic procedure of 2-iminothiazole compounds was described previously by us **[11]**. Promising insecticid derivatives were selected for docking data set and illustrated on Table 1.

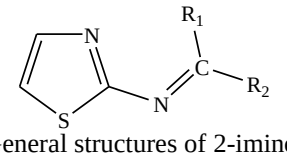

Fig. 15. General structures of 2-iminothiazoles

Table 1. The structures of tested compounds:

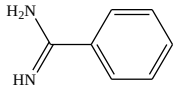

Benzamidine

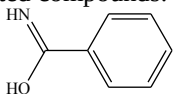

Benzimidic acid

Tested comp. ID	The structures of tested compounds	Tested comp. ID	The structures of tested compounds	Tested comp. ID	The structures of tested compounds
6	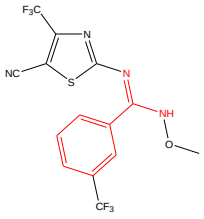 N-(5-Cyano-4-trifluoromethyl-thiazol-2-yl)-N'-methoxy-3-trifluoromethyl-benzamidine	9	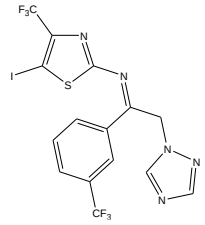 (5-Iodo-4-trifluoromethyl-thiazol-2-yl)-[2-[1,2,4]triazol-1-yl-1-(3-trifluoromethyl-phenyl)-ethylidene]-amine	26	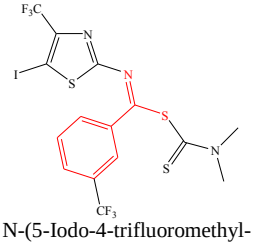 N-(5-Iodo-4-trifluoromethyl-thiazol-2-yl)-3-trifluoromethyl-thiobenzimidic acid dimethyldithiocarbamyl ester
95	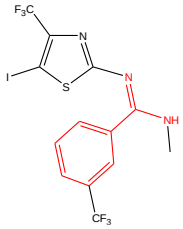 N-(5-Iodo-4-trifluoromethyl-thiazol-2-yl)-N'-methyl-3-trifluoromethyl-benzamidine	98	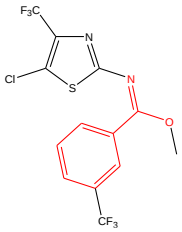 N-(5-Chloro-4-trifluoromethyl-thiazol-2-yl)-3-trifluoromethyl-benzimidic acid methyl ester	99	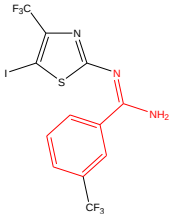 N-(5-Iodo-4-trifluoromethyl-thiazol-2-yl)-3-trifluoromethyl-benzamidine

121

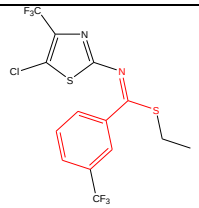

N-(5-Chloro-4-trifluoromethyl-thiazol-2-yl)-3-trifluoromethyl-thiobenzimidic acid ethyl ester

143

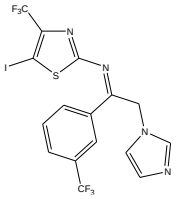

[2-Imidazol-1-yl-1-(3-trifluoromethyl-phenyl)-ethylidene]-(5-iodo-4-trifluoromethyl-thiazol-2-yl)-amine

Materials

Literature search were performed by using SciFinder, Web of Science and Protein Data Bank databases. Chemical drawing programs: 2D Drawings were made using ChemDraw and ISIS Draw programs. 3D drawing of chemical molecules was carried out using the MOE 2016 program (AUBAP, 2017, 1701S009). All text writing and chemical drawing, application procedure were accomplished by Intel Core i7 processor (7700 HQ), Windows 2010 operating system workstation (AUBAP, 2017, 1701S009). For docking study, reference ligand-receptor/protein complexes were transferred from RCSB Protein Data Bank for known active site placement. For docking study, the active chemical compound (ligand) was removed from the ligand-receptor/protein complex crystal which is transferred from the Protein Data Bank, and replaced with designed compounds, then investigate to whether show similar interactions with the reference ligand.

Methods

As initial, data set compounds overlay and observed the alignments. As a first attempt to docking, imidacloprid (IMI) was selected as model and its crystal complex structure with nicotinic acetilcholine receptor (nAChRs) was retrieved from the RCSB Protein Data bank (PDB: 2ZJ**U**).

Molecular docking

Preparation of receptor

Molecular Operating Environment (MOE 2016) was used for current studies **[12]**. The protein preparation step involved 3D protonation energy minimization and active site identification. The crystal structure of Ls-AChBP was obtained from protein data bank (PDBID 2ZJU) **[2]**. The co-crystallized bound compound and water molecules were stripped off from the crystal structure. Protein was energy minimized and 3-D protonated by using the structure preparation module of MOE. As the protein contains the co-crystallized ligand, the active site was identified by using site finder module of the MOE. The pocket was found to be deep cleft lined with the key residues including both hydrophobic and hydrophilic amino acids.

Preparation of ligands

The ligand files for molecular docking studies were prepared in Molecular Operating Environment (MOE-2016.0802) by chemical computing group (CCG) and were followed by energy optimization at standard MMFF94 force field level, with a 0.0001 kcal/mol energy gradient convergence criterion **[12]**. The optimized geometries were saved in molecular data base file for further studies.

Molecular docking studies

The optimized ligands were docked with the Ls-AChBP (PDBID 2ZJU) protein using the MOE-Dock program. For docking, default MOE docking parameters, i.e. Triangle Matcher Algorithm with two rescoring functions, London dG and GBVI/WSA dG were utilized to generate 30 poses of each compound. As a result of docking run, mdb output files were generated enclosing all docking results with scoring and multiple conformations of ligands. All the docked conformations were analyzed and the best scored pose for each compound was selected for further studies of interaction evaluation. The 2D ligand-protein interactions were visualized using the MOE ligand interactions program.

RESULTS

Activity on nicotinic acetilcholine receptors (nAChRs) has been checked by using Ls-AchBP crystal structure complexed with imidacloprid (PDBID 2ZJU) replaced by data set. Docked compounds on 2ZJU showed correspondence interaction with imidacloprid.

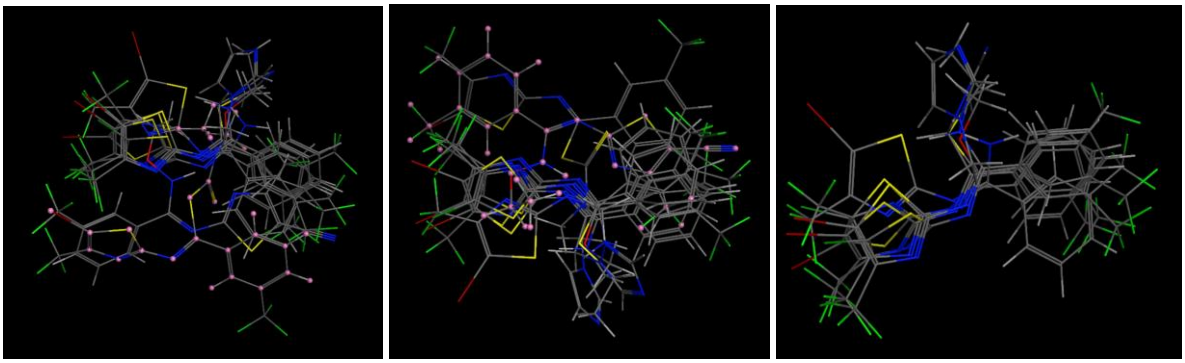

Fig. 16. Alignment of dataset compounds. (a) Selected compound as pink is Comp. 26;(b) Selected compound as pink is Comp. 6; (c) Alignment of all dataset compounds except Comp. 26 and Comp. 6.

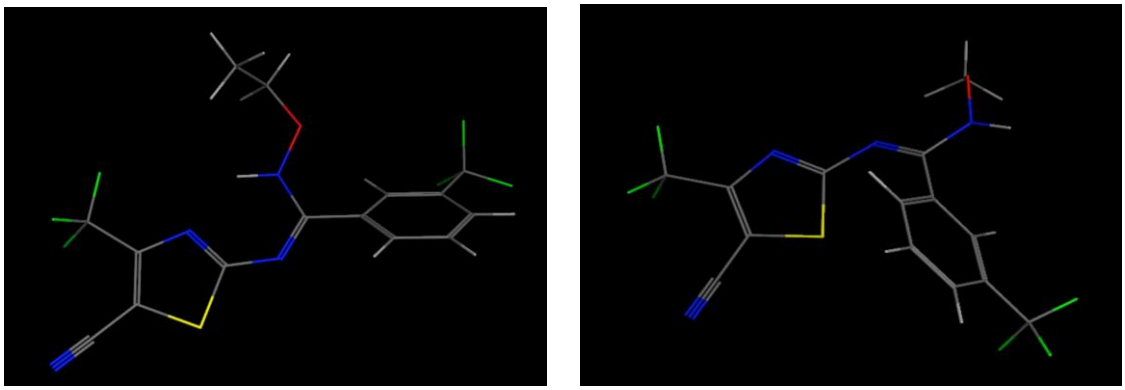

Fig. 17. Two possible configuration of Comp. 6.

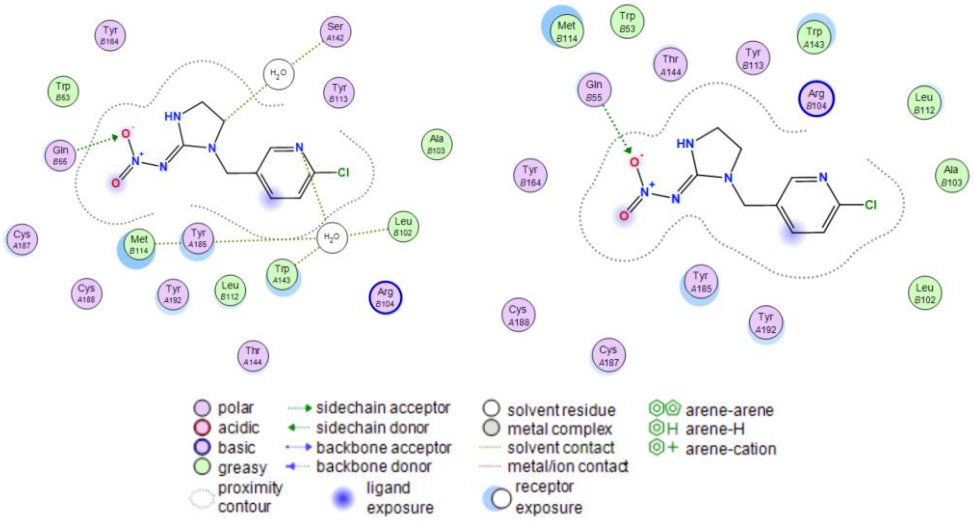

Fig. 18. PDB: 2ZJU ligand interaction with its own ligand IMI **(a)** together with water, **(b)** later than removed water.

CONCLUSIONS

It is stand out that the alignment of data set is not able to accomplish because of non-symmetric property of imines. Their configuration of imines may result in different activity or ranging from more to less affinity to related enzyme binding. To identify clearance of activity, further purification and elucidation of structures i.e. X-ray crystallography may offer valuable activity results for non-symmetric imines. Based on the preliminary docking study of data set, we observed favourable interaction complexes of the designed compounds with target protein Ls-AchBP. Further biological testing will be carried out to verify the docking studies. In accordance with the *in-silico* docking and activity results would allow us to develop new strategies for novel active compounds.

Acknowledgements. *This work is partly supported by Anadolu University, Scientific Research Projects Commission, 2017, Project Number ≠1701S009.*

REFERENCES

1.https://products.basf.com/documents/pim;view/en/879746.5586133.Insecticide%20Mode%20of%20Action%20Technical%20Training%20Manual.pdf
2. M. Ihara, T. Okajima, A. Yamashita, T. Oda, K. Hirata, H. Nishiwaki, T. Morimoto, M. Akamatsu, Y. Ashikawa, S. Kuroda, R. Mega, S. Kuramitsu, D.B. Sattelle, K. Matsuda, *Invert. Neurosci*., **8,** 71 (2008).
3. M. Suganthi, K.P. Elango, *Phys. Chem. Liq.*, **55,** 165 (2017).
4. A.C.V. Martins, F.W.P. Ribeiro, G. Zanatta, V.N. Freire, S. Morais, P. Lima-Neto, A.N. Correia, *Bioelectrochemistry*, **108**, 46 (2016).
5. R.R.K. Niraj, V. Saini, A. Kumar, *Env. Toxic. Pharm*., **40,** 886 (2015).
6. T.-T. Yao, J.-L. Cheng, B.-R. Xu, M.-Z. Zhang, Y.-Z. Hu, J.-H. Zhao, X.-W. Dong, *RSC Advances*, **5**, 49195 (2015).
7. W.A. Carroll, M.J. Dart, A. Perez-Medrano, J.M. Frost, S. Peddi, *US Patent* 20080287510 A1 (2008).
8. T.C. Ramalho, A.A. Castro, D.R. Silva, M.C. Silva, T.C.C. Franca, B.J. Bennion, K. Kuca, *Cur. Med. Chem*., **23,** 1041 (2016).
9. D.-R. Ahn, J. Lee, D. Shin, *Bull. Korean Chem. Soc*., **34,** 2861 (2013).
10. N. Pietrancosta, F. Maina, R. Dono, A. Moumen, C. Garino, Y. Laras, S. Burlet, G. Quelever, J.-L. Kraus, *Bioorg. Med. Chem. Lett*., **15,** 1561 (2005).
11. I. Iwataki, A. Meriç, E.L. Moyano, R. Hatano, *US Patent 6 617 341 B1* (2003).
12. https://www.chemcomp.com/MOE2016.htm

Bulgarian Chemical Communications, Volume 49, Speial Issue I (pp.15-20) 2017

Solid-state characterization of poly(ethylene glycol) samples prepared by solvent cast technique

C. Özdemir Dinç[a,*], A. Güner[b]

[a] *Mustafa Kemal University, Department of Chemistry, Physical Chemistry Division, TR-31034 Serinyol, Antakya, Turkey*

[b] *Hacettepe University, Department of Chemistry, Polymer Chemistry Division, TR-06532 Beytepe, Ankara, Turkey*

Submitted June 1; Accepted Septembe 1, 2017

The effect of solvents (H-donor; H-acceptor and both H-acceptor and H-donor solvents) casted on the poly(ethylene glycol) (PEG) samples with varying molecular weights (2000, 4600, 8000 and 10000) was performed solid-state characterization by Fourier Transform Infrared Spectroscopy (FTIR), Raman and X-ray Diffraction (XRD) in submitted study. In this study, spectral differences were classified with respect to stretching, bending, rocking, angle bending, internal rotation frequencies and low-frequency Raman region according to functional groups and thus crystallinity were evaluated as related with solvent character and polymer molecular weight. Crystalline and amorphous regions in the XRD diffractograms have been found by Polynomial Regression method through Microsoft Office Excel program and subsequently, crystallinity percentages were evaluated. From XRD spectra of PEG/solvent systems, the highest decrease in crystallinity percent has been detected in the sample cast from tetrahydrofuran. On the other hand, the largest frequency shifts of various stretching and bending vibrations of PEG have been observed for the samples cast from chloroform and especially tetrahydrofuran in FTIR and Raman spectra.

In the end of trio study, the parallelism of both computation and thermodynamic and spectroscopic data about solubility profiles of PEG/solvent systems has been determined. The results indicated that association power of solvents in PEG samples prepared by solvent cast technique was decreased below order:

tetrahydrofuran > chloroform > dimethyl sulfoxide > methanol > water.

Key words: Poly(ethylene glycol); solvent cast technique; fourier transform infrared spectroscopy; raman; x-ray diffraction.

INTRODUCTION

Insecticides are essential tools for preventing or m Poly(ethylene glycol)s (PEG)s comprehend a series of water soluble, no irritating, linear chain polymers of oxyethylene units, with low toxicity. These properties enable their use for commercial and technological applications such as purification of biological materials, pharmaceutical drugs, edible films for food coating and water treatment [1-6]. Chen et al. [7] remarked that PEG aqueous solutions can profoundly affect water structure, reducing cohesivity and some aspects of H-bonding and thereby increasing the solubility of relatively less polar species. Dinc et al. [8] have calculated solubility parameters with group contribution methods among indirect methods for PEG and different solvents. They have been determined as the best solvent is THF and weakest solvent is water with algorithmic calculations. In addition, have been investigated solution thermodynamics of PEG/solvent systems with viscometric studies [9]. The unperturbed molecular dimensions of PEG samples have been evaluated. The thermodynamic aspects of PEG in dilute solutions have been explained. The investigation of spectral evidences for algorithmic calculations and thermodynamic magnitudes presents purpose of offered study. In the submitted spectroscopy study, PEG samples prepared by solvent casting technique and pristine PEG samples (no solvent interaction) were compared and characterized in solid-state by FTIR, Raman and XRD imagines.

MATERIALS AND METHODS

Reagents

PEG samples used in this study were supplied from Aldrich. The molecular weight distribution and densities of polymer samples were determined by the manufacturer and are given in Table 1.

Different solvents **(**H-donor solvent: chloroform; H-acceptor solvents: THF and DMSO; both H-acceptor and H-donor solvents: methanol and water) were used without further purification to prepare sample by casting technique. All other reagents were of analytical grade and used without further purification. The water used in the study was of ultrapure grade.

* To whom all correspondence should be sent.
E-mail: ozdemir.cemile@gmail.com or cozdemir@mku.edu.tr

Table 1. The molecular weight characteristics and densities of pristine PEG samples.

polymer	density at 25 °C (g /ml)	$\overline{M}_n$	$\overline{M}_w$	$\overline{M}_z$	polydispersity index
PEG 2000	1.127	1880	2030	2666	1.080
PEG 4600	1.127	3940	4040	4099	1.025
PEG 8000	1.270	7330	7550	7659	1.030
PEG 10000	1.070	10850	10950	11069	1.009

*GPC-RALS study conditions:

Solvent: NaH_2PO_4, NaCl, Column set: 2xG2500PWXL aqueous column. Triple detector: refractive index, right angle light scattering, viscometer. Detector temperature: 35 ºC.

Preparation of samples by solvent casting technique

Twenty different solutions were prepared by adding of the appropriate amount of the each solvent (water, chloroform, DMSO, THF and methanol) on PEG samples with different molecular weights (2000, 4600, 8000 and 10000). The concentrations of PEG solutions were changed between 1.0-0.2 g/dL according to molecular weight of polymer. And then, these solutions were magnetically mixed for 2h until completely homogenized at room temperature and dried at 25°C under vacuum.

XRD measurements

Casting technique for XRD samples was done by using best solvent (THF), and weakest solvent (water) determined for PEG from algorithmic calculations [8]. XRD patterns were taken at Hacettepe University, in Physics Engineering Department by using a Rigaku DMAX 2200 X-ray Powder Diffractometer in the $2\theta = 5^o - 60^o$ range with CuK_α radiation. This diffractometer consists of a RINT2000 wide angle goniometer with a 1/2º dispersion slit, a 0.73 mm scatter slit and a 0.3 mm receiving slit. The Cu anode X-ray tube was operated at 40kV and 36mA in combination with a Ni filter to give monochromatic $CuK\alpha$ X-rays. Measurements were taken from 5º to 60º in the Bragg's angle 2θ scale at a step size of 4º per min for qualitative analysis. Diffractograms were taken at room temperature consecutively. Crystalline and amorphous regions were found by polynomial regression method subsequently, crystallinity percentages were evaluated.

FTIR measurements

Samples (0.01 g) were finely ground and analyzed by dispersing them in 0.09 g of dried spectroscopic grade KBr (Merck) by pressed-disc technique. The FTIR spectra were recorded on an ATI UNICAM Mattson 1000 FTIR spectrometer at room temperature. The spectra were collected over the range 4000-400 cm^{-1} by averaging 40 scan at a maximum resolution of 2 cm^{-1}.

Raman Measurements

Casting technique for Raman samples was done by using best solvent (THF), mediate solvent (chloroform) and weakest solvent (water) determined for PEG from algorithmic calculations [8]. Raman spectra of samples were recorded using Labram HR800 Raman spectrometer (Jobin Yvon) with a He-Ne laser source emitting at 633 nm, 600-1200 grooves/mm holographic grating and a charge coupled device (CCD) detector. Raman spectra were obtained in 250 s integrations with an average of three scans. Spectra were recorded with reproducibility within 1 cm^{-1}, hole: 400 μm, slit: 150 μm, resolution: 0.1μm.

RESULTS AND DISCUSSION

XRD analysis

X-ray powder diffractograms of PEG samples are shown in Figs. 1-2 which show diffuse areas with sharp band, suggesting uniform crystallization.

In Figs. 1 and 2, diffractions were mainly observed at two angles (2θ =19.3° and 23.5°). It was found that these two angles are in quite good agreement with those in literature and it is a semi-crystalline polymer [10-15].

The crystallinity results of PEG samples were given in Table 2.

In pristine polymer samples, percentage of crystallinity for PEG 2000 and 4600 was yielded 62-63% whereas for PEG 8000 and 10000, this value is dropped to 56%. As the molecular weight of the PEG increases, concentration of the OH groups is reduced, and, in this way, the number of H-bonds and crystallinity is decreased. From Table 2, it was observed crystallinity was decreased as the solvents penetrate into the structure of pristine PEG. The crystallinity results revealed that THF being more effective than water was led to a greater change in polymer conformation with introducing to PEG structure. This behavior, in turn, was ended up with the conclusion that crystallinity of samples prepared by casting THF is drop more than those in water. While Petrova et al. [11] find the crystallinity as 65% through X-ray studies for PEG 2000.

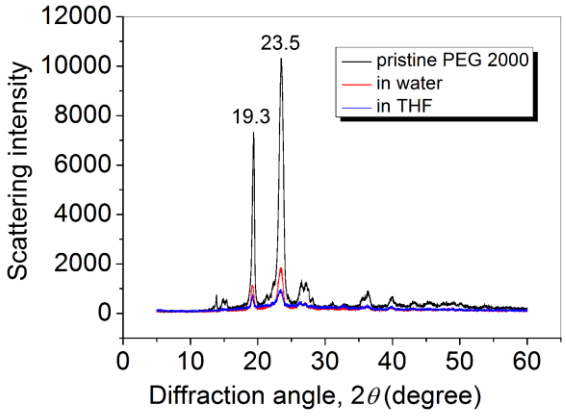

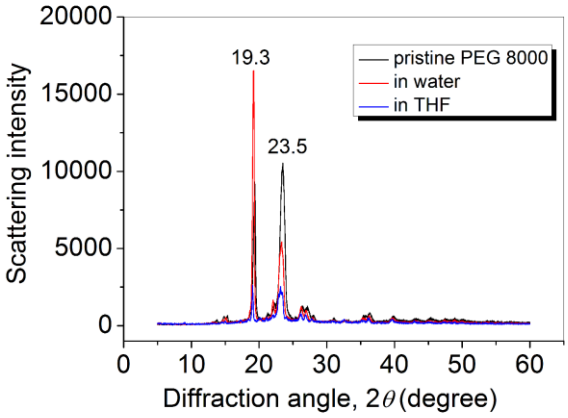

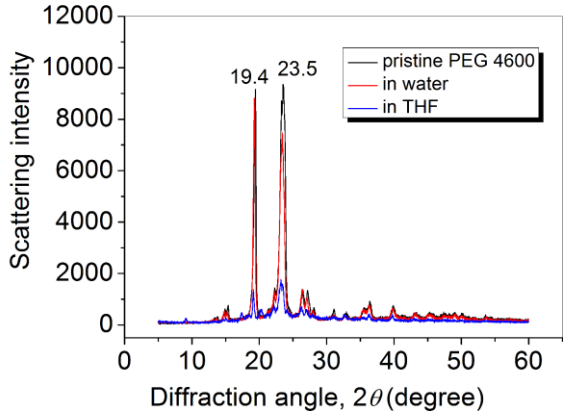

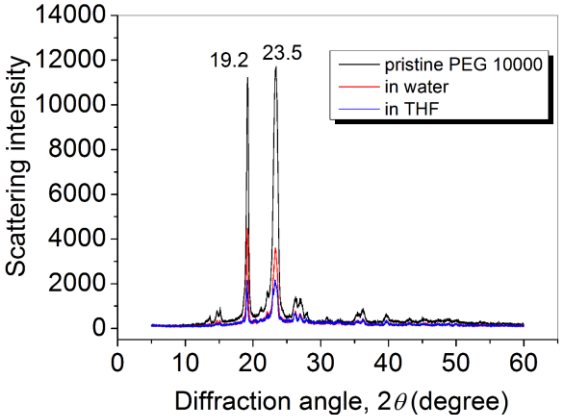

Figure 1. XRD patterns of the pristine and solvent-treated PEG (2000 and 4600).

Figure 2. XRD patterns of the pristine and solvent-treated PEG (8000 and 10000).

Table 2. The percent crystallinity of pristine and solvent-treated PEG samples.

	X_c (%)		
	pristine PEG	PEG prepared by casting water	PEG prepared by casting THF
PEG 2000	62	44	33
PEG 4600	63	44	33
PEG 8000	56	46	33
PEG 10000	56	46	32

FTIR and Raman spectroscopy

In this part, spectral differences have been grouped with respect to characteristic fields and thus changes related with solvent character and molecular weight was evaluated.

O-H stretching

When investigated on the basic of molecular weight among pristine PEG samples, whilst the OH stretching frequency of the pristine PEG 2000 was observed at 3426 cm^{-1}, the OH stretching frequency of pristine PEG 10000 was shifted towards 3504 cm^{-1}. This shift is around ~80 cm^{-1} . It can be clearly stated that much higher OH stretching frequency is attributed to the presence of intra- and intermolecular H-bonding interactions $[O-H\cdots O-H$ as well as $O-H\cdots O$ (ether oxygen)] in PEG [16]. PEG 2000, as a consequence of the abundance of OH end-groups and H-bond formation of these groups among themselves, the OH stretching frequency is weakened and the spectrum shifted towards lower wavenumbers. As the molecular weight increases, peak areas were decreased relatively because the number of end groups fall by increasing molecular weight. The shift of free OH vibrations to higher wavenumbers displayed in pristine PEG samples with increasing molecular weight was also observed in the samples prepared by casting solvent (Table 3).

Table 3. FTIR bands of OH end-group stretching for different molecular weight PEG/solvent systems.

Polymer	ν_{-OH} (cm^{-1})					
	pristine PEG	PEG casting from				
		water	methanol	DMSO	chloroform	THF
PEG 2000	3426(m)	3494(m) 3421(m)	3424 (m)	3475(m)	3444(m)	3289(m)
PEG 4600	3478(m)	3490(m) 3428(m)	3490 (m) 3424 (m)	3475(m)	3482(m)	3270(m)
PEG 8000	3484(m)	3498(m) 3421(m)	3486 (m)	3490(m)	3478(m)	3289(m)
PEG 10000	3504(m)	3579(m) 3509(m) 3421(m)	3552 (m)	3594(m)	3583(m)	3278(m)

*) m: medium, w: weak

C-H stretching

C-H stretching vibrations display a broad and multishouldered spectral behavior in a wide frequency range of 2800-2950 cm^{-1} [17-19]. In FTIR spectra of pristine (PEG)s, antisymmetrical CH_2 stretching vibration is determined as a shoulder between 2942 and 2952 cm^{-1}. On the other hand, this frequency was shifted to lower fields and occurred ~10 cm^{-1} in samples prepared by casting solvent. This is clear evidence that implies that the hydrophobic interactions between the CH_2 groups of polymer were being destructed in the presence of solvent. The frequency values were not vary much for the samples prepared by casting the other solvents whilst this shift was occurred at much lower frequency values in the sample prepared by casting THF. This behavior implies that symmetrical stretching was weakened as a consequence of the hydrophobic interactions of CH_2 groups.

CH_2 Bending

Scissoring vibrations of CH_2 groups (in-plane bending) displayed in the range 1468-1473 cm^{-1} for pristine PEG samples were observed to weaken and shifted towards lower frequencies for samples prepared by casting of different solvents from FTIR spectra. The highest CH_2 bending shift was observed on the sample prepared by casting THF. It was considered that scissoring motion is more flexible within the measure of disruption of hydrophobic interactions of CH_2 groups. CH_2 in-plane bending vibrations almost impossible to detect in FTIR were also mostly observed as doublet peaks at around 1480 cm^{-1} at Raman spectra of submitted study.

C-O stretching

In FTIR evaluations of all PEG samples, bands observed at 1000-1200 cm^{-1} are extremely broad and highly shouldered. After treatments with the solvents, the three specific bands (two shoulders and a weak band) were become more prominent. The first one among these is the band appearing at the wavenumber range 1145-1153 cm^{-1}. This region may be described as the region of C-O-C asymmetrical stretching vibrations [20] and these vibrations may be observed as two distinct bands [21]. The band appearing at a higher frequency value was the one participating in intramolecular H-bond while the latter occurring at a lower wavenumber was characterized the C-O stretchings vibrations participating in intermolecular H-bond.

The bands occurring at 1145-1153 cm^{-1} in pristine PEG samples were considered as C-O stretchings which do not participate in H-bonding. The shift towards lower frequency (about 5 cm^{-1}) of these bands in samples prepared by casting other solvents apart from THF is quite significant. However, more important than this, in THF which is considered as the best solvent, this band surprisingly was vanished. Polymer coil extends in good solvents thus leading to H-bond formation between etheric oxygen and OH groups, consequently weakening C-O stretching vibration, shifting of spectrum towards a down-field and even with the complete extinction of that band.

The quite significant band observed at 1103-1106 cm^{-1} in all samples was showed somewhat spectral variations although very slight. This band may be considered as the C-O stretching incorporated in intermolecular H-bond formation together with the OH group.

CH_2 rocking

In FTIR studies, spectral distinctions in this region were observed at two specific wavenumbers (842 and 962 cm^{-1}). These frequency values were shifted towards lower wavenumber for samples prepared by casting the different solvents. The behavior supporting previous implications were existed here as well. As a consequence of the disruption of CH_2 groups through hydrophobic interactions, it was considered that bending vibrations of these groups certainly was disrupted and the spectrum was shifted towards lower frequency values.

C-C-O and C-O-C bending

C-C-O and C-O-C bending vibrations were observed as three prominent peaks at 363-365 cm^{-1}, 536-538 cm^{-1} and 582-585 cm^{-1} in Raman spectra of this study. As a consequence of the H-bonding between the etheric oxygen and OH end groups in PEG, both two bending vibrations were violated and subsequently, the spectrum was shifted towards lower frequency values.

C-O-C angle bending and C-O internal rotation

The Raman bands characterizing two vibrations within the range of 215-230 cm^{-1} were observed in submitted study. The spectral behavior of PEG samples prepared by casting solvent was exhibited discriminates significantly from that of the pristine (PEG)s. As the solubility power of the employed solvent rises, a shift towards higher wavenumbers was unavoidable. In the samples prepared by casting chloroform and THF (qualified as good solvents), shifts were observed towards highest wavenumbers.

Low-frequency Raman region (<400 cm^{-1})

Bending ($O-H\cdots O$ bending, C-O rotation, C-C-O angle bending and C-O-C) vibrations have been investigated in detail within the range of 48-88 cm^{-1} at the Raman analyses. The spectral evaluations were highly illustrated the spectral distinctions in the behavior of pristine (PEG)s and those prepared by casting different solvents. It was shifted towards higher frequency values for the samples prepared by casting solvent when compared with pristine PEG samples. The highest frequency shift values were displayed for the samples prepared by casting chloroform and THF. It was considered that $O-H\cdots O$ in-plane deformation, C-O rotation and C-C-O angle bending vibrations were shifted towards higher wavenumbers. This observation is a strong evidence illustrating the achieve role of H-bond for the samples prepared by casting THF and chloroform.

The shifts towards higher frequency values were observed within the measure of H-bond achieved by H-acceptor oxygen atom and OH end groups at the Raman analyses. This behaviour implies that the mentioned vibrations were occurred less favorably as long as the degree of H-bond formations increases. The greatest frequency shifts were observed in the samples prepared by casting chloroform and THF samples. Consequently, it is noteworthy to say that, in the end of trio study, the parallelism of both computation [8] and thermodynamic [9] and spectroscopic data about solubility profiles of PEG/solvent systems were determined.

CONCLUSIONS

In this study, it was investigated association of solvents to the pristine PEG by FTIR, Raman and XRD spectroscopic analyses. The solubility profile of PEG/solvent systems was evaluated as connected with solvent character and molecular weight.

When the XRD charts of PEG samples were compared, it was observed that THF is more effective than water in decreasing the crystallinity of the polymer. On the other hand, it was perceived that frequency shifts of various stretching and bending vibrations was risen to maximum for PEG samples prepared by casting chloroform and especially THF as a consequence of both FTIR and Raman interpretations' evaluation.

Solid-state characterization revealed that THF being more effective than water with introduction to PEG structure. The results were indicated that the shift was occurred towards higher frequency values with increased interaction because number of OH end groups and H-bonds for low molecular weight PEG 2000 was increased.

As a consequence of the interaction of end groups with etheric oxygen resulting from the unfolding of the polymer coil in a good solvent it can be clearly stated association power of solvents in PEG samples prepared by solvent cast technique decreased below order: THF > chloroform > DMSO > methanol > water.

PEG chains could easily be attached to several molecules due to of the reactive OH end groups, constituted copolymer or blend. In recent years, it have been found applications in a variety of purposes as conservation material, cellular material, binding agent, anti-foaming agent in food ingredient of e-liquid used in electronic cigarettes, electrolyte solvent in lithium polymer cells, preservative objects salvaged from underwater, lubricating coating for various surfaces, skin creams or toothpastes. As revealed that solvent factor is very important for PEG.

Acknowledgments. *The authors gratefully thank Prof. Dr. Filiz Ercan for providing XRD data and Assoc. Prof. Dr. Mustafa Kemal Özdemir for helps about polynomial regression analysis.*

REFERENCES

1. G.M. Powel, Poly(ethylene glycol). in: Davidson, R.L. (Ed). Handbook of Water-soluble Gums and Resins; McGraw-Hill: New York, 1980, p. 1.
2. L.H.M. Da Silva, J.S.R. Coimbra, A.J.A. Meirelles, *J. Chem. Eng. Data*, **42**, 398 (1997).
3. Y.Y. Choi, Y. Jeong, M.K. Joo, B. Jeong, *Macromolecular Biosci.*, **9**, 869 (2009).
4. T. Shen, M. Lu, D. Zhou, L. Liang, *J. Appl. Polym. Sci.*, **125**, 2071 (2012).
5. H. Zhao, S. Xiong, M. Li, Q. Zhang, G. Liu, *Adv. Mater. Sci. Eng.*, 819464 (2012).
6. M.K. Calabretta, A. Kumar, A.M. McDermott, C. Cai, *Biomacromolecules*, **8**, 1807 (2007).
7. J. Chen, S. K. Spear, J.G. Huddleston, R.D. Rogers, *Green Chemistry*, **7**, 64 (2005).
8. C. Ozdemir, A. Güner, *Eur. Polym. J.*, **43**, 3068 (2007).
9. C.O. Dinc, G. Kibarer, A. Güner, *J. Appl. Polym. Sci.*, **117**, 1100 (2010).
10. D.O. Corrigan, A.M. Healy, O.I. Corrigan, *Int. J. Pharm.*, **235**, 193 (2002)
11. T. Petrova, N. Manolova, I. Rashkov, *Polym. Int.*, **45,** 419 (1998).
12. H.G. Elias, An Introduction to Polymer Science; VCH, Weinheim, 1997, p. 470.
13. F.M. Gray, Homopolymer Hosts, in: Solid Polymer Electrolytes: Fundamentals and Technological Applications, Wiley-VCH, Weinheim, 1991, p. 245.
14. F.E. Bailey, J.V. Koleske, Poly(ethylene oxide); Academic Press, 1976, p. 169.
15. H. Tadokoro, Structure of Crystalline Polymer; Robert E. Krieger Publishing Co., Malabar, Florida, 1990, p. 465.
16. F.Y. Wang, C.C.M. Ma, W.J. Wu, *J. Appl. Polym. Sci.*, **80,** 188 (2001).
17. V.Z. Bermudez, L.D. Carlos, M.M. Silva, J.M. Smith *J. Chem. Phys.* **112**, 3293 (2000).
18. N.P. Huang, G. Csucs, K. Emoto, Y. Nagasaki, K. Kataoka, M. Textor, N.D. Spencer, *Langmuir*, **18,** 252 (2002).
19. H. Matsuura, T. Miyazawa, K. Machida, *Spectrochim. Acta A*, **29,** 771 (1973).
20. T. Kondo, *Cellulose*, **4**, 281 (1997).
21. M. Morssli, G. Cassanas, L. Bardet, B. Pauvert, A. Terol, *Spectrochim. Acta*, **47A**, 529 (1991).

Bulgarian Chemical Communications, Volume 49, Speial Issue I (pp.21-29) 2017

Investigation thermal and mechanical properties of PP/beech flour composite

Ç. Kadi[*1], H. Evlen[2], A. Özmert[2]
[1*]*Karabuk University, Science Faculty, Karabuk, Turkey*
[2]*Karabuk University, Technology Faculty, Karabuk, Turkey*

Submitted June 1, 2017; accepted September 1, 2017

Composite materials are put into use while their properties are improved by the researchers each passing day due to the advantages they provide and their variety in the application fields. One such renewable material is wood flour which is one of the most common forms of reinforcement in thermoplastics. Wood plastic composites (WPCs) are preferred in our study due to their advantages such as good resistance, low costs, availability and low wear on the processing equipment.

In this study beech tree flour and polypropylene (PP) composites were produced and this composites mechanical properties were investigated. It has been observed that 5 composites which were produced by increasing the beech flour by 5wt% , have increased in Elasticity Module and hardness based on the ratio of the beech flour but on the other hand, its elongation and tensile strength has decreased. PP-20% beech flour mixture is seen to have the highest Elasticity Module and hardness. 61% decrease has been observed in tensile strength with the increasing flour ratio. Characterization of PP and PP-Wood beech composites has been carried out via thermal analysis and SEM methods.

Keywords: Polypropylene, thermo plastic, wood plastic composites (WPCs), thermal and mechanical properties.

INTRODUCTION

Forestry products companies and plastic factories show a great deal of interest in Wood Polymer Composites (WPCs) which are one of the most dynamic units in Plastics sector. As a result of this interest, the properties of the wood polymer composites are constantly being improved and renewed.

Wood polymer composites add advanced properties to wood panels such as water absorption, resistance against biodegradation. However, correct compatibilizers are required to bridge over between wood and polymer in order to achieve this.

There are a lot of studies with regard to the mechanical properties of the composites reinforced with wood flour in different properties and thermoplastic PP [1-4].

Although particle filling/reinforcement materials are generally used on polymeric materials in order to decrease the cost, mechanical, thermal, electrical and chemical properties of the composite materials which are produced with the use of particles with advanced properties are improved.

Wu et al. studied the effect of carrying out preliminary processes on the wooden filling surface to the interfacial tension by Polypropylene (PP) composites with wood flour.

As a result of their study they proved that the bond structure between the surfaces of the filling matrix effect the interfacial tension and the mechanical properties of the composite [5].

Adhesive properties of the interface between the polymer matrix and wooden filling can be improved by using coupling agents. Surface bonding materials used improve the mechanical and chemical bonding properties by establishing a bond between wood flour (reinforcement) and thermoplastic (matrix).

Dalvag et al. have shown that in case the maleated polypropylene (MAPP) is used as a bonding agent in Polypropylene (PP)/wood flour composite there are improvements in tensile strength, rupture, elongation and Charpy impact properties [6-7].

Wood flour is an industrial product used in the production of natural composite. There are different studies with regard to the effect of process parameters on polymer-wood composite processing [8-12].

Le and Gauther have studied the effects of different parameters such as the rate of maleic anhydride (MA) in PP-graft-MA, sisal fiber fractions, chemical treatment of the fibers in the composites during the reactive extrusion. They have shown that the grafting of the fibers by PP-graft-MA enhanced both the impact strength and breaking stress [13].

Stamhuis has used Styrene Butadiene Styrene (SBS), SEBS, Nitrile Butadiene Rubber (NBR), Ethyl Vinyl Acetate (EVA) and Ethylene propylene monomer (EPDM) as impact modifier within PP with filling, composite. He reported that with the addition of such materials there is an improvement in the impact properties but the best result is achieved with covering the filling surface with the reinforcement. He has also shown that MA

* To whom all correspondence should be sent.
E-mail: ckadi@karabuk.edu.tr

contents within PP-g-MA have caused an increase in impact tension and the tension in the rupture [14].

Bledzki et al. have studied the effect of MAPP contents on physico-mechanical properties of PP which has been reinforced with hard and soft wood flour [15].

L.Soccalingame et al. evaluated the bonding effect of PP-g-MA on flour particle size and degradation of the spruce flour dust – PP composite after injection molding. In order to evaluate the level of degradation we need to consider process parameters, flour and bonding agents. Additionally, strong effect of PP-g-MA bonding agent on tensile properties was observed while no effect was observed on the impact [16].

Property of water absorption of composites is important to determine various application potentials such as floor covering in outdoor use [17-18].

Composite prepared with fibers which are not covered with MAPP has a lower tensile and higher humidification properties when compared to composite prepared with fibers which are covered with MAPP. It correlates with low interface bonding among these components [16].

Bhaskar et al. have prepared a wood polymer composite (WPCs) by using recycled polypropylene (rPP) together with pine tree flour (Pine radiate). Researchers have compared the water absorption property of polymer processed with (rPP), virginPP (vPP) and maleated polypropylene (MAPP) which is a bonding agent. In accordance with the test results, water absorption has increased in accordance with the increased flour ratio. On the other hand bonding agent MAPP has greatly decreased the water absorption property [19].

The aim of this study is to evaluate the effects of MA and flour ratio on composite material after the sieving and injection molding cycle. In the study wood reinforced polymer composite materials were produced in the ratios of 5%, 10%, 15%, and 20% by increasing the wood flour ratio by 5wt%. For determining the strength, ductility and elongation parameters of the composite materials produced they have been subjected to single axis tensile test and Shore D hardness test for determining their hardness values. Wood flour is used to increase the resistance and hardness of the polypropylene composite material and to decrease the costs.

2.MATERIALS AND METHODS

2.1.Materials

In this study beech tree flour (WB) which grows in Karabük-Yenice (Turkey) is used. The flour which has been sieved using laboratory test sieves with the pores in 200 microns and dried for 24 hours.

Wood flour consists of the composition of cellulose, hemicellulose, lignin and foreign materials. Chemical properties of the beech flour dust are shown in Table 1.

Table 1. Chemical properties of the beech wood (WB)

Chemical Composition	%
Cellulose	40-50
Hemicellulose	20-35
Lignin	20
Foreign substance	0-5

Table 2. Mechanical properties of maleic anhydride

Maleic anhydride	Value
Purity wt %	99.5
Solidification point (°C)	52.4
Boiling Point (°C)	202
Density g/cm^3	1,48

Maleic anhydride is used to enable the binding effect at interfaces of the polymer-wood flour mixtures. Mechanical properties of maleic anhydride material are shown in Table 2. Maleic anhydride is procured from As Kimya (İstanbul, Turkey).

Mechanical properties of polypropylene (PP) material are shown in Table 3. Polypropylene block copolymer was procured from Sabic (SABIC PP 48M40).

Phenolic antioxidant material with Anox20 serial is used to prevent the degradation due to temperature during the injection processes of Polymer-Wood flour mixtures. It has very low volatility and provides a better resistance in polymer extraction. Antioxidant Anox 20 has been procured from Addivant (USA). Mechanical properties of antioxidant are given in Table 4.

2.2 Production of polymer-beech flour composites

Five composite samples have been prepared in the ratios given in Table 5. Each sample mixed in vertical type mixer with three blades (DMS DER-SAN Vertical Type) with 700 dev/min. speed for 15 minutes. The mixture was molded with the injection molding method which can be seen in Figure 1 by using Arburg 50T brand injection machinery. Sizes of single axis tensile test sample (ASTM D412) produced as a result of the molding process is given in Figure 2. Injection molding parameters are given in Table 6. For each parameter, 10 units of samples were molded and tensile test is applied to five of them. Tensile and hardness tests were carried out within ISO 294 standards.

Figure 1. Plastic injection mold.

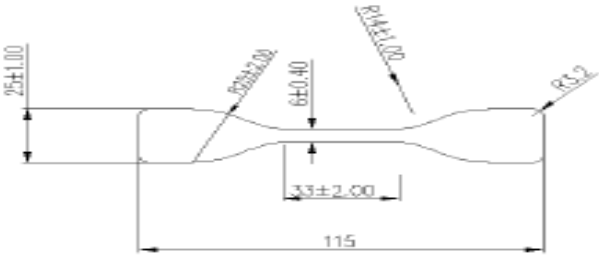

Figure 2. Tensile test sample.

Table 3. Mechanical properties of polypropylene block copolymer (PP) [20]

Polymer Properties	**Unit(SI)**	**Values**	**Standard**
Density	kg/cm^3	0.905	ISO 1183
MFR at 230 °C and 2.16 kg	g/10 min	15	ISO 1133
Mechanical Properties			
Tensile Test			
Stress at yield	MPa	29	ISO 527
Stress at break	MPa	20	
Strain at break	%	300	
Flexural Test			
Flexural Modulus	MPa	1650	ASTMD790
Izod impact notched			
at 23^0C	kJ/m^2	7.0	ISO 180/4A
at 0^0C	kJ/m^2	4.5	
at -20^0C	kJ/m^2	3.5	
Charpy impact notched			
at 23^0C	kJ/m^2	7.0	ISO 179
at 0^0C	kJ/m^2	4.0	
at -20^0C	kJ/m^2	2.5	
Hardness Shore D	-	70	ISO868
Thermal Properties			
Head Deflection Temperature			
at 1.80 MPa (HDT/A)	^{0}C	56	ISO 75/A
at 0.45 MPa (HDT/B)	^{0}C	88	ISO 75/B
Vicat Softening Temperture			
at 10 N (VST/A)	^{0}C	147	ISO306/A
at 50 N (VST/B)	^{0}C	79	ISO306/B

Tensile test is applied to the composite samples which are in accordance with the ASTM D412 standard by using ZWICK Z010 brand single axis tensile test device. Preloading time, preload and test speed for all samples in tensile test are kept at a fixed rate. Preloading time is used as 50 sec. and preload is used as 1 N/mm^2. Tensile tests are performed with 50 mm/min speed. Tensile test is applied to all the samples in line with these parameters.

Table 4. The properties of Anox 20 antioxidant

Antioxidant	Value
Bulk density (kg/m^3)	Powder 650/Granular 570
Flash point (°C)	299
Melting range (°C)	110-125
Molecular weight	1178
Appearance	White, free-flowing solid
Thermogravimetric analysis (10 mg 10°C /min. under N_2)	350 (Weight loss %5)

Table 5. Mixture ratios of the wood flour and additives added to polypropylene

Samples	Group1 (wt%)	Group 2 (wt%)	Group 3 (wt%)	Group 4 (wt%)	Group 5 (wt%)
PP	PP	PP	PP	PP	PP
Wood flour	-	5	10	15	20
Maleic Anhydride	-	2	2	2	2
Antioxidant	-	0.10	0.10	0,10	0,10

Table 6. Conditions injection molding for PP-wood flour mixture

Parameters	Value
Injection temperature (°C)	190-210
Injection pressure (bar)	1400-1500
Waiting Ttme in Mold (sec)	15

Also, the hardness of the composite material is measured with ZWICK Shore D durometer. ZWICK (Shore D) durometer is given in Figure 3.

The specimens were coated with Au/Pd by using Sputter coater Q150R and transferred to FE-SEM for imaging. The microstructures of specimens were observed using a field emission scanning electron microscope (FESEM) Carl Zeiss Ultra Plus machine with an energy-dispersive X-Ray spectroscopy (semi-quantitative EDX) analysis system.

Thermogravimetric analysis (TGA), derivative thermogravimetric analysis (DTG) and differential thermal analysis (DTA) studies were carried out in nitrogen at scanning rates 10^0C min^{-1} in nitrogen atmosphere using module of a Tetra Hıtachı DSC 7000x and STA 7300 Thermal Analyzer with 10-11 mg of samples on ceramic pans. The thermal degradation of the samples was studied from a temperature 40 to 700^0C.

Differential scanning calorimetry (DSC) studies were carried out scanning rates 10^0C min^{-1} in nitrogen atmosphere using module of a Tetra Hıtachı DSC 7000x and STA 7300 Thermal Analyzer with 10-11 mg of samples on alumina pans. The thermal degradation of the samples was studied from a temperature 40 to 500^0C.

3.RESULTS AND DISCUSSION

3.1. Mechanical properties

In the study, composite samples are produced by increasing the wood ratio by 5 wt.% regularly (in a range of 5%~20%). 5 of the samples produced from each mixture are subjected to tensile test. Elasticity Module in accordance with the wood ratio, % Elongation and Tensile Stress graphics are given in Figure 4. Average of Elasticity module for composites, elongation, tensile stress values is taken and they are shown in Table 7.

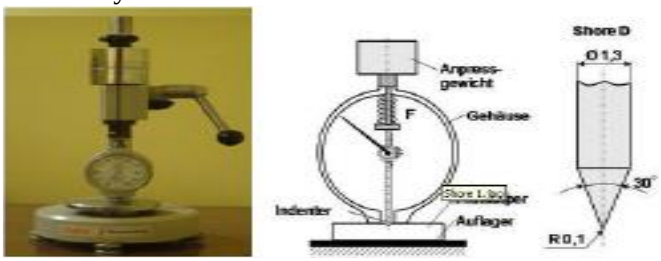

Figure 3. ZWICK durometer.

Table 7. Mechanical properties of the materials wich have different wood flour ratios

Mechanical Properties	PP	PP - 5% Wood Flour	PP -10% Wood Flour	PP -15% Wood Flour	PP -20% Wood Flour
Elasticity Modulus *(*MPa)	440.66	667.17	709.40	726.26	748.52
Tensile Strength (MPa)	39.27	29.25	27.60	25.73	23.84
Elongation (%)	19.62	7.75	6.76	4.96	4.21

In the study elasticity module of Polypropylene is found to be 440,66 MPa, elongation is found to be 19,62% and tensile stress is found to be 39,27 MPa.

When the Beech flour is added in a ratio of 5% to Polypropylene, Elasticity Module increased to 667,17MPa, elongation is found to be 7,75% and tensile stress is found to be 29,25MPa. Highest elasticity module is achieved from PP-%20 mixture containing wood Flour as 748,52MPa. Elongation value of this composite is 4,21% and tensile stress is 23,84 MPa.

Tensile and % elongation graphic belonging to the samples are shown in Figure 5. As it can be seen from the graphic, elongation percent is decreased and mechanical resistance of the composites are increased based on the increasing wood flour ratio.

Hardness graphic and its values are given in Figure 6 and Table 8 for PP-wood flour composites in different ratios. Five measurements were made from the samples belonging to each parameter and average of the values gained as a result of the measurement are taken and evaluated.

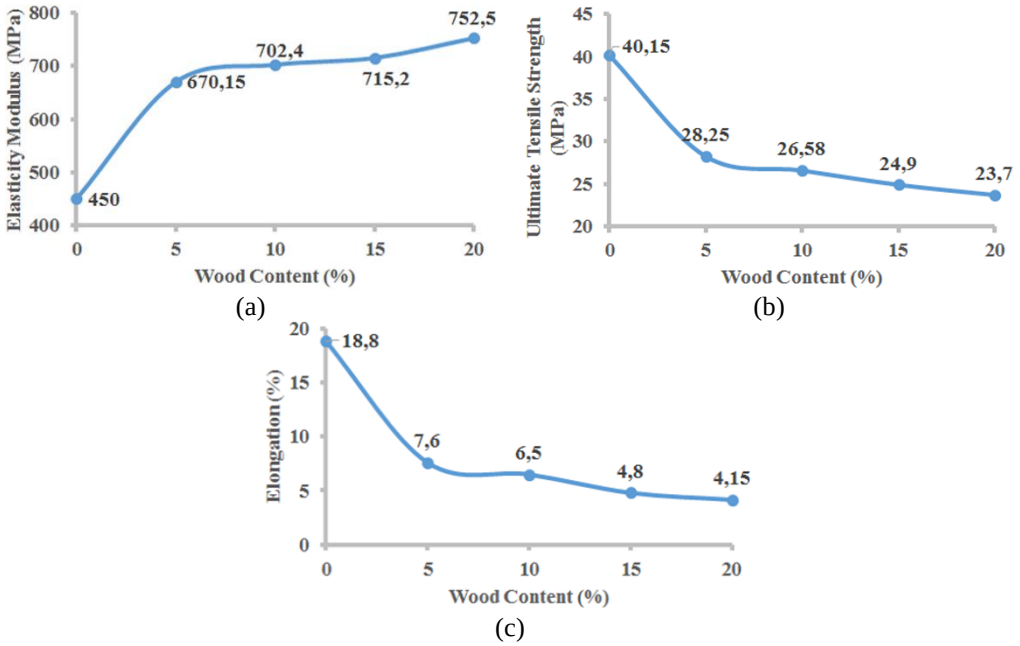

Figure 4. Tensile curves in accordance with increasing wood ratios a) Elasticity Module - %Wood flour content, b) %Elongation - %Wood flour content, c) Tensile Strength - %Wood flour content.

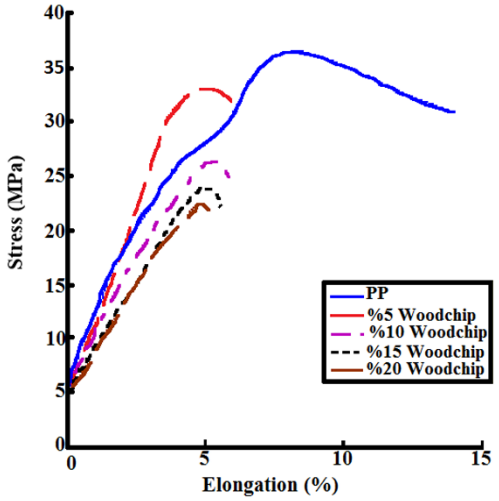

Figure 5. Tensile-% elongation graphic.

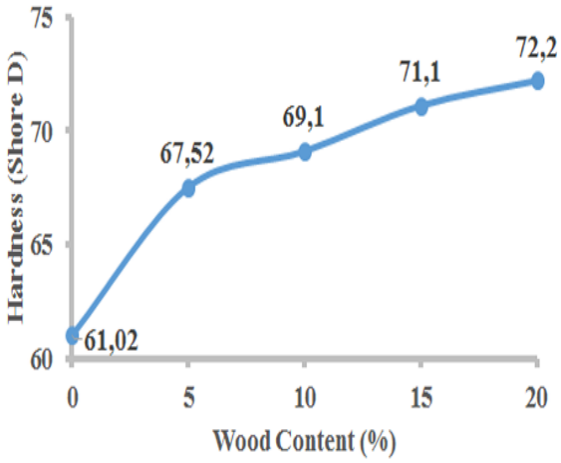

Figure 6. Hardness graphic for polypropylene-wood flour composite.

When the hardness values of the samples are analyzed after wood dust ratio is increased in a ratio of 5% regularly, it is found out that the highest hardness value belongs to PP-%20 Wood Flour mixture with 71,36 Shore D value. Hardness value of the composite material gained from the PP-%15 wood flour is 70,50 Shore D. Hardness value of the material gained from the PP-%10 Wood Flour is 69,20 ShoreD. Hardness value of the material gained from the PP-%5 Wood Flour is 66,54 Shore D. Hardness value for polypropylene is 60,89 Shore D.

Table 7. Mechanical properties of the materials wich have different wood flour ratios

Mechanical Properties	PP	PP - 5% Wood Flour	PP -10% Wood Flour	PP -15% Wood Flour	PP -20% Wood Flour
Elasticity Modulus (MPa)	440.66	667.17	709.40	726.26	748.52
Tensile Strength (MPa)	39.27	29.25	27.60	25.73	23.84
Elongation (%)	19.62	7.75	6.76	4.96	4.21

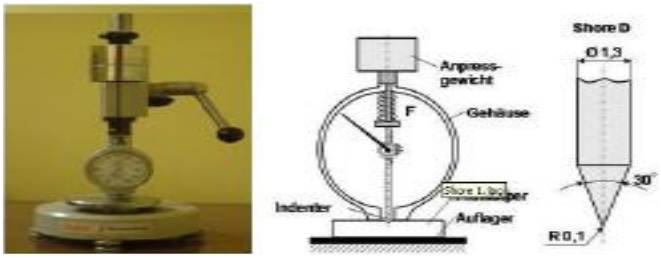

Figure 3. ZWICK durometer.

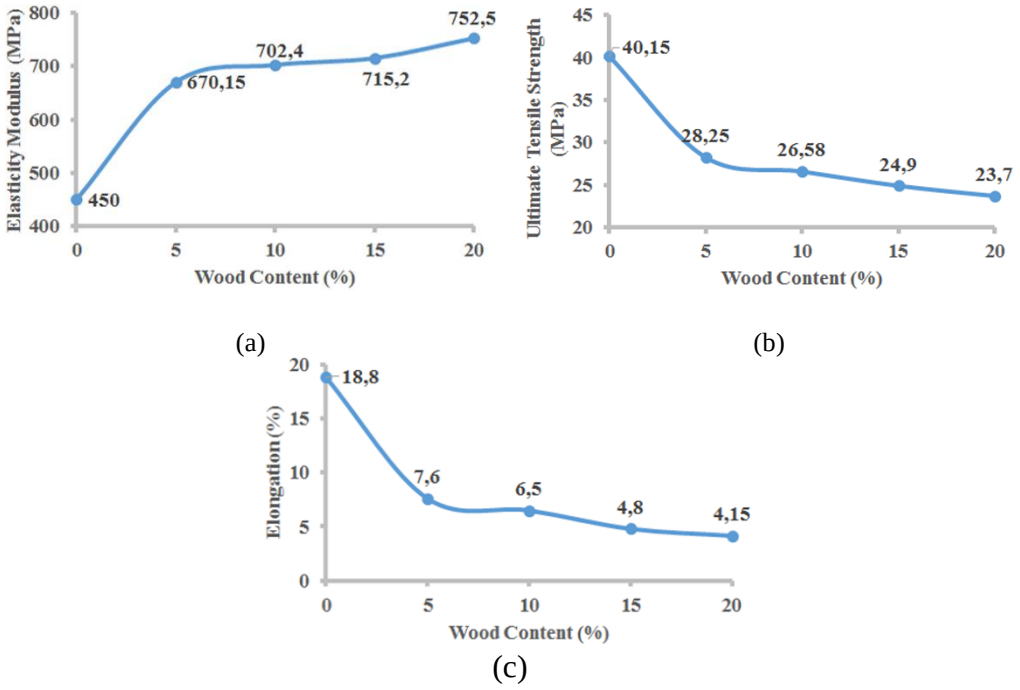

Figure 4. Tensile curves in accordance with increasing wood ratios a) elasticity module - % wood flour content, b) % elongation - %wood flour content, c) tensile strength - %wood flour content.

Table 8. Hardness values of polypropylene-wood flour composites

Mixture	Standard Deviation	Average (Shore D)
PP	0.71	60.89
PP - 5% Wood Flour	0.87	65.54
PP - 10% Wood Flour	0.45	69.20
PP -15% Wood Flour	0.42	70.50
PP- 20% Wood Flour	0.45	71.36

3.2. SEM analysis

In this study microstructure images are taken from the composite samples which have different wood flour ratios. Images were taken by SEM from both the surface and fractured surface with 500X zoom in order to understand the effect of the wood flour.

Figure 7a shows the SEM image of polypropylene. As it can be seen from Figure 7b, PP and wood flour is blended in a homogenous way. In Figure 7c, when the fractured surface SEM image of the PP-%20 wood composite is analyzed, it is seen that gaps are caused by wood flour which are not completely bonded to the composite and which are ruptured. However, the number of the gaps is few and in general terms a composite which is compatible with polymer is formed.

3.3. Thermal properties

DSC and TGA thermal analyses are evaluated for PP and PP-Wood flour composites. Thermal properties of the materials produced from PP under

different conditions were analyzed by other researchers [20-25].

Table 9 shows the thermal analysis result of the PP and PP-20% wood composite.

When we have a look at the TGA curve of the PP in Figure 8a there is a single decomposition in 98,5% between 254-473^{0}C. Polypropylene starts to degrade at a temperature over 253^{0}C

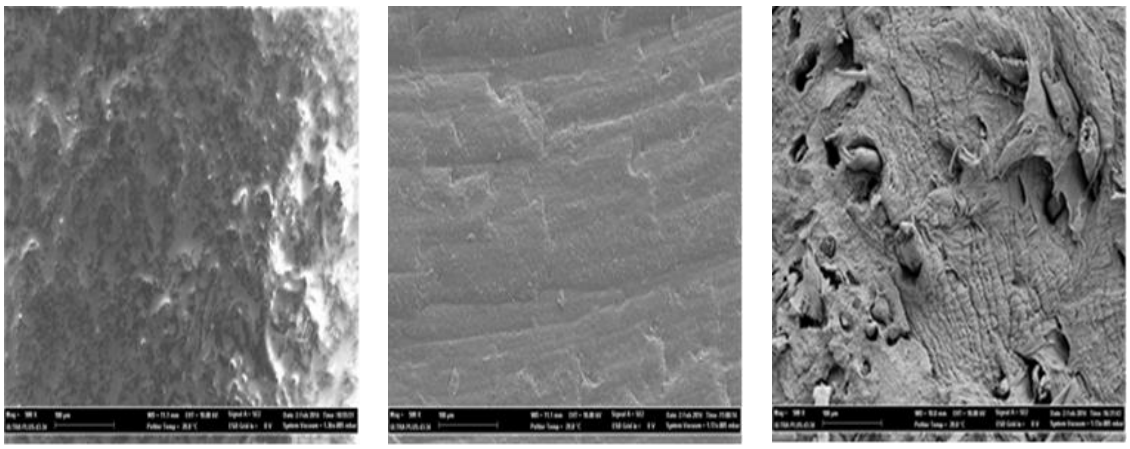

a) b) c)

Figure 7. Scanning electron microscope (SEM) micrographs of samples (magnification 500X) . a) PP , b) PP-20% wood flour composite, c) PP-20% fractured surface SEM image of wood flour Composite

Table 9. Thermal analysis results of the PP and PP-20% wood flour composite

Polymer	DSC(^0C)			TGA(^0C)		
	T*m*	T*d*	ΔH_m	Td_1	Td_2	Td_3
PP	168	190	79.0	-	254	473
PP-wood comp.	168	203	88.3	114	377	537

T*m* - melting temperature, T*d* - decomposition temperature, ΔH_m *(mJ/mg)* - melting enthalpy .

In Figure 8 b, single mass degradation of the PP-wood flour composite occurred between the temperatures of 114 and 537^{0}C. First decrease occurred between 114.4-377^{0}C as 7.3% (1,23mg mass loss) and second weight decreased occurred between 377-537,4^{0}C as (96.46%) (15,53mg mass loss).

In thermogram, in the temperature range up to 377^{0}C, there is only 7% loss of mass arising out of the water contained in the composite structure, removal of volatile molecules and degradation of the wood flour and additives over this temperature. Composite material from Figure 8 b is completely degraded at 537^{0}C.

When Figure 8a and 8b is compared, pure PP lost 98.8% of its total and PP-wood composite lost 96% of its total within the range of 170-500^{0}C. Also when the Td_2 degradation temperatures of pure PP and Pp-wood composite in Table 9 are compared, it has been observed that the degradation temperature is increased from 253^{0}C to 473^{0}C with the effect of additives. Degradation temperatures increased when wood flour and additives are added to polymer while the loss of mass is decreased. This shows that the thermal resistance of the composite is good.

When the DSC thermal analysis results in Figure 8c and 8d are compared, it is seen that melting and decomposition temperatures are not changed that much. While the PP melting temperature is (T*m)* 167.9; melting temperature of PP-wood composite (T*m)* is 167.8^{0}C, decomposition temperatures (T*d*) are; 190^{0}C for PP and 203^{0}C for PP-wood composite. Comparison of these two melting temperatures belonging to PP and PP-wood composite can be seen in Fig.8e.

The ΔH_m of the PP increased with increasing wood flour content. The ΔH_m of the PP increased from 79.0 to 88.3 mJ/mg as the wood flour content increased to 20%.

Our results are conclusive with the studies made with regard to the thermal properties of PP [16-24].

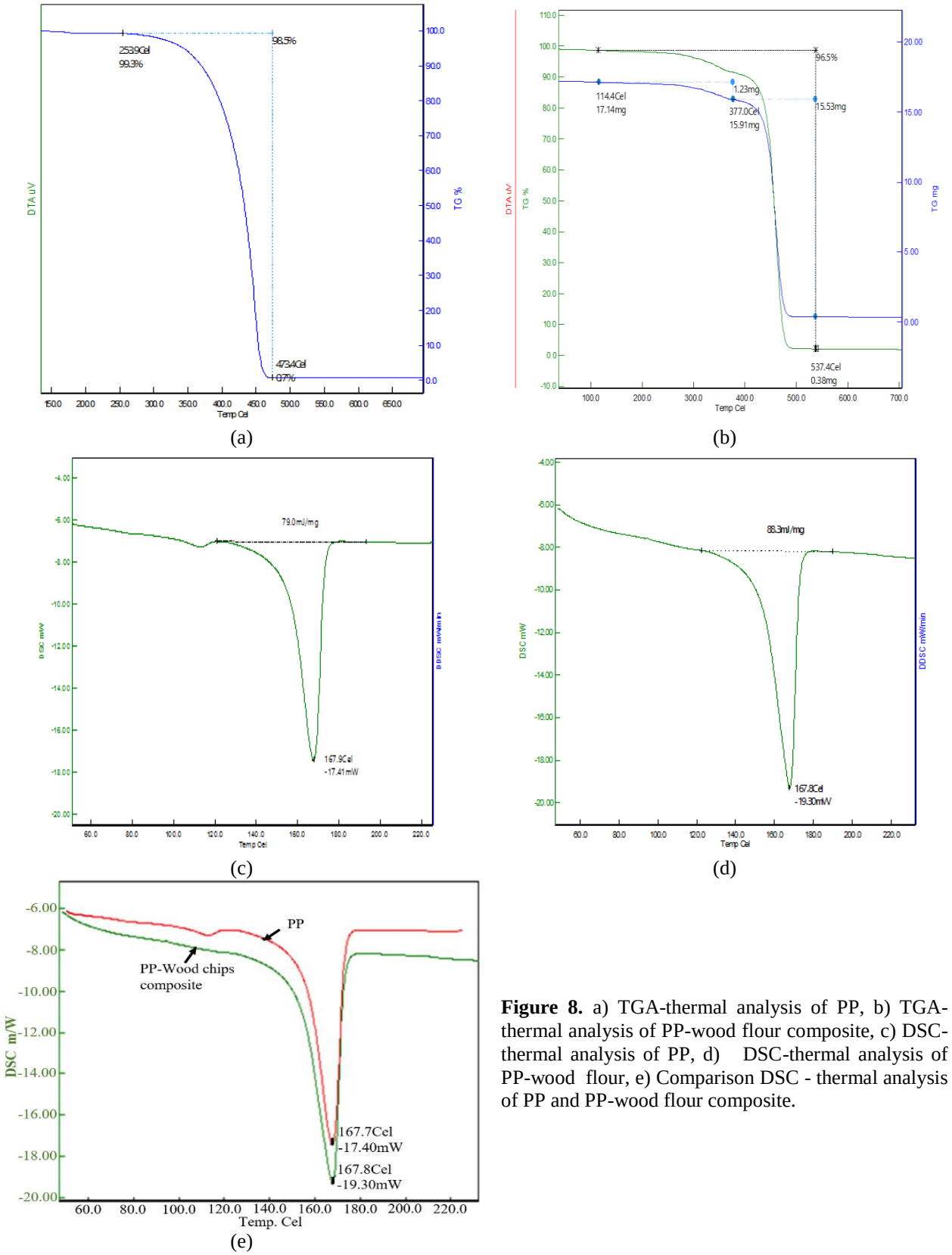

Figure 8. a) TGA-thermal analysis of PP, b) TGA-thermal analysis of PP-wood flour composite, c) DSC-thermal analysis of PP, d) DSC-thermal analysis of PP-wood flour, e) Comparison DSC - thermal analysis of PP and PP-wood flour composite.

4. CONCLUSION AND DISCUSSION

Mechanical properties of the composite materials produced from the mixture of polypropylene with wood flour are analyzed in this study. Wood flour is added to increase the strength and hardness of the polypropylene material.

Ratio of wood flour is increased by 5% regularly within the mixture in the composite material produced. Hardness and tensile test are applied to the new mixtures produced and their mechanical properties are analyzed.

When the wood ratio is increased regularly it has been observed that the elasticity module of the composites has increased as well. While the Polypropylene has high ductility and low elasticity module, increase in the wood ratio by mixing it with wood flour caused an increase in the Elasticity module, decrease in the elongation percent and decrease in the tensile stress. It has been determined that stress of composite material increased per unit of elongation when compared to polypropylene.

It has been observed that when the amount of wood within the mixture is regularly decreased the hardness of the composite material is decreased. The highest hardness value is achieved from the mixture with PP-20% Wood flour and the lowest hardness value belongs to pure Polypropylene material.

It has been observed from the SEM images taken from the material that wooden flour bonds to plastic appropriately and it becomes integrated with the plastic.

Thermal decomposition and melting temperature of the composite materials were investigated by TGA and DSC. Composites have shown high thermal decomposition temperature at 377^0C in a nitrogen atmosphere. Most of the weight loss occurred between the temperature range of 377-537^0C.

In order to achieve a good and accurate mechanical property homogenous mixture of the composite material is an important matter. For a homogenous microstructure, wood flour particles and polypropylene should be blended well and should be combined. Usage of mixer is important for well blended mixtures and for achieving a homogenous microstructure. Also, gaps created by the wood flour should be refrained and wood flour should be in a size of small sieve size which is at least 250μm.

Acknowledgements. *The authors would like to express appreciation for the support of Karabuk University Coordinating Office of Scientific Research Projects (BAP) for sponsoring the conference attendance [Project Number: KBÜBAP-17-YD-242]*

This paper includes data extracted from the master's thesis in the University of Karabuk of the third author.

REFERENCES

1. N.E. Bekhet, *Wear*, **236**, 55 (1999).
2. M. Taşdemir, *J. Appl. Polym. Sci*, **13**, 3485 (2003).
3. D. G. Dikobe, A. S. Luyt, *EXPRESS Polymer Letters*, **4**, 729 (2010).
4. M.D.H. Beg, K.L. Pickering, *Composites: Part A*, **39**, 1091 (2008).
5. J. Wu, D. Yu, C.M. Chan, J. Kim, Y. W. Mai, *J. Appl. Polym. Sci.*, **76**, 1000 (2000).
6. H. Dalväg, C. Klason, H. E. Strömvall, *Int. J. Polym. Mater.*, **11,** 9 (1985).
7. M.A. Fuqua, S. Huo, C.A. Ulven, *Polymer Reviews*, **52**, 259 (2012).
8. K. Oksman, C. Clemons, *Int. J. Appl. Polym. Sci*., **67**, 1503, (1998).
9. M. Tasdemir, H. Biltekin, G. T. Caneba, *J. Appl. Polym. Sci*., **112,** 102 (2009).
10. L.P. dos Santos, T.S. Flores-Sahagun, K.G. Satyanarayana, *J. Comp. Mater.*, **49,** 3727 (2015).
11. V.N. Hristov, M. Krumova, St. Vasileva, G.H. Michler, *J. Appl. Polym. Sci*., 1286 (2004).
12. O. Faruk, A. K. Bledzki, L.M. Matuana, *Macromol.. Mater. Eng.*, **292,** 113 (2007).
13. T.T. Le Thi, H. Gauthier, R. Gauthier, B. Chabert, J. Guillet, B.V. Luong, V.T. Nguyen, *J. Macromol. Sci. Part A, Pure and Appl. Chem.,* **A-33**, 1997 (1996).
14. J.E. Stamhuis, *Polym. Comp.*, **9**, 72 (1988).
15. A.K. Bledzki, O. Faruk, M. Huque, *Polym Plast Technol and Eng*, **41**, 435 (2002).
16. L. Soccalingame, A. Bourmaud, D. Perrin, J.-C. Bénézet, A. Bergeret, *Polymer Degradation& Stability*, **113**, 72 (2015).
17. R. Liu, Y. Peng, J. Cao, S. Luo, *BioRes*, **9,** 54 (2014).
18. K. Englund, V. Villechevrolle, *Journal of Applied Polymer Science*, **120**, 1034–1039, (2011).
19. J. Bhaskar, S. Haq, A.K Pandey, N. Srivastava, *J. Mater. Environ. Sci.*, **3**, 605 (2012).
20. H.M. da Costa, V.D. Ramos, M.G. Oliveira, *Polymer Testing*, **26**, 676 (2007).
21. J. Gu, H. Xu, C. Wu, *Adv. Polymer Technol.*, **32**, 2, (2013).
22. W. Zhua, C. Yan, Y. Shi, S. Wen, J. Liu, Y. Shi, *Materials and Design*, **82**, 37 (2015).
23. N. Ayrilmis, A. Kaymakci, F. Ozdemir, *J. Indust Eng. Chem.*, **19**, 908 (2013).
24. A.C.-Y. Wong, F. Lam, *Polymer Testing*, **21**, 691 (2002).

Bulgarian Chemical Communications, Volume 49, Issue I (pp. 30 – 36) 2017

Electropolymerization and characterization of salophen derivative Schiff base Co(II) and Ni(II) complexes on the graphite electrode and electrocatalytic investigations

D. Cakmak[1*], T. Bulut

[1]*Department of Chemistry, Faculty of Arts and Sciences, Mustafa Kemal University, 31040, Hatay, TURKEY*

Submitted: June 1, 2017; Accepted: September 1, 2017

In this study, pencil graphite electrode surfaces were modified with Salophen derivative Schiff base Co(II) and Ni(II) complexes. Surface modification procedure was carried out by electrochemical oxidation method at 0.0-2.0 V potential range in acetonitrile containing 0.15 M $LiClO_4$ as a supporting electrolyte medium. The prepared modified surfaces were characterized by cyclic voltammetry, EIS, FT-IR UV-Vis and SEM/SEM-EDX techniques. Modification of surfaces was confirmed by results of characterization studies. The electrocatalytic activity of modified electrodes was investigated upon bioanalytical species like ascorbic acid, catechol, cysteine etc. It was seen that both modified electrodes showed excellent electrocatalytic activity on catechol, but the catalytic activity potential of the electrode modified with Co (II) complex was higher on the other species.

Keywords: Schiff Base metal complex, electropolymerization, surface characterization, electrocatalytic investigation.

INTRODUCTION

Schiff bases are compounds that were first used as a ligand by Schiff in 1864. Schiff bases and its metal complexes are still being worked on remarkably in recent years because they have antibacterial, antiviral, anticancer and antifungicide properties as well as a wide variety of applications in different fields such as chemical analysis, catalytic systems, pesticide structures, oxygen transmission and sensor systems [11, 12]. Schiff bases, and especially its metal complexes, are attracting attention as modifying materials because of their stable and easily synthesizable structures, since they allow the functional groups to be varied in surface modification studies [13]. In recent years, development of new working electrode materials prepared by electropolymerization of Schiff metal complexes by electrochemical methods have been attracting considerable attention and also the determination of electrocatalytic activities on different types of analytes and the development of new analytical methods by using of these modified electrodes [14-15]. With the appropriate modification materials, new working electrode surfaces can be prepared and rapid, selective and sensitive determination of species are possible as electrochemically [16-19].

This study was concerned with the preparation of modified electrodes with electropolymerization of Schiff base metal complex onto pencil Graphite electrode and also investigation of electocatalytic activity of these electrodes. Characterization of modified electrodes was realized with electrochemical, spectroscopic and microscopic techniques.

EXPERIMENTAL

Materials and methods

Electropolymerization studies of Schiff base metal complexes were performed by using of conventional three electrode system and a CHI 604E model electrochemical analyzer for cyclic voltammetry (CV) measurements. All the electrochemical studies were carried out by using a pencil graphite (GFE), Pt wire and saturated Ag/AgCl (3 M NaCl) were used as working, counter and reference electrodes, respectively. The outer surface of the graphite pencil electrode was covered with polyester for the purpose of controlling the surface area in electrochemical studies and polishing device (Polisher) was used for cleaning of working electrodes.

Schiff base [H_2L] and metal complexes ([CoL], [NiL]) were synthesized according to the literature [20]. The proposed structures of [H_2L, [CoL] and [NiL] are given below.

* To whom all correspondence should be sent.
E-mail: didem.deleti@gmail.com, dcakmak@mku.edu.tr

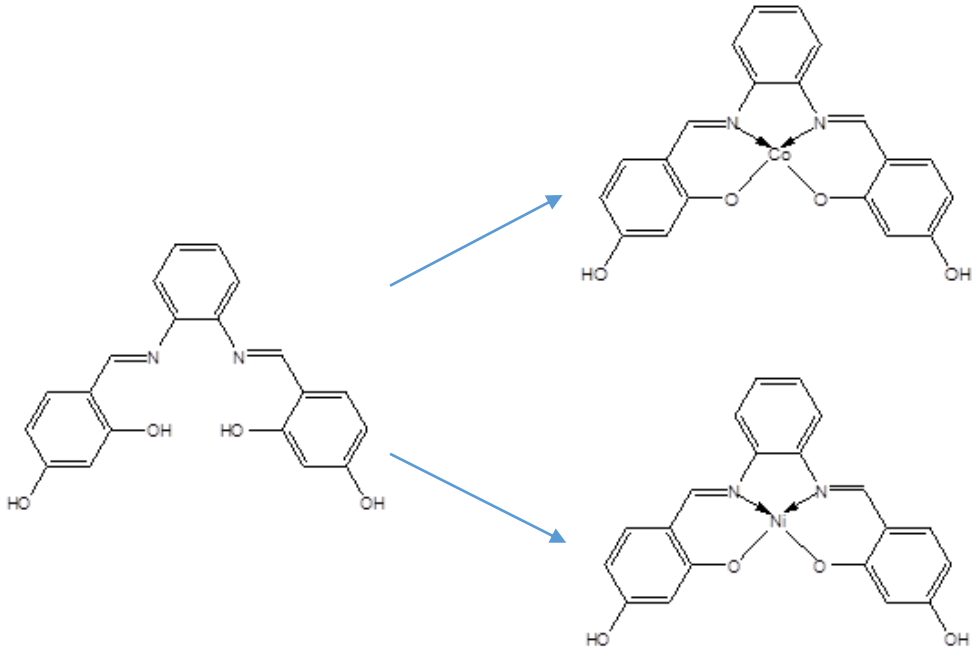

Proposed structure of H_2L, [CoL] and [NiL].

Modification procedure was performed by CV with scanning from 0.0 to 2.0 V at a sweep rate of 50 mV s^{-1} for 25 cycles in 1 mM [CoL] and 1 mM [NiL] solutions in acetonitrile containing 0.15 M $LiClO_4$.

Stability of modified surfaces CoL-GFE, NiL-GFE was tested by CV method using sequential potential scans in a 0.3 M KCl support electrolyte medium. The CV method has also been used for the electrochemical characterization of modified surfaces by using of redox probes (ferrocene, ferricyanide). The 1.10^{-3} M ferrocene solution was prepared in an acetonitrile containing 0.1 M $LiClO_4$. Ferricyanide test was carried out in 0.1 M KCl solution containing 1.10^{-3} M $K_3[Fe(CN)_6]$.

For electrocatalytic activity studies, Phosphate buffer solution (PBS) pH=7 was used as supporting electrolyte. Solutions of Ascorbic acid (AA, 1mM), Catechol (CC, 1mM), Cysteine (Cys, 1mM) and Sulfide (SO_3^{2-}, 1 mM) were prepared daily by dissolving them in water.

RESULTS AND DISCUSSION

A typical multicycle CV voltammograms for electropolymerizations of [H_2L], [CoL] and [NiL] on GFE were given in Fig.1. In the voltammograms of [CoL] and [NiL], the irreversible oxidation behavior was observed nearly 1.0 V at the first cycle. This oxidation peak was not observed in the voltammogram of the ligand. This situation was thought that the observed irreversible oxidation behavior due to the electrochemical activity of the transition metal in the structure. Decrease of the peak current values after the first cycle, at the end of 25 cycles, supports the modification of the species to the electrode surface. Thus, the electrode surfaces has changed and gained a new character after modification of electrodes with metal complexes and the electrochemical behavior of the electroactive species has also changed [21]. The electrochemical stability voltammograms (successive CVs) were also given in Fig.1. Stability voltammograms have given to get the information about the stability and electroactivity of films obtained on GFE with investigating of electrochemical behavior during successive cycles. If the coating material is stable on modified surfaces, it is expected that in the voltamogram taken in the electrolytic solution will be no current change by repetitive potential scans in the anodic or cathodic direction. In particular, the fact that the current decline with sequential scans is that film degrades and is beginning to lose electrochemical stability (charge storage and unloading) [22]. When voltamograms are investigated, it is observed that there is a current change for modified surfaces after the first cycle. It is believed that this decrease in current is due to the removal of adsorbed monomers from the surface during cycling. No change in current is observed in subsequent cycles and the films on the electrode surfaces appear to maintain their stability during potential scanning.

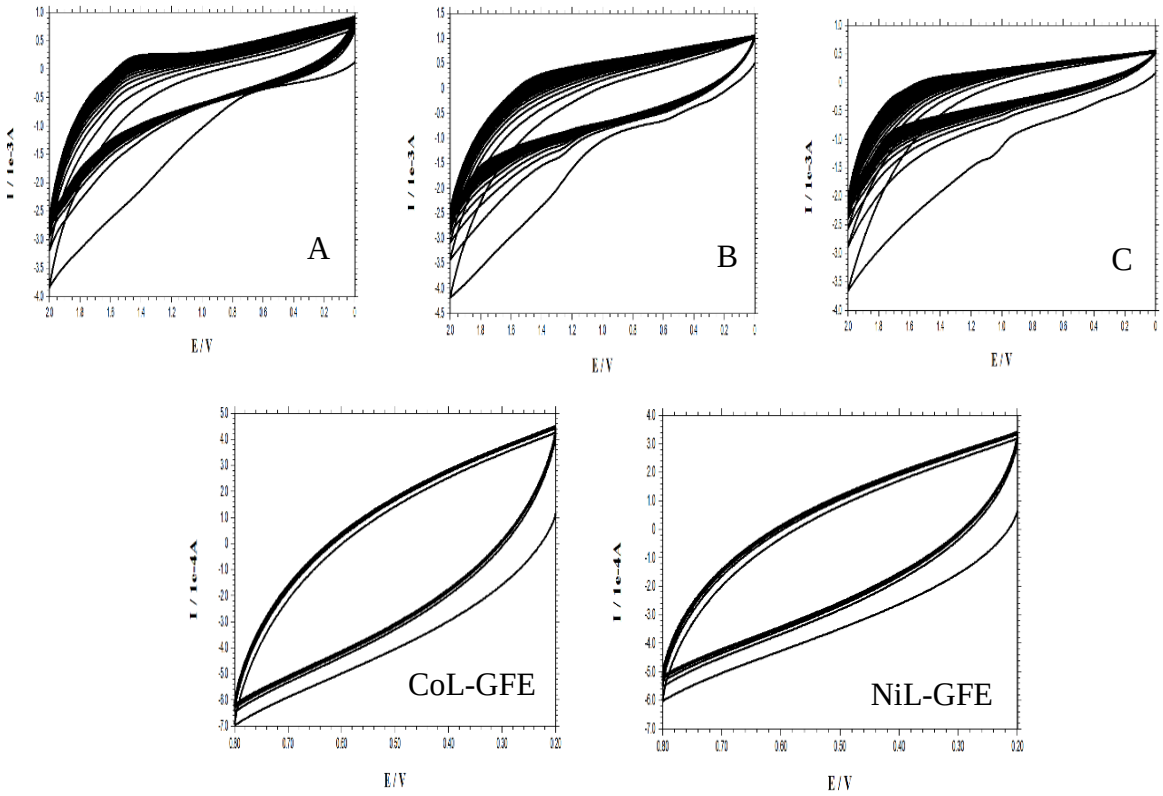

Fig.1. Multicycle voltammograms of [H_2L] (A); [CoL] (B) and [NiL] (C) in 0,15 M $LiClO_4$/acetonitrile solution as supporting electrolyte at GFE; Successive CVs of [CoL] and [NiL] films in 0.3 M KCl solution at 0.2-0.6 V potential range.

Electrochemical characterization of CoL-GFE and NiL-GFE surfaces were carried out using ferrocene and ferricyanide redox probes. Redox probes are usually reversible species with fast electron transfer at the surface of the bare electrode. Electrochemical behavior of redox probes on the modified electrode surface may differ from that of electron transfer kinetics. Such differences and similarities from time to time may provide information at the stage of modification during the electrochemical characterization [23, 24]. The cyclic voltammograms of the modified surfaces and the bare GFE with redox active molecules are shown in Fig.2. When voltamograms are evaluated, it appears that electron transfer of ferrocene is almost completely inhibited at the modified electrodes. For ferricyanide, electron transfer was observed to be blocked in large amounts on the surface of the modified electrodes compared to the bare GFE, but the electron transfer of the ferricyanide on the modified surface was found to be carried out at a certain amount by electroactive species diffusing from possible pinholes.

From the Nyquist plot given Fig. 2., it appears that the charge transfer rate of the $[Fe(CN)_6]]^{3-/4-}$ redox couple on the bare GFE surface is higher than the modified surfaces. It is understood that the lower value of the charge transfer resistance, which is effective in the high frequency regions on the bare GFE surface, is observed at higher values, which is also effective in the lower frequency regions on the modified surfaces.

SEM images of [CoL] and [NiL] films were recorded in order to investigate the surface morphology and structure. The SEM images were given in Fig.3. It can be easily seen from SEM images that the crystalline structures occurred on the electrode surfaces after electropolymerization different from the bare GFE surface belongs to metal complexes.

In the UV spectrum of the [CoL] and [NiL] films, the band was observed at range of 330–450 nm were attributed to the $n–\pi*$ transition of the non-bonding electrons present on the nitrogen of the azomethine group of the Schiff base moiety [25]. In addition, the weak bands observed in the 500–700 nm region can be attributed to *d–d* transitions of the metal ions [26].

Cobalt and nickel ions distribution at modified surfaces were illustrated as red points at spectrum of SEM-EDX mapping analysis (Fig.3.). According to the SEM-EDX analysis, percentage distribution of cobalt and nickel ions on modified electrodes were determined as 0.50% and 0.54% respectively. These results have also give an important evidence about the electropolymerization of [CoL] and [NiL] onto GFE surfaces.

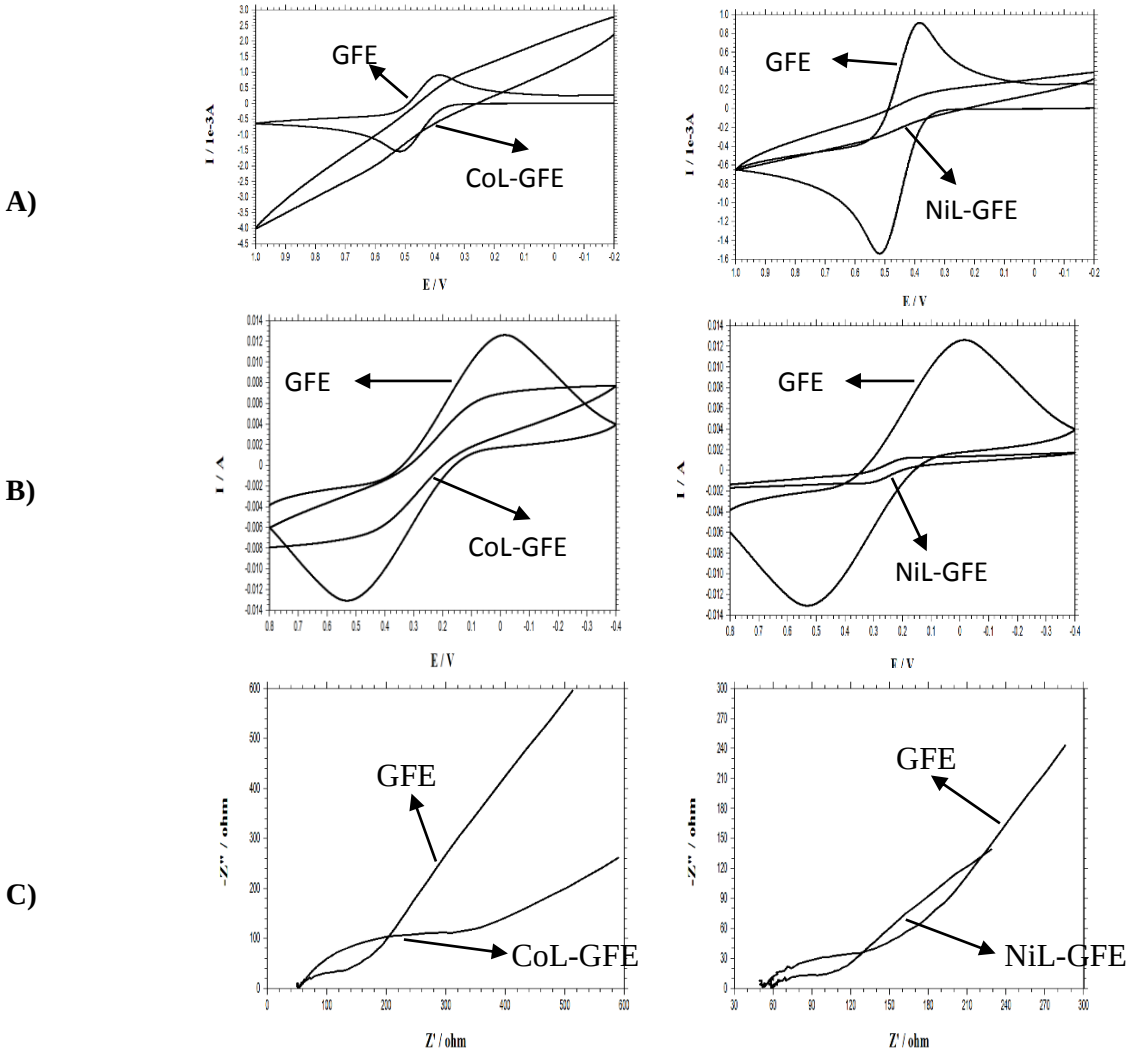

Fig. 2. Cyclic voltammograms of 1 mM (A) ferrocene (in acetonitrile containing 0.1 M $LiClO_4$), (B) ferricyanide (in 0.1 M KCl), scan rate is 100mVs^{-1} and (C) Nyquist plots for bare GFE and modified GFEs in $[Fe(CN)_6]^{3-/4-}$(in 0.1 M KCl), frequency range is 100kHz-0.05 Hz.

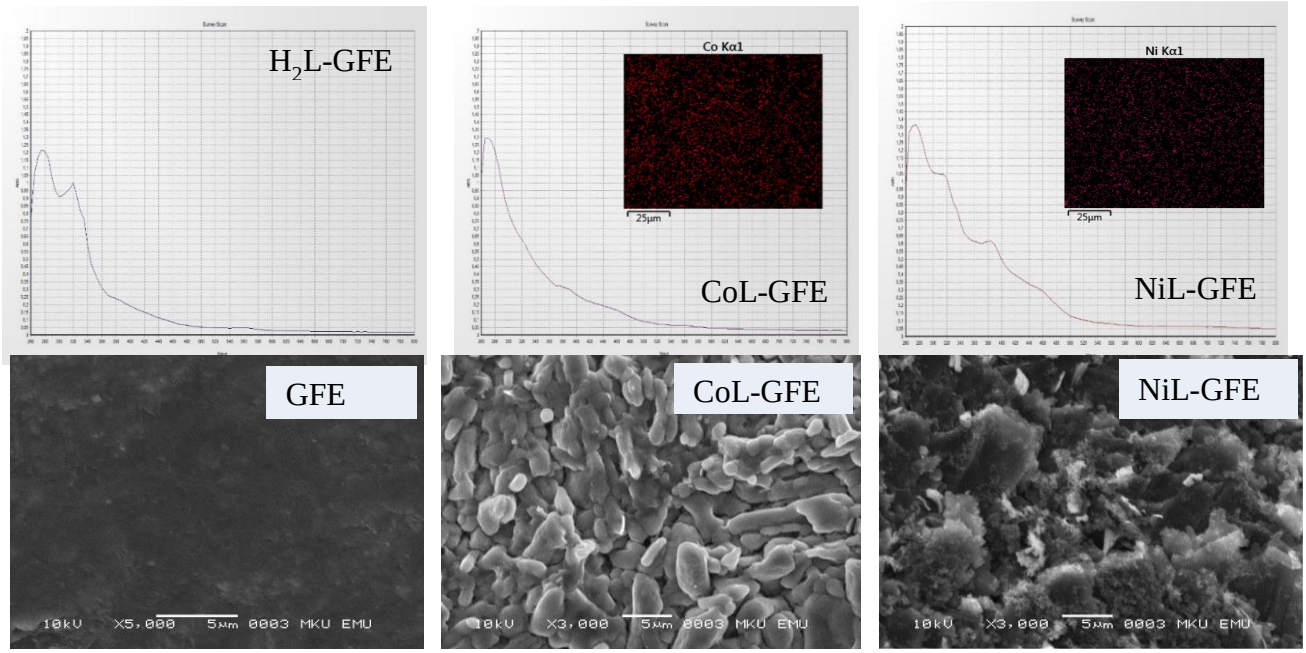

Fig.3. Uv-Vis spectrums for H_2L-GFE, CoL-GFE and NiL-GFE; SEM-EDAX mapping analysis for CoL-GFE and NiL-GFE and SEM micrographs for bare GFE, CoL-GFE and NiL-GFE.

In the UV spectrum of the [CoL] and [NiL] films, the band was observed at range of 330–450 nm were attributed to the $n–\pi*$ transition of the non-bonding electrons present on the nitrogen of the azomethine group of the Schiff base moiety [25]. In addition, the weak bands observed in the 500–700 nm region can be attributed to *d–d* transitions of the metal ions [26].

Cobalt and nickel ions distribution at modified surfaces were illustrated as red points at spectrum of SEM-EDX mapping analysis (Fig.3.). According to the SEM-EDX analysis, percentage distribution of cobalt and nickel ions on modified electrodes were determined as 0.50% and 0.54% respectively. These results have also give an important evidence about the electropolymerization of [CoL] and [NiL] onto GFE surfaces.

FT-IR spectra of NiL monomer, H_2L-GFE and NiL-GFE film are shown in Fig.4. In the spectra of NiL-GFE film, the bands are broader than the bands belongs to monomer. It is clear that after electropolymerization, due to either increasing molecular weight or the molecular weight distribution of the polymers, the signals of polymers become broader than their monomers [27, 28]. This result is significant evident for polymer formation in this study. At the same time, the presence of different vibration bands from the ligand known to belong to the metal complex at low wavelength values supports the presence of metal on the modified surfaces in accordance with other analysis methods [29].

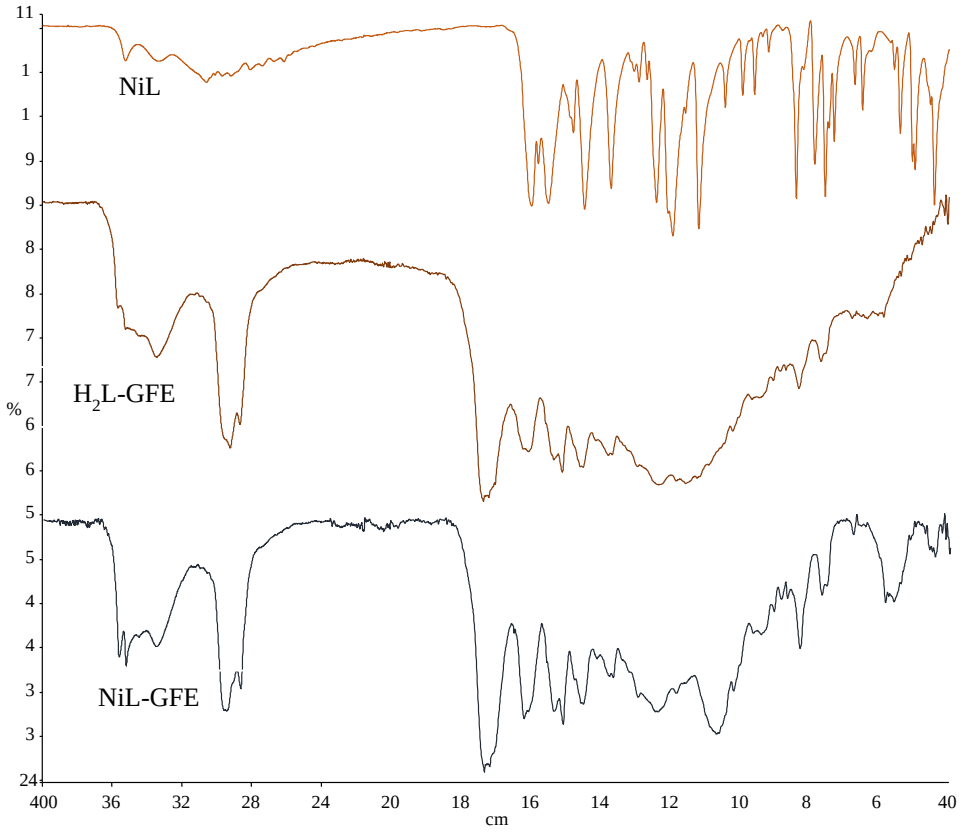

Fig.4. FT-IR spectra of [NiL] monomer, H_2L-GFE and NiL-GFE.

Catalytic activity studies for DA, AA CC and Cys were investigated at CoL-GFE and for CC and Cys were examined at NiL-GFE in pH=7 phospate buffer solution and were presented in Fig.5-6. As a result of these studies, although NiL-GFE and CoL-GFE modified electrodes have almost the same catalytic activity potential, it has been found that CoL-GFE possesses comparatively better catalytic effect.

As can be seen in the voltammograms (Fig.5., Fig.6.), best electrocatalytic activity was obtained at CoL-GFE for CC oxidation in pH=7 PBS. In comparison with the bare GFE, at this modified electrode, anodic peak current belongs to CC oxidation has increased for six times peak potential of CC oxidation appeared more positive potential value at modified electrode than bare GFE and peak shape was more sharply at modified electrode than bare electrode. Similar results were obtained for NiL-GFE in terms of the catalytic activity on CC oxidation. Additionally less significant catalytic activity was observed upon AA, Cys and sulfite bioanalytical species at CoL-GFE and for Cys at NiL-GFE, too.

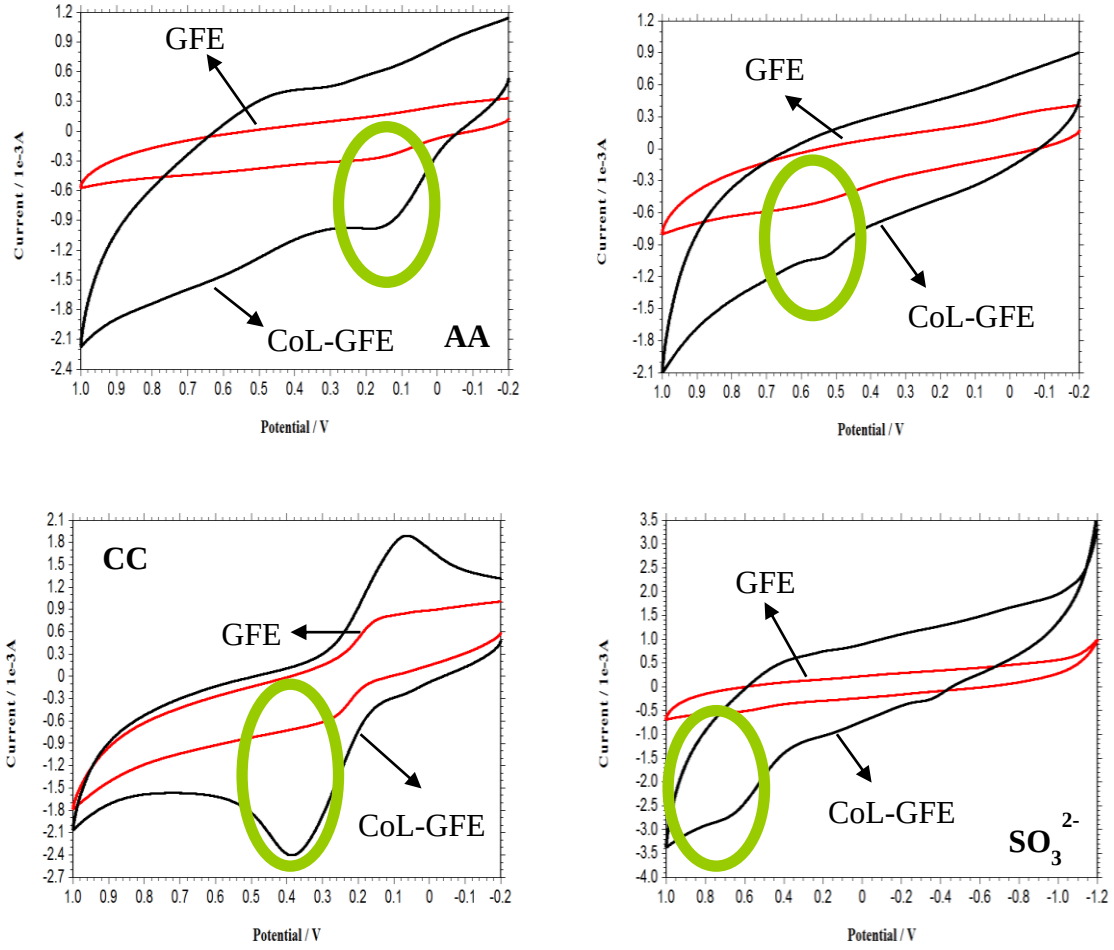

Fig.5. CVs of AA, Cys, CC and SO_3^{2-} at bare GFE and CoL-GFE in pH=7 PBS scan rate is 100 mVs^{-1}.

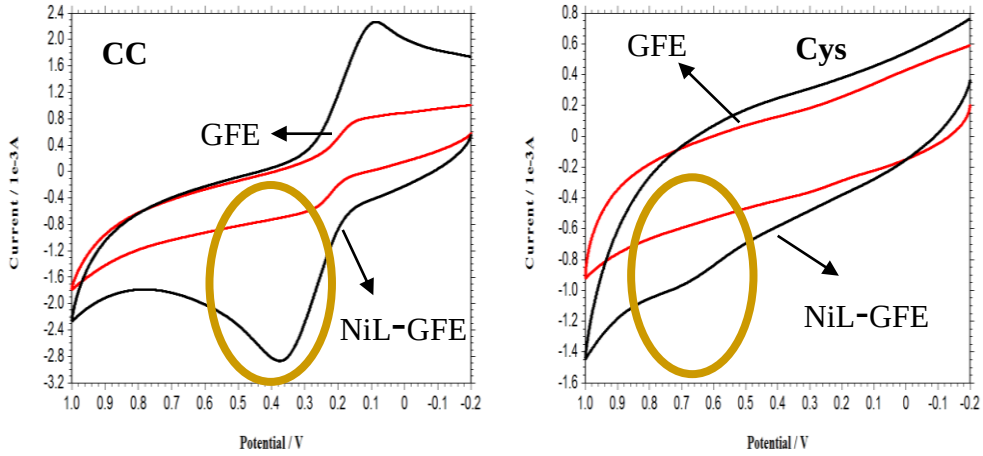

Fig.6. CVs of CC and Cys at bare GFE and NiL-GFE in pH=7 PBS, scan rate is 100 mVs^{-1}.

CONCLUSIONS

This study shows that metal complexes have been successfully coated onto the Ggraphite electrode surfaces by using electrochemical methods. In this way, alternative electrode materials can be developed for many various applications. Modified surfaces were characterized by electrochemical, spectroscopic and microscopic techniques. The results of the characterization studies have shown that the films are homogeneous, very stable and conductive. Modified electrodes have potential use for bioanalytical species at electroanalytical applications.

Acknowledgements. *This study is supported by Scientific Research Projects Committee of Mustafa Kemal University (Project number:15101).*

REFERENCES

1. M. Shen, Z. Zhang, Y. Ding, *Microchem. J*. **124,** 209 (2016).
2. U.T. Yilmaz, T. Melekogullari, A. Kekillioglu, D. Uzun, *Microchem. J*. **124,** 364 (2016).
3. A.A. İ.Turan, Z. Üstündağ, A. O. Solak, E. Kılıç, A. Avseven, *Thin Solid Films*, **517,** 2871 (2009).
4. D.D. Hu, Q. Z. Shi, Z. X. Tang, Y. Fang, J.F. Kennedy, *Carbohydrate Polymers*, **45,** 385 (2001) .
5. D. Deletioglu, S. Yalcınkaya, C. Demetgul, M. Timur, S. Serin, *Mat. Chem. and Phys.*, **128,** 500 (2011).
6. D. Uzun, A. B. Gunduzalp, E. Hasdemir, *J. of Electroanal. Chem.*, **747,** 68 (2015).
7. D. Uzun, H. Arslan, A. B. Gündüzalp, E. Hasdemir, *Surf. & Coat. Tech.*, **239,** 108 (2014).
8. 8. A. Özcan, S. İlkbaş, A. A. Özcan, *Talanta*,**165,** 489 (2017).
9. 9. S. Yalçınkaya, C. Demetgül, M. Timur, N. Çolak, *Carbohydrate Polymers*, **79,** 908 (2010).
10. 10. S. Yalçinkaya, T. Tuken, B. Yazici, M. Erbil, *Prog. in Org. Coat.*, **63,** 424 (2008).
11. 11. S.P. Kumar, R. Suresh, K. Giribabu, R. Manigandan, S. Munusamy, S. Muthamizh,
12. V. Narayanan, *Spectrochim. Acta Part A: Molec. Biomolec. Spec,*. **139,** 431 (2015).
13. 12. N. Beyazit, B. Çatıkkas, S. Bayraktar, C. Demetgül, *J. of Molec. Struct.*, **1119,** 124 (2016).
14. 13. C. Friebe, M. D. Hager, A. Winter, *Advanced Materials*, **24,** 332 (2012).
15. 14. S. Shahrokhian, Z. Kamalzadeh, A. Bezaatpour, D. M. Boghaei, *Sens. and Act. B: Chem.*, **133,** 599 (2008).
16. 15. K. Wang, J. Xu, H. Chen, *Biosens and Bioelect.* **20,** 1388 (2005).
17. 16. A. Ourari, D. Aggoun, L. Ouahab, *Inorg. Chem. Commun.*, **33,** 118 (2013).
18. 17. M. R. Parra, T. Garcıa, E. Lorenzo, F. Pariente, *Sens. and Act. B*, **130,** 730 (2008).
19. 18. C.S. Martin, M. F. S. Teixeira, *Procedia Engineering*, **47,** 1161 (2012).
20. 19. K. Cheung, W. Wong, D. Ma, T. Lai, K. Wong, *Coord. Chem. Reviews*, **251,** 2367 (2007).
21. 20. M. Niu, G. Liu, D. Wang, J. Dou, *Acta Cryst.*,. **65,** 1357 (2009).
22. 21. D. Deletioğlu, E. Hasdemir, A. O. Solak, Z. Üstündağ, R. Güzel *Thin Solid Films*, **519,** 84 (2010).
23. 22. S. Yalcınkaya *Prog. in Organic Coat.* **76,** 181 (2013).
24. 23. Y. Chen, L.R. Guo, W. Chen, X.J. Yang, B. Jin, L.M. Zheng, X.H. Xia, *Bioelectrochem.*, **75,** 26 (2009).
25. 24. D. Uzun, A. B. Gündüzalp, E. Hasdemir, *J. of Electroanal. Chem.*, **747,** 68 (2015).
26. 25. C. Çelik, M. Tümer, S. Serin, *Synth. React. Inorg. Met.-Org. Chem.*, **32,** 1839 (2002).
27. 26. M. Tümer, D. Ekinci, F. Tümer, A. Bulut, *Spectrochim. Acta Part A*, **67,** 916 (2007).
28. 27. H. Mart, A. R. Vilayetoğlu, *Polym. Degrad. Stabil.*, **83,** 255 (2004).
29. 28. C. Demetgül, M. Karakaplan, S. Serin, *Des. Mon. Polym.*, **11,** 565 (2008).
30. 29. N. Beyazit, D. Çakmak, C. Demetgül, *Tetrahedron*, **73,** 2774 (2017).

Bulgarian Chemical Communications, Volume 49, Issue I (pp. 37 – 42) 2017

Preparation of nanopores and their application for the detection of metals

D. Kaya, K. Kececi*

[1]*Department of Chemistry, Istanbul Medeniyet University, 34700, Istanbul, Turkey.*

Submitted: June 1, 2017; Accepted: September 1, 2017

We have prepared nanopores with conical geometries and we have shown the translocation properties of poly(ethylene terephthalate) (PET) membranes. In order to obtain conically shaped nanopores, asymmetric etching procedure was followed. The characterization of PET membranes were performed by electrochemical methods and SEM measurements. The sensing was performed based on resistive-pulse sensing and current-potential (I-V) measurements. Finally, we have reported the resistive-pulse sensing of Ba^{2+} using single nanoporous membranes and examined the potential dependence of resistive-pulse sensing. Effect of metal ion concentration on the ion - current rectification was also shown and it was concluded that a higher Ba^{2+}concentration can be correlated with rectification ratios.

Keywords: Resistive-pulse sensing; track-etched nanopore; metal sensing; PET membrane

INTRODUCTION

Resistive-pulse sensing, which is a powerful technique for the detection and analysis of molecules without labeling is an emerging field of research [1-3]. The resistive-pulse sensing paradigm was built on the well-known Coulter-counter principle, which was used to count particles and measure their sizes [4]. Basically, a pore (micron or sub-micron sized) is placed between two electrolyte solutions and particles are electrophoretically driven to the oppositely charged electrode. During the translocation of particles through the pore, the ionic current drops and this signal is used for counting particles and identifying their properties. This technique was miniaturized by using biological nanopores and enabled the detection of individual molecules without labelling and discriminate different types of molecules [5].

Several resistive-pulse studies have been conducted using biological nanopores, especially α-Hemolysin [6, 7]. However, there are many shortcomings of biological nanopores which limit their efficiency as sensors such as their fixed size, instability and the fragility of the lipid bilayer in which the pore is placed. Therefore, chemically and mechanically robust synthetic nanopores were developed that are low cost, user friendly and enable highly sensitive and specific rapid analysis [8]. The precise control over the pore size and geometry, the ability to change the surface characteristics and to integrate with electronics or optical systems made the synthetic nanopores even more advantageous [9, 10]. Also, surface functionalization is more diverse in synthetic systems, which enhances the sensibility and selectivity for certain molecules [11, 12].

Some of the techniques that are widely used for the fabrication of synthetic nanopores are electron beam lithography [13, 14], nanopipettes [15, 16], ion-beam sculpting [17], micromolding [18], and track-etching [19-22]. Compared to other nanopore fabrication techniques, track-etch method emerges as a viable alternative to obtain the desired nanopores in size and shape with uniform pore density without the limitations of the others [23].

In track-etch method membranes (or films) are first irradiated with accelerated heavy ions in order to create latent tracks inside the membranes. When the irradiated membranes are exposed to appropriate etching solution, the obtained tracks turn into nanopores and the etching process is controlled by neutralization of etching solution. If the polymer film is irradiated with a single-ion (i.e., 1 ion/membrane) and goes through chemical etching, single-pore membranes which are optimal for studying the detection and identification of individual molecules can be formed [24]. In track-etch method, some of the most widely used membranes are poly(ethylene terephthalate) (PET), polycarbonate (PC) and polyimide (PI). Different types of analytes such as proteins [25], DNAs [24, 26] etc. [27] have been detected using these polymer nanoporous membranes. Various nanopore geometries have also been reported in PET films which can affect the efficiency of sensing [28].

In this study, we showed the interaction of PET nanopores with divalent cations and monitor the real-time signals based on resistive-pulse sensing. The main reasons for choosing PET was that it is a mechanically and chemically stable, flexible material with a slightly negative surface charge.

* To whom all correspondence should be sent.
E-mail:kaan.kececi@medeniyet.edu.tr

Chemical etching of PET membranes leads to the formation of carboxylate groups (-COO^-) on the surface of the membranes and pore walls [29]. The negative -COO^- groups on the walls of PET membrane had enhanced the affinity to cation analytes so in contrast to the previous studies, no chemical modification has been used on nanopore surface to promote the capture the cations. Successful stochastic sensing (resistive-pulse sensing) of divalent cations using α-Hemolysin was previously shown by others [30-33].

EXPERIMENTAL

Materials and methods

PET membranes (3 cm diameter, 12 μm thickness) were provided by Gesellshaft für Schwerionenforschung (GSI, Darmstadt-Germany). The membranes were irradiated with heavy ions (i.e., Au ion, 11.4 MeV) at various ion densities even down to 1 ion/membrane. This was succeeded by defocusing the ion beam and using a metal mask with a 0.1 mm diameter aperture with a shutter system which shuts down the ion beam as the single ion passage was detected. All the membranes were exposed to UV irradiation overnight (λ = 320 nm) to saturate the damages in tracks. All solutions were prepared from deionized water (Millipore Direct-Q 5, Millipore Co.). Formic acid (HCOOH), sodium hydroxide (NaOH), barium chloride ($BaCl_2$) and potassium chloride (KCl) were purchased from Sigma Aldrich. All chemicals were used as received without further purification.

Preparation of nanopore membranes

Prior to etching, membranes were treated with long-wave UV irradiation overnight in order to increase the track etching rate and make the pores more homogeneous in size by sensitizing the tracks. Conically shaped nanopores were obtained using asymmetric chemical etching whose conditions were previously discussed [34]. Shortly, the membrane was placed in a conductivity cell with one side of the cell facing the UV-treated side of the membrane, filled with alkaline etching solution (9 M NaOH) and the other half-cell was filled with the stopping solution (1 M HCOOH and 1 M KCl). Platinium (Pt) electrodes were immersed into each cell and 1 V transmembrane potential was applied to monitor the breakthrough moment. The etching process was continued for two hours and then the etching solution was replaced with stopping solution for neutralization. Then both cells were rinsed with di-water to remove possible residues from the membrane surface. After this etching process, a conically shaped nanopore was obtained with two different sized openings called base (large opening) and tip (small opening).

Characterization of the nanopores

The large opening of the nanopore (d_{base}) was determined by the SEM images of multipore membranes (10^8 nanopores/cm^2). Single pore membranes were etched under the same conditions as multipore membranes and the small opening (d_{tip}) was determined through electrochemical measurements [12]. For the electrochemical measurement, each side of the conductivity cell was filled with electrolyte solution (i.e., 1 M KCl, 10 mM PBS buffer at pH = 7). Ag/AgCl electrodes (BAS, West Lafayette, IN) were immersed into both sides of the cell and potential was stepped (50 mV) between -1 V and +1 V (Keithley 6487 picoammeter/voltage source, Cleveland, OH, USA). Since the resistance of the nanopore (R) is proportional to the conductivity of solution (ρ), the length of nanopore (L, thickness of the membrane), d_{base} and d_{tip}; the tip diameter (d_{tip}) can be calculated with Eqn. 1. R value was calculated from the reciprocal of the slope of the current – voltage (I-V) curve [34]. The average of three sequential measurements was used for the calculations.

$$R = \frac{4\rho L}{\pi d_{tip} d_{base}} \quad (1)$$

The conductivity of the solution was measured using a conductivity meter (Mettler-Toledo FE 30, Colombus, OH, USA).

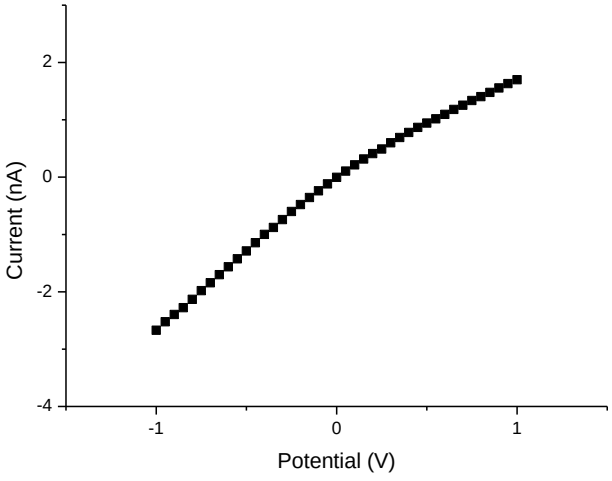

Fig. 1. I-V Curve of a PET single conical nanopore in 1 M KCl (d_{base}: 515 nm; d_{tip}: 6 nm).

Electroless gold plating

The formation of gold replicas inside the nanopores by electroless gold plating method, which is a templating technique, gives valuable information about the geometry of the nanopore. This is simply achieved by filling the pores with Au and removing

the polymer template by dissolving it. The exact geometry of the replicas obtained from multiporous membranes can be visualized using SEM. The schematic representation of chemical plating of the nanopore wall is given in Fig. 2. The process mainly consists of three steps. Firstly Sn^{2+} is coated on the negatively charged pore wall of PET. After washing the membrane with methanol, it is immersed in the $AgNO_3$ solution containing ammonia to form a redox reaction on the pore wall of the membrane where Ag (I) is converted to elemental Ag while Sn (II) is oxidized to Sn (IV). The gold coating solution contains $Na_3Au(SO_3)_2$, Na_2SO_3, $NaHCO_3$ and formaldehyde in various proportions. When the membrane is immersed in this solution, once more a redox reaction occurs on the pore wall. Since gold has a more positive reduction potential than silver, the gold particles switch place with the silver on the surface. These gold particles serve as catalysts in the presence of formaldehyde, thereby reducing the Au (I) ions to Au (0). After Au deposition into the nanopores, the membrane was dissolved and the remaining gold nanocones were filtered with a Whatman Anodisc membrane. The obtained nanocones were investigated with SEM.

Resistive-pulse sensing experiments

The chemically etched nanopore membrane was placed between two halves of a conductivity cell and each half-cell was filled with 100 mM KCl. Background current-time measurements were recorded between (+1000 mV) – (-1000 mV) with 100 mV steps. Cation analytes at predetermined concentrations were added to the tip side of the conductivity cell. Ag/AgCl electrodes were used to measure the current-pulses (events). An Axopatch 200B (Molecular Devices Corporation, CA, USA) was used in voltage-clamp mode to apply a transmembrane potential between Ag/AgCl electrodes with a low-pass Bessel filter at 2 kHz bandwidth. The signal was digitized using a Digidata 1440 analog-to-digital converter (Molecular Devices Corporation, CA, USA) at a sampling frequency of 5 kHz. Data were analyzed using pClamp 10.5 (Molecular Devices Corporation).

RESULTS AND DISCUSSION

Characterization of the nanopores

PET membranes were etched with alkali solution (i.e., 9M NaOH) from one side only for a conical geometry. After the etching process, the base diameters of conical nanopores were determined by SEM images of these multipore membranes (average of minimum 10 pores) (Figure 3). The base diameter of the conical membranes etched for 2 hours was found to be 533 ± 46 nm.

The conical geometry of the pores was confirmed using the SEM images of gold nanocones obtained with electroless gold plating method (Fig. 4).

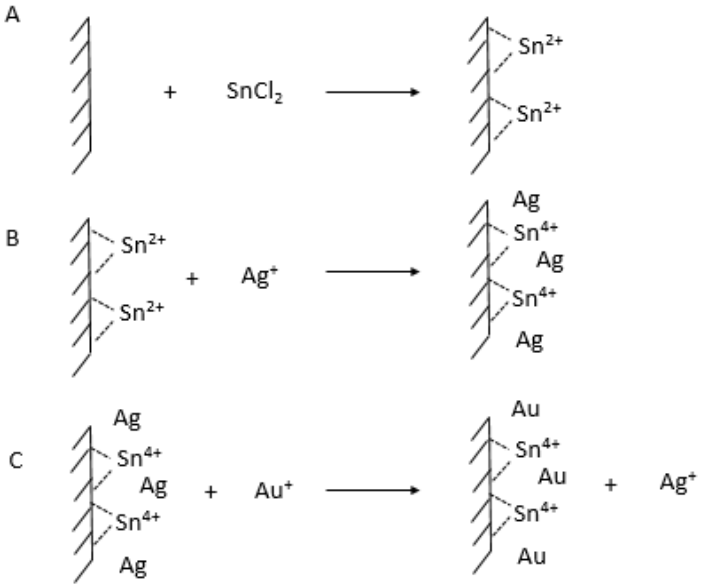

Fig. 2. Au plating steps of the nanopore surface.

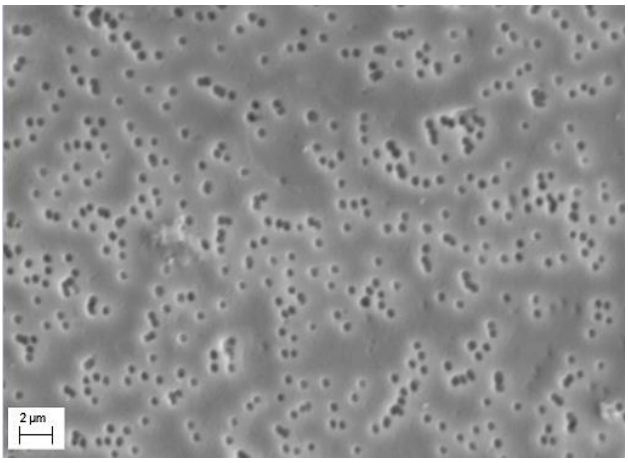

Fig. 3. SEM image of multi-porous PET membrane etched for 2 hours.

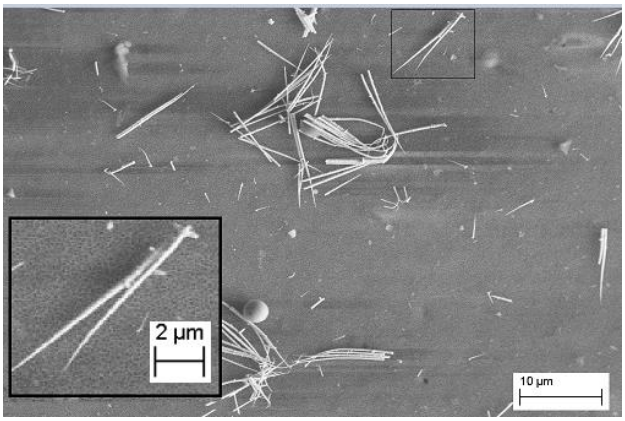

Fig. 4. SEM image of Au cone replicas by template synthesis

Resistive-pulse sensing of Ba^{2+} ions

In order to examine the transport properties of Ba^{2+} ions, potential dependence of the current-pulses and effect of ion concentration on the current rectification were studied. The current was recorded with 100 mM KCl at 400 mV before adding the metal analyte and was found to be stable, showing no current-pulses (Fig. 5 - A). When the Ba^{2+} ions (10 mM in 100 mM KCl) were added to the tip side of the membrane, current-pulses were observed under same potential due to the translocation of the metal ions (Fig. 5 - B). The current-pulse signals of Ba^{2+} showed an upward trend due to the higher binding affinity to carboxylate groups on the surface, decreasing the overall resistance of the pore. These conductive pulses can also be attributed to the high conductance of the particles relative to the electrolyte and the effect of particle charge on the ionic distribution near the pore opening, increasing the conductance temporarily [35].

The potential was stepped down to 250 mV and no current pulses were observed below this value (Fig.5 - C-E).

The potential dependence of Ba^{2+} translocation is given in Fig. 6. The current-pulse frequency was calculated by averaging the number of current-pulses of three 5 minute current-time recordings and a linear correlation was observed between the examined potential values. A similar linear potential dependency was shown for DNA translocation in various studies [34, 36]. Harrell and co-workers have explained the translocation phenomenon in track-etched nanoporous membranes in detail [36] and they have derived an equation (Eqn. 2) giving the relationship between the frequency of current-pulses (f) and electric field (E) where, z is the charge of the analyte, D_t is the diffusion coefficient, C is the concentration and A is the Avogadro's number.

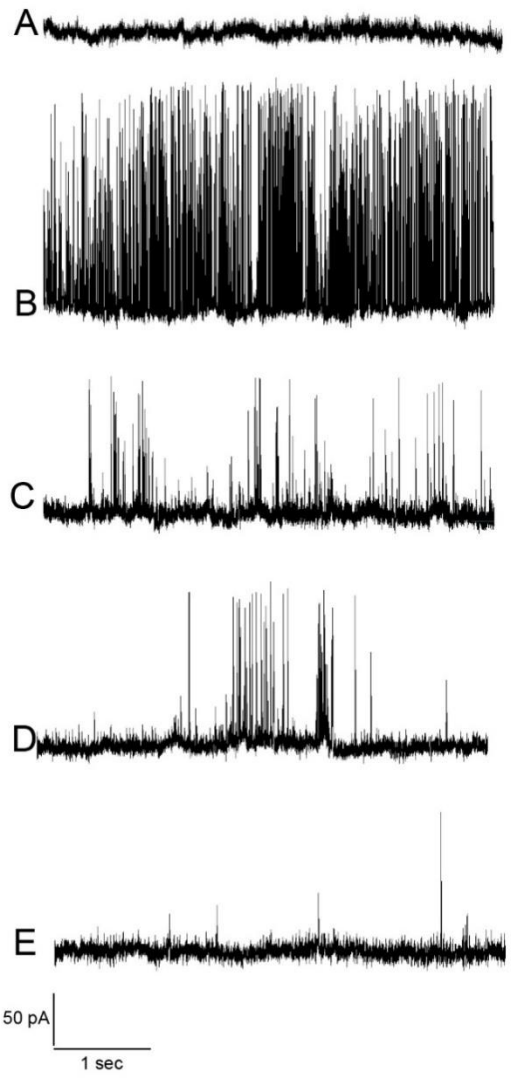

Fig. 5. Current-time traces of Ba^{2+} (10 mM) at 400 mV (without analyte) (A), 400 mV (B), 350 mV (C), 300 mV (D), 250 mV (E) Tip diameter = 6 nm.

$$f = -zFD_tCE\left(\pi r_{tip}^2\right)A/RT \qquad (2)$$

According to previous studies, for conically shaped track-etched nanopores, the electric field strength (E) ranges between 1.3 and 2 MV/m [37], which forms a trapping zone to capture the molecule easily at the tip [38]. So the increase in the electric field at the nanopore entrance causes a linear increase in the current-pulse frequency. The linear dependence to potential and the occurrence of a threshold voltage suggest that the current-pulse frequency was dominated by the transport of Ba^{2+} ions through the nanopore.

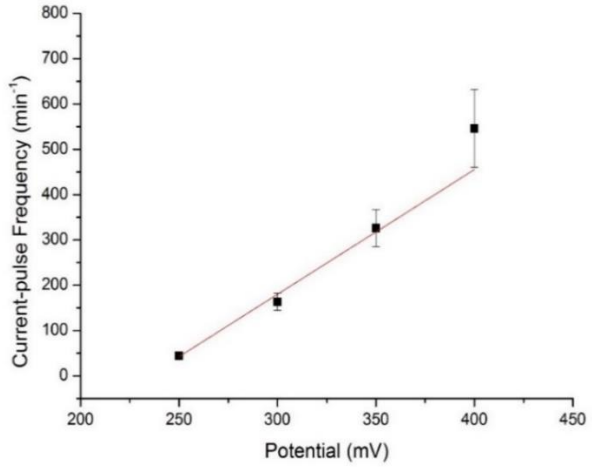

Fig. 6. Current-pulse frequency versus potential (10 mM Ba^{2+}).

Effect of concentration on ion current rectification

It has previously been discussed by Siwy that asymmetric nanopores cause rectification on the ionic current even though the concentration of the electrolyte on both sides of the nanopore are the same and as a result asymmetric I-V curves are observed [39]. This non-linear behavior which is dependent on the surface charge can be described as the 'on' and 'off' state of the nanopore.

The ion current rectification (ICR) is the ratio between the current values at -1 V and +1 V (see Eqn. 3). PET nanopores have a negative surface charge at neutral pH due to the carboxylate groups produced during etching and at neutral pH the ICR is expected to be higher than 1 as the nanopore surface charge is negative.

$$ICR = {|i_{-1}|}/{|i_{+1}|} \quad (3)$$

In order to investigate the effect of Ba^{2+} concentration on the ion current rectification, a series of Ba^{2+} solutions at varying concentrations (10 µM – 10 mM) were prepared in 100 mM KCl. I-V curves obtained with Ba^{2+} solutions at different concentrations are presented in Fig. 7.

Ion- current rectification ratios were calculated and plotted against log [Ba^{2+}] values in order to further examine the effect of analyte concentration on the rectification behaviour (Fig. 8). It is shown that a decrease in ICR was observed with increasing Ba^{2+} concentrations. This finding indicates that through the interactions between the negatively charged pore surface and positive Ba^{2+} ions, the surface charge was decreased and ICR decreased accordingly since the I-V curves are able to give information about the surface charge on the pore walls. A similar behaviour was shown by Zhai et.al. for a conical PET nanopore for Cr^{3+} detection [40].

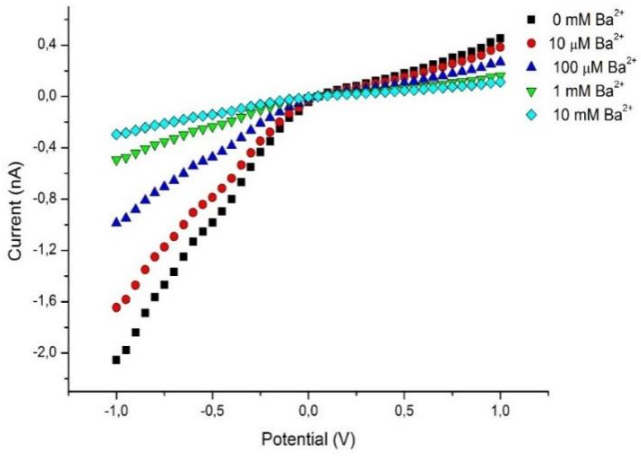

Fig. 7. I-V plots of Ba^{2+} at various concentrations (Tip diameter = 5 nm).

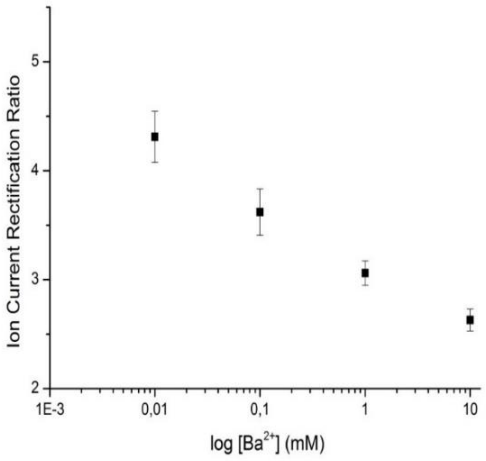

Fig. 8. Dependence of ion current rectification ratio on Ba^{2+} concentration.

CONCLUSION

In this work, track-etched PET membranes were used to fabricate asymmetric nanopores with conical

geometries. The potential use of these nanoporous membranes as resistive-pulse sensor for metal ions was shown and Ba^{2+} ion was chosen as model showed the only resistive-pulse signal and correlation of metal ion (i.e., Ba^{2+}) using track-etched polymer membranes. The current-pulse frequency had a linear dependence on applied potential. This linear dependence to potential indicated that the current-pulse frequency was dominated by the transport of Ba^{2+} ions through the nanopore. Ion-current rectification ratios were calculated and their dependence to Ba^{2+} concentration was also investigated. The opposite correlation between Ba^{2+} and ICR was shown. This was due to the interactions between the negatively charged pore surface and positive Ba^{2+} ions, decreasing the overall surface charge and ICR accordingly.

Acknowledgement. *This work is financially supported by Istanbul Medeniyet University Scientific Research Projects Coordination Unit (Project Number: FKD-2015-432)*

REFERENCES

1. B.M. Venkatesan, R. Bashir, *Nature Nanotechnol.*, **6**, 615 (2011).
2. Y.R. Kim, J. Min, I.H. Lee, S. Kim, A.G. Kim, K. Kim, K. Namkoong, C. Ko, *Biosensors Bioelectronics*, **22**, 2926 (2007).
3. M. AdelaBooth, R. Vogel, J.M. Curran, S. Harbison, J. Travas-Sejdic, *Biosensors Bioelectronics*, **45**, 136 (2013).
4. W.H. Coulter, Means for Counting Particles Suspended in a Fluid, U. Patent, Editor. 1953, USA.
5. J.J. Kasianowicz, E. Brandin, D. Branton, D.W. Deamer, *Proc. Natl. Acad Sci. USA*, **93**, 13770 (1996).
6. J. Chu, M. Gonzalez-Lopez, S.L. Cockroft, M. Amorin, M.R. Ghadiri, *Angew Chem Int Edit*, **49**, 10106 (2010).
7. J.Schmidt, *Curr. Opinion Biotechnol.*, **39**, 17 (2016).
8. M. Kuhnemund, M. Nilsson, *Biosens Bioelectron*, (2014).
9. D. Kaya, A. Dinler, N. San, K. Kececi, *Electrochimica Acta*, **202**, 157 (2016).
10. R. Patricio, A. PavelYu, C. Javier, M. Salvador, *Nanotechnology*, **19**, 315707 (2008).
11. S.M. Iqbal, D. Akin, R. Bashir, *Nat Nanotechnol*, **2**, 243 (2007).
12. K. Kececi, L.T. Sexton, F. Buyukserin, C.R. Martin, *Nanomedicine-UK*, **3**, 787 (2008).
13. A.J. Storm, J.H. Chen, X.S. Ling, H.W. Zandbergen, C. Dekker, *Nature Materials*, **2**, 537 (2003).
14. Y. Liebes-Peer, V. Bandalo, Ü. Sökmen, M. Tornow, N. Ashkenasy, *Microchim Acta*, **183**, 987 (2016).
15. Y.X. Wang, K. Kececi, M.V. Mirkin, V. Mani, N. Sardesai, J.F. Rusling, *Chem Sci*, **4**, 655 (2013).
16. C.A. Morris, A.K. Friedman, L.A. Baker, *Analyst*, **135**, 2190 (2010).
17. A.L. Biance, J. Gierak, É. Bourhis, A. Madouri, X. Lafosse, G. Patriarche, G. Oukhaled, C. Ulysse, J.C. Galas, Y. Chen, L. Auvray, *Microelectronic Engineering*, **83**, 1474 (2006).
18. O.A. Saleh, L.L. Sohn, *Nano Letters*, **3**, 37 (2003).
19. L.X. Cao, Y.G. Wang, *Radiat Meas*, **44**,1093 (2009).
20. T.W. Cornelius, B. Schiedt, D. Severin, G. Pepy, M. Toulemonde, P.Y. Apel, P. Boesecke, C. Trautmann, *Nanotechnology*, **21 (15)** (2010).
21. Q.H. Nguyen, M. Ali, R. Neumann, W. Ensinger, *Sensors and Actuators B-Chemical*, **162**, 216 (2012).
22. J. Wang, C.R. Martin, *Nanomed*, **3**, 13 (2008).
23. A. Kocer, L. Tauk, P. Dejardin, *Biosensors Bioelectronics*, **38**, 1 (2012).
24. A. Mara, Z. Siwy, C. Trautmann, J. Wan, F. Kamme, *NanoLetters*, **4**, 497 (2004).
25. Z. Siwy, L. Trofin, P. Kohli, L.A. Baker, C. Trautmann, C.R. Martin, *JACS*, **127**, 5000 (2005).
26. B. Schiedt, K. Healy, A.P. Morrison, R. Neumann, Z. Siwy, *Nuclear Instruments and Methods in Physics Research Section B: Beam Interactions with Materials and Atoms*, **236**, 109 (2005).
27. E.A. Heins, Z.S. Siwy, L.A. Baker, C.R. Martin, *NanoLett*, **5**, 1824 (2005).
28. P.Y. Apel, I.V. Blonskaya, S.N. Dmitriev, O.L. Orelovich, B.A. Sartowska, *Nuclear Instruments and Methods in Physics Research Section B: Beam Interactions with Materials and Atoms*, **365, Part A**, 409 (2015).
29. Z. Siwy, P. Apel, D. Baur, D.D. Dobrev, Y.E. Korchev, R. Neumann, R. Spohr, C. Trautmann, K.O. Voss, *Surface Science*, **532**, 1061 (2003).
30. O. Braha, L.Q. Gu, L. Zhou, X. Lu, S. Cheley, H. Bayley, *NatBiotechnol*, **18**, 1005 (2000).
31. S. Wen, T. Zeng, L. Liu, K. Zhao, Y. Zhao, X. Liu, H.-C. Wu, *J AmChemSoc*, **133**, 18312 (2011).
32. C. Yang, L. Liu, T. Zeng, D. Yang, Z. Yao, Y. Zhao, H.-C. Wu, *Anal. Chem.*, **85**, 7302 (2013).
33. H.-Y. Wang, Z.-Y. Song, H.-S. Zhang, S.-P. Chen, *Microchim Acta*, **183**, 1003 (2016).
34. K. Kececi, N. San, D. Kaya, *Talanta*, **144**, 268 (2015).
35. E. Weatherall, G.R. Willmott, *The Journal of Physical Chemistry B*, **119**, 5328 (2015).
36. C.C. Harrell, Y. Choi, L.P. Horne, L.A. Baker, Z.S. Siwy, C.R. Martin, *Langmuir*, **22**, 10837 (2006).
37. L.T. Sexton, L.P. Horne, S.A. Sherrill, G.W. Bishop, L.A. Baker, C.R. Martin, *JACS*, **129**, 13144 (2007).
38. S. Lee, Y. Zhang, H.S. White, C.C. Harrell, C.R. Martin, *Anal Chem*, **76**, 6108 (2004).
39. Z.S. Siwy, *Adv. Funct. Mater.*, **16**, 735 (2006).
40. Q. Zhai, J. Wang, H. Jiang, Q. Wei, E. Wang, *Talanta*, **140**, 219 (2015).

Bulgarian Chemical Communications, Volume 49, Issue I (pp. 43 – 49) 2017

Zetasizer measurements of copolymer-drug carrier system: poly (maleic anhydrite-co-vinyl acetate) -acriflavine conjugate

D. Sakar Dasdan*[a], A. Dizdar[a], G. Karakus[b]

[a]*Yildiz Technical University, Faculty of Arts and Sciences, Department of Chemistry, 34220 Esenler, Istanbul, Turkey*
[b]*Cumhuriyet University, Faculty of Pharmacy, Department of Pharmaceutical Chemistry, 58140, Sivas, Turkey*

Submitted: June 1, 2017; Accepted: September 1, 2017

Copolymeric drug carrier system, poly (maleic anhydrite-*co*-vinyl acetate) copolymer (MAVA) carrying acriflavine drug (AF) has been examined by Zeta Potential Analyzer to determine the stability and controlled drug release tests in water with different pHs and simulated body fluids. Zetasizer measurements such as zeta potential, mobility, and particle size of prepared copolymer, drug and copolymer-drug conjugate (MAVA-AF) were done. The activity of copolymer-drug conjugate in different pHs and simulated body fluids was checked via UV-VIS spectrophotometer as a function of time.

Keywords: copolymer-drug conjugate, stability, particle size, zeta potential

1. INTRODUCTION

Recently, synthetic polymers are used for controlled drug delivery systems or drug carrier as biomaterials. There has been a growing interest in polymer conjugation with biologically active components. Such conjugates usually accumulate in tumors and can reduce toxicity in the body. Depending on the desired location, polymer conjugates can be synthesized to either have degradable or non-degradable chemical bonds with their associated drug. There is a strong desire to synthesize polymeric conjugates with bioactive components and other drugs. Polymer-drug conjugates are drug molecules held up in polymer molecules and have shown very promising results. The drugs remain attached to the polymer and are not activated until the enzymes associated with the diseased tissue are present. This process severely minimizes damage to healthy tissue [1-3]. Surface properties of drug carrier systems are responsible for their interactions with plasma proteins. Zetasizer measurements which are zeta potential, particle size and mobility provide valuable properties of particles or molecules in liquid medium. These characteristics directly affect bioavailability, dissolution and immunotoxicity [4-8].

In the present work, the particle size, mobility and zeta potential of novel copolymer-drug conjugate including nontoxic drug carrier MAVA [9], MAVA-AF [10] were measured as a function of pH in water and as a function of time in the simulated body fluids.

2. EXPERIMENTAL

2.1. Instrument and materials

The particle size and particle size distribution of MAVA, AF and MAVA-AF solutions in water were measured via Brookhaven 90 Plus/BI-MAS (Multi Angle Particle Sizing) and electrophoretic mobility and zeta potential measurements of all solutions were also determined by Brookhaven Zeta Potential Analyzer in water as a function of pH and in the different medias such as phosphate buffer saline (PBS; biotechnology grade, 137 mM NaCl, 2 mM KCl ve 10 mM phosphate buffer, pH 7.4 ± 0.1) tampon (Sigma) and Dextrose (5 %) at physiological temperature (37ºC) as a function of time. The Shimadzu UVmini-1240. UV/Visible spectrophotometer was used to check the activity of MAVA, AF and MAVA-AF.

2.2. Zetasizer Measurements

Electrophoretic mobility, μ_e referred as mobility is the average velocity of dispersed particles in an electiric field of 1V/m:

$$V_S = \mu_e E \quad (1)$$

Where E is electric field and V_S is an average drift velocity of particles. The sign of mobility shows the surface charge of particles. A positive mobility of a particle means the surface is positively charged, negative mobility means the surface is negatively charged. The zero mobility value shows the velocity is zero and electrostatic repulsion is small.

Zeta potential is the electrostatic potential at the electrical double layer surrounding a nanoparticle in solution. In other words, zeta potential is the potential difference between the dispersion medium and the stationary layer of fluid attached to the dispersed particle [4].

Zeta potential, ζ was determined ten times for each sample. Results were automatically calculated by the analyzer using the following Smoluchowski equation:

* To whom all correspondence should be sent.
E-mail: dolunaykar@yahoo.com

$$\mu_e = \frac{\varepsilon\zeta}{\eta} \quad (2)$$

where μ_e is electrophoretic mobility, ε is the dielectric constant, ζ is the zeta potential and η is the viscosity of electrolyte [11]. Nanoparticles with a zeta potential between -10 and +10 mV are considered approximately neutral, while nanoparticles with zeta potentials of greater than +30 mV or less than -30 mV are considered strongly cationic and strongly anionic, respectively [12].

According to general colloid chemistry principles, a dispersed system typically loses stability when the magnitude (i.e. absolute value) of the zeta potential decreases to less than approximately 30 mV. As a result, there will be some region surrounding the condition of zero zeta potential (i.e. the isoelectric point, or IEP) for which the system is not particularly stable. Within this unstable region, the particles may agglomerate, thereby increasing the particle size [4].

3. RESULTS AND DISCUSSION

The particle size, mobility and zeta potential of MAVA, AF and MAVA-AF solutions in water were measured as a function of pH and different media such as PBS buffer (Sigma) and dextrose (5 %). The copolymer-drug activity in studied pHs and medias was monitored by UV-VIS spectrophotometer.

The pH effects on particle size, mobility and Zeta Potential of MAVA solution, AF and MAVA-AF were given in Table 1, Table 2 and Table 3, respectively.

MAVA in water is negatively charged and it is anionic. Particle size of MAVA increases via increasing pH and MAVA showed maximum zeta potential at pH=7. MAVA was stable in water all studied pH.

AF in water is negatively charged and it is anionic. Particle size of AF does not change with increasing pH and AF is stable at basic media. it is more stable via increasing pH.

MAVA-AF in water is negatively charged and it is anionic. Particle size of MAVA-AF does not change via increasing pH and it is nearly neutral at acidic media and it is more stable via increasing pH.

The activity of MAVA, AF and MAVA-AF in water at the different pHs were checked by UV-VIS and spectrums were given in Fig.1.

Table 1. pH effect on particle size, mobility and zeta potential of MAVA in water

pH	Particle Size (nm)	Mobility	Zeta Potential (mV)
2	145	-2.8	-35.7
3	160	-3.7	-47.2
4	150	-3.4	-43.1
5	170	-4.5	-58.2
6	180	-2.2	-28.5
7	185	-5.5	-71.1
8	195	-5.3	-67.7
9	220	-5.0	-63.6
10	260	-4.6	-58.3
11	320	-3.5	-50.0

Table 2. pH effect on particle size, mobility and zeta potential of AF in water

pH	Particle Size (nm)	Mobility	Zeta Potential (mV)
2	335	-0.7	-8.5
3	345	-0.8	-9.9
4	315	-1.1	-13.7
5	570	-1.2	-15.8
6	660	-2.3	-29.5
7	560	-2.5	-30.3
8	470	-2.8	-36.0
9	440	-2.9	-37.3
10	270	-2.6	-33.3
11	260	-2.8	-35.8

Table 3. pH effect on particle size, mobility and zeta potential of MAVA-AF in water

pH	Particle Size (nm)	Mobility	Zeta Potential (mV)
2	380	-0.1	-1.0
3	420	-0.2	-2.3
4	475	-0.3	-3.3
5	685	-0.8	-9.6
6	710	-1.2	-14.7
7	680	-2.1	-27.0
8	650	-1.9	-25.2
9	600	-1.6	-20.9
10	530	-1.7	-21.3
11	500	-1.8	-23.5

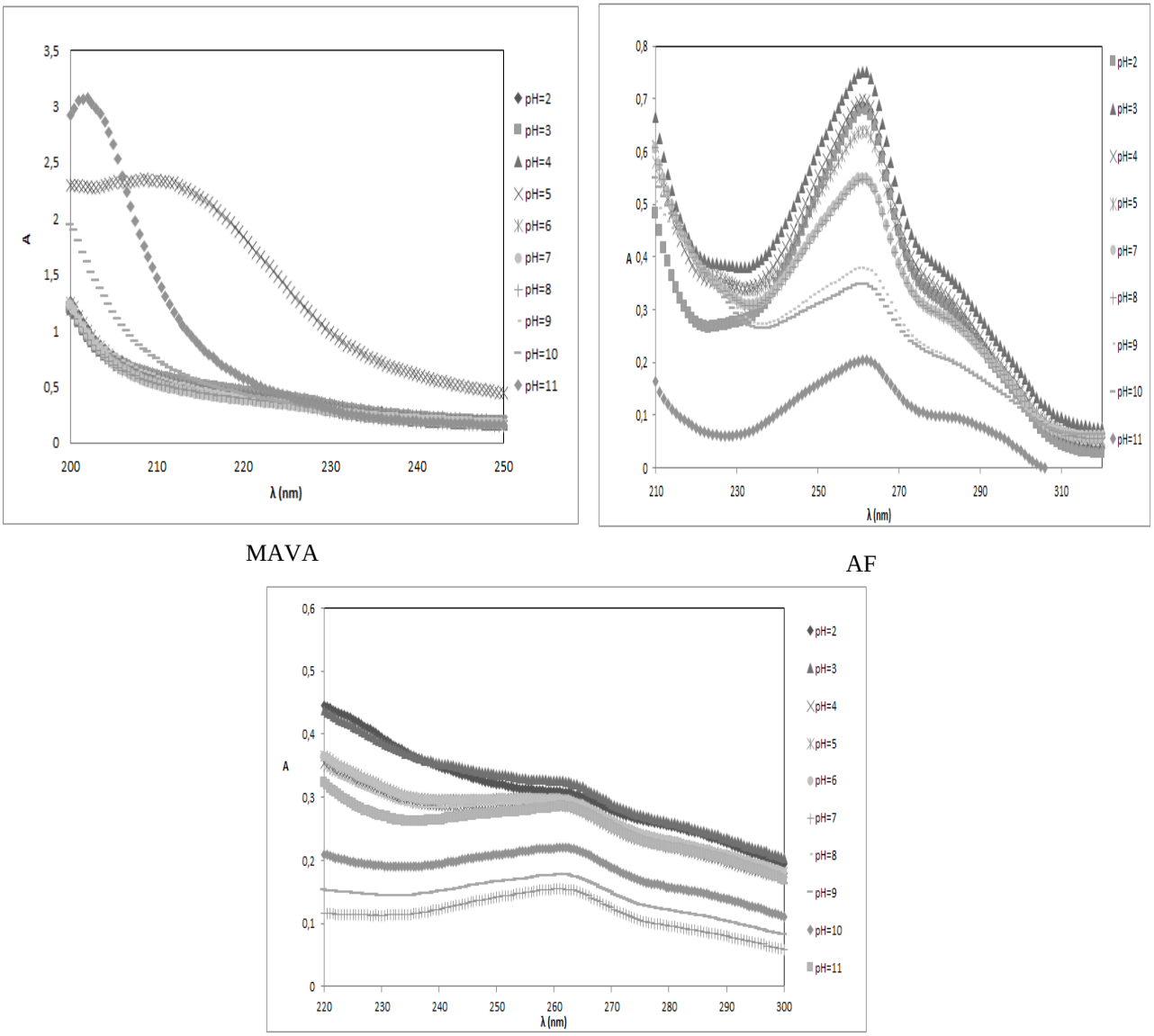

MAVA AF

MAVA-AF

Figure 1. pH effect on activity of MAVA, AF and MAVA-AF in water as a function of pH

According to Figure 1, the activities of MAVA, AF and MAVA-AF were shown as pH=8 (the lowest), pH=11(the highest); pH=11 (the lowest), pH=3 (the highest) and pH=7 (the lowest), pH=3 (the highest), respectively.

The results of particle size, mobility and zeta potential measurements of MAVA, AF and MAVA-AF in 5 % dextrose as a function of time were given in Table 4, 5 and 6, respectively.

Table 4. Time effect on particle size, mobility and zeta potential of MAVA in 5 % dextrose

Time (h)	Particle Size (nm)	Mobility	Zeta Potential (mV)
0	120	-1.4	-17.6
0.5	119	-1.7	-21.8
1	119	-1.5	-19.4
2	120	-2.3	-28.9
3	120	-1.2	-15.0
96	120	-1.7	-21.3
168	100	-1.3	-16.5

MAVA in 5 % Dextrose is negatively charged and it is anionic. Particle size of MAVA does not change with time and it means it did not show any aggregation with time.

Table 5. Time effect on particle size, mobility and zeta potential of AF in 5 % dextrose

Time(h)	Particle Size (nm)	Mobility	Zeta Potential (mV)
0	960	-1.1	-13.6
0.5	620	-1.2	-15.4
1	270	-1.6	-20.1
2	170	-1.0	-12.8
3	270	-2.3	-28.9
96	590	-1.2	-15.3
168	480	-0.7	-9.0

AF in 5 % dextrose is negatively charged and it is anionic. Particle size and zeta potential of AF does not change with time and it means it did not show any aggregation with time.

Table 6. Time effect on particle size, mobility and zeta potential of MAVA-AF in 5 % dextrose

Time(h)	Particle Size (nm)	Mobility	Zeta Potential (mV)
0	380	-1.3	-16.9
0.5	390	-1.4	-17.8
1	390	-1.3	-16.8
2	390	-1.5	-19.5
3	390	-1.1	-14.0
96	560	-1.1	-13.6
168	580	-1.4	-18.3

MAVA-AF in 5 % dextrose is negatively charged and it is anionic. Particle size and zeta potential of MAVA-AF did not change with time and it means it did not show any aggregation with time. According to the zeta potential results of MAVA, AF and MAVA-AF in 5 % dextrose, conjugation of MAVA and AF is good and no any size and stability change. The activity of MAVA, AF and MAVA-AF in 5 % Dextrose as a function of time were checked by UV-VIS and spectrums were given in Fig.2.

According to Fig.2, activity of MAVA, AF and MAVA-AF in 5 % dextrose is increasing as a function of time. It means they did not show any degradation in 5 % dextrose with time.

The results of particle size, mobility and zeta potential measurements of MAVA, AF and MAVA-AF in PBS as a function of time were given in Table 7, 8 and 9, respectively.

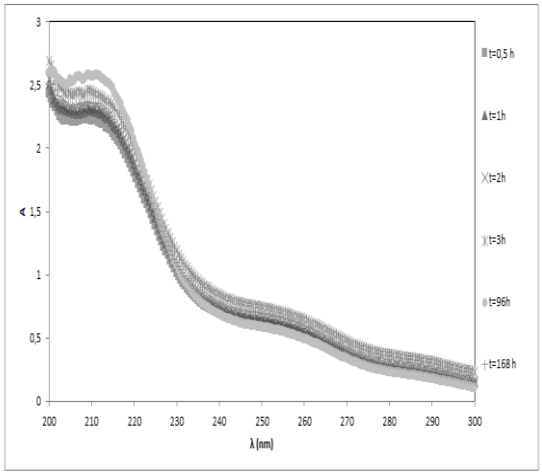

MAVA

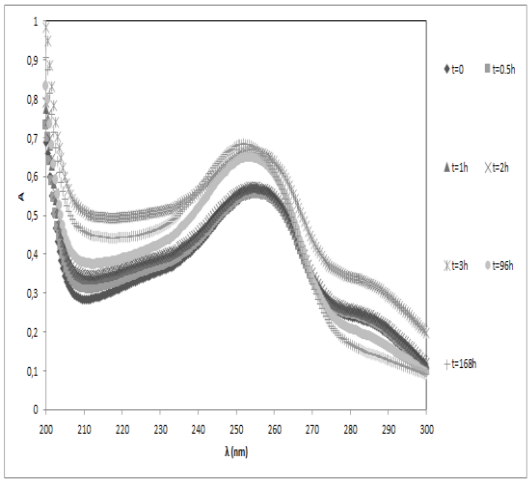

AF

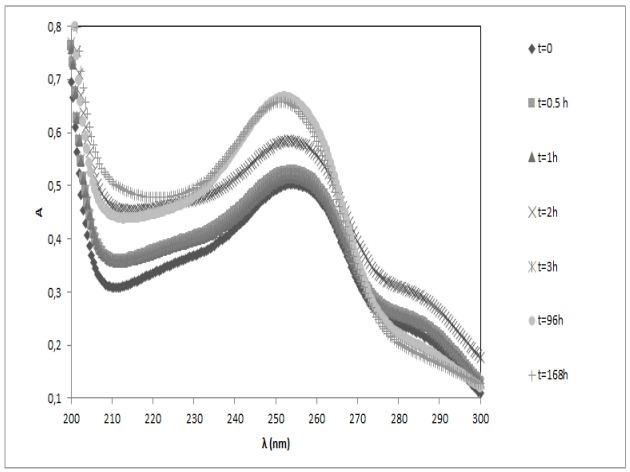

MAVA-AF

Figure 2. Time effect on the activity of MAVA, AF and MAVA-AF in 5 % dextrose.

Table 7. Time effect on particle size, mobility and zeta potential of MAVA in PBS

Time(h)	Particle Size (nm)	Mobility	Zeta Potential (mV)
0	180	-1.2	-15.1
0.5	190	-1.1	-15.0
1	230	-1.2	-15.1
2	240	-1.2	-15.1
3	250	-1.2	-15.0
96	270	-1.7	-21.3
168	290	-1.3	-16.5

MAVA in PBS is negatively charged and it is anionic. Particle size and zeta potential of MAVA in PBS did not change with time and it means it did not show any aggregation and coagulation with time.
Table 8 Time effect on Particle size, Mobility and Zeta potential of AF in PBS.

AF in PBS is negatively charged and it is anionic. particle size and zeta potential of AF in PBS did not change with time and it means it did not show any aggregation and coagulation with time.

Table 8. Time effect on particle size, mobility and zeta potential of AF in PBS.

Time(h)	Particle Size (nm)	Mobility	Zeta Potential (mV)
0	460	-1.0	-12.9
0.5	360	-1.1	-13.6
1	280	-1.2	-15.7
2	340	-1.3	-17.5
3	310	-1.2	-15.7
96	270	-1.3	-17.5
168	230	-1.1	-13.6

Table 9. Time effect on particle size, mobility and zeta potential of MAVA-AF in PBS

Time(h)	Particle Size (nm)	Mobility	Zeta Potential (mV)
0	810	-6.4	-8.1
0.5	870	-5.8	-10.3
1	880	-1.3	-16.4
2	810	-1.6	-20.2
3	850	-1.7	-21.4
96	810	-1.8	-22.1
168	850	-1.9	-24.8

MAVA-AF in PBS is negatively charged and it is anionic. Particle size and zeta potential of AF in PBS did not change with time and it means that it did not show any aggregation and coagulation with time. Particle size of MAVA-AF in PBS is bigger than MAVA and AF in PBS. It means conjugation of MAVA and AF is successful.

The activity of MAVA, AF and MAVA-AF in PBS as a function of time were checked by UV-VIS and spectrums were given in Fig.3.

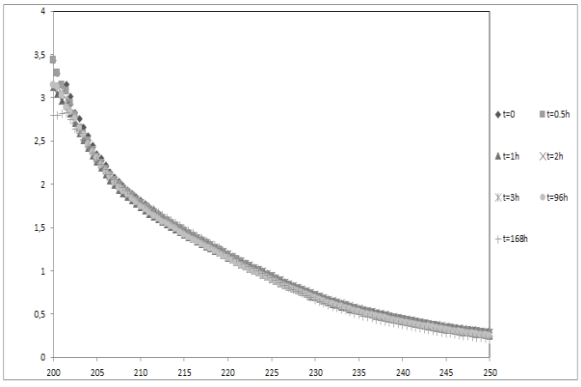

MAVA

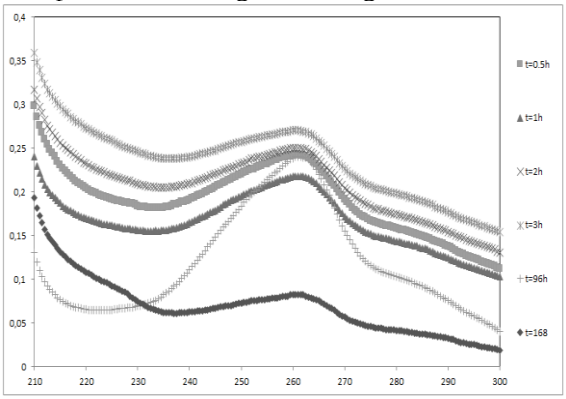

AF

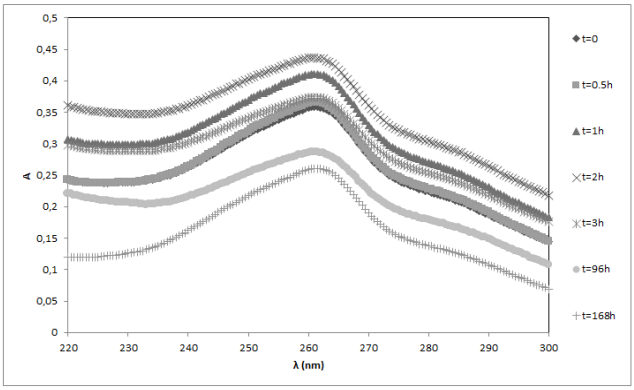

MAVA-AF

Figure 3. Time effect on the activity of MAVA, AF and MAVA-AF in PBS.

According to Fig.3, activity of MAVA did not change with time in PBS, maximum activity of AF and MAVA-AF in PBS was shown at 2 h and their activities decreased with time.

4. CONCLUSIONS

Determination of stability and charge of novel copolymer-drug conjugate, MAVA-AF was carried out using zetasizer measurements in water as a function of pH and in simulated body fluids as a function of time. Activity of novel copolymer-drug conjugate was controlled via UV spectrophotometer in water as a function of pH and in simulated body fluids as a function of time. It was determined that the copolymer, drug and copolymer-drug conjugate are negatively charged. They show anionic character in water and simulated body fluids. The change of pH showed positive effect on the stability of copolymer-drug conjugate. Activation of copolymer-drug conjugate is increasing with time in dextrose solution and it was not shown any degradation or aggregation in this solution.

Acknowledgements. *This work was supported by the Scientific Research Project Coordination Center of Yildiz Technical University, Turkey (Project no: 2016-01-02-YL06) and Sciences Research Projects Foundation of Cumhuriyet University, (CUBAP, Project No: F258).*

REFERENCES

1. N. Larson, H. Ghandehari, *Chemistry of Materials*, **24**, 840 (2012).
2. E.R. Kenawy, F. Abdel-Hay, M. El-Newehy, R.M. Ottenbrite, *Polymer International*, **57**, 85 (2008).
3. A.N. Semenov, *Macromolecules*, **41**, 2243 (2008).
4. http://www.horiba.com/uk/scientific/products/particle-characterization/applications/drug-delivery/
5. V.G. Kadajji, G.V.Betageri, *Polymers*, **3**, 1972 (2011)
6. K. Knop, R. Hoogenboom, D. Fischer, U.S. Schubert, *Angew. Chem. Int*. Ed. **49**, 6288 (2010)
7. M. Wisniewska, *J. Dispers. Sci. Technol*., **32**,1605 (2011)
8. H.L. Kutschera, P. Chaoa, M. Deshmukha, S.S. Rajana, Y. Singha, P. Hua, L.B. Josephb, S.Steina, D.L. Laskinb, P.J. Sinkoa, *Int. J. Pharm*., **402,** 64 (2010)
9. G. Karakuş, H.Bç Zengin, Z. Akin-Polat, A.F. Yenidunya, S. Aydin, *Polym. Bull*., **70**, 1591 (2013).
10. G. Karakuş, *Hacettepe J. Biol. & Chem*., **44**, 549 (2016)
11. Brookhaven Instruments Corporation, Instruction Manual for Zeta Potential Analyzer Instruction Book
12. J.D. Clogston, A.K. Patri, Characterization of Nanoparticles Intended for Drug Delivery, Part of the Methods in Molecular Biology Book Series, Zeta Potential Measurements, **697**, pp. 63-70.

Bulgarian Chemical Communications, Volume 49, Issue I (pp. 50 – 56) 2017

[Mn(CO)$_3$(bpy)(N-2-chlorobenzylbenzimidazole)]OTf complex as a new photoactivatable CO-releasing molecule

E. Üstün[a*], S. Demir Düşünceli[b], İ. Özdemir[b]

[a] *Department of Chemistry, Faculty of Art and Science, Ordu University, 52200, Ordu, Turkey*

[b] *Department of Chemistry, Faculty of Science, İnönü University, 44280, Malatya, Turkey*

Submitted: June 1, 2017; Accepted: September 1, 2017

Metal carbonyl complexes have been accepted major for storage and transportation of carbon monoxide which is an important gasotransmitter. We synthesized novel manganese(I)carbonyl complex with general formula [Mn(CO)$_3$(bpy)L]OTf (bpy =2,2'-bipyridyl, L= N-(2-chlorobenzyl)benzimidazole, OTf = SO_3CF_3). The complex was characterized by LC-MS, ^{1}H NMR, 2D-COSY NMR, ^{13}C NMR, IR and elemental analysis. The CO-releasing properties of the complex were investigated. The DFT/TDDFT analyses were also made by ORCA package program.

Key words: CORM, carbonyl complexes, manganese

INTRODUCTION

Carbon monoxide (CO) is a tasteless, odorless, and colorless gas that often referred to as "silent killer" due to its well established toxicity. CO which binds to hemoglobin to form carboxyhemoglobin (COHb) blocks the oxygen transport in the bloodstream whereas COHb levels of up to 10% caused by CO inhalation are asymptomatic. Furthermore, CO which is a byproduct of heme catabolism has been recognized as an important gasotransmitter in mammals and plays versatile roles in tissue protection [1-5]. Although the mechanism of action has not been understood yet, the researches have pointed out that CO could take part in heme oxygenase equilibrium of hemoglobin degradation process [6]. Many papers about anti-inflammatory, antiapoptotic, antiprofilerative, antioxidant, and anticancer activities have supported the therapeutic characteristic of CO [7-9]. The studies about the CO have divided into two ways: (1) analysis of the bioactivities and the mechanism of action [5, 10-13] and (2) transport the CO with controllable amount and speed to the tissue. Transition metal carbonyl complexes have considered as promising candidates to provide certain amount of CO to biological systems within a certain time [14, 15]. CO-releasing molecules (CORMs) can provide CO with ligand substitution [16, 17], enzyme-triggered [18, 19] and photo-activation [20-23] reactions. Photoactivatable CO-releasing molecules (PhotoCORMs) have to be sensitive to certain wavelength of UV/Vis light but stable in dark within used solvent or solvent systems. It is well-known that penetration depth of light into tissue depends on wavelength and ideal PhotoCORM must release CO by long wavelength within steady times.

Irradiation into the low-lying metal-to-ligand charge transfer (MLCT) bands, which belong to transitions from the metal to the lowest π* orbital of the ligand, may give rise to photo-dissociation of carbonyl ligand and this is, in fact, the main mechanism of CO release with UV-light. An understanding of photochemistry of transition metal compounds requires knowledge of the properties of molecular orbitals, and appropriate excited states. Density functional theory (DFT) and time-dependent DFT approach (TDDFT) plays a crucial role in characterization of the excited states coordination complexes [24-29]. Furthermore, applications of TDDFT approaches have recently been reported on transition metal complexes and got good results. Structures and electronic transitions predicted with the popular BP86 functional are no worse or in many cases are even slightly better than those predicted by the hybrid B3LYP functional [30-35].

In this study, novel [Mn(CO)$_3$(bpy)(N-2-chlorobenzylbenzimidazole]OTf (bpy: 2,2'-bipyridyl; OTf: SO_3CF_3) were synthesized as a CORM. The structures of ligand and compound were elucidated by ^{1}H NMR, 2D-COSY NMR, ^{13}C NMR, IR, LC-MS, and elemental analysis. CO-releasing properties of the compound were investigated. Also DFT/TDDFT analysis of complex was made with ORCA package program by both BP86 and B3LYP functionals for obtaining the optimized geometries, MO electron densities and having insights electronic transitions that promote CO-release.

*) To whom all correspondence should be sent:
E-mail: elvanustun77@gmail.com

EXPERIMENTAL

Materials and methods

All reactions were carried out under argon using standard Schlenk and vacuum techniques. Solvents were freshly distilled after refluxing over metallic sodium or phosphorous pentoxide for 3-4 days [36]. IR spectra were recorded on solid samples with a Shimadzu IRAffinity-1 ATR spectrometer. Band intensities are marked as strong (s), medium (m), weak (w), or shoulder (sh). NMR spectra were recorded on a Bruker Ultra Shield 300 MHz spectrometer. Chemical shifts δ in ppm indicate a downfield shift relative to tetramethylsilane (TMS) and were referenced relative to the solvent signals. Coupling constants J are given in Hertz. Absorption spectra were measured using a Shimadzu UV-1800 spectrophotometer equipped with quartz cuvettes (d=1 cm). Elemental analysis (C, H, and N) were obtained using a CHNS-932 (LECO) instrument. LC-MS was carried out on an Agilent 1100 Series instrument. All chemicals were purchased from Sigma Aldrich and used without further purification.

Synthesis of ligand

Small pieces of lithium (45 mmol, 312 mg) were added slowly to ethylene diamine at 110 °C. The solution was allowed to reach room temperature after stirring for 1 hour and n-alkylbenzylchloride (50 mmol) and toluene (40 mL) were added. Precipitated lithium chloride was filtered and the N-(n-alkyl benzyl)ethylene diamine was isolated by distillation from the oily mixture (120 °C/0.01 mmHg) after solvents were removed under vacuum. N-(n-alkylbenzyl)ethylenediamine (35 mmol) and N,N-dimethylformamide dimethylacetal (40 mmol) were stirred for 2 hours at 100 °C and methanol and dimethyl amine were separated at 120 °C by distillation. The last product was isolated from yellow oily residual by distillation under vacuum (124 °C/0.01 mmHg). Yield:1.96 g (81%). ^{1}H NMR (399.9 MHz, $CDCl_3$) δ (ppm) = 8.05 (s, 1H, NC*H*N), 7.86-7.89 (m, 1H, NC_6H_4N), 7.45-7.48 (m, 1H, NC_6H_4N), 7.26-7.37 (m, 4H, $CH_2C_6H_4$Cl), 7.17-7.22 (m, 1H, NC_6H_4N), 6.89-6.92 (m, 1H, NC_6H_4N), 5.49 (s, 2H, $CH_2C_6H_4$Cl). ^{13}C NMR (100.5 MHz, $CDCl_3$) δ (ppm) = 143.8 (N*C*HN), 133.7, 133.1, 133.0, 130.0, 129.7, 128.7, 127.5, 123.4, 122.6, 120.4, 110.0 (NC_6H_4N ve $CH_2C_6H_4$Cl), 46.5 ($CH_2C_6H_4$CI). Anal. Calc. for $C_{14}H_{11}N_2Cl$ (242.70 gmol-1): C, 69.28; H. 4.57; N, 11.54. Found: C, 69.32, H, 4.60, N, 11.50. M.P:80-82 °C.

Synthesis of complex

$Mn(CO)_3$(bpy)Br was prepared according to literature methods by Staal [37]. $Mn(CO)_3$(bpy)Br (100 mg, 0.267 mmol) were added into the solution of AgOTf (82.2 mg, 0.320 mmol) in acetone (10 mL). Precipitated AgBr was filtrated by Celite and the ligand was added after stirring for a day in room temperature. Acetone was evaporated under vacuum. Precipitated orange product was filtered and washed with 5 mL cold methanol and 10 mL cold diethyl ether. Yield: 152.2 mg (83.1%). ^{1}H NMR (300 MHz, DMSO-D_6) δ (ppm) = 5.456 (s, 2H, $NCH_2C_6H_4Cl$), 7.784 (s, 1H, NCHN), 9.453 (d, J=5.0, 2H, $N_2C_{10}H_8$, 6/6'), 8.637 (d, J=3.0, 2H, $N_2C_{10}H_8$, 3/3'), 8.305 (t, J=8.0, 2H, $N_2C_{10}H_8$, 4/4'), 7.821 (t, J=7.0, 2H, $N_2C_{10}H_8$, 5/5'), 7.901 (d, J=8.0, 1H, $NCH_2C_6H_4Cl$), 7.015 (d, J=7.5, 1H, $NCH_2C_6H_4Cl$), 7.518 (d, J=8.0, 1H, NC_6H_4N),7.25-7.4 (m, 5H, $NCH_2C_6H_4Cl$ ve NC_6H_4N). ^{13}C NMR (300 MHz, DMSO-D_6) δ (ppm) = 46.86 ($NCH_2C_6H_4Cl$), 165.39 (NCHN), 155.02, 154.72, 140.44, 127.84, 124.06 ($N_2C_{10}H_8$), 146.60, 141.31, 133.12, 132.55, 132.14, 121.69 ($NCH_2C_6H_4Cl$), 130.27, 130.16, 129.89, 129.67, 127.62, 124.34 (NC_6H_4N), 190.58 (CO). LCMS: m/z 452.1 [M-OTf-3CO]$^+$. IR (cm^{-1}, ATR): 1444.75, 1475.61 (s, C-H), 1603.88 (s, C-N), 2035.95, 1944.33, 1930.83 (s, CO)

Myoglobin assay

Stock solutions of the complexes for myoglobin assays were prepared in DMSO. PBS (0.1 M, pH=7.4), 100 mM sodium dithionite (100 µL), 15 µM carbonyl complex and 60 µM myoglobin were combined in a cuvette to give a total volume of 1000 µL. Solutions were degassed by bubbling with argon at each step of the procedure. Horse muscle myoglobin solution prepared in PBS (0.1 M, pH = 7.4) was reduced to deoxymyoglobin by addition of a solution sodium dithionite in PBS (0.1 M, pH = 7.4). Irradiation was made with a 365 nm CAMAG UV Lamp at 1 min intervals during the initial 20 min, then continued at 5 min intervals until no further difference in MbCO concentration was observed. The final solution was placed 5 cm front of the UV lamp. All irradiation experiments were carried out in triplicate. Solutions were freshly prepared for the dark stability and photo-activation experiments. Dark stability spectra were collected automatically for the required period of time by the spectrometer software.

THEORY/CALCULATION

DFT calculations were carried out with ORCA version 2.8 using the BP86 and B3LYP functional with the resolution-of-the-identity (RI) approximation, a def2-TZVP/ def2-TZVP/J basis set, the tightscf and grid4 options, and the COSMO solvation model with water as the solvent for geometry optimizations [30, 31].

RESULTS AND DISCUSSION

Novel ligand of complex was synthesized by adding 2-chlorobenzylchloride to benzimidazole and characterized by ^{1}H NMR, ^{13}C NMR, IR and elemental analysis as detailed in the experimental section. NCHN hydrogen of free ligand shows a singlet at 8.05 ppm in ^{1}H NMR and the NCHN carbon of free ligand shows resonance at 143.8 ppm in ^{13}C NMR. Also, benzyl CH_2 hydrogens are seen at 5.49 ppm as a singlet at ^{1}H NMR and at 46.5 ppm in ^{13}C NMR. IR spectroscopy and elemental analysis were used for confirmation the characterization of free ligand.

The complex was synthesized by stepwise ligand addition to pre-synthesized Mn(CO)$_3$(bpy)Br. The characterization of the complex was performed with ^{1}H NMR, ^{13}C NMR, IR, and LC-MS. NMR signals at 9.45 ppm (t), 8.64 ppm (d), 8.31 ppm (t) and 7.82 ppm (t) with good splitting and integration are assigned to bpy moiety of the complex. Single signal at 7.78 ppm also indicates the hydrogen atom between nitrogens of benzimidazole moiety. All the assignments of the ^{1}H NMR spectrum was confirmed by 2D-COSY NMR spectrum. The signal at 165.4 ppm of the ^{13}C NMR of complex is attributed to NCHN carbon of the benzimidazole moiety. The benzyl CH_2 of benzimidazole moiety shows signal at 46.9 ppm ^{13}C NMR.

IR spectra must have three C-O bands due to the Cs point group and the C-O bands were recorded 2035.9, 1944.3 and 1930.8 cm^{-1}. The band at 1603.8 cm^{-1} is assigned to C-N. Also remarkable 1261.4, 1228.9, 1145.6, and 1030.0 cm^{-1} bands are labeled as OTf that used as precipitant of the complex. LCMS analysis of complex is consistent with expectations. The strongest band of LCMS is attributed to M-OTf-3CO form of the compound. The complex displayed broad maximum on 380 nm and two shoulders on 325 and 276 nm, the extinction coefficients were calculated 2834.4, 5972.5, and 17171.2 M^{-1}cm^{-1} according to Lambert-Beer law, respectively.

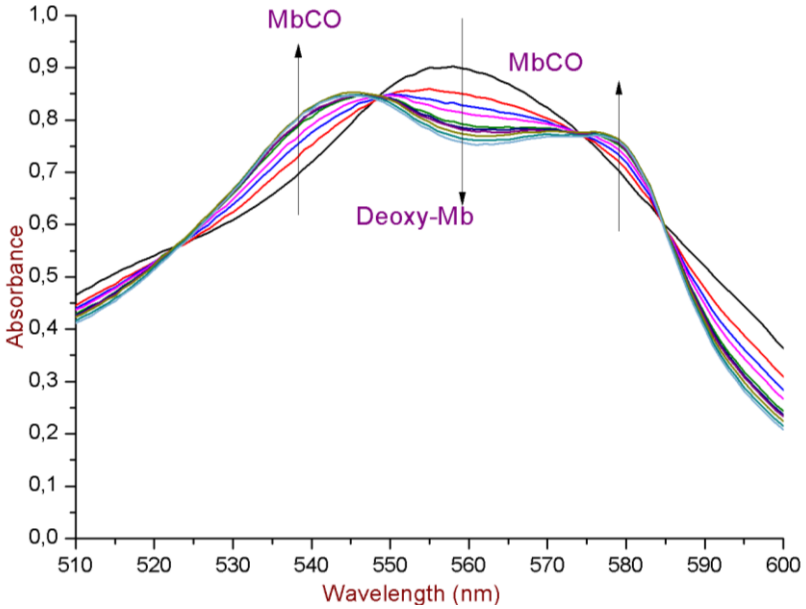

Figure 1. Change of absorption of myoglobin with the irradiation at 365 nm UV light for a solution of complex (15 μM) in 0.1 M PBS (pH=7.4) in the presence of myoglobin (60 μM) and sodium dithionite (10 mM) under argon atmosphere as monitored by UV/Vis spectroscopy.

CO-releasing properties of the complex was identified by myoglobin-assay as detailed above. The absorption of the complex in DMSO for 380 nm (the main maximum of the complex) and myoglobin assay solution for 510, 540, 557 and 577 nm (510 nm: isobestic point; 540 nm: Mb-CO; 557 nm: deoxy-Mb; 577 nm: Mb-CO) was measured in the dark in 16 h. The compound has showed good dark stability with only negligible spectral fluctuations (Figure 2). Then the complex was irradiated with 366 nm UV-lamp for confirmation the light sensitivity (Figure 3). The light sensitivity and CO-releasing of the complex were also confirmed with IR (Figure 4). In myoglobin assay, due to binding of released CO with myoglobin, the reaction is forced towards product side. Carbonmonoxy myoglobin concentration [MbCO] and equivalence CO (eq. CO) which become fixed after a while have indicated total released CO. Total released CO, CO equivalents, and half-life ($t_{1/2}$) were determined with UV-Vis Spectrophotometer at 1 minute intervals with 366 and 410 nm UV-lamps (Figure 1). The $t_{1/2}$

in this study is defined as the time taken to release 50% of the total CO ligands present per molecule. Carbonmonoxy myoglobin concentration of the complex is 34.8 µM while the equivalence CO is 2.32 with 366 nm UV-lamp. But carbonmonoxy myoglobin concentration of the complex is 23.6 µM while the equivalence CO is 1.9 with 410 nm UV-lamp. Half-life of the complex can be used for kinetic analysis. The complex has released half of its CO in 20.8 min with 366 nm UV-lamp while the half-life is calculated 69.2 min with 410 nm UV-lamp.

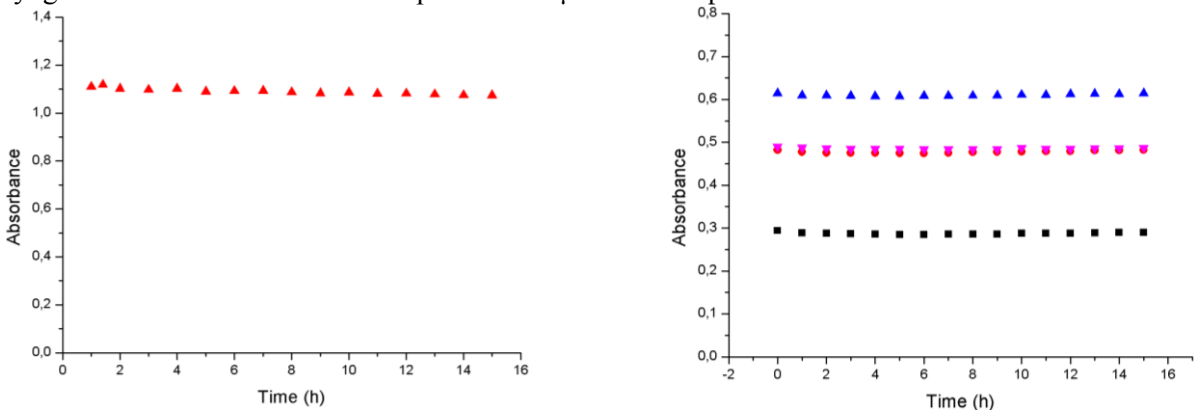

a b

Figure 2. a) Change of absorption spectra of complex with in dark in DMSO **b)** Change of absorption at selected wavelengths (510 nm: isobestic point ,black; 540 nm: Mb-CO, red; 557 nm: deoxy-Mb, blue; 577 nm: Mb-CO, pink) with increasing incubation time in the dark (0 to 16 h) for a solution of complex (15 µM) in 0.1 M PBS at pH 7.4 in the presence of myoglobin (60 µM) and sodium dithionite (10 mM) under a dinitrogen atmosphere as monitored by UV/vis spectroscopy.

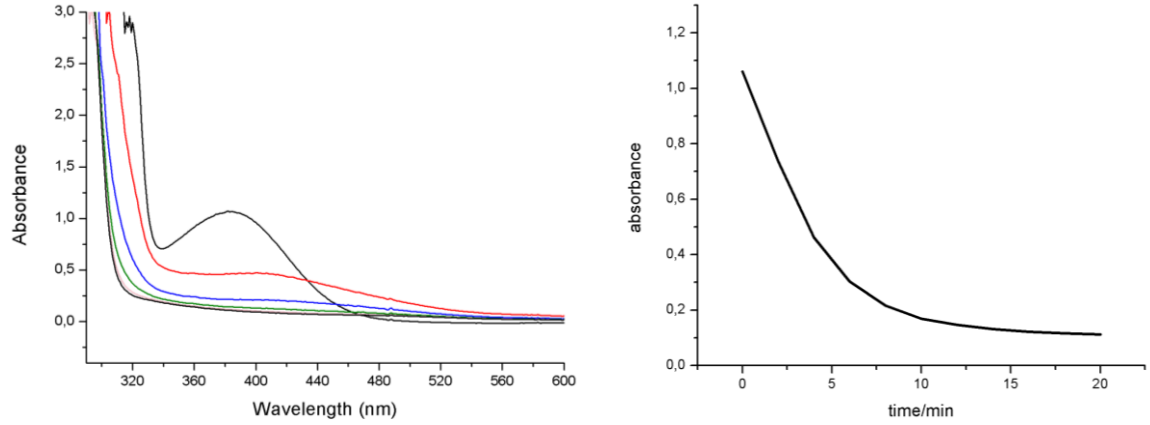

Figure 3. Change of absorption of the complex with 366 nm light in DMSO.

If the CO releasing occurs as observed in the myoglobin assay, the reactions must result with the formation of di- or mono-carbonyl complexes of manganese. Typical IR spectra for fac-manganese (I) tricarbonyl complex is detailed the experimental section. During excitations, strong IR bands of parent complex have disappeared that indicates the dissociation of $[Mn^{I}(CO)_3]$-units of complex. On the other hand new IR bands have emerged in the region around 1975 cm^{-1} and 1860 cm^{-1}. These bands could be attributed to cis-manganese (I) dicarbonyl complexes [38, 39]. The new IR bands around 1850 cm^{-1} and 1875 cm^{-1} might be considered as monocarbonyl manganese (I) complexes [40] (Figure 4).

The complex was structurally optimized by DFT with ORCA package program with COSMO model in water. Manganese compounds containing aromatic ligands usually exhibit intense metal-to-ligand charge transfer (MLCT) transitions in UV-Vis spectrum. Electronic transitions and molecular orbitals which have contribution to electronic transitions were analyzed. Only strong transitions with an oscillator strength >0.01 are reported and contributions >20% are listed in Table 1. HOMO of molecule intensively The HOMO-LUMO transition is a kind of MLCT which is expected to occur in 584.5 nm theoretically, but this transition could not be observed in UV-spectrum of the complex practically because of weak oscillation strength.

Electronic states with highest oscillating force in 376.6 nm is state 11 in which electrons flow from manganese to 2,2'-bipyridyl. This state mostly includes HOMO-1→LUMO+2 transition and is in excellent agreement with experimental maximum in 380 nm. However, state 18 in which electrons flow from metal to benzimidazole by HOMO-1→LUMO+3 in 336.6 nm and state 22 in which electrons flow from benzimidazole to 2,2'-bipyridyl by HOMO-5→LUMO+2 in 327.4 nm are also agree with the shoulders on the UV-Vis spectrum in 325 nm. These three states can be considered as broadness of the maximum of the complex (Table 1).

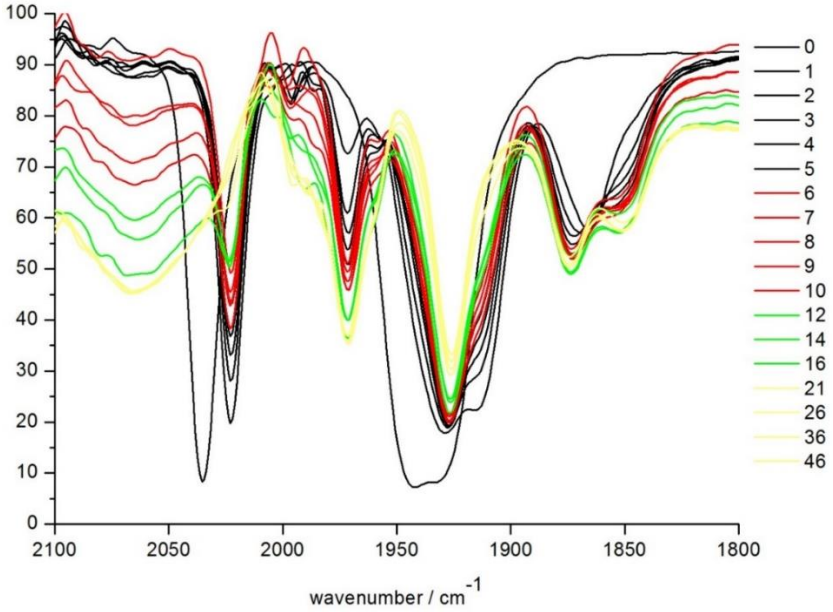

Figure 4. Time-dependent changes in the IR spectra of the complex consists of transition metal orbitals while LUMO is formed completely from 2,2'-bipyridyl orbitals.

Table 1. Energies (in nm), Oscillator Strength (f_{osc}), Main Orbital Contributions, and Type of Transition Involved in the Most Important Singlet Excitations of the complex Calculated with TDDFT/BP86

State	Molecular Orbitals	Main Transitions
1	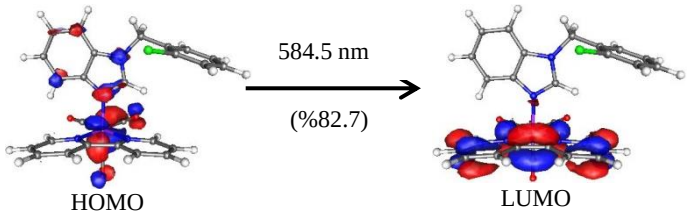	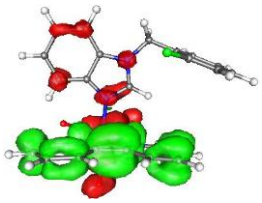 MLCT (f_{osc}:0.0157)
2	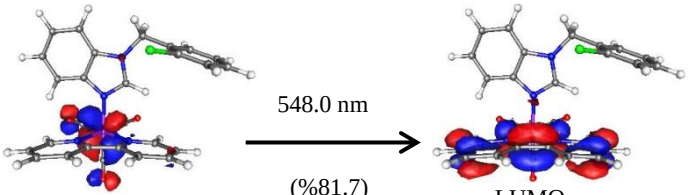	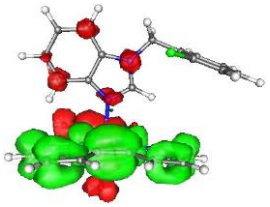 MLCT (f_{osc}:0.0192)
11	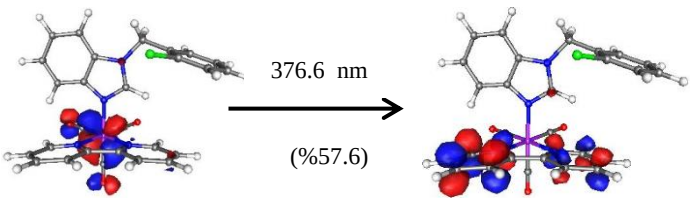	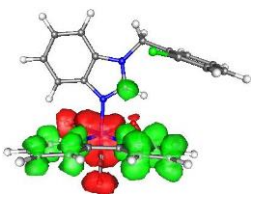

		MLCT (f_{osc}:0.0605)
18	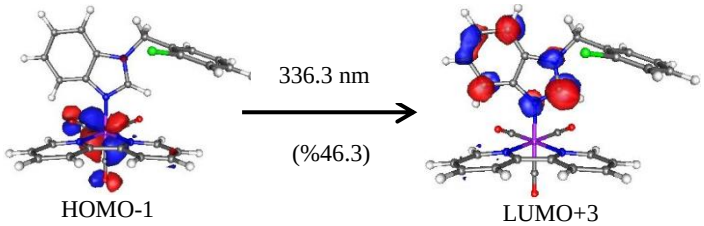	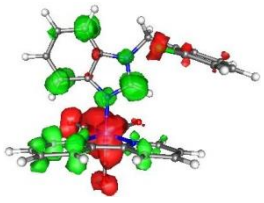
19	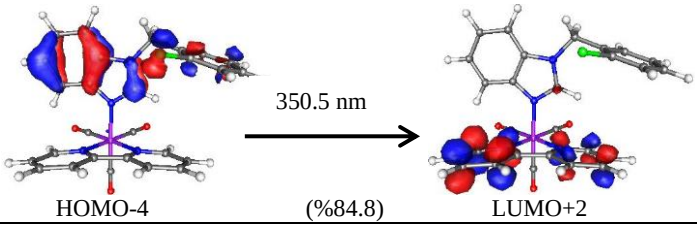	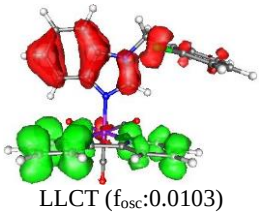
20	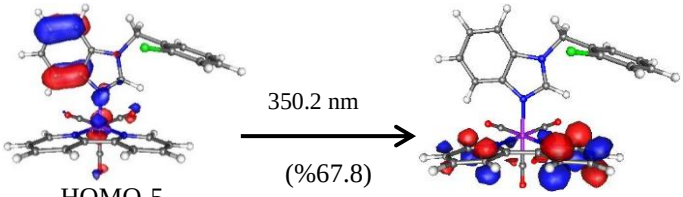	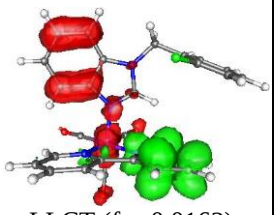
22	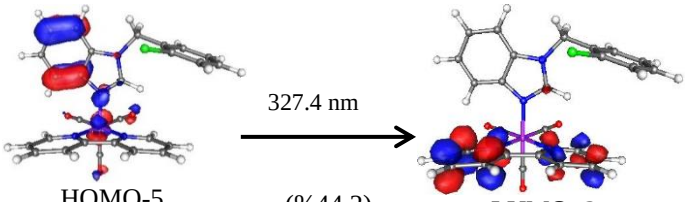	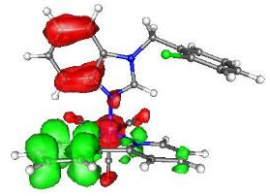
26	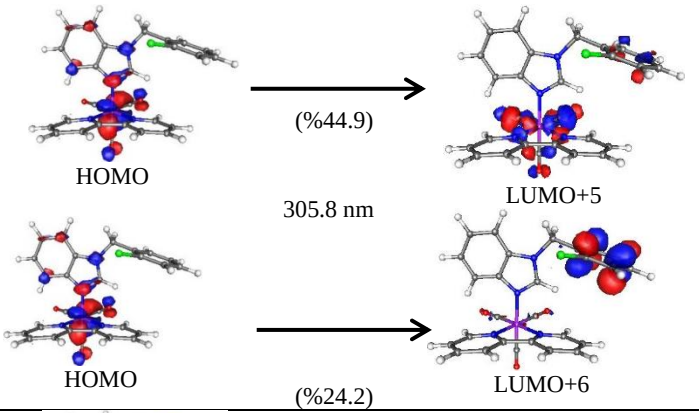	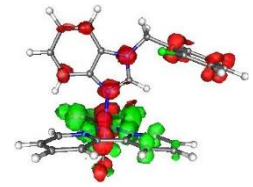
30	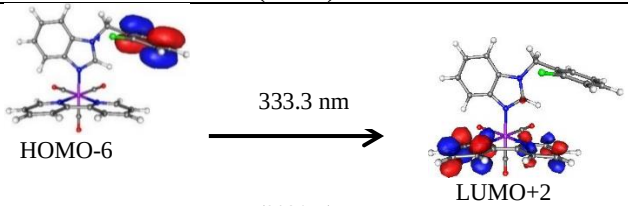	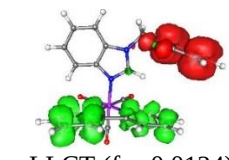

31	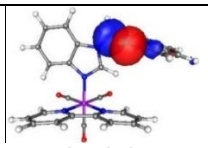 HOMO-8	338.2 nm 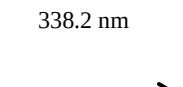	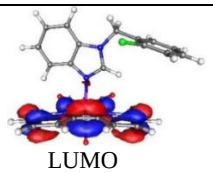 LUMO	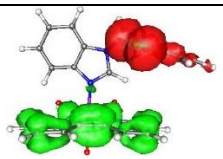 LLCT (f_{osc}:0.0113)

Acknowledgement. *Support of Scientific and Technological Research Council of Turkey (TÜBİTAK, Project No: 112T320) is gratefully acknowledged.*

REFERENCES

1. C.C. Romão, W.A. Blättler, J.D. Seixas, G.J.L. Bernardes, *Chem. Soc. Rev.*, **41**, 3571 (2012).
2. R. Tenhunen, H.S. Marver, R. Schmid, *Biochemistry*, **61**,748 (1968).
3. U. Hasegawa, A.J. van der Viels, E. Simeoni, C. Wandrey, J.A. Hubbel, *J. Am. Chem. Soc.*, **132**, 18273 (2010).
4. A.A. Ahanger, S. Prawez, D. Kumar, R. Prasad, S.K. Tandan, D. Kumar, *Naunyn-Schmiedeberg's Archives of Pharmacology*, **384**, 93 (2011).
5. R. Motterlini, B. Haas, R. Foresti, *Medical Gas Research*, **2**, 28 (2012).
6. L.Y. Chau, *Journal of Biomedical Science*, 22, **22** (2015).
7. R. Motterlini, L.E. Otterbein, *Nat. Rev. Drug. Discov.*, **9**, 728 (2010).
8. E. Üstün, M.Ç. Ayvaz, M.S. Çelebi, G. Aşcı, S. Demir, İ. Özdemir, *Inorganica Chimica Acta*, **450**, 182 (2016).
9. E. Üstün, A. Özgür, K.A. Coşkun, S. Demir, İ. Özdemir, Y. Tutar, *J. Coord. Chem.*, 69, 3384 (2016).
10. V.L. Mahan, *Medical Gas Research*, **2**, 32 (2012).
11. V.M. Zacharia, M.U. Shiloh, *Medical Gas Research*, **2**, 30 (2012).
12. E.K. Patterson, D.D. Fraser, A. Capretta, R.F. Potter, G. Cepinskas, *Free Radical Biology and Medicine*, **70**, 167 (2014).
13. D. Babu, R. Motterlini, R. A. Lefebvre, *British Jornal of Pharmacology*, **172**, 1557 (2015).
14. T.R. Johnson, B.E. Mann, J.E. Clark, R. Foresti, C.J. Green, R. Motterlini, *Angew. Chem. Int. Ed*., **42**, 3722 (2003).
15. T. Szymańska-Buzar, *Coordination Chemistry Reviews*, **250**, 976 (2006).
16. I.J.S. Fairlamb, A.K. Duhme-Klair, J.M. Lynam, B.E. Moulton, C.T. O'Brien, P. Sawle, J. Hammad, R. Motterlini, *Bioorganic & Medicinal Chemistry Letters*, **16**, 995 (2006).
17. F. Zobi, O. Blacque, R.A. Jacobs, M.C. Schaub, A.Y. Bogdanova, *Dalton Trans.*, **41**, 370 (2012).
18. S. Romanski, B. Kraus, U. Schatzschneider, J.M. Neudörfl, S. Amslinger, H.G. Schmalz, *Angew. Chem. Int. Ed*., **50**, 2392 (2011).
19. S. Botov, E. Stamellou, S. Romanski, M. Guttentag, R. Alberto, J.M. Neudörfl, B. Yard, H.G. Schmalz, *Organometallics*, **32**, 3587 (2013).
20. J. Niesel, A. Pinto, H.W.P. N'Dongo, K. Merz, I. Ott, R. Gust, U. Schatzschneider, *Chem. Commun.*, 1798 (2008).
21. A.E. Pierri, A. Pallaoro, G. Wu, P.C. Ford, *J. Am. Chem. Soc.*, 134, 18197 (2012).
22. R.D. Rimmer, A.E. Pierri, P.C. Ford, *Coordination Chemistry Reviews*, **256**, 1509 (2012).
23. T.M.A. Jazzazi, H. Görls, G. Gessner, S.H. Heinemann, W. Westerhausen, *J. Organomet. Chem.*, **733**, 63 (2013).
24. L. Salassa, C. Garino, G. Salassa, R. Gobetto, C. Nevi, *J. Am. Chem. Soc.*, **130**, 9590 (2008).
25. P. Datta, A.P. Mukhopadhyay, P. Manna, E.R. Tiekink, P.C. Sil, C. Sinha, *J. Inorg. Biochem.*, **105**, 577 (2011).
26. M.A. Gonzalez, S.J. Carrington, N.L. Fry, J.L. Martinez, P.K. Mascharak, *Inorg. Chem.*, **51**, 11930 (2012).
27. S. Pai, M. Hafftlang, G. Atongo, C. Nagel, J. Niesel, S. Botov, H.G. Schmalz, B. Yard, U. Schatzschneider, *Dalton Trans.*, **43**, 8664 (2014).
28. E. Üstün, Ş. Koç, S. Demir, İ. Özdemir, *J. Organomet. Chem.*, **815**, 16 (2016).
29. E. Üstün, S. Demir, F. Coşkun, M. Kaloğlu, O. Şahin, O. Büyükgüngör, İ. Özdemir, *Journal of Molecular Structure*, **1123**, 433 (2016).
30. F. Neese, *Coordination Chemistry Reviews.*, **253**, 526 (2009).
31. F. Neese, *Computational Molecular Structure.*, **2**, 73 (2012).
32. E. van Lenthe, R. van Leeuwen, E.J. Baerends, J.G. Snijders, *Int. J. Quantum Chem.*, **57**, 281 (1996).
33. E. van Lenthe, E.J. Baerends, J.G. Snijders, *J. Chem. Phys.*, **101**, 9783 (1994).
34. F. Weigend, R. Ahlrichs, *Phys. Chem. Chem. Phys.*, **7**, 3297 (2005).
35. L. Goerigk, S. Grimme, *Phys. Chem. Chem. Phys.*, **13**, 6670 (2011).
36. W.L.F. Armarego, C.L.L. Chai, *Purification of Laboratory Chemicals, sixth ed.*, USA:Butterworth-Heinemann Publications, 2009.
37. L.H. Staal, A. Oskam, K. Vrieze, *J. Organomet. Chem.*, **170**, 235 (1979).
38. H.M. Berends, P. Kurz, *Inorganica Chimica Acta.*, **380**, 141 (2012).
39. W. Huber, R. Linder, J. Niesel, U. Schatzschneider, B. Spingler, P.C. Kunz, Eur. J. Inorg. Chem., **3140** (2012).
40. F.J. Garcia-Alonso, V. Riera, M.J. Misas, *Transition Met. Chem.*, **10**,19 (1985).

Bulgarian Chemical Communications, Volume 49, Issue I (pp. 57 – 63) 2017

Controlled release of donepezil hydrochloride from the ternary sodium alginate based hydrogels

E. Akyol*, S. Senol, Ö. Dogan

Department of Chemical Engineering, Yıldız Technical University, 34210 Istanbul, Turkey

Submitted: June 1, 2017; Accepted: September 1, 2017

In the presented work, synthesis of the ternary sodium alginate based hydrogels as drug delivery systems having different properties and drug release experiments were performed. For this purpose, gelatine, α-cellulose, clinoptilolite, modified clinoptilolite and 4-acryloyl morpholine (4 AcM) were combined with sodium alginate (NaAlg). Hydrogels were characterized by Fourier transform infrared spectroscopy (FT-IR) and digital microscope. In vitro drug release studies have been performed for Donepezil hydrochloride loaded hydrogels at pH 1.2, 6.8 and 7.4. The results showed that these hydrogels can be used for drug delivery systems.

Keywords: The ternary sodium alginate based hydrogels, drug release, Donepezil hydrochloride**.**

INTRODUCTION

Alzheimer's disease (AD) is an irreversible, progressive brain disorder which leads to deterioration of intellectual and social functions, memory loss, personality changes and inability for self-care. AD is the fourth leading cause of death in developed countries [1-2]. In 2013, Alzheimer's Disease International (ADI) reported the worldwide prevalence of dementia to be more than 44 million [3].

Drug delivery systems have been attracted a great deal of attention for the past few decades since it offers the effective and targeted drug delivery in the field of pharmaceutics [4-10]. Hydrogels are used control drug release because they change the gel structure in response to environmental situation [11]. The important physicochemical and biological characteristics of hydrogels, along with their huge diversity, collectively, have led to desirable attention to these polymeric materials as important candidates for delivery systems of therapeutic agents [12-18]. Donepezil Hydrochloride (DH) is a second-generation cholinesterase inhibitor (ChEI). It is used for the treatment of Alziemers disease (AD) having greater specificity for the brain acetyl cholinesterase enzyme (AchE) [19].

In this study; an Alzheimer drug donepezil hydrochloride (DH) which was encapsulated in to sodium alginate (NaAlg) hydrogels which were combined with gelatine, α-cellulose, clinoptilolite, modified clinoptilolite and 4-acryloyl morpholine. Fourier transform infrared (FT-IR) spectroscopy and digital microscope were used to characterize the hydrogels.

EXPERIMENTAL

Materials

Sodium alginate (Protonal LF 10/60) was purchased from FMC Biopolymer. Donepezil HCl was provided by Abdi İbrahim Company. Clinoptilolite was provided by Gordes Zeolit Company. Gelatine was provided by Carlo Erba, α-cellulose, and 4 Acryloyl morpholine were purchased from Sigma Aldrich. Calcium chloride, was provided by Merck.

Preparation and Characterization of Hydrogels

Donepezil HCl 0.05 % (w/v) and 1% (w/v) NaAlg were dissolved in deionized water and mixed by using a magnetic stirrer at 40°C and 200 rpm. According to hydrogel type, 1% (w/v) gelatine, clinoptilolite, modified clinoptilolite, 4 AcM, α-cellulose were added. The solution was added drop wise into $CaCl_2$ solution (2 % (w/v) under constant stirring at 100 rpm. Hydrogels were washed and dried at room temperature.

Preparation of modified clinoptilolite: 50 g clinoptilolite was added in to 3M NaCl solution at 60°C for 30 sec in ultrasonic bath. This procedure was twice repeated. After that clinoptilolite washed with deionized water and dried for 24 h. Synthesis conditions of hydrogels are summerized in Table 1.

Diameter of hydrogels were calculated by using microscope photos (Veho, VMS- 004 USB Microscope). Characterization of functional groups present in the hydrogels were performed by FT-IR spectroscopy (Perkin Elmer Spectrum 100).

Swelling behavior was studied by a gravimetric method. Drug loadded hydrogels were used for swelling behaviour at 37°C. At predetermined time point, the hydrogels were taken out and weighed

*) To whom all correspondence should be sent:
E-mail: eakyol@yildiz.edu.tr

after removal of surface water. Swelling ratio was calculated as follows:

$$Swelling\ ratio = (W_s - W_i)/ W_i * 100$$

where W_i is the initial weight of the prepared hydrogel and W_s is the weight of the hydrogel in swollen state.

Table 1. Experimental synthesis conditions for the sodium alginate based composite

Hydrogels	NaAlg	4AcM	Clinoptilolite	Modified Clinoptilolite	Gelatine	α-cellulose
Hydrogel 1 (H1)	%1	% 1	-	-	-	-
Hydrogel 2 (H2)	%1	%1	%1	-	-	-
Hydrogel 3 (H3)	%1	%1	-	%1		
Hydrogel 4 (H4)	%1	%1	-	-	%1	-
Hydrogel 5 (H5)	%1	%1	-	-	-	%1
Hydrogel 6 (H6)	%1	-	%1	-	%1	-
Hydrogel 7 (H7)	%1	-	%1	-	-	%1
Hydrogel 8 (H8)	%1	-	-	%1	%1	-
Hydrogel 9 (H9)	%1	-	-	%1	-	%1
Hydrogel 10 (H10)	%1	-	-	-	%1	%1

RESULTS AND DISCUSSION

Characterization of the prepared hydrogels

Characterization of hydrogels by FT-IR was carried out to determine the chemical structure and to confirm the combination. Figure 1 displays the FT-IR spectrum of hydrogels. As seen in Figure 1, the broad absorption band around 3388 cm^{-1} is ascribed to the peaks of -OH groups. The absorption peaks at 1620 and 1416 cm^{-1} is assigned to stretching characteristic of alginate.

Figure 1(a-b-c-d-e) illustrates the FT-IR spectra of the AcM based hydrogels. The band at 1615 cm^{-1} displays the shift of C=O vibration of the AcM structure due to hydrogen bonding interactions. Also, the ring stretching vibration (mainly asymmetric ν(C-O-C)) in morpholine is observed at about 1112 cm^{-1}. As seen in Figure1(b) and (e), the FT-IR band connected with the internal Si–O(Si) and Si–O(Al) vibrations in tetrahedral or alumina- and silica oxygen bridges lies at 795 cm^{-1}. The band at 1268 cm^{-1} representing amid groups in gelatine (c). The band at 1427 cm^{-1} is ascribed to the OH groups which belonged to α-cellulose (d). Two different clinoptilolite was used in this study: clinoptilolite and modified clinoptilolite. When the difference spectrum of clinoptilolite and modified clinoptilolite was investigated, it was seen the presence of the same typical bands clinoptilolite and modified clinoptilolite. Figue 1(d-f-g-h), exhibits FT-IR analyses for gelatine based hydrogels. The band of gelatin centered at about 3400 cm^{-1}, which was the stretching vibration, broadened and coupled with –OH band of sodium alginate at 3450 cm^{-1}, included by the addition of sodium alginate to gelatin, implied the occurrence of hydrogen bonds between –OH groups of sodium alginate and –NH groups of gelatin molecules. Figure 1(e-g-i-j) shows the FT–IR spectra of α-cellulose based hydrogels modified by 4 AcM, gelatine, clinoptilolite and modified clinoptilolite, respectively.

The sizes of hydrogels were between 1.67 and 2.57 mm, which were obtained by digital microscope. Diameter of hydrogels are given in Table 2.

Table 2. Diameter of hydrogels

Hydrogels	(mm)
H1	1,67
H2	1,70
H3	1,93
H4	1,93
H5	2,28
H6	1,85
H7	2,57
H8	1,99
H9	2,20
H10	2,29

Figure 1(a-b-c-d-e) illustrates the FT-IR spectra of the AcM based hydrogels. The band at 1615 cm^{-1} displays the shift of C=O vibration of the AcM structure due to hydrogen bonding interactions. Also, the ring stretching vibration (mainly asymmetric ν(C-O-C)) in morpholine is observed at about 1112 cm^{-1}. As seen in Figure1(b) and (e), the FT-IR band connected with the internal Si–O(Si) and Si–O(Al) vibrations in tetrahedral or alumina- and silica oxygen bridges lies at 795 cm^{-1}. The band at 1268 cm^{-1} representing amid groups in gelatine (c). The band at 1427 cm^{-1} is ascribed to the OH groups which belonged to α-cellulose (d).

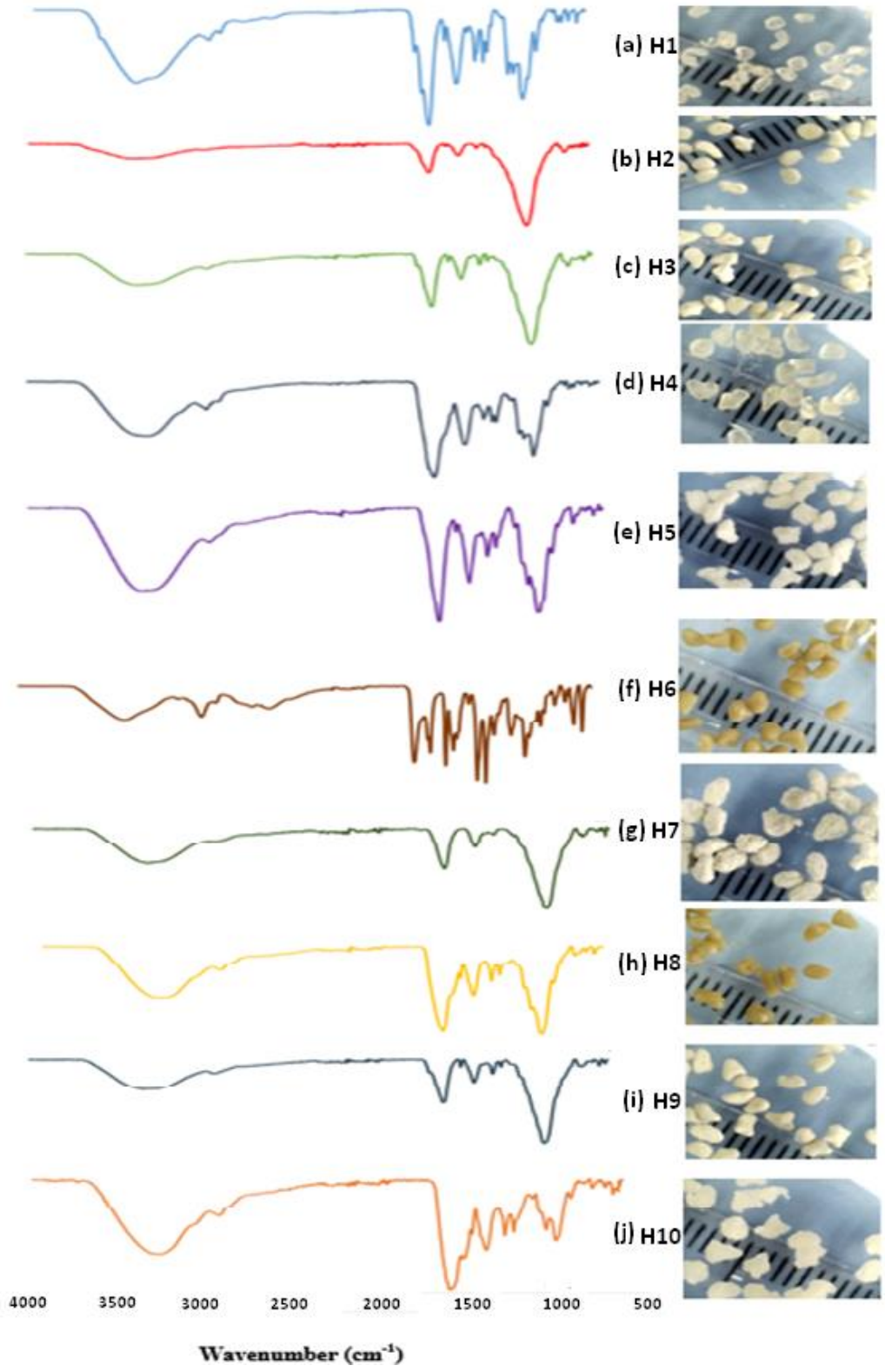

Figure 1. FT-IR analyses of hydrogels.

Two different clinoptilolite was used in this study: clinoptilolite and modified clinoptilolite. When the difference spectrum of clinoptilolite and modified clinoptilolite was investigated, it was seen the presence of the same typical bands clinoptilolite and modified clinoptilolite. Figue 1(d-f-g-h), exhibits FT-IR analyses for gelatine based hydrogels. The band of gelatin centered at about 3400 cm^{-1}, which was the stretching vibration, broadened and coupled with –OH band of sodium alginate at 3450 cm^{-1}, included by the addition of sodium alginate to gelatin, implied the occurrence of

hydrogen bonds between –OH groups of sodium alginate and –NH groups of gelatin molecules. Figure 1(e-g-i-j) shows the FT–IR spectra of α-cellulose based hydrogels modified by 4 AcM, gelatine, clinoptilolite and modified clinoptilolite, respectively.

The sizes of hydrogels were between 1.67 and 2.57 mm, which were obtained by digital microscope. Diameter of hydrogels are given in Table 2.

Table 2. Diameter of hydrogels

Hydrogels	(mm)
H1	1,67
H2	1,70
H3	1,93
H4	1,93
H5	2,28
H6	1,85
H7	2,57
H8	1,99
H9	2,20
H10	2,29

Swelling properties of the hydrogels

The swelling properties of hydrogels were studied as function of time and pH. Swelling curves and maximum equilibrium swelling of hydrogels in deionized water and in solutions with of pH 1.2, pH 6.8, pH 7.4 at 37°C were shown in Figure 2 and 3, respectively.

It has been well-known that the swelling–deswelling behavior is mainly due to the interaction between polymer and water molecules. It was observed that the swelling of hydrogels are depended on medium. As shown in Figures 2 and 3, for all hydrogels, maximum swelling was obtained at pH 6.8 and minimum at pH 1.2. Hydrogels presented a very low swelling ratio at pH 1.2, due to the protonation of carboxylate group in sodium alginate lowering the electrostatic repulsion. Three hours later, it was observed that hydrogels started to break into pieces at pH 6.8 and 7.4. Also, hydrogels which content gelatine presented the best swelling capacities. The percentage of swelling of H4 (NaAlg/4AcM/Gelatine) reached up 84 % within 24 h in pH 1.2, 104% within 24 h in deionized water, 424 % within 3h in pH 7.4 and 1309 % within 3 h in pH 6.8.

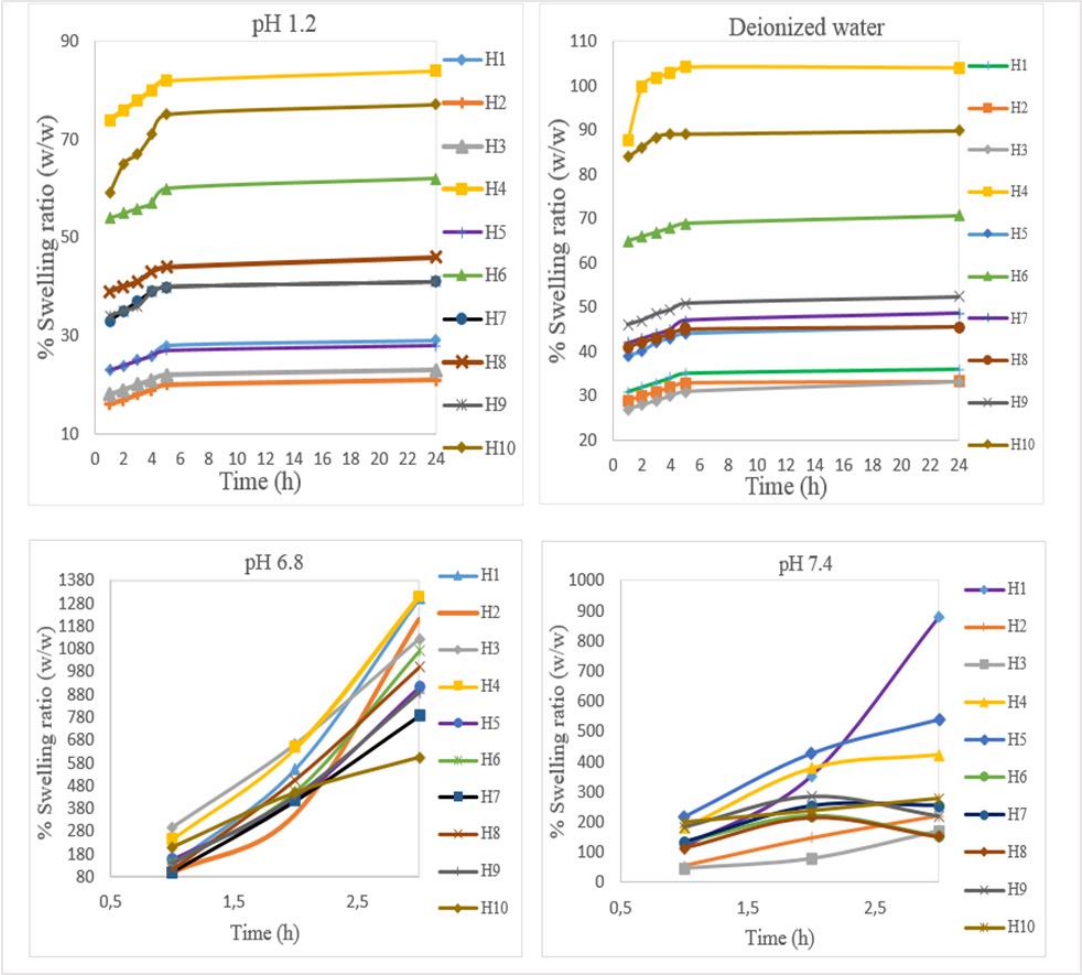

Figure 2. Swelling rate curves of hydrogels

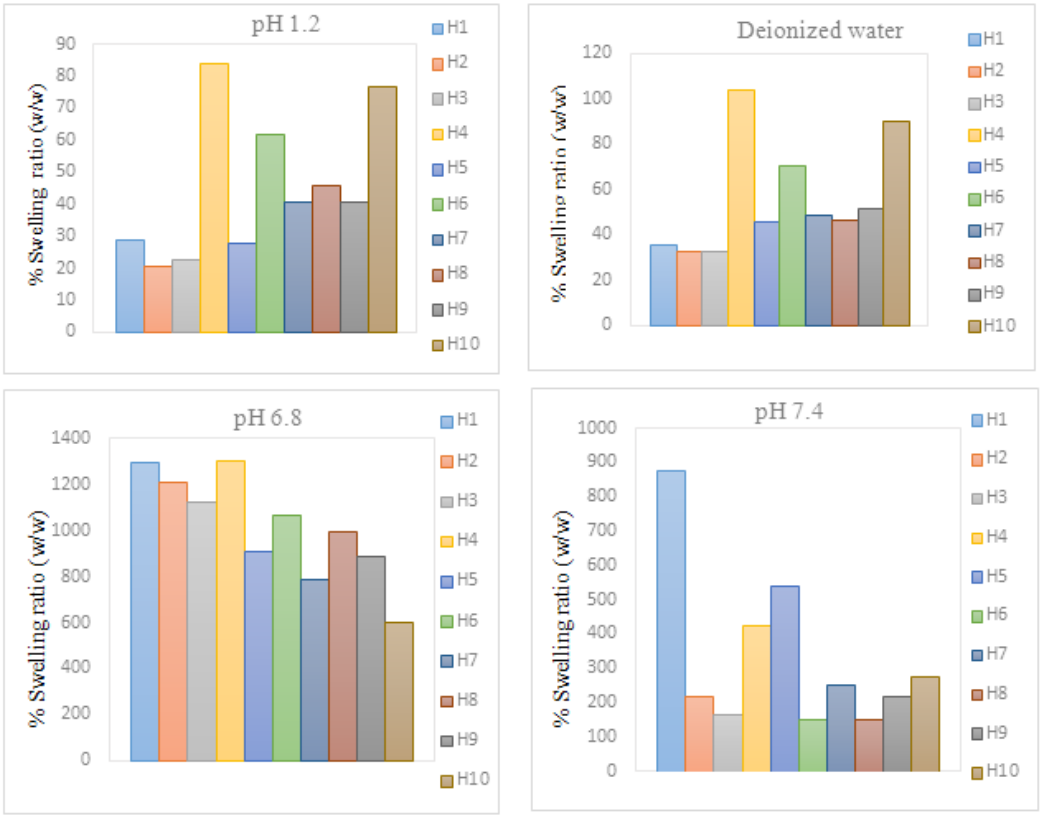

Figure 3. Swelling ratio of hydrogels.

Donepezil HCl release studies

In this section the interaction of the hydrogels with donepezil hydrochloride was studied. pH 1.2, pH 6.8 and pH 7.4 were selected as mediums for the study of the hydrogels interaction with donepezil hydrochloride. Figure 4, 5 and 6 depict the percent cumulative release of donepezil hydrochloride from hydrogels at pH 1.2, pH 6.8 and pH 7.4, respectively, at 37°C.

It has been found that the hydrogels of NaAlg/α-cellulose/Clinoptilolite show the highest release ratio in all mediums. While the gelatine based hydrogels showed prolonged release profiles, the AcM based hydrogels did not. When compared the release of clinoptilolite, modified clinoptilolite, there is not significant difference between them. Also the release behavior of donepezil hydrochloride from the hydrogel was very sensitive to pH. It has been determined that release duration of Donepezil Hydrochloride at pH 1.2 was longer than pH 6.8 and pH 7.4. Since extending the time of release of hydrogels were obtained at pH 1.2, hydrogels can lead to a successful application for localized drug delivery used for gastric medium. The percentage cumulative release of donepezil HCl from AcM based hydrogels was lower in all medium pH.

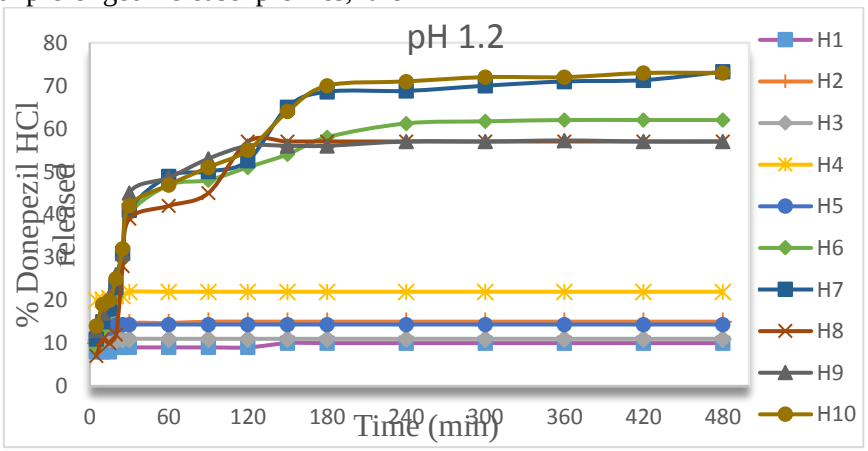

Figure 4. Donepezil HCl release of hydrogels in pH 1.2 media.

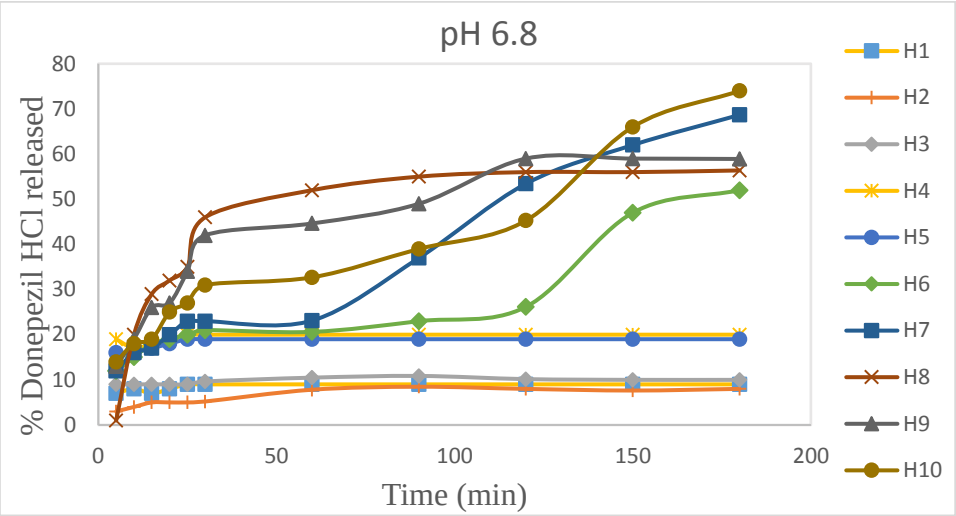

Figure 5. Donepezil HCl release of hydrogels in pH 6.8 media.

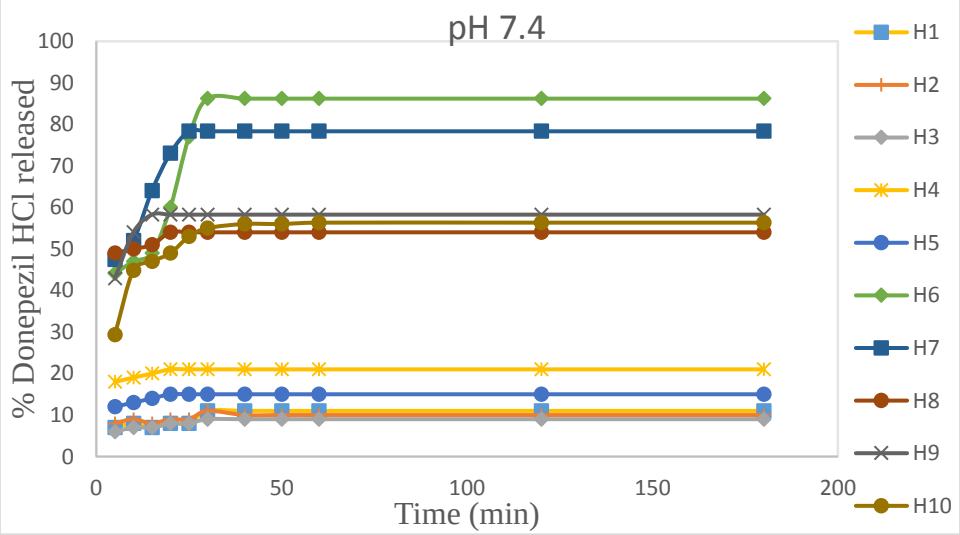

Figure 6. Donepezil HCl release of hydrogels in pH 7.4 media.

CONCLUSIONS

In this study, the ternary sodium alginate based hydrogels were prepared successfully with gelatine, α-cellulose, clinoptilolite, modified clinoptilolite and 4-acryloyl morpholine. It has been found that the hydrogels content gelatine show the highest degree of swelling and release rate. Also the release behavior of donepezil hydrochloride from the hydrogels was very sensitive with the medium pH. It was seen that the time of release of hydrogels was very high at pH 1.2. These results suggest that the sodium alginate based composite hydrogels may be appropriate for use in the controlled release of drugs.

REFERENCES

1. P. Zhang, L. Chen, W. Gu, Z. Xu, Y. Gao, Y. Li, *Biomaterials*., **28**, 1882 (2007).
2. A. F. Habibyar, N. Sharma, N. Khurana, *Eur. J. Pharmacol*.., **789,** 385 (2016).
3. W. Guo, P. Quan, L. Fang, D. Cun, M. Yang, *Asian J. Pharmac. Sci*,., **10**, 404 (2015).
4. J. K. Park, Y. B. Choy, J-M. Oh, J.Y. Kim, S-J. Hwang, J-H. Choy, *Int. J. Pharmac*., **359**, 198 (2008).
5. F. Martínez-Gómez, J. Guerrero, B. Matsuhiro, J. Pavez, *Carbohydrate Polymers*., **155**, 182 (2017).
6. W-F. Lai, Z-D. He, *J. Controll. Release*., **243**, 269 (2016).
7. G. Marcelo, M. López-González, I. Trabado, M. M. Rodrigo, M. Valiente, F. Mendicuti, *Mater.Today Commun*.., **7**, 73 (2016) 73–80.
8. V. M. O. Cardoso, B. S. F. Cury, R. C. Evangelista, M. P. D. Gremiao, *J. Mech.Behavior Biomed. Mater*., **65**, 317 (2017).
9. B. J. Kong, A. Kim, S.N. Park, *Carbohydrate Polymers*., **147**, 473 (2016).
10. Y. Baimark, Y. Srisuwan, *Adv. Powder Technol*., **25**, 1541, (2014).
11. Y. Qiu, K. Park, *Adv. Drug Delivery Rev*., **64**, 49 (2012).

12. M. Hamidi, A. Azadi, P. Rafiei, *Adv.Drug Delivery Rev.*, **60**, 1638 (2008).
13. M.A. Patel, M. H. H. AbouGhaly, J.V. Schryer-Praga, K. Chadwick, *Carbohydrate Polym.*, **155**, 362 (2017).
14. J. Yan, Y. Miao, H. Tan, T. Zhou, Z. Ling, Y. Chen, X. Xing, X. Hu, *Mater. Sci. Eng. C.*, **63**, 274 (2016).
15. K. Pak, A.T. Paulson, D. Rousseau, Biopolymers in Controlled-Realese Delivery Systems, in: Handbook of Biopolymers and Biodegradable Plastics, Properties, Processing, and Applications., Elsevier, , 2009, p. 526.
16. H. Efe, M. Bicen, M. Kahraman, N. Apohan, *J. Braz. Chem. Soc*., **24**, 814 (2013).
17. F. F. Azhar, A. Olad, *App.Clay Sci.*, **101**, 288 (2014).
18. J. F. Almeida, J. F. Ferreira, A. Lopes, M. H. Gil, *Int. J. Biol. Macromol.*, **49**, 948 (2011).
19. P. R. Deepthi, V. Prasad, P. W. Diwan, *IOSR J. Pharm.Biol. Sci.*(IOSR-JPBS), **9**, 83 (2014).

Bulgarian Chemical Communications, Volume 49, Special Issue I (pp.64 – 69) 2017

Outdoor air quality sulphur dioxide in Istanbul

E. Bozkurt Kopuz[1]*, B. Dincer[2],

[1]*Marmara University, Department of Civil Engineering, 34722, Kadikoy/Istanbul, Turkey*
esin.bozkurt@marmara.edu.tr
[2] *Marmara University, Department of Environmental Engineering, 34722, Kadikoy/Istanbul, Turkey*

Submitted: June 1, 2017; Accepted: September 1, 2017

Oxidation of sulfur dioxide (SO_2) may form various atmospheric air pollutants, which is caused by natural processes or human activity. Chemical composition of the atmosphere and biosphere can change depending on the efficiency of the oxidation processes. Atmospheric gases like H_2SO_4 released by the oxidation of SO_2 is naturally removed from the atmosphere through oxidizing chemical reactions. Human activity can increase the amount of gases in the atmosphere, therefore it can affect the oxidation capacity. As a result of OH reaction, these gases are destroyed and removed from the atmosphere. OH reaction converts SO_2 to sulfuric acid H_2SO_4. Rain carries the sulfuric acid to biosphere or hydrosphere.

Free radicals are found in the atmosphere in small amounts, however, they rapidly react with other substances and thus spread through the atmosphere. SO_2 is one of the reactive radicals which has an effect on the oxidation processes. It plays an important role in the balance of atmospheric composition.

This study evaluates the SO_2 values in Kandilli, Sultanbeyli and Umraniye districts in Istanbul that was measured by Istanbul Marmara Clean Air Centre between March 1, 2013 and April 30, 2016. According to the measurements, the level of SO_2 was below the minimum level recommended by Turkish Government. Accordingly, it has been determined that the air quality was satisfactory; and the air pollution poses little or no risk to human health. In addition, temperature was found to have a significant impact on SO_2 compared to wind velocity and humidity. It was observed that SO_2 concentrations increased in winters compared to other seasons. SO_2 mean concentrations were lower in Istanbul compared to other countries.

Key words: outdoor air quality; SO_2; oxidation; Istanbul

1. INTRODUCTION

SO_2 is a colorless, pungent gas emitted by the combustion of sulfur-bearing fuels like coal or fuel-oil, metal smelting and other industrial facilities. The main sources of SO_2 in the atmosphere are domestic heating, thermal power plants and industrial boilers. Highest concentrations of SO_2 are generally measured in the settlements where low-quality coke is burned for heating or where there are large industrial facilities.

Children, elderly and the people suffering from asthma are the most vulnerable group to the effects of SO_2. SO_2 exposure harms the respiratory system by narrowing the respiratory tract, which can be detected with the symptoms such as wheezing, chest compression and cutaneous breathing. These symptoms may emerge as a result of high concentrations of SO_2 and increased breathing rate. After the exposure stops, lung returns to its normal functioning within one hour. Moreover, high concentrations of SO_2 may cause wheezing, chest compression, cut-off breathing.

Long-term exposures to SO_2 can lead to respiratory illnesses and changes in defense mechanisms of the lungs, and worsen the existing cardiac diseases. Children, elderly and the people who have chronic lung or heart diseases are the most sensitive group to this effect of SO_2.

Meteorological parameters may also be effective in dispersion or chemical transformation of air pollutants. For example, when the temperature decreases, the amount of combustion pollutants increases in the atmosphere, which in the end leads to the emission of SO_2 [1].

There are various studies which investigated the level of atmospheric SO_2 in different urban region areas [2-7].

2. EXPERIMENTAL

Figure 1(a) shows the areas of investigation, which are certain locations selected from crowded districts of İstanbul (Figure 1b). The residents in these districts use heating systems in winter and the main sources for heating systems are coal, and natural gas. Only the Kandilli district (Uskudar) is located on the Marmara Sea coast among the three locations. SO_2 values of these 3 areas are shown in Figure 1(c), which were measured by staff of Marmara Clean Air Center. Ambient air quality was measured through TS EN 14212 method by determining the level of sulfur dioxide using ultraviolet fluorescence [8].

SO_2 limit values determined and implemented by Turkish authorities, EU and WHO in order to protect human health are shown in Table 1. The limit value of SO_2 determined by EU for 1 hour is 350 $\mu g/m^3$ and permitted number of exceedence is 24 times per year [9].

* To whom all correspondence should be sent.
E-mail: esin.bozkurt@marmara.edu.tr

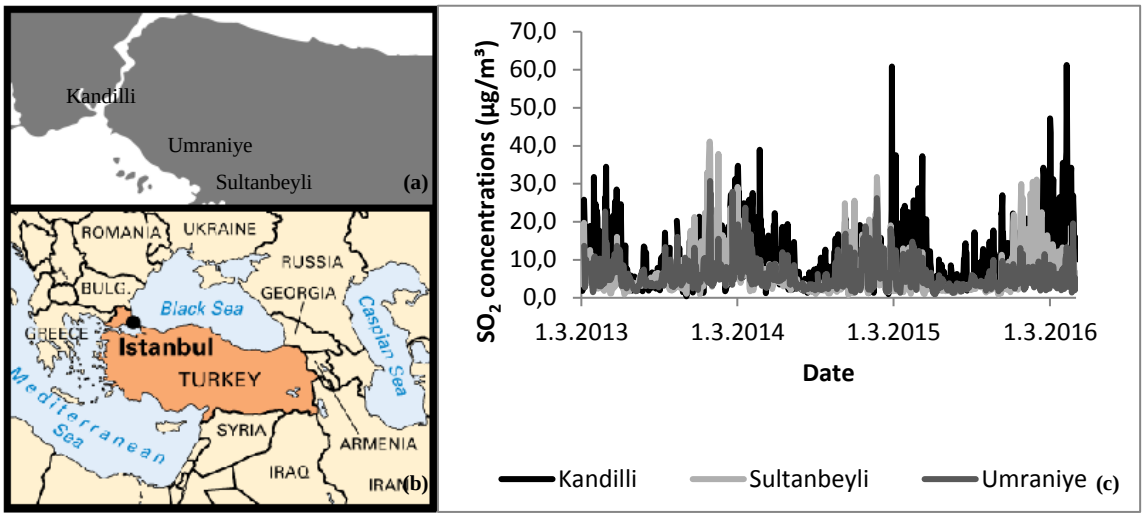

Fig. 1. (a) Investigation sites: Kandilli, Sultanbeyli, and Umraniye; (b) Istanbul, Turkey; (c) SO_2 concentrations

Table 1. Daily limit values for SO_2 (µg/m³) [9,10,11]

Year	Turkey	EU (Permitted exceedences each year)	WHO
2013	280	125 (3)	20
2014	250	125 (3)	20
2015	225	125 (3)	20
2016	200	125 (3)	20

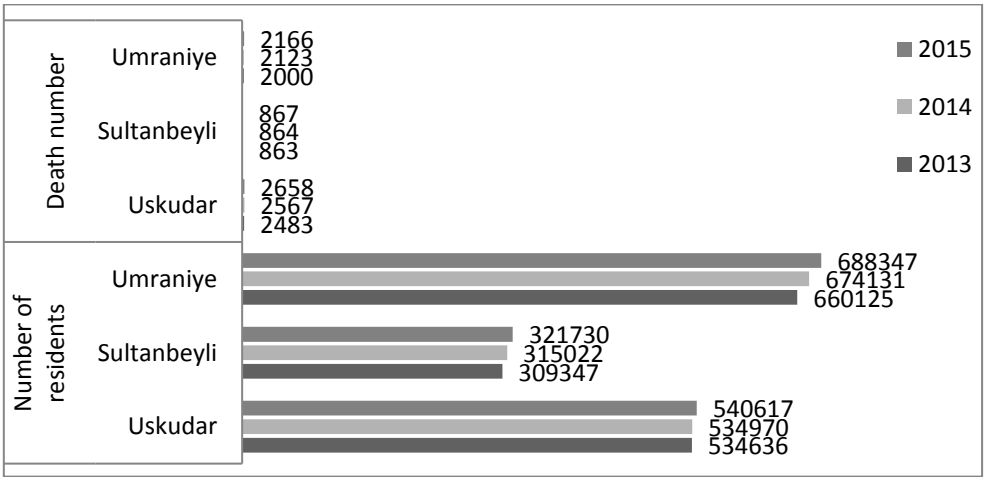

Fig. 2. Mortality rate and resident numbers for Umraniye, Sultanbeyli, and Uskudar [12].

3. RESULTS AND DISCUSSION

According to the measurements, the levels of SO_2 in three locations did not exceed the limit value during the 2013-2016 period. According to Turkish health index, air quality was assessed through SO_2 concentration and determined as good with 100 µg/m³. Therefore, it was determined that the health risk of SO_2 emissions was low in Kandilli, Sultanbeyli and Umraniye in the years between 2013-2016, the air quality was suitable for outdoor activities.

There was a correlation between the number of residents and mortality, which was determined as 0.99 for Umraniye and 0.85 for Sultanbeyli. The mean SO_2 concentration value between Umraniye and Sultanbeyli was 0.98. As indicated in Fig. 2, as the mortality and resident numbers increased, the mean SO_2 concentration did not increase.

Monthly mean SO_2 values for all areas were higher in winter than in summer during 2013-2016 period (Figure 3).

There was an incident occurred in this period which has appeared in the newspaper. After a fuel tank explosion in Sultanbeyli on 22 April, 2014 [13], SO_2 level in the environment was measured. Accordingly, SO_2 concentrations were found to be high, which were 38.9 µg/m³ in Kandilli, 6.1 µg/m³ in Sultanbeyli, and 8.7 µg/m³ in Umraniye. Highest concentration was observed in Kandilli due to westward direction of the wind blowing from Kartal (265°). For this reason, substances emitted after the explosion were carried to Kandilli from Sultanbeyli through the wind.

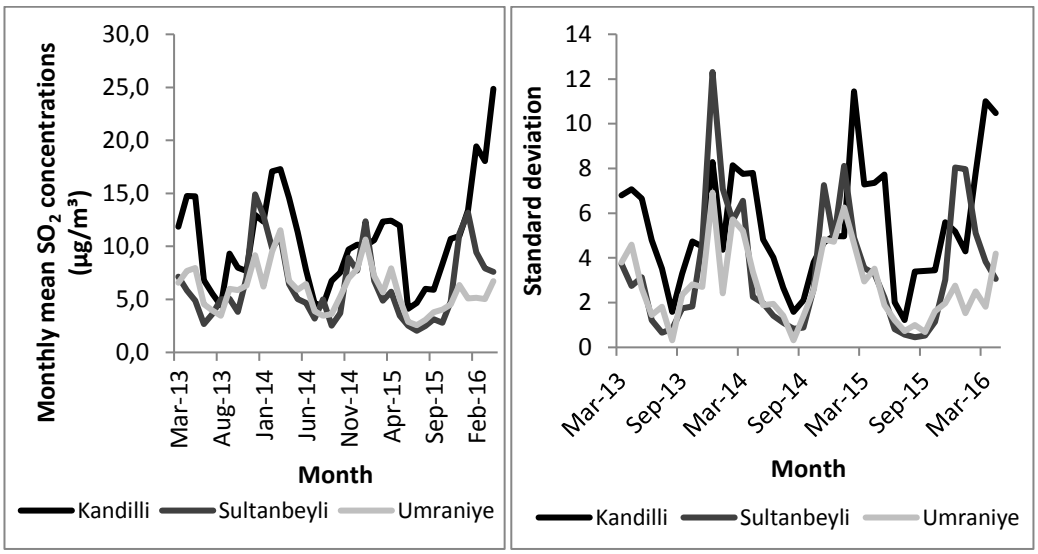

Fig. 3. (a) Monthly mean of SO_2 concentrations; (b) monthly standard deviation

In January, SO_2 values were higher in Sultanbeyli than the other areas. Rest of the months, SO_2 values were higher in Kandilli compared to other regions. In August, SO_2 decreased in all the locations. Highest SO_2 values were observed in February and March. It was determined that high SO_2 concentrations in Kandilli are caused by the ship activities.

Table 2. Annual maximum, minimum, and mean values for SO_2 (µg/m³)

	Year	Kandilli	Sultanbeyli	Umraniye
Maximum	2013	34.50	41.12	30.73
	2014	38.94	37.84	27.92
	2015	60.89	31.76	26.19
Minimum	2013	0.39	0.89	1.46
	2014	1.23	0.70	1.40
	2015	0.99	0.77	0.96
Mean	2013	10	6	6
	2014	10	6	6
	2015	9	5	5

Annual maximum, minimum and mean SO_2 concentrations were calculated for each district. Maximum values were below 61µg.m^{-3} (Table 2). Annual maximum values for Kandilli, Sultanbey li, and Umraniye were determined 34.50, 41.12, and 30.73 µg/m³, respectively, which are below the limit values determined by Turkey, EU, and WHO. The annual mean SO_2 concentrations were observed below the limit value (20 µg/m³ for annual and winter) that is specified in the Air Quality Assessment and Management Regulation for Turkey.

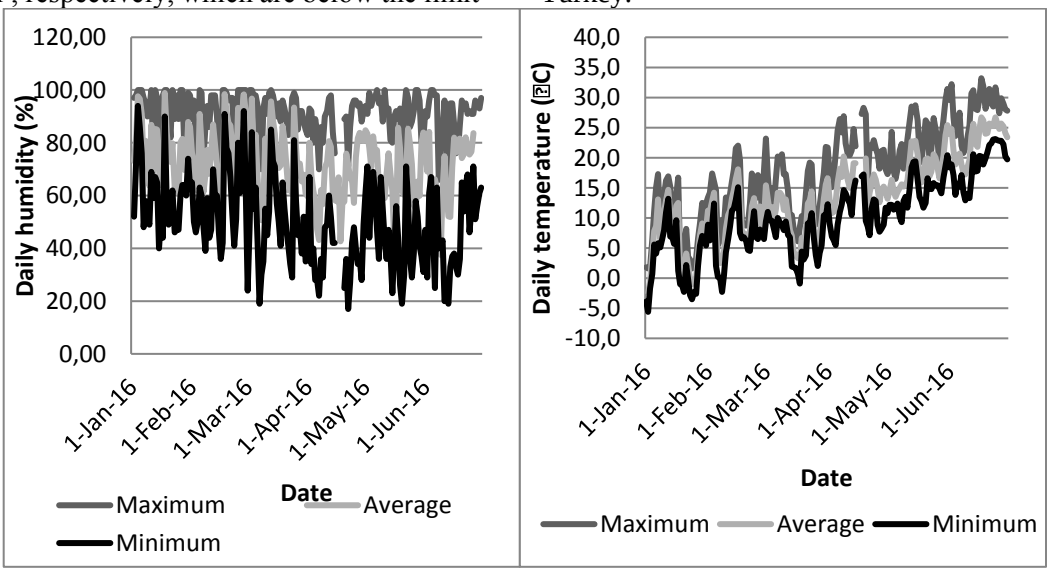

Fig. 4. (a) Daily humidiy for Kandilli; (b) daily temperature for Kandilli.

Table 3. Descriptive statistics of the data: SO_2 (µg/m³) in Umraniye, Sultanbeyli, Kandilli, January-April 2016

Variable	Mean	±SD	Minimum	Maximum	Station
Daily humidity (%)	73.52	12.58	17.00	100.00	Kandilli
	74.32	16.39	14.00	100.00	Umraniye
	74.41	13.03	12.00	100.00	Sultanbeyli
Daily temperature (°C)	10.14	5.15	-5.60	28.30	Kandilli
	9.39	5.54	-6.00	27.80	Umraniye
	9.72	5.23	-10.70	29.10	Sultanbeyli
Daily wind speed (m/sec.)	3.21	1.47	1.30	23.20	Kandilli
	3.24	1.23	1.30	21.90	Umraniye
	2.61	1.34	0.60	21.90	Sultanbeyli
Daily SO_2(µg/m³)	19.31	9.75	4.42	61.25	Kandilli
	5.50	2.75	1.40	19.58	Umraniye
	9.52	5.68	2.80	31.10	Sultanbeyli
Daily wind direction	192.53	109.58	5.00	359.00	Kandilli
	191.66	105.01	5.00	360.00	Umraniye
	204.02	107.62	3.00	359.00	Sultanbeyli

Daily mean values for humidity, temperature, wind speed, and wind direction in all stations were %74; 10°C; 3m/sec.; and SSW, respectively (Table 3). Daily mean SO_2 concentrations in Kandilli were higher than in other districts due to wind direction and the ship activities (Figure 4 and 5).

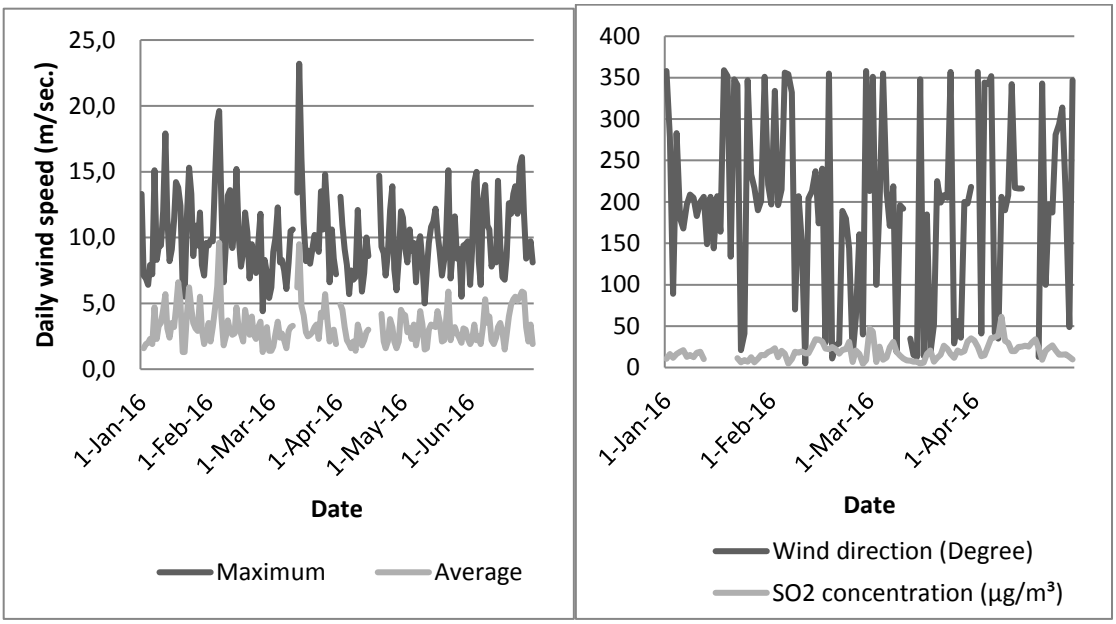

Fig. 5. (a) Daily wind speed for Kandilli; (b) daily wind direction and SO_2 concentration for Kandilli.

Pearson correlation coefficient (r) between temperature and SO_2 in Umraniye is found to range between 0.3 and 0.5, which represents a positive medium strength association between these variables (Table 4). Pearson's r between temperature and SO_2 levels in Kandilli ranges between 0.5 and 1, which means there is a strong positive association between these variables. Pearson's r between humidity and SO_2 levels in Kandilli and Umraniye ranged between -0.3 and -0.5, which indicates a medium negative association between these variables. Pearson's r values between SO_2 and meteorological parameters in Sultanbeyli take a range from -0.1 to -0.3, which indicates a weak negative association between two variables.

Table 4. Daily values of Pearson correlation coefficient between SO2 (μg/m³) and meteorological data in Umraniye, Sultanbeyli, and Kandilli, 2013-2016

Pearson correlation between daily SO_2 and	Kandilli	Umraniye	Sultanbeyli
Daily maximum humidity (%)	-0.34	-0.40	-0.05
Daily Mean humidity (%)	-0.47	-0.55	-0.12
Daily minimum humidity (%)	-0.41	-0.42	-0.15
Daily maximum temperature (°C)	0.65	0.47	-0.06
Daily Mean temperature (°C)	0.62	0.48	-0.14
Daily minimum temperature (°C)	0.58	0.43	-0.24
Daily maximum wind speed (m/sec.)	-0.32	0.01	-0.17
Daily Mean wind speed (m/sec.)	-0.42	-0.09	-0.23
Wind direction (Degree)	0.05	0.25	0.17

High mean values were generally observed in winter (Table 5).

Table 5. Seasonal SO_2 (μg/m³) in Umraniye, Sultanbeyli, Kandilli, 2013-2016

Year	Period (season)	Kandilli	Sultanbeyli	Umraniye
2013	Spring	13.8	5.9	7.6
	Summer	5.6	3.8	4.0
	Autumn	8.3	5.3	6.0
	Winter	14.0	12.6	8.1
2014	Spring	14.4	7.4	8.1
	Summer	5.3	3.4	4.3
	Autumn	8.0	4.9	5.2
	Winter	10.3	9.0	8.6
2015	Spring	12.2	4.7	6.2
	Summer	4.9	2.3	2.8
	Autumn	8.31	3.56	4.11
	Winter	14.62	11.29	5.55
2016	Spring	21.40	7.77	5.87

In 1989, mean and maximum SO2 concentrations were calculated as 102 and 630 μg/m³, respectively in Beijing, China [14]. In the Esino Valley, Italy, hourly mean(±SD) values were calculated as 20.02 μg/m³ (±17.18) in summer and 36.22 μg/m³ (±14.92) in winter [1]. In the seven cities of Korea, mean SO2 level was calculated as 23.3 μg/m³ from 1991 to 1997 [14]. Second highest daily mean value was measured in Philadelphia as 299 μg/m³ from 1973 to 1980 [15]. In this study, SO2 concentrations in Istanbul were lower than the previous data in the literature.

4. CONCLUSIONS

The aim of this study was to investigate the correlation between meteorological parameters and SO_2 concentration levels, and monthly and seasonal variations of SO_2 in the atmosphere. Mean seasonal values for Kandilli took a range from 4.9 to 21.4 μg/m³, for Umraniye from 2.8 to 8.6 μg/m³, for Sultanbeyli from 2.3 to 12.6 μg/m³.

The amount of air pollution in İstanbul has considerably declined in 2015 thanks to the advancements in heating system of the city like widespread use of natural gas. Nowadays, air pollutants pose a significant threat to human health by harming respiratory system. Intense and long-term exposure to SO_2 is especially dangerous for people with asthma, chronic lung patients and children. In addition, high concentrations of SO_2 can cause asthma attacks. There are some precautions which can be taken to reduce the adverse effects of SO_2 on human health such as moving the industrial and business centers out of the settlement areas, promotion of public transport instead of using

personal vehicles, developing and using electric transport vehicles, using air filters in industrial areas and using natural gas as fuel, increasing the forestation especially in areas where the air pollution is intense.

Compared to China, Italy, Korea, Philadelphia, SO_2 values in Istanbul were low.

Acknowledgements. *This study was supported by the Marmara University, Scientific Research Projects Committee (BAPKO) with the project number FEN-D-120417-0189. The Study data was supported by Marmara Clean Air Centre in Ministry of Environment and Urban Planning and Istanbul Regional Directorate of Meteorology.*

REFERENCES

1. G. Latini, R.C. Grifoni, G. Passerini, *WIT Tran. Ecol. Environ.*, **53** (2002).
2. A. Gaur, S.N. Tripathi, V.P. Kanawade, V. Tare, S.P. Shukla, *J. Atm. Chem.*, **71,** 283 (2014).
3. M. Bralić, M. Buljac, N. Periš, M. Buzuk, P. Dabić, S. Brinić, *Croatica chemica acta,* **85,** 139 (2012).
4. X. Xu, J. Gao, J. Gao, Y. Chen, *Arch. Environ. Health: An International Journal,* **49,** 216 (1994).
5 R.W. Buechley, W.B. Riggan, V. Hasselblad, J.B. VanBruggen, *Arch. Environ. Health: An International Journal*, **27,** 134 (1973).
6. N. Kato, H. Akimoto, *Atm. Environ. Part A. General Topics,* **26,** 2997 (1992).
7. N. Kato, H. Akimoto, *Atm. Environ.*, **41,** 171 (2007).
8. Ambient air quality standard, Online at: http://standards.globalspec.com/std/1060373/tse-ts-en-14212
9. European Union Air Quality Limit Values, EU Regulation 2008/50/EC, Online at: http://ec.europa.eu/environment/air/quality/standards.htm
10. Turkish Air Quality Limit Values, Air Quality Assessment and Management Regulation, 6 June 2008, No: 26898 Revision date: 5 May 2009 No: 27219
11. World Health Organisation Air Quality Limit Values 2005, 2000 ve 1997
12. Turkstat Causes of Death Statistics, 2013 and 2014, (2016), On line at: https://biruni.tuik.gov.tr/medas/?kn=114&locale=tr
13. Milliyet news, Online at: http://www.milliyet.com.tr/sultanbeyli-de-yakit-tankeri/gundem/detay/1871218/default.htm
14. J.T. Lee, H. Kim, Y.C. Hong, H.J. Kwon, J. Schwartz, D.C. Christiani, *Environ. Research*, **84**, 247 (2000).
15. J. Schwartz, D.W. Dockery, *Amer. Review Resp. Diseases*, **145**, 600 (1992.

Bulgarian Chemical Communications, Volume 49, Special Issue I (pp.70 – 77) 2017

Synthesis of new Rh(I) and Ru(III) complexes and investigation of their catalytic activities on olefin hydrogenation in green reaction media

H. Ünver*, F. Yilmaz

Chemistry Department, Faculty of Science, Anadolu University, 26470, Eskişehir, Turkey

Submitted: June 1, 2017; Accepted: September 1, 2017

Two new Ru(III) and Rh(I) complexes of N-acyl benzotriazole derivative ligand have been synthesized and characterized. The catalytic activities of complexes were tested on styrene and 1-octene hydrogenation in ionic liquid ([bmim][BF_4]), DMSO and toluene media. For styrene hydrogenation, 100 % ethyl benzene conversion was obtained with Rh(I) complex, while the conversion ratio was found to be 86.6 % with Ru(III) complex. The catalytic experiments was also conducted in DMSO and toluene to make comparison with ionic liquid under the same conditions (393 K and 6h). 1-octene conversion was found to be 94.5 % with Rh(I) complex at 373 K for 1h. The effect of H_2(g) pressure and catalyst amount was also tested on catalytic reactions. Reusability tests of complexes was investigated over five reaction cycle under 10 bar H_2 in [bmim][BF_4]. No activity loss was observed during five cycle with Rh complex.

Keywords: *N-acyl benzotriazole, ionic liquid, hydrogenation, rhodium, ruthenium*

1. INTRODUCTION

Environmental friendly chemical processes are being important for sustainable chemistry day by day. One of the alternative reaction media as ionic liquid is the promising solvent appearing at this point. Having numerous advantages rather than organic solvents [1,2] make ionic liquids preferable green media for numerous reaction types [3] (Table 1).

Table 1. Several reaction types studied in ionic liquid

Reaction type	Ionic Liquid	Catalyst	Reference
Hydrogenation	Graphene oxide-[mpim][Cl]	Ionic liquid-Ru cat.	[4]
Friedel-Crafts	[bmim][PF_6]	Acid catalyst	[5]
Diels-Alder	[emim][Cl]/$AlCl_3$	Acid catalyst	[6]
Dimerization	[bmim][Cl]/$AlCl_3$	Nickel complex	[7]
Alkylation	$Net_3HCl/AlCl_3/CuCl$	No catalyst	[8]
Allylation	[bmim][BF_4]	Palladium catalyst	[9]
Heck	[bmim][Br], [nbu_4][Br]	Palladacyl catalyst	[10]
Suzuki coupling	[bmim][BF_4]	Palladium catalyst	[11]
Hydroformylation	[bmim][PF_6]	Rhodium catalyst	[12]
Oxidation	[bmim][PF_6]	Chiral Mn(II) catalyst	[13]

Bidentate ligands have been extensively studied and the catalytic activities of their transition metal complexes have been proved many times [14-17]. Benzotriazole derived ligands are much attractive molecules with their relatively cheap, easily obtainable and good coordination abilities to the metal centers. However, transition metals containing benzotriazole ligands are rarely investigated on catalytic reactions (Table 2). To the best of our knowledge, catalytic reactions conducted in ionic liquid media with N-acyl benzotriazole ligand containing rhodium and ruthenium complexes found to be only one which was reported before by our research group [18].

In this study, two new rhodium and ruthenium complexes having furan bridged N-acyl benzotriazole ligand was synthesized and characterized by Elemental analysis, FT-IR, UV-VIS, LC-MS, ^{1}H-NMR and ^{13}C-NMR techniques. The catalytic hydrogenation activities of synthesized complexes was investigated on styrene and 1-octene mainly in 1-butyl-3-methylimidazolium tetrafluoroborate ([bmim][BF_4]) ionic liquid, besides DMSO and toluene as organic solvents.

2. RESULTS AND DISCUSSION

2.1. Characterization of ligand and complexes

In the FT-IR spectrum of ligand, furan dicarboxylic acid O–H stretching vibration at 3100-

*) To whom all correspondence should be sent:
E-mail: hakanunver@anadolu.edu.tr

2882 cm^{-1} disappeared after the substitution via benzotriazole. Also carbonyl (C=O) vibration frequency shifted from 1689 cm^{-1} to 1710 cm^{-1}. Furthermore, C=N stretching vibration of benzotriazole moiety was observed at 1379 cm^{-1} and 1249 cm^{-1}. In the ^{1}H- NMR spectrum of ligand, furan ring protons were observed at δ = 8.34 ppm as a singlet peak. The doublet peaks observed at δ = 8.48 and 8.24 ppm and triplet peaks at δ = 7.78 and 7.62 ppm were associated with benzotriazole moiety of the ligand. Total nine carbon signals were observed in ^{13}C-NMR because of symmetrical structure of ligand. The carbonyl carbons were observed at δ = 154.39 ppm and the thiophene ring carbon atoms were observed at δ = 147.66 and δ = 145.72 ppm. The other carbon signals were observed between δ = 131.98 and 114.78 ppm.

Table 2. Several benzotriazole complexes and their catalytic activities

Complex	Substrate	Reaction type	Reference
$[(TMClBTP)_2Cu]$	L-Lactide	Polymerization	[19]
$[(5CBiIBTP)Ni_2[OAc)_2])$	CO_2 + CHO	Copolymerization	[20]
$[(C8FuIBTP)_2Zn]$	Propylene oxide + CO_2	Coupling	[21]
BiBTP-Zr(IV) alkoxide	Lactide	Ring opening polymerization	[22]
[Rh(COD)L]Cl, $[Ru(L)(H_2O)Cl_3]$	Styrene, 1-octene, cyclohexene	Hydrogenation	[18]
P-BTA-Cu	Ethyl benzene	Oxidation	[23]
[(C8NNBTP)ZnEt]	Lactide	Ring opening polymerization	[24]

In the FT-IR spectra of [RhL(COD)]Cl complex, carbonyl (C=O) group stretching vibration of ligand shifted to higher wavelength (1718 cm^{-1}) and C-N vibration of benzotriazole moiety appeared at 1285 cm^{-1}. Peak observed at 424 cm^{-1} is dedicated to Rh-N coordination [25]. In the ^{1}H-NMR of complex, singlet peak of furan ring shifted from 8.34 ppm to 8.27 ppmand doublet peak of free benzotriazole ring shifted to upfield and observed at 8.39 ppm as doublet of doublets after bonding with metal center. The ^{1}H-NMR signals of cyclooctadiene (COD) emerged at 4.27 and 2.15 ppm as multiple peaks [26]. From the ^{13}C-NMR spectrum of [RhL(COD)]Cl complex, carbonyl carbon (C=O) signal was observed at 170.34 ppm, aromatic ring carbons appeared between 132.12-114.88 ppm values. Additionally, peaks of carbon atoms of COD group were observed at 127.57 and 28.15 ppm. The signals which was observed at 67.03 and 23.89 ppm are related to carbons of solvent (THF) molecule. In the UV-VIS spectrum of the ligand, π→π* and n→π* intraligand charge transfer transitions were observed at 279 nm and 333 nm. There is no d→d transitions after ligand-metal interaction in [RLh(COD)]Cl complex spectra. The molecular ion peaks of rhodium complex was observed at *m/z* 606.2, which supports the formulation of [RhL(COD)]Cl, as shown by the optimized molecular structure in Figure 1. The magnetic susceptibility measurements of Rh complex indicated that this complex is diamagnetic (μ_s= 0) and the structure of complex is a square planar geometry.

In the FT-IR spectrum of $[RuL(H_2O)Cl_3]$ complex, broad aqua peak observed at 3445 cm^{-1}. Aromatic C-H, carbonyl, aromatic C=C and C-N vibration peaks observed at 3077-2797, 1705, 1531-1455 and 1368-1251 cm^{-1} respectively. Ru-O and Ru-N bond stretching appeared as two new peaks at 450 and 434 cm^{-1} respectively [27]. These peaks indicated that two different ligand coordinated to metal centre. The water is coordinated through the oxygene atom and benzotriazole ligand is coordinated via nitrogen atom. Since $[RuL(H_2O)Cl_3]$ complex was found to be paramagnetic, nuclear magnetic resonance measurement can not be clear as Rh complex but observed signals are suitable for suggested complex structure. The protons of furan ring were observed at 8.12 ppm as singlet peak after metal-ligand interaction. Doublet proton peaks of benzotriazole ring of free ligand, which were observed at 8.48 ppm and 8.24 ppm shown as quartet peak at 7.89 ppm and the other proton peaks also observed as quartet at 7.42 ppm after metal-ligand interaction. The observed peak at 3.77 ppm is related to aqua ligand [28]. In the UV-VIS spectrum of ruthenium complex in DMSO, three absorption bands were observed at 272, 362 and 532 nm. The π→π* transition of ligand observed at 272 nm in the complex spectrum. M-L charge transfer transition and d→d (d^5) transitions of metal were observed 362 and 532 nm respectively. The molecular ion peak of $[RuL(H_2O)Cl_3]$ complex including solvent (THF) observed *m/z* 663.3. The magnetic susceptibility measurement of the $[RuL(H_2O)Cl_3]$ complex is found to be 1.24 BM and this means that d orbitals have one unpaired electron and the electronic

configuration is $t_{2g}^5e_g^0$. According to the results, geometry of paramagnetic $[RuL(H_2O)Cl_3]$ complex suggested as octahedral. Based on all spectroscopic results, ligand and complex structures were given in Figure 1.

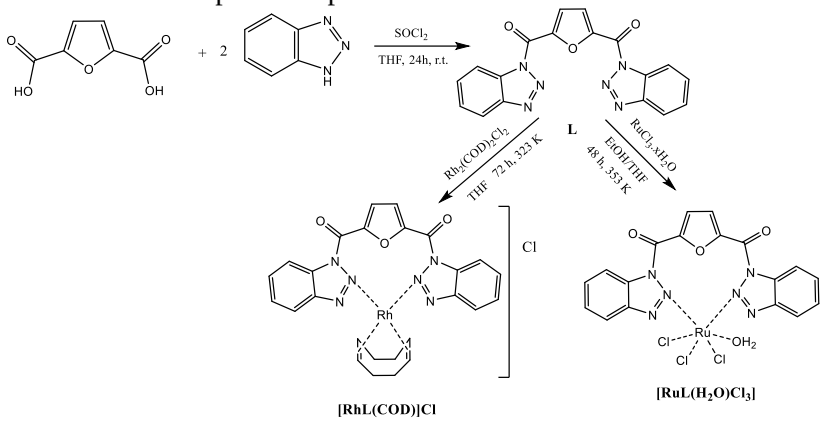

Figure 1. Synthesis and suggested structures of ligand (L) and complexes.

2.2. Hydrogenation activity of complexes

To test the solubility of complexes, catalyst (10 mg) and solvent (IL, DMSO or Toluene) were mixed together in a high pressure reactor via sapphire windows. Sapphire windows provide for monitoring solubility of complexes. It was found that both of complexes are soluble in all solvent media under 10-60 bar H_2(g) between 323-393 K temperatures. During catalytic reactions, catalyst, substrate and solvent were added to the reaction vessel, then reactor was heated to the reaction temperature. Reactor was purged three times with argon gas and then filled with H_2 gas. After the reaction finished, products were extracted with hexane and analyzed by gas chromatography.

2.2.1. Catalytic activity of rhodium catalyst

Styrene and 1-octene were selected as olefin in all catalytic hydrogenation reactions. The results obtained with [RhL(COD)]Cl are given in Table 3. Experiments were conducted with different H_2 pressures, catalyst amount and temperature (Entries 1-12). With a view to testing the temperature effect on hydrogenation of styrene, experiments were conducted between 363-393K in 1 hour reaction time (Entries 1-4). Results indicated that increasing reaction temperature lead to increasing product conversion as expected. The highest product conversion was 50.1 % at 393 K, under 10 bar H_2 pressure (Entry 4). When the reaction time extended to 6 hours, ethyl benzene formation reached to 100 % (Entry 5).

To determine the solvent effect, experiments were conducted in DMSO and toluene besides ionic liquid media (Entries 6-7). It was found that ethyl benzene conversion was high in $[bmim][BF_4]$ than in other organic solvents. Also, activity of catalyst in toluene is better than DMSO.

The effect of H_2 pressure on styrene hydrogenation was tested under 10, 30 and 60 bar pressures at 373 K (Entries 2, 8, 9) in 1h. It was observed that the product formation increased with the pressure and substrate completely converted to ethyl benzene both at 30 and 60 bar H_2(g).

To investigate the effect of s/c ratio, catalytic experiments were performed tree different values as 103, 173 and 518 at 10 bar H_2 at 393 K in 6h (Entries 5, 10, 11). The ethyl benzene conversion was higher at 518 s/c ratio and TON value was reached to 457 at this conditions (Entry 10).

Reusability of catalyst was tested under the best conversion conditions (393 K, 10 bar H_2, 6 h). Results are given in Figure 2. After each cycle, remaining product(s) and substrate were extracted with hexane at least three times, not to observe any residue. It was found that there was no activity loss after five cycles.

To determine the catalytic effect of [RhL(COD)]Cl complex on hydrogenation of 1-octene, experiments were conducted between 333-373 K temperatures in 1h reaction time (Entries 1-5). Results are given in Table 4. The best conversion (94.5 %) and n-octane selectivity were obtained at 373 K, under 10 bar H_2 (Entry 5). The solvent effect in 1-octene hydrogenation reactions also investigated and total conversion did not go over 48.7% in DMSO and it remained only 32% in toluene media (Entries 6, 7).

Reusability test of [RhL(COD)]Cl catalyst in 1-octene hydrogenation was conducted at 373 K, under 10 bar H_2 in 1h reaction time (Figure 3). It is detected that catalyst can be reused at least five times with only 5% activity loss and more importantly n-octane selectivity was found to be higher in the first three cycles than the others (Entries 2, 3).

Table 3. Styrene hydrogenation with [RhL(COD)]Cl catalyst

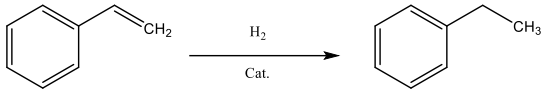

Styrene Ethyl benzene

Entry	T(K)	P_{H2} (Bar)	t(h)	n_s/n_c	Total conv. (%)	TON	TOF
1	363	10	1	103	18.3	19	19
2	373	10	1	103	28.5	30	30
3	383	10	1	103	45.2	47	47
4	393	10	1	103	50.1	52	52
5	393	10	6	103	100	105	18
6[a]	393	10	6	103	36.1	38	6
7[b]	393	10	6	103	65.1	68	11
8	373	30	1	103	100	105	105
9	373	60	1	103	100	105	105
10	393	10	6	518	87.3	457	76
11	393	10	6	173	98.2	171	29
12[c]	393	10	6	103	55.2	55	9

[Reaction cond.: $n_{cat.}$= 8.30 x10^{-6} mol, $n_{styr.}$= 8.69 x 10^{-4} mol, $V_{solv.}$= 0,5 mL, P_{H2}=10 Bar], [a]DMSO, [b]Toluene, [c]Cat.= $[Rh_2Cl_2(COD)_2]$

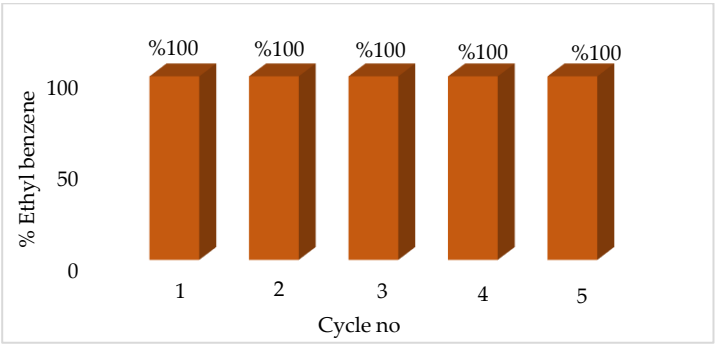

Figure 2. Reusability of [RhL(COD)]Cl catalyst in styrene hydrogenation
[Reaction cond.: T= 393 K, P_{H2}= 10 Bar, $n_{sub..}$= 8,69 x 10^{-4}, $n_{cat.}$= 8,30 x10^{-6} mol, s/c= 103, t= 6 h]

Table 4. 1-Octene hydrogenation with [RhL(COD)]Cl catalyst

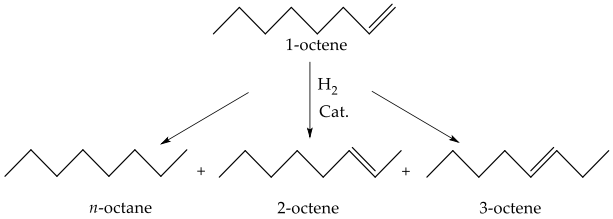

Entry	Cycle No	T(K)	Total conv. (%)	Products (%)			TON	TOF
				(n-octane)	**(2-octene)**	**(3-octene)**		
1		333	35.8	32.6	1.8	1.3	27	27
2		343	67.2	63.7	2.0	1.5	52	52
3		353	71.1	62.3	5.5	3.2	55	55
4		363	86.4	78.3	4.9	3.1	66	66
5		373	94.5	82.8	8.8	1.9	73	73
6[a]		373	48.7	21.6	19.7	7.4	37	37
7[b]		373	32.0	17.4	8.8	5.8	25	25
8	2	373	93.9	93.9	0	0	73	73
9	3	373	92.8	92.8	0	0	71	71
10	4	373	91.7	84.5	4.1	3.1	70	70
11	5	373	90.8	83.2	4.2	3.4	70	70

[Reaction cond.: $n_{cat.}$= 8.30 x10^{-6} mole, $n_{1\text{-}oct.}$= 6.37 x 10^{-4} mole, n_s/n_c= 77, $V_{solv.}$= 0,5 mL, P_{H2}=10 Bar, t=1 h], [a]DMSO, [b]Toluene, [c]cat = $[Rh_2Cl_2(COD)_2]$

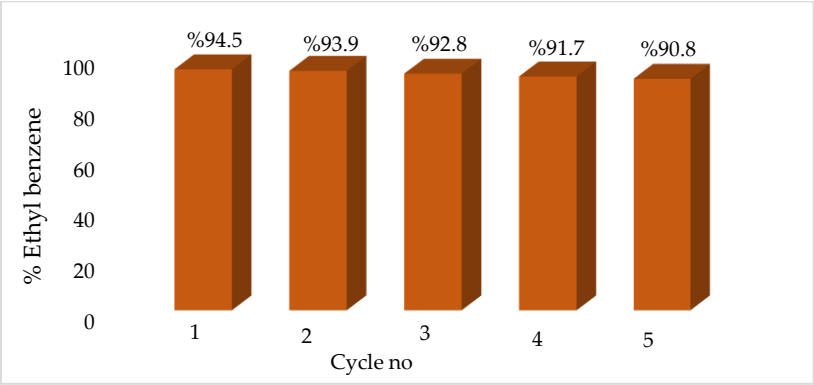

Figure 3. Reusability of [RhL(COD)]Cl catalyst in 1-octene hydrogenation
[Reaction cond.: T= 373 K, P_{H2}= 10 Bar, $n_{sub.}$= 8,37 x 10^{-4}, $n_{cat.}$= 8,30 x10^{-6} mol, s/c= 77, t= 1 h]

2.2.2. Catalytic activity of ruthenium catalyst

[RuL(H_2O)Cl_3] catalyst activity was tested on styrene hydrogenation between 353-393 K temperatures in 1h reaction times (Entries 1-6). All other conditions being the same, reaction temperature has positive effect on catalytic reaction Reaction time increased to 6 h for the determine time effect and it was observed that there is no significant change in the total conversion value. At this conditions, catalytic tests were also performed at organic solvent media and To investigate the solvent effect on catalytic reaction, experiments were conducted in toluene and DMSO under 10 bar H_2 at 393 K and these solvents have negative effect on hydrogenation reactions. Ethly benzene conversion reached to 23.4% in toluene while only 12 % in DMSO (Entries 7,8). [bmim][BF_4] was detected the best reaction media for [RuL(H_2O)Cl_3] catalyst at styrene hydrogenation.

To test the H_2 pressure effect on catalytic reactions, experiments were conducted under 10, 30 and 60 bar H_2 pressures at 353 K (Entries 1, 9-10) and H_2 pressure had negative effect over catalytic reaction. This may be due to the decreased the solubility of [RuL(H_2O)Cl_3] complex. All of these experiments were performed with s/c ratio 100. When the s/c ratio increased TON was reached the best value (185) in 6h at 393K (Entry 11).

Table 5. Styrene hydrogenation with [RuL(H_2O)Cl_3] catalyst

Entry	T(K)	P_{H2} (Bar)	t(h)	s/c	Total conv. (%)	TON	TOF
1	353	10	1	100	29.1	29	29
2	363	10	1	100	38.6	39	39
3	373	10	1	100	39.9	40	40
4	383	10	1	100	44.5	45	45
5	393	10	1	100	81.1	82	82
6	393	10	6	100	86.6	88	15
7a	393	10	6	100	12	12	2
8b	393	10	6	100	23.4	24	4
9	353	30	1	100	21.4	22	22
10	353	60	1	100	13.7	14	14
11	393	10	6	500	36.6	185	31
12	393	10	6	167	43.1	73	12
13c	393	10	6	100	42.1	43	7

[Reaction cond.: $n_{cat.}$= 8.58 x10^{-6} mol, $n_{styr.}$= 8.69 x 10^{-4} mol, $V_{solv.}$= 0,5 mL, P_{H2}=10 Bar] [a]DMSO, [b]Toluene, [c]cat= $RuCl_3$.x H_2O

Reusability of [RuL(H_2O)Cl_3] catalyst on styrene hydrogenation were tested during five cycles under 10 bar H_2 at 393 K for 6h (Figure 4). Conversion of ethyl benzene was found to be 86.6 % at first cycle and after decreased gradually to 78.1 % at the last cycle.

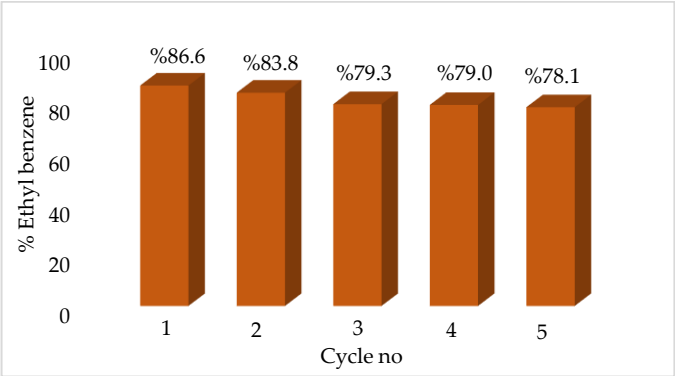

Figure 4. Reusability of [RuL(H_2O)Cl_3] catalyst in styrene hydrogenation
[Reaction cond.: T= 393 K, P_{H2}= 10 Bar, $n_{sub.}$= 8.69 x 10^{-4}, $nc_{at.}$= 8.58 x10^{-6} mol, s/c= 100, t= 6 h]

To investigate the catalytic activity of [RuL(H_2O)Cl_3] complex on 1-octene hydrogenation, experiments were conducted between 353-393 K under 10 bar H_2 in 1h. The results are given in Table 6. Catalyst activity gradually increased from 353 K to 373 K. Conversion decreased at higher temperatures. There may be the catalyst is decomposed at high temperatures. The most effective reaction temperature was found to be as 373 K and the total conversion reached to 44.1 % (Entry 3). The selectivity of catalyst to n-octan was higher at all temperature degrees. Catalyst had almost no activity in organic solvents as compared with ionic liquid media and the activitiy was found to be only 10.6 % in toluene (Entries 6, 7).

Table 6. 1-Octene hydrogenation with [RuL(H_2O)Cl_3] catalyst

Entry	Cycle No	T(K)	Total conv. (%)	Products(%)			TON	TOF
				(n-octane)	(2-octene)	(3-octene)		
1		353	27.4	19.9	5.2	2.2	20	20
2		363	35.1	24.2	7.5	3.4	26	26
3		373	44.1	26.0	12.7	5.3	33	33
4		383	18.1	16.4	1.7	0	13	13
5		393	12.3	12.3	0	0	9	9
6[a]		373	0	0	0	0	0	0
7[b]		373	10.6	1.9	5.4	3.3	8	8
8	2	373	45.7	25.4	13.8	6.4	34	34
9	3	373	54.0	39.9	9.4	4.6	40	40
10	4	373	59.1	49.4	6.6	3.1	44	44
11	5	373	45.9	36.0	6.9	2.9	34	34

[Reaction cond.: $n_{cat.}$= 8.58 x10^{-6} mol, $n_{1\text{-}oct.}$= 6.37 x 10^{-4} mol, n_s/n_c= 74, $V_{solv.}$= 0,5 mL, P_{H2}=10 Bar, t=1 h] [a]DMSO, [b]Toluene, [c]cat= $RuCl_3$.x H_2O

[RuL(H_2O)Cl_3] activity in 1-octene hydrogenation was monitored during five cycle under 10 bar H_2 at 373 K for 1h reaction time (Figure 5) and it was shown that product conversion gradually increased from 44.1% to 59.1% at fourth step (59.1 %). The reason of increase is that the catalyst gains activity with temperature. It was found that the catalyst was deactivated after this cycle and conversion decreased to 45.9 %.

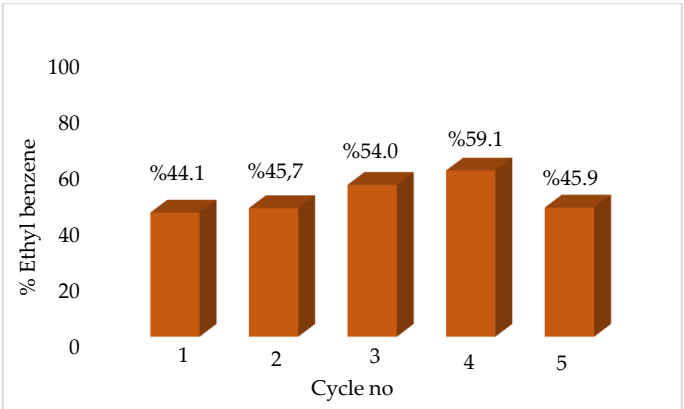

Figure 5. Reusability of [RuL(H_2O)Cl_3] catalyst in 1-octene hydrogenation
[Reaction cond.: T= 373 K, P_{H2}= 10 Bar, $n_{sub.}$= 6,37 x 10^{-4}, $n_{cat.}$= 8,58 x10^{-6} mol, s/c= 74, t= 1 h]

To test the activity of metal precursors, All catalytic experiments were conducted with $[Rh_2Cl_2(COD)_2]$ and $RuCl_3.x\ H_2O$ in $[bmim][BF_4]$. The main aim of this study is whether or not ligand has positive effect on catalytic experiments. The results showed that metal precursors are less effective than complexes under the same conditions.

3. MATERIALS AND METHODS

3.1. General

All the reagents were commercially obtained (Sigma-Aldrich and Merck) and used without further purification. Ligand and complexes synthesis was carried out under inert (nitrogen) atmosphere using standard schlenk techniques. The catalytic reactions were performed in a 100 mL stainless steel high pressure reactor (Parr inst.) containing a magnetic bar, temperature controller and sapphire window. FT-IR spectra were recorded with Perkin Elmer Spectrum 100 Spectrometer using KBr. ^{1}H-NMR and ^{13}C-NMR spectra were recorded on Bruker (500 MHz) DPX FT spectrometer. Mass spectra were recorded on Agilent LC-MSD Trap SL spectrophotometer. Elemental analysis was conducted using Elementar Vario EL III micro analyzer device. Melting points were measured with a Stuart SMP-30 melting point apparatus. Magnetic susceptibility measurements were performed with the Sherwood Scientific MK-1 device. The product conversions in catalytic reactions were determined with Thermo Finnigan Trace GC using a Permabond SE-54-DF-0.25 25 m x 0.32 mm ID column and using helium as carrier gas.

3.2. Synthesis of ligand and complexes

Synthesis procedure of ligand and its rhodium and ruthenium complexes are summarized in Figure 1. Benzotriazole ligand and complexes were successfully prepared with good yields. Synthesized compounds are solid and stable during laboratory storage and the complexes are found to be soluble in mentioned solvents under studied conditions.

3.2.1. Ligand synthesis. Ligand synthesis procedure was following as described before using furan-2,5-dicarboxylic acid instead of thiophene-2,5-dicarboxylic acid [18]. White solid (Figure 1). Yield: %70 (1.8 g), m.p.: 536 Anal. Calc. (%) for $C_{18}H_{10}N_6O_3$: C=60.3; H=2.8; N=23.4. Found: C=59.4; H=2.5; N=23.2. FT-IR (cm^{-1}): 1710, 1379, 1249. ^{1}H-NMR: (500 MHz, $CDCl_3$, δ ppm): 8,48 (2H, d, ^{3}J=8,27), 8,34 (2H, s), 8,24(2H, d, ^{3}J=8,28), 7,78 (2H, t, ^{3}J=7,33), 7,62 (2H, t, ^{3}J=7,34). ^{13}C-NMR:(500 MHz, $CDCl_3$, δ ppm): 154,39, 147,66, 145,72, 131,98, 131,06, 126,90, 124,41, 120,52, 114,78.

3.2.2. Synthesis of [RhL(COD)]Cl catalyst. Ligand (L) (220 mg, 0.6 mmole) was dissolved in THF (20 mL), and $Rh_2(COD)_2Cl_2$ (150 mg, 0.3 mmole) solution in 5 mL THF was added slowly to the first solution. The solution was stirred during 72 h at 323 K. When the reaction completed, the mixture was filtered, and the yellow product was washed with cold THF and dried under vacuum (Figure 2). Yield: 53% (200 mg, 0.33 mmole) m.p.: 458-461 K. Anal. Calc. (%) for $C_{26}H_{22}ClN_6O_2SRh$: C=51.6; H=3.6; N=13.9. Found: C=50.4; H=3.1; N=14.1. LC-MS, m/z (calc./found): 602.3/606.2 FT-IR (cm^{-1}): 1718, 1379, 1285, 424. ^{1}H-NMR: (500 MHz, d^6-DMSO, δ ppm): (500 MHz, d^6-DMSO, δ ppm): 8,39 (3H, dd, ^{3}J=8,27), 8,27 (2H, s), 7,89 (2H, t, ^{3}J=7,67), 7,71 (2H, t, ^{3}J=7,67), 4,27 (2H, t), 2,15 (4H, m). ^{13}C-NMR: (500 MHz, d^6-DMSO, δ ppm):170,34, 131,73, 125,25, 125,04, 120,82, 119,19, 118,87, 114,88, 68,71, 67,03, 28,15, 23,89.

3.2.3. Synthesis of [RuL(H_2O)Cl_3]. The ligand (175 mg, 0.49 mmol) was dissolved in etanol/THF (1:1, 40 mL) mixture and heated for complete solubility, then $RuCl_3.xH_2O$ (100 mg, 0.48 mole) solution in THF (5 mL) was added dropwise to the solution. The mixture was stirred at 353 K for 36 h. After completion of reaction, precipitated black solid was filtered, washed with cold ethanol and dried under vacuum (Figure 2). Yield: 83% (230 mg, 0.39 mmole), m.p.:>593 K (decomp.). Anal. Calc. (%) for $C_{18}H_{12}Cl_3N_6O_3SRu$: C=37.0; H=2.0; N=18.3. Found: C=36.3; H=2.2; N=18.5. LC-MS, m/z (calc./found): 654.9/663.3 FT-IR (cm^{-1}): 3445, 1706, 451, 434. ^{1}H-NMR: (500 MHz, d^6-DMSO, δ ppm): 8,12 (s, 2H), 7,89 (5H, q, ^{3}J=4,0), 7,42 (5H, q, ^{3}J=4,0) ^{13}C-NMR: (500 MHz, d^6-DMSO, δ ppm): 177,26, 141,81, 139,96, 130,18, 125,92, 117,31, 115,47, 56,13, 14,82.

CONCLUSIONS

In this study, two new benzotriazole derived Rh and Ru complexes were synthesized and characterized successfully. The catalytic hydrogenation activities of synthesized complexes were tested in styrene and 1-octene substrates in $[bmim][BF_4]$ as green solvent and also conventional organic solvents. The results indicated that ionic liquid media more effective in hydrogenation catalytic reactions for [RhL(COD)]Cl and $[RuL(H_2O)Cl_3]$ catalysts rather than conventional organic solvents. The activity and n-octane selectivity of rhodium complex was found higher than ruthenium complex for both of substrate (styrene and 1-octene). Besides. [RhL(COD)]Cl complex can be used several times without any loss of activity.

Acknowledgements: *We thank Anadolu University Plant Drug and Scientific Research Center (AUBIBAM) for NMR measurements and The Scientific and Technological Research Council of Turkey (TUBITAK), 2211-Doctorate Grant Program for its financial support.*

Conflicts of Interest: *The authors declare no conflict of interest.*

REFERENCES

1. T. Welton, *Angew. Chem. Int. Ed.*, **39,** 3772 (2000).
2. N. V. Plechkova, K. R. Seddon, *Chem. Soc. Rev.*, **37,** 123 (2008).
3. D. Zhao, M. Wu, *Catalysis Today*, **74**, 157 (2002).
4. J. Y. Lee, L. K. Liu, *International Journal of Hydrogen Energy*, **39,** 17492 (2014).
5. J.A. Boon, J.A. Levisky, *J. Org.Chem.*, **51,** 480 (1986).
6. M.J. Earle, P.B. McCormack, *Green Chem.*, **1,** 23 (1999).
7. L.C. Simon, J. Dupont, *Appl. Catal. A:General*, **175,** 215 (1998).
8. R. Zhang, H. Ma, *Energy Fuels*, **28,** 5389 (2014).
9. W. Chen, L. Xu, C. Chatterton, J. Xao, *Chem. Commun.*, 1247 (1999).
10. W. A. Herrmann, P.W. Böhm, *J. Organometal. Chem.*, **572,** 141 (1999).
11. C.J. Mathews, P.J. Smith, *Chem. Commun.*, 1249 (2000).
12. C.E. Song, E.J. Roh, *Chem. Commun.*, 837 (2000).
13. C. Wheeler, K.N. West, *Chem. Commun.*, 887 (2001).
14. J. Wassenar, J.N.H. Reek, *Org. Biomol. Chem.*, **9**, 1704 (2011).
15. M. R. Zubiri, M. L. Clarke, *J. Chem. Soc., Dalton Trans.*, 969 (2001).
16. D. Cauzzi, M. Costa, *Journal of Organometallic Chemistry*, **593-594,** 431 (2000).
17. N. V. Kaminskaia, I. A. Guzei, *J. Chem. Soc., Dalton Trans.*, 3879 (1998).
18. H. Ünver, F. Yılmaz., Catalysts, **6,** 147 (2016).
19. C. Y. Li, S. H. Hsu, *Journal Of Polymer Science, Part A: Polymer Chemistry*, **51,** 3840 (2013).
20. C.-Y. Yu, H-J. Chuang, B-T. Ko, *Catal. Sci. Technol.*, **6,** 1779 (2016).
21. T. Y. Chen, C. Y. Li, *Journal of Organometallic Chemistry*, **754,** 16 (2014).
22. C. K. Su, H. J. Chuang, *Organometallics*, **33,** 7091 (2014).
23. R. M. Wang, C. P. Chai, *European Polymer Journal*, **35,** 2051 (1999).
24. C. Y. Sung, C. Y. Li, *Dalton Trans.*, **41,** 953 (2012).
25. C. Richardson, P.J. Stell, Dalton Trans. 992 (2003).
26. A. Christiansen, D. Selent, A. Spannenberg, *Organometallics*, **29,** 3139 (2010).
27. K. Shanker, R. Rohini, *Spectrochimica Acta Part A*, **73,** 205 (2009).
28. Y. Takahashi, *Inorg. Chem.* **37,** 3186 (1998).

Bulgarian Chemical Communications, Volume 49, Special Issue I (pp.78 – 89) 2017

Gaussian calculations of novel 3-(methyl/ethyl/*n*-propyl)-4-[3-ethoxy-4-(4-methoxybenzoxy)-benzylidenamino]-4,5-dihydro-*1H*-1,2,4-triazol-5-ones

H. Medetalibeyoğlu*, H. Yüksek

Department of Chemistry, Kafkas University, 36100, Kars, Turkey

Submitted: June 1, 2017; Accepted: September 1, 2017

In this study, three new 3-alkyl-4-[3-ethoxy-4-(4-methoxybenzoxy)-benzylidenamino)-4,5-dihydro-1*H*-1,2,4-triazol-5-ones (**3a-c**) were synthesized by the reaction of 3-alkyl-4-amino-4,5-dihydro-1*H*-1,2,4-triazol-5-ones (**1a-c**) with 3-ethoxy-4-(4-methoxybenzoxy)-benzaldehyde (**2**), which was synthesized by the reaction of 3-ethoxy-4-hydroxybenzaldehyde with 4-methoxybenzoyl chloride by using triethylamine. The compounds synthesized were characterized by IR, ^{1}H-NMR,^{13}C-NMR and UV spectral data. These compounds were optimized by using the B3LYP/6-31G(d,p) and HF/6-31G(d,p) basis sets. ^{1}H and ^{13}C-NMR isotropic shift values were calculated by the method of GIAO using the program package Gaussian G09W. Experimental and theoretical values were inserted into the grafic according to equation of δ exp=a+b. δ calc. IR absorption frequencies of analysed molecules were calculated by two methods. The experimental and theoretical values were compared and found by regression analysis that are accurate. Furthermore, geometric properties (bond angles, bond lengths and dihedral angles), thermodynamic parameters, electronic properties (total energy, dipole moment), the highest occupied molecular orbital (HOMO) and the lowest unoccupied molecular orbital (LUMO), Mulliken atomic charges of compounds **3a-c** have been investigated by using Gaussian G09W program. The structural data of these compounds have been calculated by using 6-31G(d,p) basis set with density functional method (DFT/B3LYP) and Hartree-Fock method (HF).

Key words: 1,2,4-Triazol-5-one, 6-31G(d,p) basis set, DFT(B3LYP), HF

INTRODUCTION

Triazole is an unsymmetrical heterocyclic organic compound having three nitrogen atoms in the five-membered ring. 4,5-Dihydro-1*H*-1,2,4-triazol-5-one and 1,2,4-triazole derivatives are published to possess a broad spectrum of extensively biological activities such as antimicrobial, antitumor, anticancer, antifungal, anti-HIV, antiviral, anti-inflammatory, analgesic and antioxidant properties [1-10]. As well as, articles on the synthesis of some *N*-arylidenamino-4,5-dihydro-1*H*-1,2,4-triazol-5-one derivatives have been published [11-22].

Indeed, the thermodynamic properties, theoretical and experimental spectroscopic properties of some 4,5-dihydro-1*H*-1,2,4-triazol-5-one derivatives have been reported [20, 23-25].

In this paper, 3-alkyl-4-[3-ethoxy-4-(4-methoxybenzoxy)-benzylidenamino]-4,5-dihydro-1*H*-1,2,4-triazol-5-ones (**3a-c**) were obtained from the reaction of compound **(2)** with 3-ethoxy-4-(4-methoxybenzoxy)-benzaldehyde **(1)**, which was synthesized by the reaction of 3-ethoxy-4-hydroxybenzaldehyde with 4-methoxybenzoyl chloride by using triethylamine (Scheme **1**). The starting compounds 2a-i were prepared as described in the literature [26, 27]. The purpose of this study is to synthesize new compounds **3a-c** and to identify the structures of these compounds with spectroscopic methods (^{1}H-NMR, ^{13}C-NMR and FT- IR). Also, these compounds were optimized by using the B3LYP/6-31G(d,p) and HF/6-31G(d,p) basis sets. ^{1}H and ^{13}C-NMR isotropic shift values were calculated by the method of GIAO using the program package Gaussian G09W. Experimental and theoretical values were inserted into the grafic according to equation of δ exp=a+b. δ calc. IR absorption frequencies of analysed molecules were calculated by two methods. The experimental and theoretical values were compared and found by regression analysis that are accurate.

*) To whom all correspondence should be sent:
E-mail: hilalmedet@gmail.com

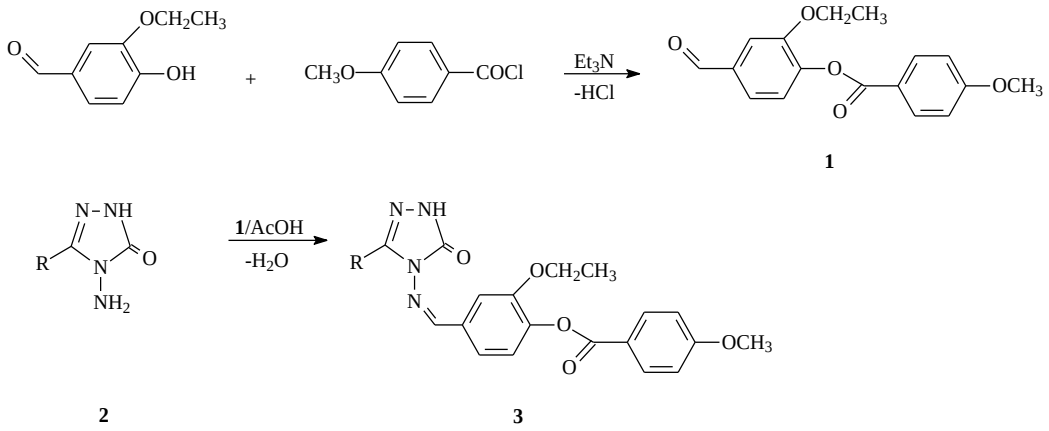

a) R=CH_3, b) R=CH_2CH_3, c) R=$CH_2CH_2CH_3$

Scheme 1. Synthetic pathway of compounds **3a-c.**

EXPERIMENTAL

General method for the preparation of 3-alkyl-4-[3-ethoxy-4-(4-methoxybenzoxy)-benzylidenamino]-4,5-dihydro-1H-1,2,4-triazol-5-ones (**3**)

The corresponding compound 2 (0.01 mol) was dissolved in acetic acid (15 mL) and treated with 3-ethoxy-4-(4-methoxybenzoxy)-benzaldehyde (1) (0.01 mol). The mixture was refluxed for 1.5 h and then evaporated at 50-55 °C in vacuo. Several recrystallizations of the residue from appropriate solvent gave pure compounds **3a-c** as colorless crystals.

3-Methyl-4-[3-ethoxy-4-(4-methoxybenzoxy)-benzylidenamino]-4,5-dihydro-1*H*-1,2,4-triazol-5-one (3a). Yield 3.73 g (94.23%). mp. 94 ºC. IR (KBr) ν 3173 (NH), 1730, 1697 (C=O), 1602 (C=N), 1256 (COO), 844 cm^{-1} (1,4 disubstituted benzenoid ring); ^{1}H NMR (200MHz, DMSO-d_6) δ 1.21 (t, 3H, OCH_2CH_3, *J*=7.52 Hz), 2.30 (s, 3H, CH_3), 3.88 (s, 3H, OCH_3), 4.11 (q, 2H, OCH_2CH_3, *J*=7.20 Hz), 7.13 (d, 2H, Ar-H, *J*=8.80 Hz), 7.35 (d, 1H, Ar-H, *J*=8.00 Hz), 7.49 (d, 1H, Ar-H, *J*=8.40 Hz), 7.61 (s, 1H, Ar-H), 8.09 (d, 2H, Ar-H, *J*=8.80 Hz), 9.73 (s, 1H, N=CH), 11.85 (s, 1H, NH); ^{13}C NMR (50MHz, DMSO-d_6) δ 11.60 (CH_3), 14.93 (OCH_2CH_3), 56.13 (OCH_3), 64.68 (OCH_2CH_3), 112.96, 114.82 (2C), 121.00, 121.06, 124.16, 132.51 (2C), 132.87, 142.76, 151.68, 163.97 (arom-C), 144.80 (triazole C_3), 151.16 (triazole C_5), 153.48 (N=CH), 164.24 (COO).

3-Ethyl-4-[3-ethoxy-4-(4-methoxybenzoxy)-benzylidenamino]-4,5-dihydro-1*H*-1,2,4-triazol-5-one (3b). Yield 3.99 g (97.50%). mp. 205 ºC. IR (KBr) ν 3174 (NH), 1733, 1696 (C=O), 1605 (C=N), 1256 (COO), 847 cm^{-1} (1,4 disubstituted benzenoid ring); ^{1}H NMR (200MHz, DMSO-d_6) δ 1.22 (t, 3H, OCH_2CH_3, *J*=6.80 Hz), 1.22 (t, 3H, CH_2CH_3, *J*=7.20 Hz), 2.71 (q, 2H, CH_2CH_3, *J*=7.42 Hz), 3.89 (s, 3H, OCH_3), 4.11 (s, 2H, OCH_2CH_3, *J*=6.80 Hz), 7.13 (d, 2H, Ar-H, *J*=8.80 Hz), 7.35 (d, 1H, Ar-H, *J*=8.80 Hz), 7.48 (d, 1H, Ar-H, *J*=8.40 Hz), 7.60 (s, 1H, Ar-H), 8.10 (d, 2H, Ar-H, *J*=8.80 Hz), 9.75 (s, 1H, N=CH), 11.90 (s, 1H, NH); ^{13}C NMR (50MHz, DMSO-d_6) δ 9.91 (CH_2CH_3), 14.39 (OCH_2CH_3), 18.49 (CH_2CH_3), 55.57 (OCH_3), 64.16 (OCH_2CH_3), 112.91, 114.25(2C), 120.33, 120.63, 123.62, 131.98 (2C), 132.43, 142.28, 151.17, 163.49 (arom-C), 148.02 (triazole C_3), 150.68 (triazole C_5), 152.78 (N=CH), 163.74 (COO).

3-*n*-Propyl-4-[3-ethoxy-4-(4-methoxybenzoxy)-benzylidenamino]-4,5-dihydro-1*H*-1,2,4-triazol-5-one (3c). Yield 4.07 g (96.00%). mp. 172 ºC. IR (KBr) ν 3165 (NH); 1724, 1697 (C=O), 1601 (C=N), 1254 (COO), 847 cm^{-1} (1,4 disubstituted benzenoid ring); ^{1}H NMR (200MHz, DMSO-d_6) δ 0.97 (t, 3H, $CH_2CH_2CH_3$, *J*=7.20 Hz), 1.22 (t, 3H, OCH_2CH_3, *J*=7.20 Hz), 1.71 (sext, 2H, $CH_2CH_2CH_3$, *J*=7.20 Hz), 2.67 (t, 2H, $CH_2CH_2CH_3$, *J*=7.20 Hz), 3.89 (s, 3H, OCH_3), 4.12 (s, 2H, OCH_2CH_3, *J*=7.20 Hz), 7.13 (d, 2H, Ar-H, *J*=8.40 Hz), 7.36 (d, 1H, Ar-H, *J*=8.00 Hz), 7.49 (d, 1H, Ar-H, *J*=8.40 Hz), 7.60 (s, 1H, Ar-H), 8.09 (d, 2H, Ar-H, *J*=8.80 Hz), 9.74 (s, 1H, N=CH), 11.89 (s, 1H, NH); ^{13}C NMR (50MHz, DMSO-d_6) δ 13.45 ($CH_2CH_2CH_3$), 14.36 (OCH_2CH_3), 18.91 ($CH_2CH_2CH_3$), 26.67 ($CH_2CH_2CH_3$), 55.56 (OCH_3), 64.11 (OCH_2CH_3), 112.91, 114.36 (2C), 120.25, 120.57, 123.64, 131.96 (2C), 132.40, 142.24, 151.56, 163.45 (arom-C), 146.88 (triazole C_3), 150.62 (triazole C_5), 152.82 (N=CH), 163.71 (COO).

THEORETICAL

The optimized molecular structures, Mulliken atomic charges, UV–Vis spectroscopic parameters, molecular electrostatic potential (MEP), vibrational frequencies, thermodynamic parameters and HOMO, LUMO energies of the compounds **3a-c** have been calculated by using DFT(B3LYP)/HF methods with 6-31G(d,p) basis set. All theoretical calculations were performed by using Gaussian 09W program and

GaussView program [28, 29]. IR absorption frequencies of analysed molecules were calculated by two methods. The veda4f program was used in defining IR data which were calculated theoretically [30].

RESULTS AND DISCUSSION

In this study, the structures of three new 3-alkyl-4-[3-ethoxy-4-(4-methoxybenzoxy)-benzylidenamino]-4,5-dihydro-1*H*-1,2,4-triazol-5-ones (**3a-c**) were carried out by using ^{1}H NMR, ^{13}C NMR and IR spectral data.

Molecular geometry

The optimized chemical structures and molecular of these compounds **3a-c** are shown in (Fig. 1). The calculated double N21=C1, N23=C3 bond lengths according to DFT/HF methods with 6-31G(d,p) basis sets of compounds **3a-c** were found as 1.30/1.27, 1.29/1.26 A^0 while the single N22-C1, N22-C2 and N20-C2 bond lengths in 1,2,4-triazol ring are calculated as 1.39/1.38, 1.42/1.38 and 1.37/1.35 A^0 respectively. The calculated double C2=O24 and C10=O27 bond lenghts were found as 1.22/1.20 and 1.21/1.18 A^0, respectively. Also the single bond lenghts of C6-O25, C10-O27, C14-O28, C7-O26, O25-O18 and O28-C17, were found as 1.37/1.35, 1.21/1.18, 1.36/1.36, 1.39/1.37, 1.44/1.42 and 1.42/1.41 A^0, respectively (Table 1). The largest C2-N22-N23 bond angles were found as 130.53/130.79, 130.44/130.73 and 130.42/130.70 ^{0} while the smallest N20-C2-N22 bond angles in 1,2,4-triazol ring were found as 101.17/102.00, 101.18/101.95 and 101.18/101.95 ^{0} for compounds **3a, 3b** and **3c**, respectively (Table 2).

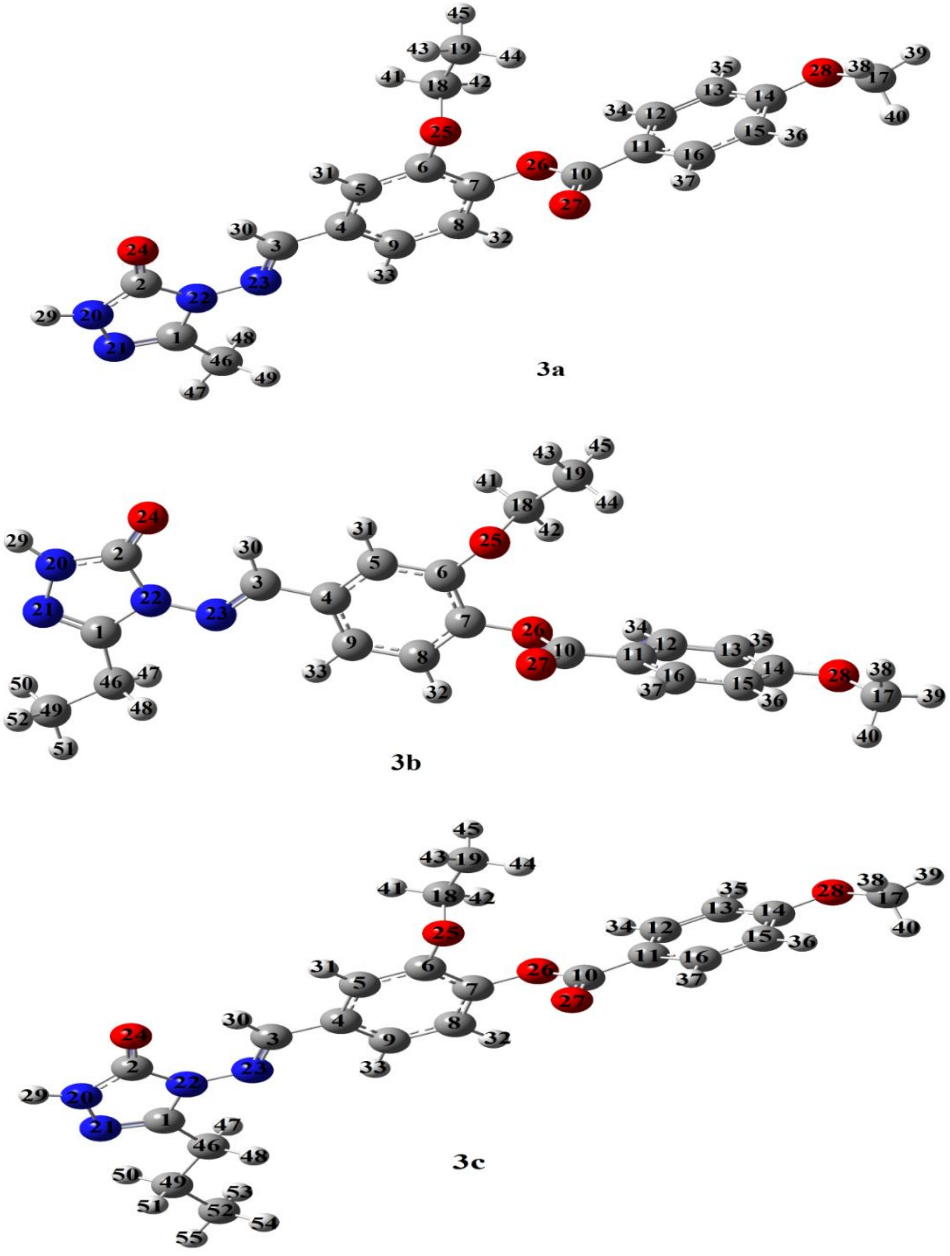

Fig. 1. Optimized molecular structure of compounds **3a-c** with DFT(B3LYP)/HF 6–31G(d,p) level

Table 1. The calculated bond lenghts of compounds **3a-c**

Bond Lenghts (A^0)	**B3LYP/HF (3a)**	**B3LYP/HF (3b)**	**B3LYP/HF (3c)**
C(1)-N(21)	1.30/1.27	1.30/1.27	1.30/1.27
C(1)-N(22)	1.39/1.38	1.39/1.38	1.39/1.38
C(1)-C(46)	1.49/1.49	1.49/1.49	1.49/1.49
N(20)-C(2)	1.37/1.35	1.37/1.35	1.37/1.35
C(2)-O(24)	1.22/1.20	1.22/1.20	1.22/1.20
C(2)-N(22)	1.42/1.38	1.42/1.38	1.42/1.38
N(20)-H(29)	1.00/0.99	1.00/0.99	1.00/0.99
N(20)-N(21)	1.38/1.37	1.38/1.37	1.38/1.37
N(22)-N(23)	1.37/1.37	1.37/1.37	1.37/1.37
N(23)-C(3)	1.29/1.26	1.29/1.26	1.29/1.26
C(3)-H(30)	1.09/1.08	1.09/1.08	1.09/1.08
C(3)-C(4)	1.47/1.48	1.47/1.48	1.47/1.48
C(4)-C(5)	1.40/1.39	1.40/1.39	1.40/1.39
C(4)-C(9)	1.41/1.39	1.41/1.39	1.41/1.39
C(5)-H(31)	1.09/1.08	1.09/1.08	1.09/1.08
C(5)-C(6)	1.39/1.38	1.39/1.38	1.39/1.38
C(6)-O(25)	1.37/1.35	1.37/1.35	1.37/1.35
O(25)-C(18)	1.44/1.42	1.44/1.42	1.44/1.42
C(18)-H(41)	1.09/1.08	1.09/1.08	1.09/1.08
C(18)-H(42)	1.09/1.08	1.09/1.08	1.09/1.08
C(18)-C(19)	1.52/1.51	1.52/1.51	1.52/1.51
C(19)-H(42)	1.09/1.08	1.09/1.08	1.09/1.08
C(19)-H(43)	1.09/1.08	1.09/1.08	1.09/1.08
C(19)-H(44)	1.09/1.08	1.09/1.08	1.09/1.08
C(6)-C(7)	1.40/1.38	1.40/1.38	1.40/1.38
C(7)-O(26)	1.39/1.37	1.39/1.37	1.39/1.37
C(7)-C(8)	1.39/1.38	1.39/1.38	1.39/1.38
C(8)-H(32)	1.08/1.07	1.08/1.07	1.08/1.07
C(8)-C(9)	1.39/1.38	1.39/1.38	1.39/1.38
C(9)-H(33)	1.08/1.07	1.08/1.07	1.08/1.07
O(26)-C(10)	1.39/1.34	1.39/1.34	1.39/1.34
C(10)-O(27)	1.21/1.18	1.21/1.18	1.21/1.18
C(10)-C(11)	1.48/1.48	1.48/1.48	1.48/1.48
C(11)-C(12)	1.40/1.39	1.40/1.39	1.40/1.39
C(11)-C(16)	1.40/1.39	1.40/1.39	1.40/1.39
C(12)-H(34)	1.08/1.07	1.08/1.07	1.08/1.07
C(12)-C(13)	1.39/1.38	1.39/1.38	1.39/1.38
C(13)-C(14)	1.41/1.38	1.41/1.38	1.41/1.38
C(13)-H(35)	1.09/1.07	1.09/1.07	1.09/1.07
C(14)-O(28)	1.36/1.36	1.36/1.36	1.36/1.36
C(14)-C(15)	1.40/1.39	1.40/1.39	1.40/1.39
O(28)-C(17)	1.42/1.41	1.42/1.41	1.42/1.41
C(17)-H(38)	1.09/1.09	1.09/1.08	1.09/1.08
C(17)-H(39)	1.09/1.09	1.09/1.08	1.09/1.08
C(17)-H(40)	1.09/1.09	1.09/1.08	1.09/1.08
C(15)-H(36)	1.08/1.07	1.08/1.07	1.08/1.07
C(15)-C(16)	1.39/1.38	1.39/1.38	1.39/1.38
C(16)-H(37)	1.08/1.07	1.08/1.07	1.08/1.07
C(46)-H(47)	1.09/1.08	1.09/1.08	1.09/1.08
C(46)-H(48)	1.09/1.08	1.09/1.08	1.09/1.08
C(46)-H(49)	1.09/1.08	-	-
C(46)-C(49)		1.53/1.53	1.53/1.53
C(49)-H(50)		1.09/1.08	1.09/1.08
C(49)-H(51)		1.09/1.08	1.09/1.08
C(49)-H(52)		1.09/1.08	-
C(49)-C(52)			1.53/1.53
C(52)-H(53)			1.09/1.09
C(52)-H(54)			1.09/1.09
C(52)-H(55)			1.09/1.09

Table 2. The calculated bond angles of compounds **3a-c**

Bond Angles (^{0})	**B3LYP/HF (3a)**	**B3LYP/HF (3b)**	**B3LYP/HF (3c)**
C(1)-N(21)-N(20)	104.48/104.96	104.59/105.12	104.60/105.03
C(1)-N(22)-N(23)	121.10/121.05	121.14/121.08	121.16/121.10
C(1)-N(22)-C(2)	108.37/108.12	108.42/108.18	108.43/108.19
N(21)-C(1)-N(22)	111.46/111.32	111.33/111.16	111.30/111.13
N(21)-N(20)-H(29)	120.43/120.62	120.46/121.02	120.47/121.01
N(21)-N(20)-C(2)	114.52/113.56	114.49/113.70	114.49/113.68
N(21)-C(1)-C(46)	125.16/125.45	125.66/126.06	125.72/126.18
H(29)-N(20)-C(2)	125.05/124.81	125.05/125.29	125.04/125.30
N(20)-C(2)-N(22)	101.17/102.00	101.18/101.95	101.18/101.95
N(20)-C(2)-O(24)	129.93/129.37	129.89/129.36	129.87/129.36
O(24)-C(2)-N(22)	128.90/128.63	128.93/128.69	128.94/128.69
C(2)-N(22)-N(23)	130.53/130.79	130.44/130.73	130.42/130.70
N(22)-N(23)-C(3)	118.73/119.69	118.77/119.81	118.75/119.82
N(23)-C(3)-H(30)	122.05/122.32	122.03/122.34	122.03/122.34
N(23)-C(3)-C(4)	120.04/120.30	120.05/120.28	120.08/120.27
H(30)-C(3)-C(4)	117.92/117.39	117.92/117.39	117.90/117.39
C(3)-C(4)-C(5)	118.32/118.15	118.31/118.16	118.29/118.17
C(3)-C(4)-C(9)	122.55/122.47	122.57/122.49	122.59/122.48
C(4)-C(5)-H(31)	120.71/120.71	120.70/120.84	120.71/120.84
C(4)-C(5)-C(6)	121.01/120.81	121.01/120.86	121.00/120.86
H(31)-C(5)-C(6)	118.28/118.70	118.29/118.30	118.29/118.30
C(5)-C(6)-O(25)	120.22/121.78	120.25/120.71	120.28/120.71
C(5)-C(6)-C(7)	118.88/118.96	118.89/118.95	118.90/118.95
O(25)-C(6)-C(7)	120.86/119.75	120.82/120.32	120.78/120.32
C(6)-O(25)-C(18)	115.16/116.21	115.11/116.05	115.10/116.05
O(25)-C(18)-H(41)	109.68/109.56	109.68/109.58	109.68/109.58
O(25)-C(18)-H(42)	109.20/109.45	109.20/109.37	109.20/109.37
O(25)-C(18)-C(19)	107.69/107.89	107.69/107.83	107.69/107.83
H(41)-C(18)-H(42)	108.00/107.93	107.98/108.01	107.96/108.01
H(41)-C(18)-C(19)	111.12/111.06	111.11/110.10	111.11/111.09
H(42)-C(18)-C(19)	111.16/110.94	111.17/111.05	111.19/111.05
C(18)-C(19)-H(43)	110.62/110.45	110.63/110.51	110.63/110.51
C(18)-C(19)-C(44)	110.11/110.18	110.12/110.15	110.54/110.15
C(18)-C(19)-C(45)	110.56/110.42	110.55/110.41	110.13/110.41
H(43)-C(19)-H(44)	108.56/108.60	108.55/108.64	108.37/108.64
H(43)-C(19)-H(45)	108.37/108.41	108.37/108.43	108.55/108.43
H(44)-C(19)-H(45)	108.56/108.74	108.56/108.65	108.57/108.65
C(6)-C(7)-O(26)	119.72/119.27	119.72/119.34	119.68/119.34
C(6)-C(7)-C(8)	120.75/120.90	120.75/120.86	120.75/120.86
C(7)-C(8)-H(32)	118.72/118.97	118.72/118.94	118.72/118.94
C(7)-C(8)-C(9)	120.05/119.93	120.04/119.97	120.04/119.97
H(32)-C(8)-C(9)	121.24/121.10	121.24/121.09	121.24/121.09
C(8)-C(9)-H(33)	120.62/120.32	120.62/120.31	120.62/120.32
C(8)-C(9)-C(4)	120.18/120.02	120.18/120.01	120.19/120.01
H(33)-C(9)-C(4)	119.20/119.67	119.20/119.68	119.19/119.67
C(9)-C(4)-C(5)	119.13/119.38	119.12/119.35	119.12/119.35
C(7)-O(26)-C(10)	117.45/118.66	117.37/118.65	117.30/118.65
O(26)-C(10)-O(27)	122.81/122.96	122.80/122.86	122.78/122.86
O(26)-C(10)-C(11)	111.47/112.29	111.50/112.16	111.54/112.16
O(27)-C(10)-C(11)	125.72/124.75	125.69/124.98	125.67/125.98
C(10)-C(11)-C(16)	117.82/117.86	117.79/118.10	117.76/118.09
C(10)-C(11)-C(12)	123.17/122.57	123.20/122.96	123.23/122.96
C(11)-C(12)-H(34)	119.63/119.89	119.62/119.85	118.47/119.85
C(11)-C(12)-C(13)	120.42/120.21	120.42/120.49	121.09/120.49
H(34)-C(12)-C(13)	119.95/119.90	119.96/119.66	120.44/119.66
C(12)-C(13)-C(14)	120.18/119.74	120.18/120.12	119.43/120.12
C(13)-C(14)-O(28)	115.55/119.54	115.56/115.67	115.56/115.67

C(14)-O(28)-C(17)	118.61/120.81	118.60/120.17	118.59/120.17
O(28)-C(17)-H(38)	111.55/111.19	111.54/111.37	111.54/111.37
O(28)-C(17)-H(39)	105.88/106.77	105.88/106.13	105.88/106.13
O(28)-C(17)-H(40)	111.52/110.98	111.51/111.37	111.51/111.37
H(38)-C(17)-H(39)	109.27/109.01	109.28/109.22	109.30/109.22
H(38)-C(17)-H(40)	109.26/109.40	109.26/109.46	109.28/109.46
H(39)-C(18)-H(40)	109.29/109.44	109.29/109.22	109.30/109.21
C(13)-C(14)-C(15)	119.87/119.58	119.43/119.92	119.87/119.34
C(14)-C(15)-H(36)	121.04/119.38	121.03/121.30	121.03/121.30
C(14)-C(15)-C(16)	119.43/119.58	119.43/119.34	119.43/119.34
H(36)-C(15)-C(16)	119.53/121.04	119.53/119.36	119.54/119.36
C(15)-C(16)-H(37)	120.43/120.63	120.44/119.95	120.44/119.95
H(37)-C(16)-C(11)	118.49/118.96	118.48/118.87	118.47/118.87
C(15)-C(16)-C(11)	121.08/120.41	121.09/121.18	121.09/121.18
C(16)-C(11)-C(12)	119.02/119.58	119.01/118.94	119.01/118.94
C(1)-C(46)-H(47)	110.98/110.54	108.34/108.08	108.48/108.08
C(1)-C(46)-H(48)	110.96/110.51	108.33/108.07	108.44/108.08
C(1)-C(46)-H(49)	108.66/108.56	-	-
H(47)-C(46)-H(49)	109.45/109.79	-	-
H(48)-C(46)-H(49)	109.43/109.66	-	-
H(47)-C(46)-H(48)	107.34/107.68	105.22/105.94	105.16/105.87
C(1)-C(46)-C(49)	-	112.98/112.88	113.36/113.24
C(46)-C(49)-H(50)	-	111.15/111.21	109.22/109.39
C(46)-C(49)-H(51)	-	111.19/111.22	109.19/109.39
C(46)-C(49)-H(52)	-	109.10/109.66	-
H(50)-C(49)-H(52)	-	108.48/108.42	-
H(51)-C(49)-H(52)	-	108.45/108.43	-
H(50)-C(49)-H(51)	-	107.51/107.81	105.91/106.31
C(46)-C(49)-C(52)	-	-	112.06/111.74
H(50)-C(49)-C(52)	-	-	110.14/110.81
H(51)-C(49)-C(52)	-	-	110.14/110.81
C(49)-C(52)-H(53)	-	-	111.04/111.37
C(49)-C(52)-H(54)	-	-	111.39/111.32
C(49)-C(52)-H(55)	-	-	111.40/111.52
H(53)-C(52)-H(54)	-	-	107.54/107.74
H(53)-C(52)-H(55)	-	-	107.64/107.69
H(54)-C(52)-H(55)	-	-	107.54/107.74

Atomic charges and dipole moments

The electronegative N20, N21, N22, N23, O24, O25, O26, O27, O28 atoms have negative atomic charge values. The C1, C2, C3, C6, C7, C10, C14, C18 atoms surrounded with electronegative atoms have positive atomic charge values for compounds **3a, 3b** and **3c**. The Mulliken atomic charges of these atoms given in Table **3**. The C1 atom which is surrounded with two electronegative atoms (N, N), C2 atom surrrounded with three electronegative atoms (N, N, O), C10 atom surrrounded with two electronegative atoms (O, O), C3 atom surrrounded with one electronegative atom (N) and C6, C7, C14 and C18 atoms surrrounded with one electronegative atom (O) have positive atomic charge values. The C1 atom which is surrounded with two electronegative atoms (N, N), C2 atom surrrounded with three electronegative atoms (N, N, O) have the highest positive atomic charge values. All hydrogen atoms of these compounds **3a, 3b** and **3c** have positive atomic charge values. Total energy values and dipole moments of above mentioned compounds (**3a-c**) were calculateted by using B3LYP/HF 6-31G(d,p) methods. The calculated dipole moment and energy values are given in Table **4** and **5.**

Table 3. Mulliken atomic charges of compounds **3a-c**

Comp. 3a Atoms	DFT/HF	Comp. 3b Atoms	DFT/HF	Comp. 3c Atoms	DFT/HF
C1	0.53/0.50	**C1**	0.54/0.61	**C1**	0.54/0.61
C2	0.82/0.88	**C2**	0.82/1.05	**C2**	0.82/1.05
C3	0.12/0.18	**C3**	0.12/0.18	**C3**	0.12/0.18
C4	0.09/-0.08	**C4**	0.08/-0.08	**C4**	0.09/-0.08
C5	-0.17/-0.17	**C5**	-0.17/-0.17	**C5**	-0.17/-0.17
C6	0.33/0.36	**C6**	0.33/0.38	**C6**	0.33/0.38
C7	0.32/0.36	**C7**	0.32/0.36	**C7**	0.32/0.36
C8	-0.11/-0.12	**C8**	-0.11/-0.15	**C8**	-0.11/-0.15
C9	-0.11/-0.14	**C9**	-0.11/-0.13	**C9**	-0.11/-0.13
C10	0.60/0.86	**C10**	0.60/0.86	**C10**	0.60/0.86
C11	0.01/-0.18	**C11**	0.01/-0.23	**C11**	0.01/-0.23
C12	-0.10/-0.11	**C12**	-0.10/-0.09	**C12**	-0.10/-0.09
C13	-0.12/-0.18	**C13**	-0.12/-0.20	**C13**	-0.12/-0.20
C14	0.36/0.37	**C14**	0.36/0.44	**C14**	0.36/0.44
C15	-0.14/-0.18	**C15**	-0.14/-0.24	**C15**	-0.14/-0.24
C16	-0.11/-0.10	**C16**	-0.11/-0.09	**C16**	-0.11/-0.09
C17	-0.08/-0.02	**C17**	-0.08/-0.04	**C17**	-0.08/-0.04
C18	0.06/0.06	**C18**	0.06/0.11	**C18**	0.06/0.11
C19	-0.34/-0.34	**C19**	-0.33/-0.35	**C19**	-0.34/-0.35
N20	-0.44/-0.46	**N20**	-0.43/-0.56	**N20**	-0.43/-0.56
N21	-0.36/-0.37	**N21**	-0.35/-0.36	**N21**	-0.35/-0.36
N22	-0.41/-0.48	**N22**	-0.42/-0.63	**N22**	-0.43/-0.64
N23	-0.33/-0.38	**N23**	-0.33/-0.33	**N23**	-0.32/-0.33
O24	-0.54/-0.61	**O24**	-0.54/-0.66	**O24**	-0.54/-0.66
O25	-0.54/-0.69	**O25**	-0.54/-0.69	**O25**	-0.54/-0.69
O26	-0.57/-0.77	**O26**	-0.57/-0.72	**O26**	-0.57/-0.72
O27	-0.47/-0.58	**O27**	-0.47/-0.56	**O27**	-0.47/-0.56
O28	-0.51/-0.68	**O28**	-0.51/-0.66	**O28**	-0.51/-0.66
H29	0.29/0.33	**H29**	0.29/034	**H29**	0.29/0.34
H30	0.16/0.25	**H30**	0.16/0.23	**H30**	0.16/0.23
H31	0.11/0.19	**H31**	0.11/0.18	**H31**	0.11/0.18
H32	0.10/0.19	**H32**	0.10/0.18	**H32**	0.10/0.18
H33	0.11/0.18	**H33**	0.11/0.18	**H33**	0.11/0.18
H34	0.11/0.19	**H34**	0.11/0.18	**H34**	0.11/0.18
H35	0.10/0.18	**H35**	0.11/0.17	**H35**	0.10/0.19
H36	0.10/0.18	**H36**	0.10/0.16	**H36**	0.10/0.17
H37	0.12/0.21	**H37**	0.12/0.20	**H37**	0.12/0.20
H38	0.12/0.11	**H38**	0.12/0.12	**H38**	0.12/0.20
H39	0.13/0.14	**H39**	0.13/0.15	**H39**	0.13/0.15
H40	0.12/0.11	**H40**	0.12/0.12	**H40**	0.12/0.12
H41	0.09/0.10	**H41**	0.09/0.11	**H41**	0.09/0.10
H42	0.10/0.10	**H42**	0.10/0.11	**H42**	0.10/0.11
H43	0.13/0.13	**H43**	0.13/0.14	**H43**	0.13/0.14
H44	0.11/0.12	**H44**	0.11/0.13	**H44**	0.11/0.11
H45	0.12/0.10	**H45**	0.12/0.11	**H45**	0.12/0.13
C46	-0.36/-0.35	**C46**	-0.23/-0.25	**C46**	-0.22/-0.24
H47	014/0.17	**H47**	0.13/0.16	**H47**	0.13/0.15
H48	0.14/0.16	**H48**	0.13/0.16	**H48**	0.13/0.15
H49	0.14/0.16	**C49**	-0.32/-0.34	**C49**	-0.18/-0.22
		H50	0.12/0.14	**H50**	0.11/0.13
		H51	0.10/0.12	**H51**	0.10/0.13
		H52	0.13/0.14	**C52**	-0.32/-0.34
				H43	0.10/0.11
				H44	0.10/0.11
				H45	0.11/0.12

Table 4. The calculated dipole moment values of compounds **3a-c**

	Dipole Moment	μ_x	μ_y	μ_z	μ_{Toplam}
3a	**B3LYP**	4.2668	-1.0725	-1.9183	4.4779
	HF	2.8429	0.5341	-2.4618	3.7984
3b	**B3LYP**	4.0357	-1.4042	-1.8976	4.6754
	HF	3.7971	-1.5293	-2.1154	4.6078
3c	**B3LYP**	3.8611	-1.7072	-1.8355	4.6035
	HF	3.6058	-1.8493	-2.0616	4.5466

Table 5. The total energy of the compounds **3a-c**

	Energy	**B3LYP**	**HF**
3a	**(a.u.)**	-1369.30	-1361.12
3b	**(a.u.)**	-1408.61	-1400.17
3c	**(a.u.)**	-1447.93	-1439.20

Vibrational frequencies

3-(methyl/ethyl/*n*-propyl)-4-[3-ethoxy-4-(4-methoxybenzoxy)-benzylidenamino]-4,5-dihydro-1*H*-1,2,4-triazol-5-ones (**3a-c**) have 49, 52 and 55 atoms. The vibrational numbers of these molecules **3a-c** are 141, 150 and 159. The observed and calculated vibrational frequencies for compund **3a, 3b** and **3c** are summarized (Table 6) (Fig. 2).

Table 6. The experimental and calculated frequencies values of compounds **3a-c**

Assignment	**Experimental**			**Scaled B3LYP**			**Scaled HF**		
	3a	**3b**	**3c**	**3a**	**3b**	**3c**	**3a**	**3b**	**3c**
ν NH	3173	3174	3166	3557	3557	3557	3552	3557	3557
ν =CH	3065	3067	3072	3044	3053	3053	3024	3024	3024
ν C=O	1730	1733	1724	1755	1755	1755	1878	1808	1808
ν C=O	1697	1696	1697	1753	1753	1752	1855	1773	1773
ν C=C	1602	1605	1602	1601	1601	1601	1714	1682	1681
ν C=N	1578	1594	1578	1613	1611	1611	1774	1714	1714
δ COO	1256	1256	1254	1252	1251	1251	1271	1270	1262

ν, stretching; δ, bending; δ_s, scissoring; ρ, rocking; γ, out-of-plane bending; τ, torsion

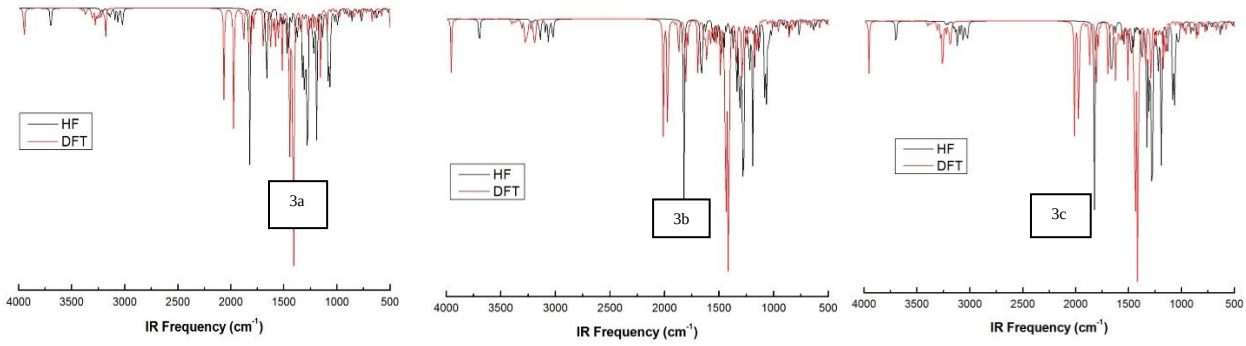

Fig. 2. IR spectrum simulated DFT/HF 6-31G(d,p) level of compounds **3a-c**

^{1}H-^{13}C-NMR chemical shifts and regression analyses

The ^{1}H-^{13}C NMR chemical shifts in gase phase and in DMSO solvent of the title compounds **3a-c** have been calculated by using the DFT(B3LYP/HF methods with 6-31G(d,p) basis set. The R^2 values of compounds **3a-c** were evaluated and ^{1}H and ^{13}C NMR chemical shift values of the compounds **3a-c** were plotted graphs. Experimental and theoretical between ^{1}H-,^{13}C-NMR chemical shifts ratios of compounds **3a-c** were observed a linear correlation except for NH proton by R^2 because N-H proton of triazole ring (namely 4,5-dihydro-1*H*-1,2,4-triazol-5-one) was displayed the acidic character. The calculated ^{1}H-,^{13}C- NMR chemical shifts values for the mentioned compounds **3a-c** are best agreement with the experimental values (Fig. 3).

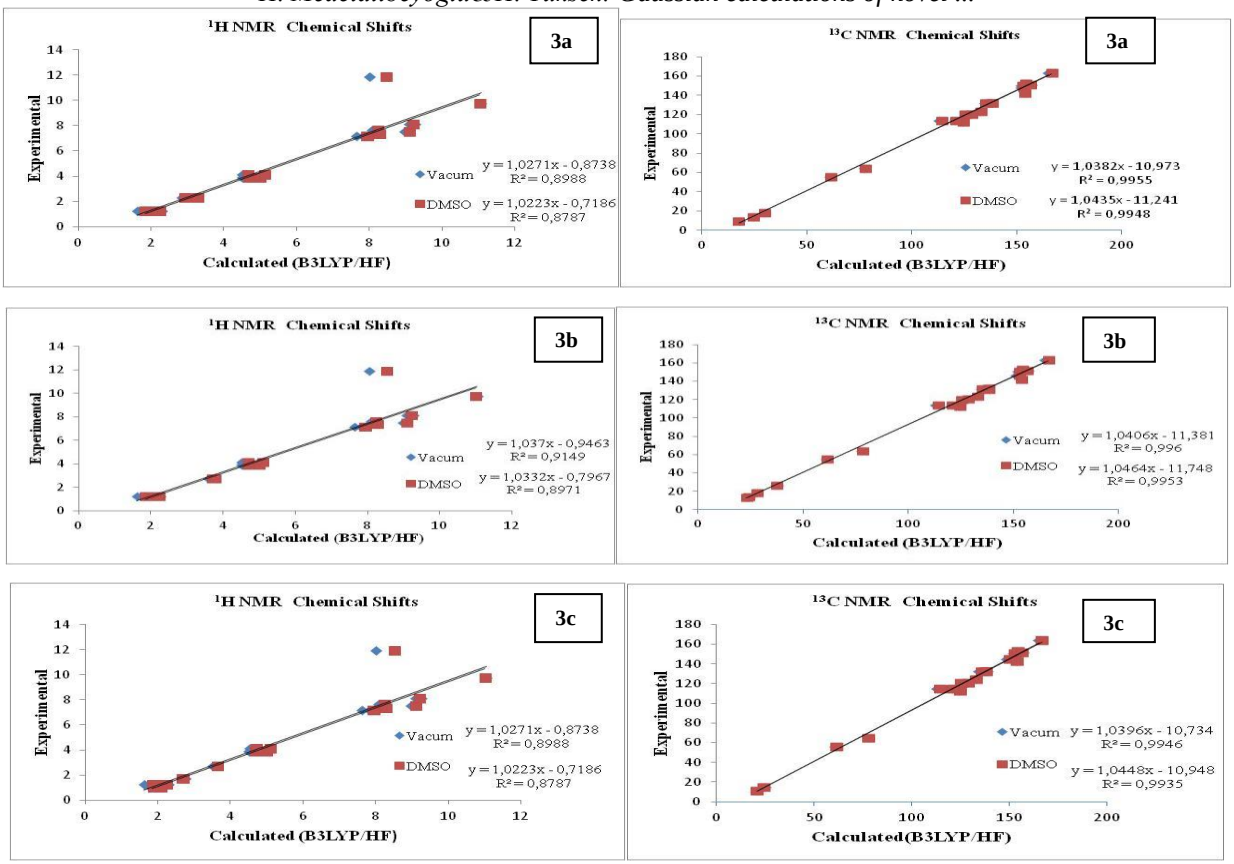

Fig. 3. The correlation graphics for ^{13}C-NMR/^{13}C-NMR (DMSO), ^{1}H-NMR/^{1}H-NMR (DMSO), chemical shifts of compounds **3a-c**

UV-vis. spectroscopy, molecular electrostatic potential (MEP) and HOMO-LUMO analyses

The oscillator strengths (*f*), absorption wavelengths (λ) and excitation energies of UV–Vis electron absorption spectroscopy of the title molecules **3a-c** have been calculated in ethanol by using DFT(B3LYP)/HF methods with 6-31G(d,p) basis set that presented in Fig. 4 and Table 6. Futhermore, the highest occupied molecular orbital (HOMO) and the lowest unoccupied molecular orbital (LUMO) have been simulated for compounds **3a-c** have been determined. In our study, HOMO and LUMO energies and their 3D plots of the compounds **3a-c** are shown in Fig. 5. The molecular electrostatic potential (MEP) of these compounds **3a-c** have been performed (Fig. 6).

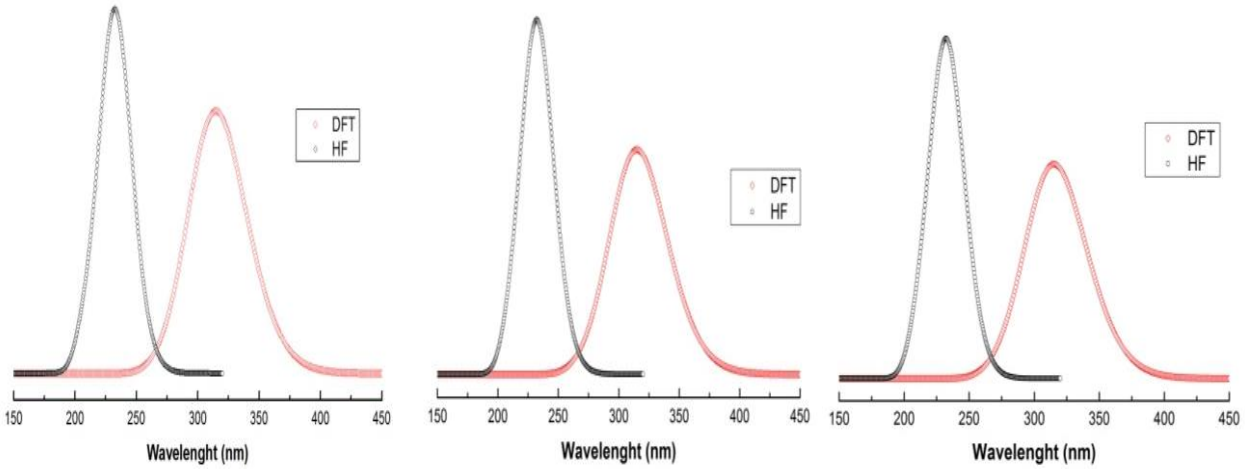

Fig. 4. UV-Visible spectra simulated with DFT/B3LYP/6-31G(d,p) and HF /6-31G(d,p) levels of compounds **3a-c.**

Table 6. The calculated absorption wavelength (λ), excitation energies and oscillator strengths (*f*) of compounds **3a-c**

Comp.	λ (nm)	Excitation energy (eV)	*f* (oscillator strength)
3a	315.17/233.52	3.9240/5.3095	0.5804/0.8013
	287.23/213.28	4.3165/5.8131	0.0353/0.0718
	282.90/213.03	4.3826/5.8201	0.0309/0.0936
3b	316.25/233.93	3.9205/5.3001	0.5772/0.8695
	286.97/216.59	4.3204/5.7243	0.0389/0.2054
	283.15/213.05	4.3788/5.7373	0.086/0.0184
3c	316.37/233.94	3.9190/5.2999	0.5738/0.8679
	286.93/216.58	4.3211/5.7245	0.0391/0.2059
	283.13/213.04	4.3791/5.8197	0.0279/0.0185

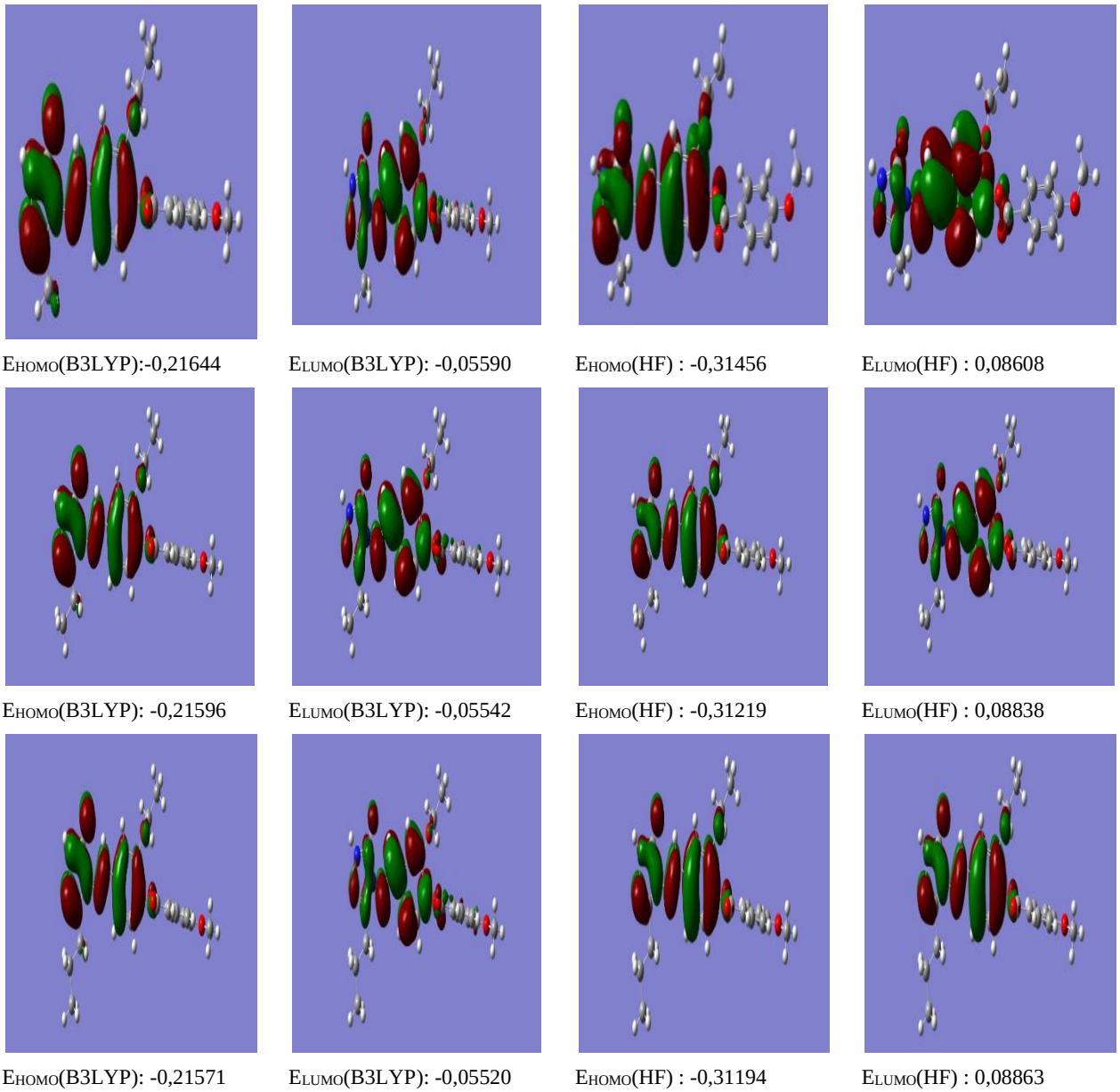

Fig. 5. 3D plots of HOMO and LUMO energies (Hatree) of compounds **3a-c** at the B3LYP/HF 6-31G(d,p) level

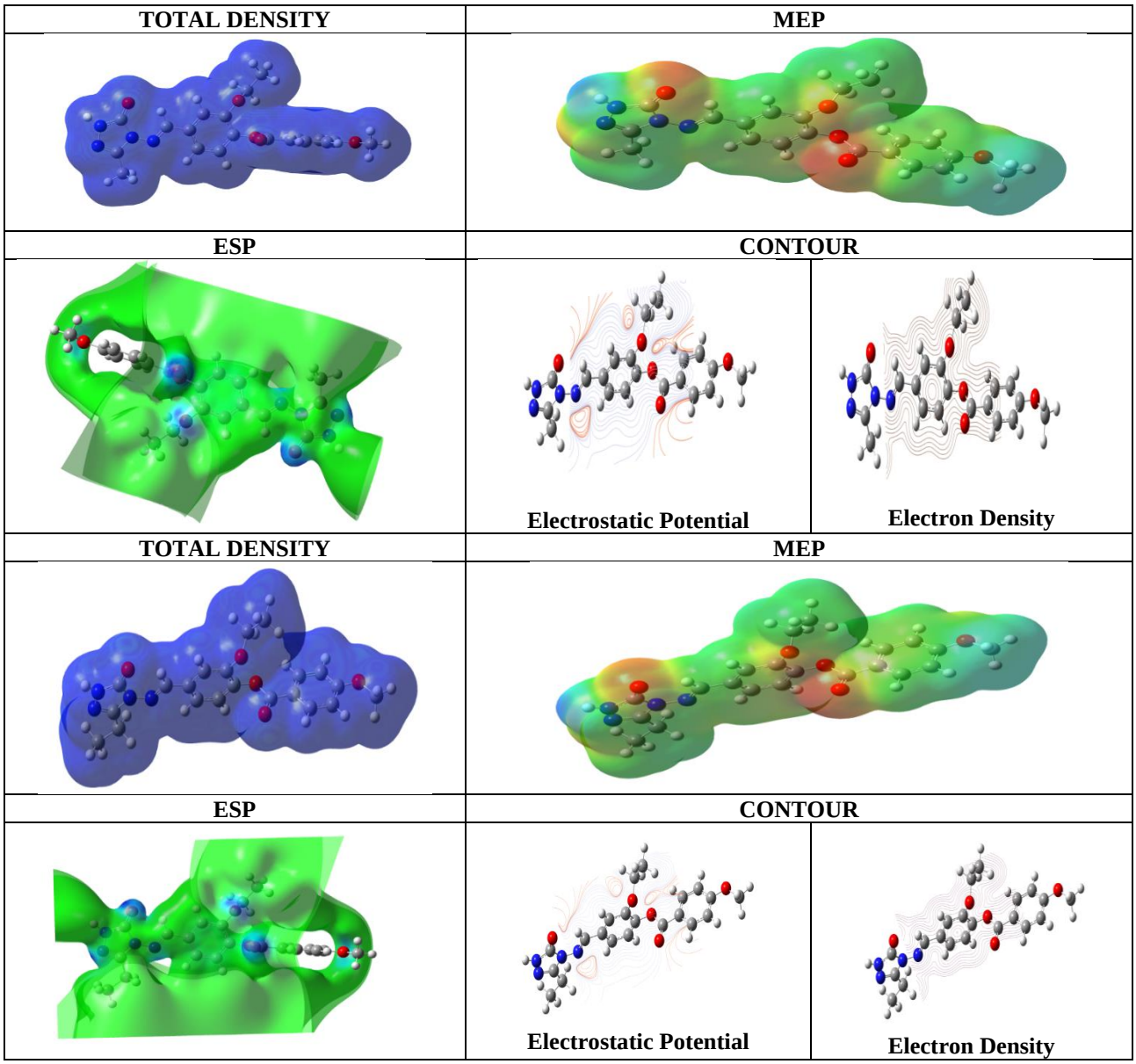

Fig. 6. The calculated molecular surfaces for compounds **3a-c**

CONCLUSION

The molecular structure, molecular electrostatic potential (MEP), vibrational wavenumbers, HOMO-LUMO, Mulliken atomic charges, electronic absorption maximum wavelenghts, and thermodynamic parameters of the synthesized new 3-(methyl/ethyl/*n*-propyl)-4-[3-ethoxy-4-(4-methoxy-benzoxy)-benzylidenamino]-4,5-dihydro-1*H*-1,2,4-triazol-5-ones (**3a-c**) have been calculated by using DFT(B3LYP)/HF 6-31G(d,p) levels. The theoretical spectral values were seen as compatible with experimental values.

REFERENCES

1. G. Turan-Zitouni, Z.A. Kaplancikli, M.T. Yildiz, P. Chevallet, D. Kaya, *Eur. J. Med. Chem*.,**40**,607 (2005).
2. H. Bayrak, A. Demirbas, N. Demirbas, S.A. Karaoglu, *Eur. J. Med. Chem*., **45**, 4726 (2010).
3. K. Sancak, Y. Unver, C. Kazak, E. Dugdu, B. Arslan, *Turk. J. Chem*., **34**, 771 (2010).
4. A.A. Ikizler, A. Ikizler, H. Yüksek, M. Serdar, *Modelling, Measurement & Control C, AMSE press*, **57**, 25 (1998).
5. A.I. Hashem, A.S.A.Youssef, K.A. Kandeel, W.S.I. Abou-Elmalgd, *Eur. J. Med. Chem*., **42**, 934 (2007).
6. N.U. Guzeldemirci, O. Kucukbasmaci, *Eur. J. Med. Chem*., **45**, 63, (2010).
7. S.P. Aytac, B. Tozkoparan, F.B. Kaynak, G. Aktay, O. Goktas, S. Unuvar, *Eur. J. Med. Chem*., **44**, 4528 (2009).
8. B. Tozkoparan, E. Kupeli, E. Yesilada, M. Ertan, *Bioorgan. Med. Chem*., **15**, 1808 (2007).
9. M. Alkan, H. Yuksek, F. Islamoglu, S. Bahceci, M. Calapoglu, M. Elmastas, H. Aksit, M. Ozdemir, *Molecules*, **12**, 1805 (2007).
10. Ö.G. Kol, H. Yüksek, *Eur–J. Chem*., **7**, 123 (2010).
11. H. Yüksek, M. Küçük, M. Alkan, Ş. Bahçeci, S. Kolaylı, Z. Ocak, U. Ocak, E. Şahinbaş, M. Ocak, *Asian J. Chem*., **18**, 539 (2006).
12. H. Yüksek, S. Kolaylı, M. Küçük, M.O. Yüksek, U. Ocak, E. Şahinbaş, E. Sivrikaya, M. Ocak, *Indian J. Chem.*, **45B**, 715 (2006).
13. A.A. Ikizler, H. Yüksek, *Coll. Czech. Chem. Commun.*, **59**, 731 (1994).
14. Ş. Bahçeci, H.Yüksek, Z. Ocak, A. Azaklı, M. Alkan, M. Ozdemir, *Coll.. Czech. Chem. Commun.*, **67**, 1215 (2002).
15. Ş. Bahçeci, H. Yüksek, Z. Ocak, C. Köksal, M. Ozdemir, *Acta Chim. Slov.*, **49**, 783 (2002).
16. H. Yüksek, O. Üçüncü, M. Alkan, Z. Ocak, Ş. Bahçeci, M. Özdemir, *Molecules*, **10**, 961 (2005).
17. H. Yüksek, Z. Ocak, M. Özdemir, M. Ocak, M. Bekar, M. Aksoy, *Indian J. Heterocyc. Chem.*, **13**, 49 (2003).
18. H. Yüksek, Ş. Bahçeci, Z. Ocak, M. Alkan, B. Ermiş, T.Mutlu, M. Ocak, M. Özdemir, *Indian J. Heterocyc. Chem.*, **13,** 369 (2004).
19. H. Yüksek, Ş. Bahçeci, Z. Ocak, M. Özdemir, M. Ocak, B. Ermiş, T. Mutlu, *Asian J. Chem.*, **17**, 195 (2005).
20. H.Yüksek, Ö. Gürsoy, İ. Çakmak, M. Alkan, *Magn. Reson. Chem.*, **43**, 585 (2005).
21. H.Yüksek, İ. Çakmak, S. Sadi, M. Alkan, *Int. J. Mol. Sci.* **6**, 219 (2005).
22. A.A. Ikizler, H. Yüksek, *Org. Prep. Proc. Int.*, **25**, 99 (1993).
23. H. Gökçe, S. Bahçeli, O. Akyıldırım, H. Yüksek, Ö. Gürsoy-Kol, *Lett. Org. Chem.*, **10**, 395 (2013).
24. H. Gökçe, O. Akyıldırım, S. Bahçeli, H. Yüksek, Ö. Gürsoy-Kol, *J. Mol. Struct.*, **1056-1057**, 273 (2014).
25. H. Yüksek, İ. Çakmak, S. Sadi, M. Alkan, H. Baykara, *Int. J. Mol. Sci.*, **6**, 219 (2005).
26. A.A. Ikizler, H. Yüksek, *Org. Prep. Proc. Int.*, **25**, 99 (1993).
27. A.A. Ikizler, R. Un, *Chim. Acta Turc.*, 1979, **7**, 269, [Chem. Abstr., 94, 15645d], (1991).
28. M.J. Frisch, G.W. Trucks, H.B. Schlegel, G.E. Scuseria, M.A. Robb, J.R. Cheeseman, G. Scalmani, V. Barone, B. Mennucci, G.A. Petersson, H. Nakatsuji, M. Caricato, X. Li, H.P. Hratchian, A.F. Izmaylov, J. Bloino, G. Zheng, J.L. Sonnenberg, M. Hada, M. Ehara, K. Toyota, R. Fukuda, J. Hasegawa, M. Ishida, T. Nakajima, Y. Honda, O. Kitao, H. Nakai, T. Vreven, J.A. Montgomery, T. Jr.Vreven, J.E. Peralta, F. Ogliaro, M. Bearpark, J.J. Heyd, E. Brothers, N. Kudin, V.N. Staroverov, R. Kobayashi, J. Normand, K. Raghavachari, A. Rendell, J.C. Burant, S.S. Iyengar, J. Tomasi, M. Cossi, N. Rega, J.M. Millam, M. Klene, J.E. Knox, J.B. Cross, V. Bakken, C. Adamo, J. Jaramillo, R. Gomperts, R.E. Stratmann, O. Yazyev, A.J. Austin, R. Cammi, C. Pomelli, J.W. Ochterski, L.R. Martin, K. Morokuma, V.G. Zakrzewski, G.A. Voth, P. Salvador, J.J. Dannenberg, S. Dapprich, A.D. Daniels, O. Farkas, J.B. Foresman, J.V. Ortiz, J. Cioslowski, and D.J. Fox, *Gaussian Inc.*, Wallingford, CT, (2009).
29. A. Frisch, A.B. Nielson, & A.J. Holder, Gaussvıew User Manual, Gaussian Inc., Wallingford, CT, (2003).
30. M.H. Jamróz, Vibrational Energy Distribution Analysis: VEDA 4 program, Warsaw (2004).

Bulgarian Chemical Communications, Volume 49, Issue I (pp. 90 – 97) 2017

Pretreatments and temperature effects on the drying kinetics of peas

I. Doymaz, I. Kucuk*

Department of Chemical Engineering, Yildiz Technical University, 34210 Esenler, Istanbul, Turkey

Submitted May 22, 2017; Revised September 1, 2017

In this study, peas were dried in convection dryer at a temperature range of 55-75°C with a constant air velocity of 2 m/s. The peas were pre-treated with ethyl oleate and blanched with hot water at 85°C before drying. Drying process continued until sample moisture fell down to 0.11 kg water/kg dry matter. The blanched samples dried faster than the other pre-treatment and control conditions. Besides, drying rate increased with increasing temperature. The experimental results illustrated the absence of constant-rate drying period and drying took place in the falling-rate period. Four well-known mathematical models were used to predict drying kinetics by nonlinear analysis of regression. Midilli and Kucuk model best fitted the experimental data for the whole range of temperatures. The moisture diffusivity coefficient at each temperature was determined by Fick's second law of diffusion, in which their value varied from 7.66×10^{-11} m^2/s to 2.44×10^{-10} over the mentioned temperature range. The dependence of effective diffusivity coefficient on temperature was expressed by an Arrhenius type equation. The calculated values of the activation energy of moisture diffusion were 36.75, 38.11 and 43.25 kJ/mol for pre-treated with ethyl oleate, blanched samples and control samples, respectively.

Keywords: Activation energy, Drying, Effective diffusivity, Pea, Pre-treatments.

INTRODUCTION

Pea (*Pisum sativum* L.) is one of the most commonly grown food legumes in the world. The worldwide pea production in 2014 was 17426421 tons. The major producer countries include China, India, USA, France and Egypt. According to Food and Agriculture Organization of United Nations (FAO) agriculture data, Pea is grown on 15300 ha areas in Turkey with a production of 105279 tons in 2014 [1]. Pea has been widely used in the human diet for a long time due to it being an excellent source of protein, vitamins, minerals and other nutrients, while being low in fat, high in fiber and containing no cholesterol [2, 3]. Because of its high moisture content, drying is one of alternative method of pea preservation. Dried peas are gaining popularity because they offer the advantage of longer self life, palatability and convenience during transport and handling [4]. Like other legumes, dried peas can be used in meals or soups [5].

Drying is an established method of food processing. It is used to extend the self-life of vegetables and to reduce the mass transportation. The low water activity of the products prevents growth of microorganisms, enzymatic reactions, and other deteriorative reactions [6]. Hot-air drying is the most widely used method for preservation of food in processing industry. The applied drying conditions and pre-treatments highly influence the resulting physical, chemical, microbial, functional and organoleptic properties of the agricultural products. Sodium and potassium hydroxide, sodium bicarbonate, potassium meta bisulphate, potassium carbonate, methyl and ethyl ester emulsions, ascorbic and citric acids, the most common and commercially used some pre-treatments [7-9]. Blanching is one of the pre-treatment methods that are used to stop some physiological processes before drying vegetables and fruits. It helps to inactivate enzymes that leads to some quality degradations and improves the acceptability of the final products. Moreover, it can accelerate drying rate and prevent quality deterioration by expelling intercellular air from the tissues and softening the texture [10].

In this study, the main objectives were to investigate the effect of pre-treatment and air temperature on the drying time, fit the experimental data to four drying models, and compute effective moisture diffusivity and activation energy.

EXPERIMENTAL

Materials and methods

Good quality fresh green peas (*Pisum sativum*) were purchased from a local market in Istanbul, Turkey. The damaged, immature, and dried pods were removed manually by visual inspection. The pea pods were shelled manually. The average diameter of the peas was 0.7±0.1 cm. Pea samples were divided in three sample groups. One sample group were blanched (BLANCH) in water at 85±1°C for 1 min. Other one sample group was dipped in solution of 2% ethyl oleate and 3% potassium carbonate (EO) at 20±1°C for 1 min. Another sample group dried as a control group (Control).

*) To whom all correspondence should be sent:
E-mail: kucuk@yildiz.edu.tr

The initial moisture content of peas was determined using a standard method [11], by vacuum drying at 70°C for 24 h over a magnesium sulphate desiccant. This was repeated three times to obtain a reasonable average. The initial moisture content of the samples was found as %77.25, wet basis (3.494 kg water/kg dry matter).

DRYING PROCEDURE

Drying experiments were performed in a cabinet type dryer (API & PASILAC Limited of Carlisle, Cumbria, UK.), and described by Doymaz [12]. Samples dried with air of 55, 65 and 75°C, and a constant air velocity of 2 m/s. The experiments were conducted with about 60±0.5 g of peas. The moisture losses were recorded at 15 minute intervals during the drying process, using a digital balance (Mettler-Toledo BB3000, AG, Grefensee, Switzerland) with a sensitivity of 0.1 g. Drying process was carried out until a moisture content of about 0.11±0.02 kg water/kg dry matter. The dried product was cooled, to normal temperature in a desiccator containing silica gel and then packed in polyethylene bags, which were then heat-sealed and stored in incubators at ambient temperature. The experiments were repeated twice and the average of the moisture ratio at each value was used for the drawing of the drying curves.

Mathematical modeling and data analysis

The moisture ratio (*MR*) of the pea was calculated using the following equation:

$$MR = \frac{M_t - M_e}{M_0 - M_e} \tag{1}$$

where M_t, M_0 and M_e are the moisture content at any time of drying (kg water/kg dry matter), initial moisture content (kg water/kg dry matter) and equilibrium moisture content (kg water/kg dry matter), respectively. The moisture ratio *(MR)* was simplified to M_t/M_0 instead of $(M_t - M_e)/(M_0 - M_e)$ (Ismail et al. 2014) because of the values of M_e small compared with M_t or M_0 for long drying time.
The drying rate *(DR)* was calculated using Eq. (2):

$$DR = \frac{M_t - M_{t+\Delta t}}{\Delta t} \tag{2}$$

where $M_{t+\Delta t}$ is moisture content at $t+\Delta t$ (kg water/kg dry matter), and t is time (min).

The regression analysis was performed by using the STATISTICA computer program. The determination of coefficient (R^2), reduced chi-square (χ^2) and root mean square error (*RMSE*) were used in this study to evaluate the goodness of fit. These parameters can be calculated by using the following equations:

$$R^2 = 1 - \frac{\sum_{i=1}^{N}\left(MR_{pre,i} - MR_{exp,i}\right)^2}{\sum_{i=1}^{N}\left(\overline{MR}_{pre} - MR_{exp,i}\right)^2} \tag{3}$$

$$\chi^2 = \frac{\sum_{i=1}^{N}(MR_{exp,i} - MR_{pre,i})^2}{N - z} \tag{4}$$

$$RMSE = \left[\frac{1}{N}\sum_{i=1}^{N}(MR_{pre,i} - MR_{exp,i})^2\right]^{1/2} \tag{5}$$

In these equations, N is the number of observations, z is the number of constants, MR_{exp} and MR_{pre} are the experimental and predicted moisture ratios, respectively. The best model describing the drying characteristics of pea samples is chosen as the one with the highest R^2 values and the lowest χ^2 and *RMSE* values [13].

Determination of effective moisture diffusivity

The values of effective moisture diffusivity (D_{eff}) of dried peas are determined by using the Fick's second law of diffusion equation:

$$\frac{\partial M}{\partial t} = D_{eff}\nabla^2 M \tag{6}$$

The analytical solution of Fick's second law (Eq. 6) unsteady state diffusion in a spherical coordinates with the assumptions of moisture migration being by diffusion, negligible shrinkage, constant effective diffusivity and temperature during the drying process is given as follows [14] :

$$MR = \frac{6}{\pi^2}\sum_{n=1}^{\infty}\frac{1}{n^2}exp\left(-n^2\pi^2\frac{D_{eff}t}{r^2}\right) \tag{7}$$

For long drying periods, Eq. (7) can be further simplified to only the first term of the series. Thus, Eq. (7) is written in a logarithmic form as follows:

$$ln(MR) = ln\left(\frac{6}{\pi^2}\right) - \left(\frac{\pi^2 D_{eff}\,t}{r^2}\right) \tag{8}$$

The effective moisture diffusivity is obtained by plotting the experimental drying data in terms of ln (*MR*) versus time (min). From Eq. (8), a plot of *ln MR* versus *time* gives a straight line with a slope of (*K*), in which:

$$K = \frac{\pi^2 D_{eff}}{r^2} \tag{9}$$

Computation of activation energy

The dependence of the effective diffusivity on temperature is generally described by the Arrhenius equation:

$$D_{eff} = D_0 \, exp\left(-\frac{E_a}{R(T+273.15)}\right) \quad (10)$$

Here D_0 is the pre-exponential factor of Arrhenius equation (m^2/s), E_a is the activation energy (kJ/mol), R is the universal gas constant (kJ/(mol.K)), and T is temperature (°C).

RESULTS AND DISCUSSION

Effect of pretreatment and air drying temperature

Figures 1 presents variations in the moisture content as a function of drying time at 55, 65 and 75°C. It is clear that the moisture content decreases continuously with drying time. The pre-treatments affected the drying time. The peas dipped in pre-treatment solutions before the drying process was found to have a shorter drying time compared to the control ones. From Figures 1, it is observed that the drying times required for reducing the moisture content of pre-treated samples were 585, 360 and 285 for BLANCH samples, and 645, 405, and 315 min for EO samples. Corresponding values for the control samples were 810, 525 and 360 min at same temperatures, respectively. As a result, the experimental results demonstrate the importance of the blanched in reducing the mass-transfer resistance of the peas. A similar effect of blanching has been found in the drying of various vegetables [9,13,15].

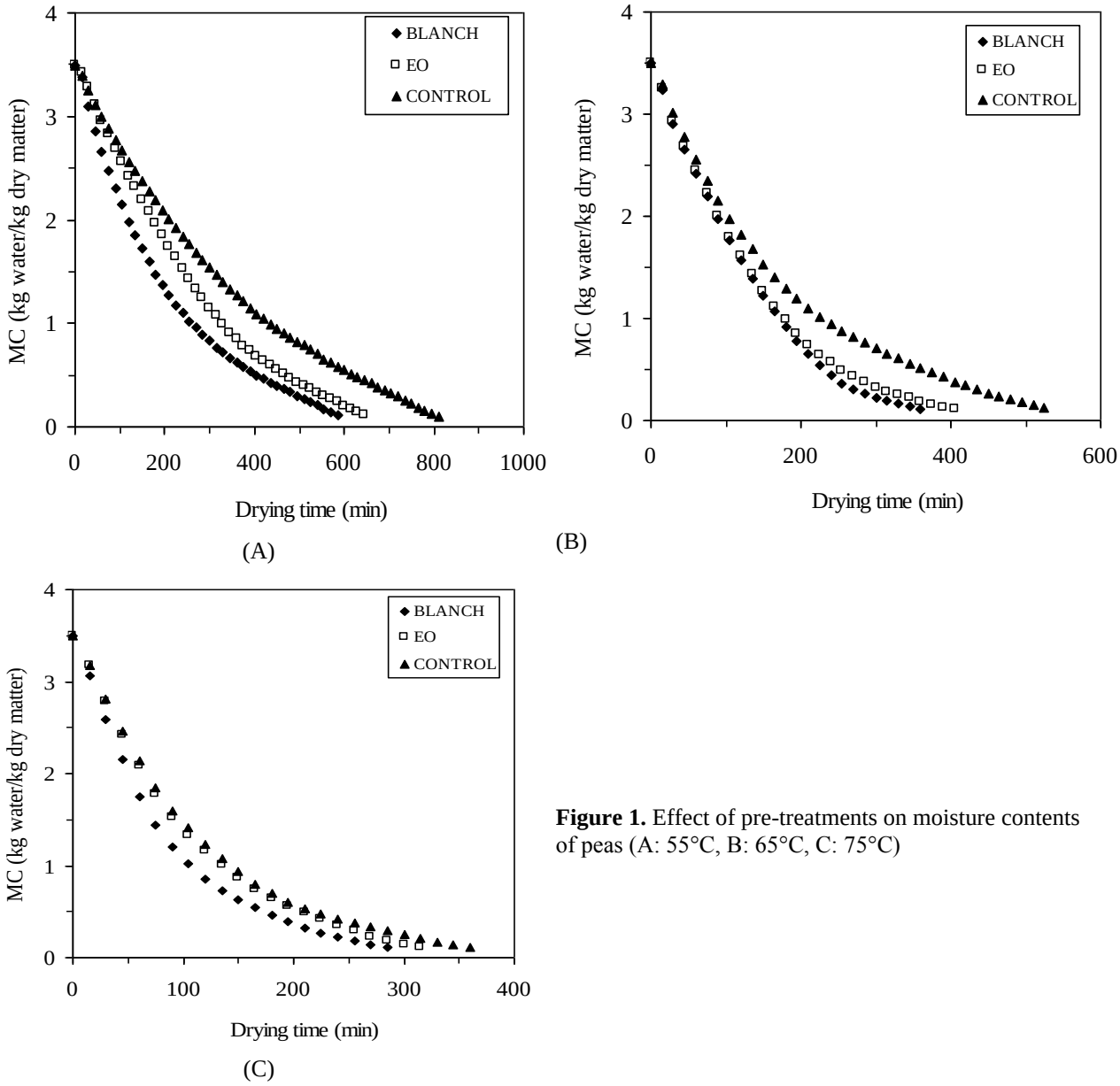

Figure 1. Effect of pre-treatments on moisture contents of peas (A: 55°C, B: 65°C, C: 75°C)

The drying times taken to reduce the moisture contents of the peas from initial moisture of 3.494 kg water/kg dry matter to final moisture of 0.11 kg water/kg dry matter are demonstrated in Figure 1. As expected, the higher air temperature of 75°C results in higher drying rate compared to 55 and 65°C. The drying air temperature of 75°C resulted in a shorter drying time than 55°C by approximately 300, 330, and 450 min for BLANCH, EO and CONTROL samples, respectively. The enhancement in drying rate at higher drying temperature is due to the fact that higher drying temperatures lead to the higher driving forces for heat transfer. The effect of temperature on drying time was similar, in accordance with earlier studies made on green pea [3,16], green bean [13], and bitter gourd [9].

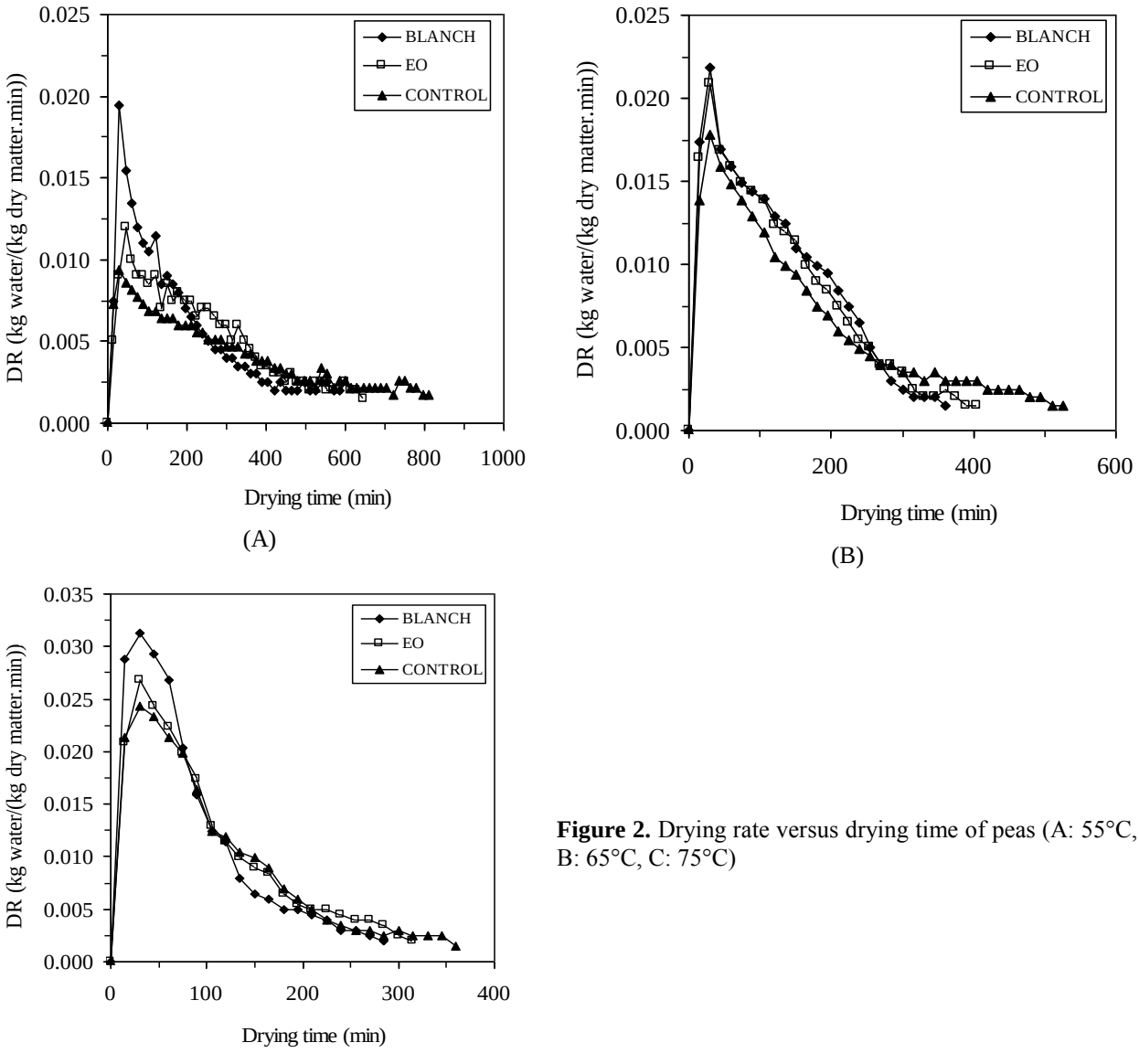

Figure 2. Drying rate versus drying time of peas (A: 55°C, B: 65°C, C: 75°C)

Table 1. List of drying models used for describing the drying kinetics

Model name	*Model*	*Reference*
Henderson and Pabis	$MR = a\exp(-kt)$	Henderson and Pabis [18]
Midilli and Kucuk	$MR = a\exp(-kt^n) + bt$	Midilli and Kucuk [19]
Weibull	$MR = exp\left(-\left(\frac{t}{b}\right)^a\right)$	Corzo et al. [23]
Aghbashlo et al.	$MR = exp\left(-\left(\frac{at}{1+bt}\right)\right)$	Aghbashlo et al. [24]

a, b, c, n: constants in drying models; *k:* drying rate coefficient (1/min)

DRYING RATE

The drying rate values of peas at different temperatures were calculated using Eq. 2 and are shown in Figure 2. At the beginning of the process the drying rate is high and the diffusion resistance increases gradually during the drying process, so this leads to a continuous reduction in drying rate. Similar result has been reported previously by Ghalavand et al. [17] has been reported. Figure 2 indicates that the moisture removal inside the peas was higher at higher air temperatures. So, the migration of moisture to the surface and the evaporation rate from surface to air slows down with decreasing the moisture in the product, the drying rate clearly decreases. As can be seen no constant drying rate period was observed, and the whole drying process occurred in the falling drying rate period. This shows that diffusion in dominant physical mechanism governing moisture movement in the samples.

EVALUATION OF THE MODELS

Nonlinear regression analysis was done according to the four mathematical models which are given in Table 1 after moisture content data of air drying was transferred into the moisture ratio (MR). The statistical analysis values are summarized in Table 2. In all cases, the R^2 values for the models were greater than 0.98, indicating a good fit. The Midilli and Kucuk model gave a higher R^2 and lower χ^2 and RMSE values, and were selected to represent the drying characteristics of peas. The R^2 values of the model varied between 0.9989 and 0.9998, χ^2 values between 0.000013 and 0.000060, and RMSE values between 0.020874 and 0.036854. The worst fit in this study belongs to the Henderson and Pabis model. Figure 3 compare the experimental data with the predicted ones using Midilli and Kucuk model for peas at 55, 65 and 75°C. The prediction using the model showed MR values banded along a straight line, which proved the suitability of these models in describing the drying characteristics of peas.

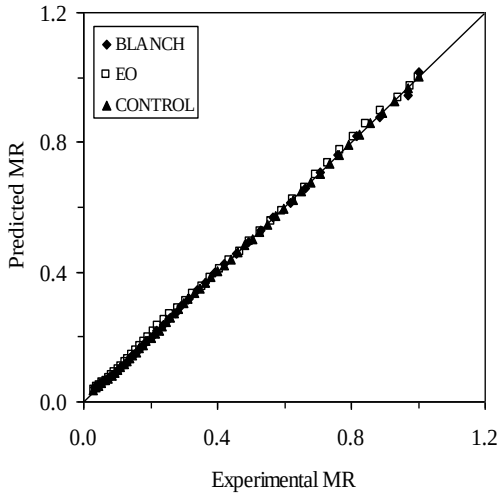

(A)

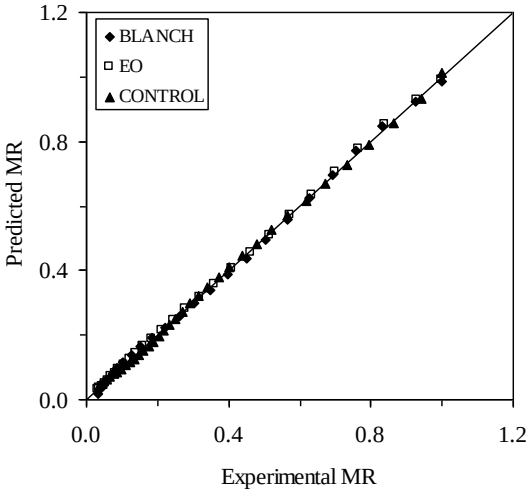

(B)

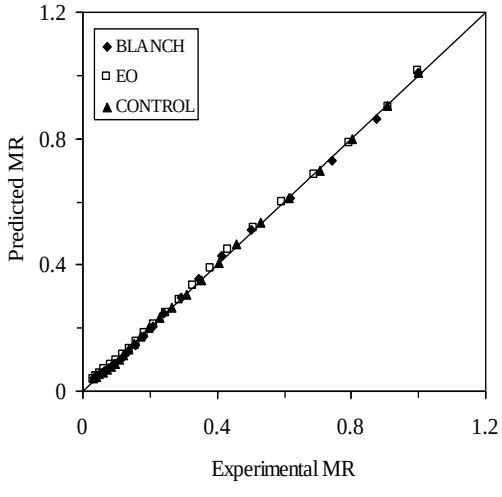

(C)

Figure 3. Experimentally determined and predicted moisture ratios of peas (A: 55°C, B: 65°C, C: 75°C)

Table 2

Code	*T (°C)*	*Model name*	R^2	χ^2	*RMSE*
BLANCH	55	Henderson and Pabis	0.9990	0.000074	0.032247
		Midilli and Kucuk	0.9994	0.000050	0.030621
		Weibull	0.9991	0.000067	0.035008
		Aghbashlo et al.	0.9990	0.000074	0.036845
	65	Henderson and Pabis	0.9885	0.001109	0.145978
		Midilli and Kucuk	0.9995	0.000044	0.026595
		Weibull	0.9981	0.000183	0.056078
		Aghbashlo et al.	0.9990	0.000104	0.041357
	75	Henderson and Pabis	0.9981	0.000122	0.038276
		Midilli and Kucuk	0.9994	0.000105	0.036854
		Weibull	0.9993	0.000124	0.040970
		Aghbashlo et al.	0.9987	0.000161	0.040648
AEEO	55	Henderson and Pabis	0.9900	0.000888	0.167948
		Midilli and Kucuk	0.9997	0.000027	0.028956
		Weibull	0.9992	0.000656	0.038987
		Aghbashlo et al.	0.9991	0.000080	0.048052
	65	Henderson and Pabis	0.9942	0.000533	0.105072
		Midilli and Kucuk	0.9997	0.000026	0.020874
		Weibull	0.9996	0.000036	0.023688
		Aghbashlo et al.	0.9994	0.000049	0.031104
	75	Henderson and Pabis	0.9986	0.000173	0.041025
		Midilli and Kucuk	0.9989	0.000060	0.028295
		Weibull	0.9986	0.000063	0.030103
		Aghbashlo et al.	0.9982	0.000111	0.034312
CONTROL	55	Henderson and Pabis	0.9927	0.000574	0.139895
		Midilli and Kucuk	0.9998	0.000013	0.023374
		Weibull	0.9973	0.000209	0.080979
		Aghbashlo et al.	0.9991	0.000064	0.041372
	65	Henderson and Pabis	0.9991	0.000069	0.038666
		Midilli and Kucuk	0.9994	0.000052	0.036212
		Weibull	0.9991	0.000068	0.040487
		Aghbashlo et al.	0.9991	0.000069	0.041805
	75	Henderson and Pabis	09989	0.000087	0.030678
		Midilli and Kucuk	0.9998	0.000034	0.021831
		Weibull	0.9993	0.000046	0.026832
		Aghbashlo et al.	0.9987	0.000098	0.036768

EFFECTIVE MOISTURE DIFFUSIVITY

The determined values of the effective moisture diffusivity are shown in Figure 4 and were found to range between 7.66×10^{-11} m^2/s and 2.44×10^{-10} m^2/s. The moisture diffusivity was affected by the pre-treatment solution and air temperature. It can be seen that D_{eff} values for blanched samples are greater than those obtained for the other samples under the same drying conditions. Moreover, D_{eff} was increased with increasing temperature. The values of D_{eff} were in the range 10^{-11} to 10^{-10} m^2/s and are comparable with reported values in literature for peas [4,15,20].

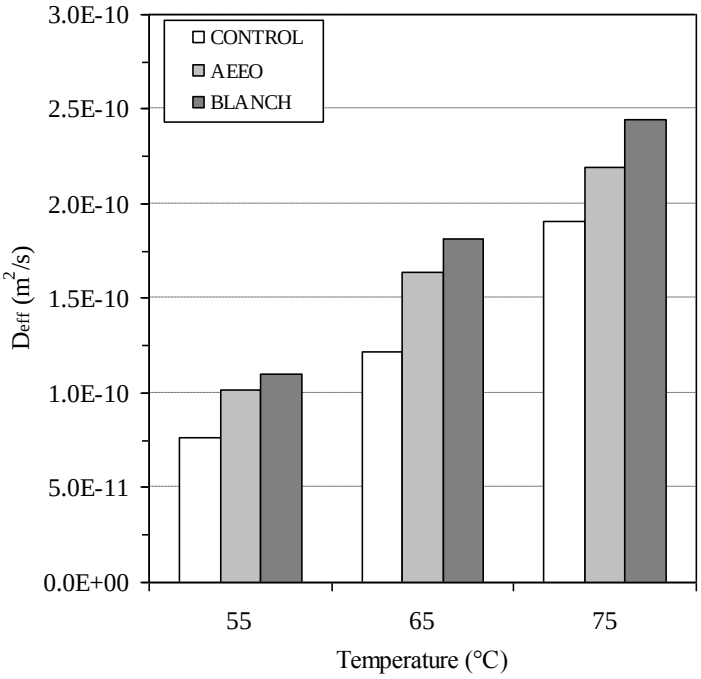

Figure 4. Variation of effective diffusivity with drying temperature.

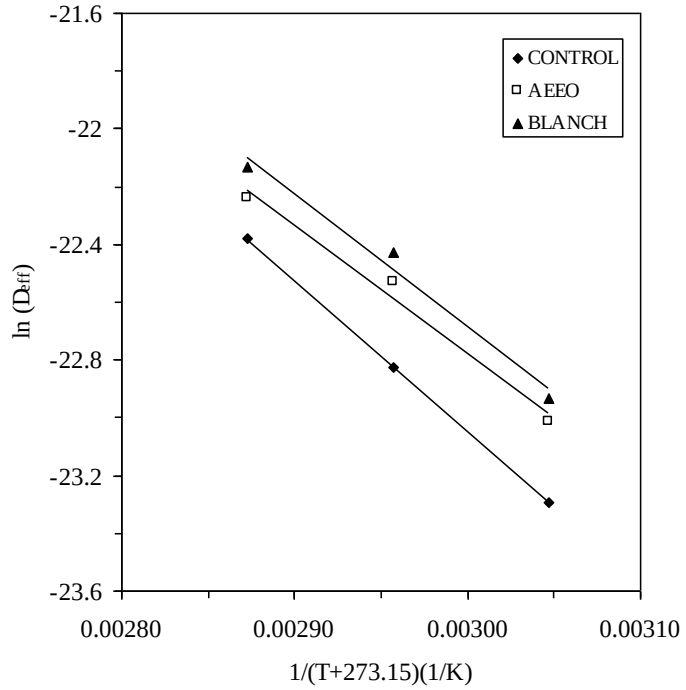

Figure 5. Arrhenius-type relationship between effective diffusivity and reciprocal absolute temperature

ACTIVATION ENERGY

The activation energy was calculated by plotting ln (D_{eff}) *versus* the reciprocal of the temperature (1/(T+273.15)), and presented in Figure 5. Eqs. (11), (12) and (13) show the effect of temperature on D_{eff} of the pre-treated and the control samples with following coefficients:

For AEEO samples:

$$D_{eff} = 7.3914 \times 10^{-5} \, exp\left(-\frac{4420.9}{(T + 273.15)}\right) (R^2: 0.9846) \quad (11)$$

For BLANCH samples:

$$D_{eff} = 1.3186 \times 10^{-4} \exp\left(-\frac{4584}{(T + 273.15)}\right) \quad (R^2: 0.9822) \qquad (12)$$

For CONTROL samples:

$$D_{eff} = 5.8887 \times 10^{-4} \exp\left(-\frac{5203.1}{(T + 273.15)}\right) \quad (R^2: 1) \qquad (13)$$

The activation energy values were found to be 36.75, 38.11, and 43.25 kJ/mol for the AEEO, BLANCH and CONTROL samples, respectively. These values are similar to those proposed by other authors for green pea and different products: 28.4 kJ/mol in green pea [14], 22.48 kJ/mol in green peas [4]; 43 kJ/mol for green beans [21], and 40.08 kJ/mol for bean grains [22].

CONCLUSIONS

Drying characteristics of peas were investigated in a cabinet dryer at various temperatures of 55, 65 and 75°C and constant air velocity of 2 m/s. Air temperature was important factor in drying of peas. High drying temperature resulted in a shorter drying time. Also, the blanched samples had shorter drying times than other pre-treated and control samples. The drying process of pea occurred in the falling drying rate period. To explain the drying kinetics of peas, four drying models were applied and fitted to the experimental data. According to the results of statistical analysis, the experimental data were well predicted by the Midilli and Kucuk model. The values of effective diffusivity of the pre-treated and control samples were in the range 7.66×10^{-11} m^2/s to 2.44×10^{-10} m^2/s. The activation energy values found to be between 36.75 and 43.25 kJ/mol.

REFERENCES

1. http://faostat.fao.org/site/567/DesktopDefault.aspx?PageID=567#ancor
2. D. A. An, S. D. Arntfield, T. Beta, S.Cenkowski, *Food Research International*, **43**, 520 (2010).
3. Y. V Shete, M. M. More, S. S Deshmukh, S. C. Karne, *Int.J. Agricultural Engineering*, **8**, 220 (2015).
4. I. L. Pardeshi, S. Arora, P. A. Borker, Drying Technology, **27**, 288 (2009).
5. O. Taskin, N. Izli, A. Vardar, *Journal of Photoenergy*, Article ID 3814262. (2016).
6. X. Jin, T. Oliviero, R. G. M. Van Der Sman, R. Verkerk, M. Dekker, A. J. B Van Boxtel, *LWT - Food Science and Technology*, **59**, 189 (2014).
7. R. P. Kingsly, R. K. Goyal, M. R. Manikantan, S. M. Ilyas, *Int. J. Food Science and Technology*, **42**, 65 (2007).
8. G. Adiletta, P. Russo, W. Senadeera, M. Di Matteo, *J. Food Engineering*, **172**, 9 (2016).
9. A. Srimagal, S. Mishra, R. C. Pradhan, *J. Food Science and Technology*, **54**, 1192 (2017).
10. H. W. Xiao, X. D. Yao, H. Lin, W. X. Yang, J. S. Meng, Z. J. Gao, *J. Food Process Engineering*, **35**, 370 (2012).
11. V. A. Arlington, AOAC Association of Official Analytical Chemists, Official Methods of Analysis, 15th Ed; 1990.
12. I. Doymaz, *Biosystems Engineering*, **89**, 281 (2004).
13. O. Ismail, A. Kanturk Figen, S. Piskin, *Heat and Mass Transfe*r, **53**, 1277 (2017).
14. J. Crank, The Mathematics of Diffusion, Clarendon Press: Oxford, 1975.
15. S. Simal, A. Mulet, J. Tarrazo, C. Rossello, *Food Chemistry*, **55**, 121 (1996).
16. M. S. Hatamipour, D. Mowla, *Food and Bioproducts Processing*, **84**, 220 (2006).
17. Y. Ghavaland, A. Rahimi, M. S. Hatamipour, *Drying Technology*, **30**, 128 (2012).
18. S. M. Henderson, S. Pabis, *J. Agricultural Engineering Research*, **6**, 169 (1961).
19. A. Midilli, H. Kucuk, *Energy Conversion and Management*, **44**, (2003).
20. D. B. Jadhav, G. L. Visavale, N. Sutar, U. S. Annapure, B. N. Thorat, *Drying Technology*, **28**, 600 (2010).
21. C. Rosselló, S. Simal, N. SanJuan, A. Mulet, *J. Agricultural and Food Chemistry*, **45**, 337 (1997)
22. O. Resende, P.C. Corréa, C. Jarén, A. J. Moure, *Spanish Journal of Agricultural Research*, **5**, 51, (2007).
23. O. Corzo, N. Bracho, A. Pereira, A. Vásquez, *LWT-Food Science and Technology*, **41**, 2023, (2008).
24. M. Aghbashlo, M.H. Kianmehr, S. Khani, M. Ghasemi, *International Agrophysics* **23**, 313 (2009).

Bulgarian Chemical Communications, Volume 49, Issue I (pp. 98 – 106) 2017

In-vitro biological activity of some new 1,2,4-triazole derivatives with their potentiometric titrations

Ö. Aktaş-Yokuş[1*], H. Yüksek[2], S. Manap[2], F. Aytemiz[2], M. Alkan[1], M. Beytur[2], Ö. Gürsoy-Kol[2]

[1]*Education Faculty, Kafkas University, 36100 Kars-Turkey*

[2]*Department of Chemistry, Kafkas University, 36100 Kars-Turkey*

Submitted May 22, 2017; Revised September 1, 2017

In this study, 3-alkyl(aryl)-4-amino-4,5-dihydro-1*H*-1,2,4-triazol-5-ones **2** have been reacted with 3-(4-methoxybenzenesulfonyloxy)-4-methoxybenzaldehyde **1** to afford the corresponding nine new 3-alkyl(aryl)-4-[3-(4-methoxybenzenesulfonyloxy)-4-methoxybenzylideneamino]-4,5-dihydro-1*H*-1,2,4-triazol-5-ones **3**. The structures of nine new compounds have been characterized by IR, ^{1}H and ^{13}C NMR spectral data. The synthesized compounds have been analyzed for their *in vitro* antioxidant and antimicrobial activities. Furthermore, the half-neutralization potential values and the corresponding pK_a values were determined for all the newly synthesized compounds.

Keywords: Synhesis, Antioxidant activity, Antimicrobial activity, pK_a, Acidity

INTRODUCTION

The compounds containing the 1,2,4-triazole moiety have been reported to possess different biological activities such as anti-inflammatory, antibacterial, antioxidant, antifungal, anticancer, analgesic, anticonvulsant, antiparasitic, antiviral, anti-HIV, antihypertensive and diuretic properties [1-16]. In addition, during the last 50 years, depending on developments in medicine, antimicrobial studies in the field of chemistry have been increased. Especially, many compounds in organic chemistry have been used in drug industry. In particularly, 1,2,4-triazoles and their derivatives are often used in antimicrobial studies. However, many studies including antimicrobial effects of triazole derivatives have also been studied [2, 6, 11, 15]. On the other hand, it is known that 1,2,4-triazole and 4,5-dihydro-1*H*-1,2,4-triazol-5-one ring have weak acidic properties, so that some 1,2,4-triazole and 4,5-dihydro-1*H*-1,2,4-triazol-5-one derivatives were titrated potentio-metrically with TBAH in non-aqueous solvents, and the pK_a values of the compounds were determined [4, 5, 14-18]. In the present study, 3-alkyl(aryl)-4-[3-(4-methoxybenzenesulfonyloxy)-4-methoxybenzylideneamino]-4,5-dihydro-1*H*-1,2,4-triazol-5-ones (**3a-i**) were synthesized from the reactions of 3-alkyl(aryl)-4-amino-4,5-dihydro-1*H*-1,2,4-triazol-5-ones (**2a-i**) with 3-(4-methoxybenzenesulfonyloxy)-4-methoxy-benzaldehyde (**1**), which was synthesized by the reaction of 3-hydroxy-4-methoxybenzaldehyde with 4-methoxy-benzenesulfonyl chloride by using triethylamine. In addition, due to a wide range of applications to find their possible radical scavenging and antioxidant activity, the newly synthesized compounds were investigated by using different antioxidant methodologies: 1,1-diphenyl-2-picryl-hydrazyl (DPPH.) free-radical scavenging, reducing power and metal chelating activities. And, the antimicrobial activities of new compounds were investigated by used agar well diffusion method. Furthermore, the newly synthesized compounds were titrated potentiometrically with tetrabutyl-ammonium hydroxide (TBAH) in isopropyl alcohol, tert-butyl alcohol, acetone and N,N-dimethylformamide (DMF) and the half-neutralization potential values and the corresponding pK_a values were determined for all cases.

EXPERIMENTAL

Materials and chemicals

Chemical reagents and all solvents used in this study were purchased from Merck, Aldrich and Fluka. The necessary solvents are obtained from domestic or foreign sources. Melting points were determined in using an electrothermal melting point apparatus which is Stuart SMP30. The IR spectra were taken in ALPHA-P BRUKER FT-IR spectrometer. ^{1}H and ^{13}C NMR spectra were recorded in deuterated dimethyl sulfoxide with TMS as an internal standard using a Bruker AVANCE III spectrometer at 400 MHz. The starting compounds **2a-i** were prepared as described in the literature [19-20].

*) To whom all correspondence should be sent:
E-mail: ozak36@gmail.com

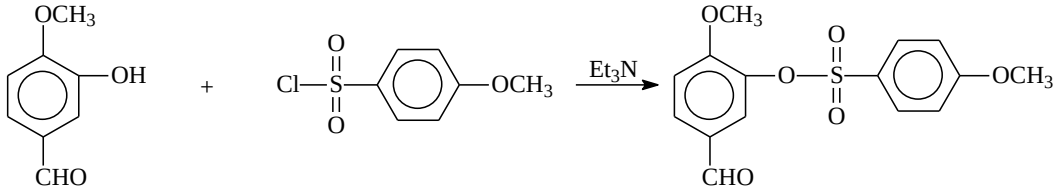

1 **(1)**

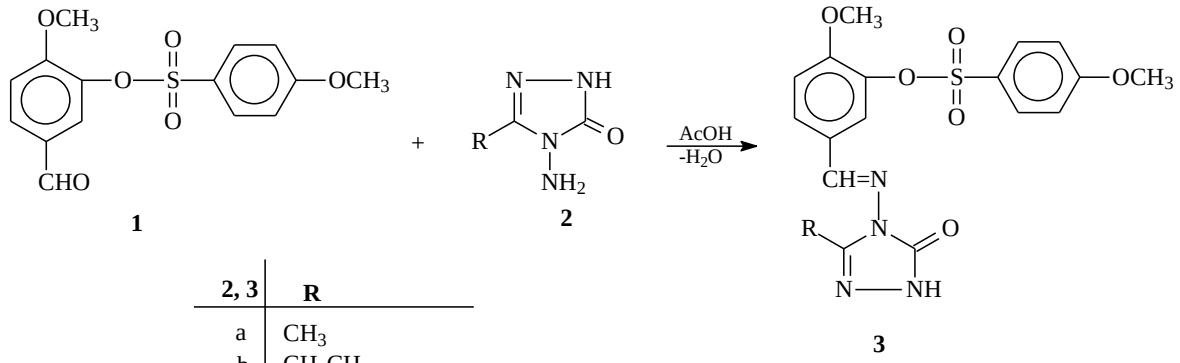

2, 3	R
a	CH_3
b	CH_2CH_3
c	$CH_2CH_2CH_3$
d	$CH_2C_6H_5$
e	$CH_2C_6H_4CH_3$(*p*-)
f	$CH_2C_6H_4OCH_3$ (*p*-)
g	$CH_2C_6H_4Cl$(*p*-)
h	$CH_2C_6H_4Cl$(*m*-)
i	C_6H_5

Scheme1. Synthetic pathway of compounds **3**

Procedure for the synthesis of 3-(4-methoxybenzenesulfonyloxy)-4-methoxybenzaldehyde (**1**)

3-Hydroxy-4-methoxy-benzaldehyde (0.01 mol) dissolved in ethyl acetate (100 mL) was treated with 4-methoxybenzenesulfonyl chloride (0.01 mol), and to this solution was slowly added triethylamine (0.01 mol) with stirring at 0-5 °C. Stirring was continued for 2 h, and then the mixture was refluxed for 3 h and filtered. The filtrate was evaporated *in vacuo*, and the crude product was washed with water and recrystallized from the DMSO-water (1:3) mixture to afford compound **1**, yield (2.87 g, 89.3 %), m.p. 134 °C. IR (KBr) υ_{max} 2830 and 2732 (CHO), 1682 (C=O), 1360 and 1170 (SO_2) cm^{-1}. ^1H NMR (400 MHz, DMSO-d_6): δ 3.64 (s, 3H, OCH_3), 3.87 (s, 3H, OCH_3), 7.16 (d, 2H, ArH; *J*=8.80 Hz), 7.27 (d, 1H, ArH; *J*=8.40 Hz), 7.63 (d, 1H, ArH; *J*=1.60 Hz), 7.76 (d, 2H, ArH; *J*=8.80 Hz), 7.88 (d, 1H, ArH; *J*=8.40, 1.60 Hz), 9.86 (s, 1H, CHO). ^{13}C NMR (100 MHz, DMSO-d_6): δ 56.43 (OCH_3), 56.75 (OCH_3), 114.02 (CH), 115.10 (2CH), 123.89 (CH), 126.28 (C), 129.85 (C), 131.20 (2CH), 131.75 (CH), 138.37 (C), 156.79 (C), 164.60 (C), 191.23 (CHO).

*General method for the preparation of 3-alkyl(aryl)-4-[3-(4-methoxy-benzenesulfonyloxy)-4-methoxy-benzylideneamino]-4,5-dihydro-1H-1,2,4-triazol-5-ones (**3a-i**)*

The 3-(4-methoxybenzene-sulfonyloxy)-4-methoxybenzaldehyde (**1**) (0.01 mol) was dissolved in acetic acid (15 mL) and treated with the corresponding compound **2** (0.01 mol). The mixture was refluxed for 1.5 h and then evaporated at 50-55 °C *in vacuo*. Several recrystallizations of the residue from appropriate solvent gave pure compounds **3a-i** as colorless crystals.

3-Methyl-4-[3-(4-methoxybenzene-sulfonyloxy)-4-methoxybenzylidene-amino]-4,5-dihydro-1*H*-1,2,4-triazol-5-one (3a). Yield (3.86 g, 92.6 %), m.p. 212 °C, IR (KBr) υ_{max} 3167 (NH), 1694 (C=O), 1593 (C=N), 1565 and 1171 (SO_2) cm^{-1}. ^1H NMR (400 MHz, DMSO-d_6): δ 2.21 (s, 3H, CH_3), 3.64 (s, 3H, OCH_3), 3.87 (s, 3H, OCH_3), 7.15 (d, 1H, ArH; *J*=7.20 Hz), 7.19 (d, 2H, ArH; *J*=8.80 Hz), 7.50 (d, 1H, ArH; *J*=2.0 Hz), 7.71 (dd, 1H, ArH; *J*=8.40, 2.0 Hz), 7.78 (d, 2H, ArH; *J*=8.80 Hz), 9.60 (s, 1H, N=CH), 11.80 (s, 1H, NH). ^{13}C NMR (100 MHz, DMSO-d_6): δ 11.44 (CH_3), 56.11 (2OCH_3), 114.03

(CH), 115.13 (2CH), 121.42 (CH), 126.53 (C), 126.70 (C), 129.88 (CH), 131.21 (2CH), 138.53 (C), 154.40 (C), 164.53 (C) (ArC), 144.62 (triazole C_3), 151.67 (triazole C_5), 152.80 (N=CH).

3-Ethyl-4-[3-(4-methoxybenzene-sulfonyloxy)-4-methoxybenzylidene-amino]-4,5-dihydro-1*H*-1,2,4-triazol-5-one (3b). Yield (4.13 g, 95.9 %), m.p. 219 °C, IR (KBr) υ_{max} 3179 (NH), 1703 (C=O), 1590 (C=N), 1367 and 1168 (SO_2) cm^{-1}. ^1H NMR (400 MHz, DMSO-d_6): δ 1.18 (t, 3H, CH_2CH_3; *J*=7.20 Hz), 2.57 (q, 2H, CH_2CH_3; *J*=7.20 Hz), 3.65 (s, 3H, OCH_3), 3.87 (s, 3H, OCH_3), (7.15 (d, 1H, ArH; *J*=7.20 Hz), 7.19 (d, 2H, ArH; *J*=8.0 Hz), 7.47 (d, 1H, ArH; *J*=1.60 Hz), 7.70 (dd, 1H, ArH; *J*=8.80, 1.60 Hz), 7.76 (d, 2H, ArH; *J*=8.00 Hz), 9.60 (s, 1H, N=CH), 11.83 (s, 1H, NH). ^{13}C NMR (100 MHz, DMSO-d_6): δ 10.38 ($CH_2\underline{CH_3}$), 18.92 ($\underline{CH_2}CH_3$), 56.40 (OCH_3), 56.52 (OCH_3), 114.04 (CH), 115.12 (2CH), 121.26 (CH), 126.56 (C), 126.73 (C), 129.90 (CH), 131.18 (2CH), 138.57 (C), 154.43 (C), 164.53 (C) (ArC), 148.38 (triazole C_3), 151.82 (triazole C_5), 152.74 (N=CH).

3-*n*-Propyl-4-[3-(4-methoxybenzene-sulfonyloxy)-4-methoxybenzylidene-amino]-4,5-dihydro-1*H*-1,2,4-triazol-5-one (3c). Yield (4.19 g, 94.3 %), m.p. 186 °C, IR (KBr) υ_{max} 3171 (NH), 1697 (C=O), 1590 (C=N), 1565 and 1169 (SO_2) cm^{-1}. ^1H NMR (400 MHz, DMSO-d_6): δ 0.94 (t, 3H, $CH_2CH_2\underline{CH_3}$; *J*=7.20 Hz), 1.65 (sext, 2H, $CH_2\underline{CH_2}CH_3$; *J*=7.20 Hz), 2.57 (t, 2H, $\underline{CH_2}CH_2CH_3$; *J*=7.20 Hz), 3.64 (s, 3H, OCH_3), 3.87 (s, 3H, OCH_3), 7.17 (d, 2H, ArH; *J*=8.80 Hz), 7.19 (d, 1H, ArH; *J*=8.40 Hz), 7.51 (d, 1H, ArH; *J*=1.60 Hz), 7.71 (dd, 1H, ArH; *J*=8.40, 1.20 Hz), 7.78 (d, 2H, ArH; *J*=8.80 Hz), 9.60 (s, 1H, N=CH), 11.83 (s, 1H, NH). ^{13}C NMR (100 MHz, DMSO-d_6): δ 13.89 ($CH_2CH_2\underline{CH_3}$), 19.34 ($CH_2\underline{CH_2}CH_3$), 27.09 ($\underline{CH_2}CH_2CH_3$), (56.41 (OCH_3), 56.51 (OCH_3), 114.07 (CH), 115.11 (2CH), , 121.42 (CH), 126.53 (C), 126.75 (C), 126.79 (CH), 131.18 (2CH), 138.54 (C), 154.40 (C), 164.52 (C) (ArC), 147.25 (triazole C_3), 151.75 (triazole C_5), 152.80 (N=CH).

3-Benzyl-4-[3-(4-methoxybenzene-sulfonyloxy)-4-methoxybenzylidene-amino]-4,5-dihydro-1*H*-1,2,4-triazol-5-one (3d). Yield (4.76 g, 96.6 %), m.p. 165 °C, IR (KBr) υ_{max} 3167 (NH), 1702 (C=O), 1594 (C=N), 1374 and 1190 (SO_2), 758 and 700 (monosubstituted benzenoid ring) cm^{-1}. ^1H NMR (400 MHz, DMSO-d_6): δ 3.60 (s, 3H, OCH_3), 3.83 (s, 3H, OCH_3), 3.99 (s, 2H, CH_2ph), 7.17 (d, 2H, ArH; *J*=8.80 Hz), 7.24-7.32 (m, 6H, ArH), 7.60 (d, 1H, ArH; *J*=2.00 Hz), 7.67 (dd, 1H, ArH; *J*=8.40, 1.60 Hz), 7.78 (d, 2H, ArH; *J*=8.80 Hz), 9.57 (s, 1H, N=CH), 11.96 (s, 1H, NH). ^{13}C NMR (100 MHz, DMSO-d_6): δ 31.64 (CH_2Ph), 56.38 (OCH_3), 56.47 (OCH_3), 113.99 (CH), 115.09 (2CH), 121.63 (CH), 126.53 (C), 126.72 (C), 127.24 (CH), 128.92 (2CH), 129.33 (2CH), 129.86 (CH), 131.18 (2CH), 136.15 (C), 138.49 (C), 154.31 (C), 164.51 (C) (ArC), 146.63 (triazole C_3), 151.65 (triazole C_5), 152.56 (N=CH).

3-*p*-Methylbenzyl-4-[3-(4-methoxy-benzenesulfonyloxy)-4-methoxy-benzylideneamino]-4,5-dihydro-1*H*-1,2,4-triazol-5-one (3e). Yield (4.88 g, 96.4 %), m.p. 198 °C, IR (KBr) υ_{max} 3167 (NH), 1703 (C=O), 1590 (C=N), 1369 and 1188 (SO_2), 833 (1,4-disubstituted benzenoid ring) cm^{-1}. ^1H NMR (400 MHz, DMSO-d_6): δ 2.25 (s, 3H, $PhCH_3$), 3.60 (s, 3H, OCH_3), 3.83 (s, 3H, OCH_3), 3.93 (s, 2H, CH_2Ph), 7.10-7.18 (m, 7H, ArH), 7.60 (s, 1H, ArH), 7.67 (d, 1H, ArH; *J*=8.40 Hz), 7.78 (d, 2H, ArH; *J*=8.80 Hz), 9.56 (s, 1H, N=CH), 11.94 (s, 1H, NH). ^{13}C NMR (100 MHz, DMSO-d_6): δ 21.09 ($PhCH_3$), 31.24 (CH_2Ph), 56.38 (OCH_3), 56.47 (OCH_3), 113.99 (CH), 115.09 (2CH), , 121.60 (CH), 126.53 (C), 126.73 (C), 129.19 (2CH), 129.49 (2CH), 129.87 (CH), 131.18 (2CH), 133.04 (C), 136.29 (C), 138.50 (C), 154.30 (C), 164.52 (C) (ArC), 146.78 (triazole C_3), 151.65 (triazole C_5), 152.51 (N=CH).

3-*p*-Methoxybenzyl-4-[3-(4-methoxy-benzenesulfonyloxy)-4-methoxy-benzylideneamino]-4,5-dihydro-1*H*-1,2,4-triazol-5-one (3f). Yield (5.0 g, 95.7 %), m.p. 230 °C, IR (KBr) υ_{max} 3168 (NH), 1704 (C=O), 1589 (C=N), 1366 and 1186 (SO_2), 834 (1,4-disubstituted benzenoid ring) cm^{-1}. ^1H NMR (400 MHz, DMSO-d_6): δ 3.61 (s, 3H, OCH_3), 3.71 (s, 3H, OCH_3), 3.83 (s, 3H, OCH_3), 3.91 (s, 2H, $PhCH_2$), 6.87 (d, 2H, ArH; *J*=8.40 Hz), 7.16 (d, 2H, ArH; *J*=8.80 Hz), 7.18 (d, 1H, ArH; *J*=8.40 Hz), 7.21 (d, 2H, ArH; *J*=8.40 Hz), 7.60 (d, 1H, ArH; *J*=1.60 Hz), 7.68 (d, 1H, ArH; *J*=8.80 Hz), 7.78 (d, 2H, ArH; *J*=8.80 Hz), 9.57 (s, 1H, N=CH), 11.92 (s, 1H, NH). ^{13}C NMR (100 MHz, DMSO-d_6): δ 30.79 (CH_2Ph), 55.46 (OCH_3), 56.38 (OCH_3), 56.48 (OCH_3), 114.00 (CH), 114.33 (2CH), 115.09 (2CH), 121.60 (CH), 126.53 (C), 126.75 (C), 127.92 (C), 129.91 (CH), 130.39 (2CH), 131.19 (2CH), 138.51 (C), 154.31 (C), 158.56 (C), 164.53 (C) (ArC), 146.93 (triazole C_3), 151.67 (triazole C_5), 152.53 (N=CH).

3-*p*-Chlorobenzyl-4-[3-(4-methoxy-benzenesulfonyloxy)-4-methoxy-benzylideneamino]-4,5-dihydro-1*H*-1,2,4-triazol-5-one (3g). Yield (5.13 g, 97.4 %), m.p. 228 °C, IR (KBr) υ_{max} 3168 (NH), 1703 (C=O), 1591 (C=N), 1368 and 1188 (SO_2), 834 (1,4-disubstituted benzenoid ring) cm^{-1}. ^1H NMR (400 MHz, DMSO-

d_6): δ 3.60 (s, 3H, OCH_3), 3.83 (s, 3H, OCH_3), 4.00 (s, 2H, CH_2Ph), 7.16 (d, 2H, ArH; *J*=8.80 Hz), 7.17 (d, 1H, ArH; *J*=8.80 Hz), 7.33 (d, 2H, ArH; *J*=8.40 Hz), 7.38 (d, 2H, ArH; *J*=8.40 Hz), 7.59 (d, 1H, ArH; *J*=2.00 Hz), 7.67 (dd, 1H, ArH; *J*=8.40,1.60 Hz), 7.78 (d, 2H, ArH; *J*=8.80 Hz), 9.57 (s, 1H, N=CH), 11.98 (s, 1H, NH). ^{13}C NMR (100 MHz, DMSO-d_6): δ 30.79 (CH_2Ph), 56.39 (OCH_3), 56.48 (OCH_3), 114.00 (CH), 115.08 (2CH), 121.68 (CH), 126.51 (C), 126.66 (C), 128.85 (2CH), 129.88 (CH), 131.19 (2CH), 131.26 (2CH), 131.92 (C), 135.15 (C), 138.48 (C), 154.34 (C), 164.52 (C) (ArC), 146.30 (triazole C_3), 151.64 (triazole C_5), 152.69 (N=CH).

3-*m*-Chlorobenzyl-4-[3-(4-methoxy-benzenesulfonyloxy)-4-methoxy-benzylideneamino]-4,5-dihydro-1*H*-1,2,4-triazol-5-one (3h). Yield (5.09 g, 96.6 %), m.p. 200 °C, IR (KBr) υ_{max} 3175 (NH), 1703 (C=O), 1594 (C=N), 1371 and 1168 (SO_2), 832 and 706 (1,3-disubstituted benzenoid ring) cm^{-1}. ^{1}H NMR (400 MHz, DMSO-d_6): δ 3.61 (s, 3H, OCH_3), 3.82 (s, 3H, OCH_3), 4.02 (s, 2H, CH_2Ph), 7.15 (d, 2H, ArH; *J*=8.80 Hz), 7.17 (d, 1H, ArH; *J*=8.40 Hz), 7.27-7.35 (m, 4H, ArH), 7.57 (d, 1H, ArH; *J*=1.20 Hz), 7.68 (d, 1H, ArH; *J*=8.40 Hz), 7.77 (d, 2H, ArH; *J*=8.80 Hz), 9.58 (s, 1H, N=CH), 11.99 (s, 1H, NH). ^{13}C NMR (100 MHz, DMSO-d_6): δ 31.15 (CH_2Ph), 56.38 (OCH_3), 54.49 (OCH_3), 114.01 (CH), 115.08 (2CH), 121.77 (CH), 126.55 (C), 126.63 (C), 127.30 (CH), 128.22 (CH), 129.27 (CH), 129.79 (CH), 130.73 (CH), 131.19 (2CH), 133.43 (C), 138.51 (2C), 154.39 (C), 164.51 (C) (ArC), 146.13 (triazole C_3), 151.62 (triazole C_5), 152.82 (N=CH).

3-Phenyl-4-[3-(4-methoxybenzene-sulfonyloxy)-4-methoxybenzylidene-amino]-4,5-dihydro-1*H*-1,2,4-triazol-5-one (3i). Yield (4.56 g, 95.2 %), m.p. 202 °C, IR (KBr) υ_{max} 3160 (NH), 1697 (C=O), 1594 (C=N), 1359 and 1170 (SO_2), 788 and 714 (monosubstituted benzenoid ring) cm^{-1}. ^{1}H NMR (400 MHz, DMSO-d_6): δ 3.61 (s, 3H, OCH_3), 3.83 (s, 3H, OCH_3), 7.12 (d, 2H, ArH; *J*=8.80 Hz), 7.19 (d, 1H, ArH; *J*=8.40 Hz), 7.51-7.54 (m, 3H, ArH), 7.62 (d, 1H, ArH; *J*=1.60 Hz), 7.73 (dd, 1H, ArH; *J*=8.40, 1.60 Hz), 7.67 (dd, 1H, ArH; *J*=8.40,1.60 Hz), 7.76 (d, 2H, ArH; *J*=8.80 Hz), 7.87-7.89 (m, 2H, ArH; *J*=8.80 Hz), 9.56 (s, 1H, N=CH), 12.37 (s, 1H, NH). ^{13}C NMR (100 MHz, DMSO-d_6): δ 56.38 (OCH_3), 56.50 (OCH_3), 114.14 (CH), 115.05 (2CH), 122.16 (CH), 126.41 (C), 126.57 (C), 127.08 (C), 128.32 (2CH), 128.96 (2CH), 129,72 (CH), 130.60 (CH), 131.14 (2CH), 138.46 (C), 155.60 (C), 164.50 (C) (ArC), 144.90 (triazole C_3), 151.80 (triazole C_5), 154.47 (N=CH).

Antioxidant activity

Chemicals. Butylated hydroxytoluene (BHT) was purchased from E. Merck. Ferrous chloride, α-tocopherol, 1,1-diphenyl-2-picryl-hydrazyl (DPPH·), 3-(2-pyridyl)-5,6-bis(phenylsulfonic acid)-1,2,4-triazine (ferrozine), butylated hydroxyanisole (BHA) and trichloracetic acid (TCA) were bought from Sigma.

Reducing power. The reducing power of the synthesized compounds was determined according to the method [21]. Different concentrations of the samples (50-250 μg/mL) in DMSO (1 mL) were mixed with phosphate buffer (2.5 mL, 0.2 M, pH = 6.6) and potassium ferricyanide (2.5 mL, 1%). The mixture was incubated at 50ºC for 20 min. after which a portion (2.5 mL) of trichloroacetic acid (10%) was added to the mixture, which was then centrifuged for 10 min at 1000 x g. The upper layer of solution (2.5 mL) was mixed with distilled water (2.5 mL) and $FeCl_3$ (0.5 mL, 0.1%), and then the absorbance at 700 nm was measured in a spectrophometer. Higher absorbance of the reaction mixture indicated greater reducing power.

Free radical scavenging activity. Free radical scavenging activity of compounds was measured by DPPH·, using the method [22]. Briefly, 0.1 mM solution of DPPH· in ethanol was prepared, and this solution (1 mL) was added to sample solutions in DMSO (3 mL) at different concentrations (50-250 μg/mL). The mixture was shaken vigorously and allowed to stand at room temperature for 30 min. Then the absorbance was measured at 517 nm in a spectrophometer. Lower absorbance of the reaction mixture indicated higher free radical scavenging activity. The DPPH· concentration (mM) in the reaction medium was calculated from the following calibration curve and determined by linear regression (R: 0.997):

$$Absorbance = 0.0003\ x\ DPPH^{\cdot} - 0.0174$$

The capability to scavenge the DPPH radical was calculated using the following equation:

$$DPPH^{\cdot}\ scavenging\ effect\ (\%) = (\underline{A_0 - A_1}/A_0) \times 100$$

where A_0 is the absorbance of the control reaction and A_1 is the absorbance in the presence of the samples or standards.

Metal chelating activity. The chelation of ferrous ions by the synthesized compounds and standards were estimated by the method [23]. Briefly, the synthesized compounds (15–45 μg/mL) were added to a 2 mM solution of $FeCl_2 \cdot 4H_2O$ (0.05 mL). The reaction was initiated by the addition of 5 mM ferrozine (0.2 mL), and then the mixture was shaken vigorously and left standing at room temperature for

10 min. After the mixture had reached equilibrium, the absorbance of the solution was measured at 562 nm in a spectrophotometer. All tests and analyses were run in triplicate and averaged. The percentage of inhibition of ferrozine–Fe^{2+} complex formation was given by the formula: % inhibition = $(A_0 - A_1 / A_0) \times 100$, where A_0 is the absorbance of the control, and A_1 is the absorbance in the presence of the samples or standards. The control did not contain compound or standard.

Antimicrobial activity

Chemicals. All test microorganisms were obtained from the Microbiologics Environmental Protection Laboratories Company in France and are follows: (E. *coli* ATCC 259222, *P. aeruginosa* ATCC 27853, *K. pneumonia* ATCC 4352, *S. aureus* ATCC 6538, *B. subtilis* ATCC 11774, *B. cereus* ATCC 11778.

Agar well diffusion method. Simple susceptibility screening test using agar well-diffusion method was used [24, 25]. Each microorganism was suspended in Mueller–Hinton (MH) broth and diluted approximately 10^6 colony forming unit (cfu)/mL. They were "flood-inoculated" onto the surface of MH agar and Sabouraud Dextrose Agar (SDA) and then dried. Five-millimeter diameter wells were cut from the agar using a sterile cork-borer, and 250-5000 μL/50 of the chemical substances were delivered into the wells. The plates were incubated for 18 h at 35 °C. Antimicrobial activity was evaluated by measuring the zone of inhibition against the test organism. Dimethylsulphoxide was used as solved control.

Potentiometric titrations

A Jenco model pH meter was used for potentiometric titrations. An Ingold pH electrode was preferred because of the advantage. For each compound that would be titrated, the 0.001 M solution was separately prepared in each non-aqueous solvent. The 0.05 M solution of TBAH in isopropyl alcohol, which is widely used in the titration of acids, was used as titrant. The mV values that were obtained in pH-meter were recorded. Finally, the HNP values were determined by drawing the mL (TBAH)–mV graphic.

RESULTS AND DISCUSSION

In this study, the structures of nine new compounds of 3-alkyl(aryl)-4-[3-(4-methoxybenzenesulfonyloxy)-4-methoxy-benzylideneamino]-4,5-dihydro-1*H*-1,2,4-triazol-5-ones were identified using IR, ^{1}H NMR and ^{13}C NMR spectral data.

Antioxidant activity

Total reductive capability using the potassium ferricyanide reduction method. The reductive capabilities of compounds were assessed by the extent of conversion of the Fe^{3+} / ferricyanide complex to the Fe^{2+} / ferrous form. The reducing powers of the compounds were observed at different concentrations, and results were compared with BHA, BHT and α-tocopherol. It has been observed that the reducing capacity of a compound may serve as a significant indicator of its potential antioxidant activity [26]. The antioxidant activity of putative antioxidant has been attributed to various mechanisms, among which are prevention chain initiation, binding of transition metal ion catalyst, decomposition of peroxides, prevention of continued hydrogen abstraction, reductive capacity and radical scavenging [27]. In this study, all of the concentrations of the compounds showed lower absorbance than blank. Hence, no reductive activities were observed.

DPPH· radical scavenging activity. The model of scavenging the stable DPPH radical model is a widely used method to evaluate antioxidant activities in a relatively short time compared with other methods. The effect of antioxidants on DPPH radical scavenging was thought to be due to their hydrogen donating ability [28]. DPPH is a stable free radical and accepts an electron or hydrogen radical to become a stable diamagnetic molecule [29]. The reduction capability of DPPH radicals was determined by the decrease in its absorbance at 517 nm induced by antioxidants. The absorption maximum of a stable DPPH radical in ethanol was at 517 nm. The decrease in absorbance of DPPH radical was caused by antioxidants because of the reaction between antioxidant molecules and radical, progresses, which resulted in the scavenging of the radical by hydrogen donation. It is visually noticeable as a discoloration from purple to yellow. Hence, DPPH· is usually used as a substrate to evaluate antioxidative activity of antioxidants [30]. In the study, antiradical activities of compounds and standard antioxidants such as BHA, BHT and α-tocopherol were determined by using DPPH· method. Fig. 1 illustrates that the radical scavenging effects of the compounds **3c**, **3g** and **3h** were concentration-dependent, the other compounds were not. Nevertheless, these newly synthesized compounds showed poor radical scavenging activity.

Ferrous ion chelating activity. The chelating effect towards ferrous ions by the compounds and standards was determined. Ferrozine can quantitatively form complexes with Fe^{2+}. In the presence of chelating agents, the complex formation

is disrupted with the result that the red colour of the complex is decreased. Measurement of colour reduction therefore allows estimation of the chelating activity of the coexisting chelator [31]. Transition metals have pivotal role in the generation oxygen free radicals in living organism. The ferric iron (Fe^{3+}) is the relatively biologically inactive form of iron. However, it can be reduced to the active Fe^{2+}, depending on condition, particularly pH [32] and oxidized back through Fenton type reactions with the production of hydroxyl radical or Haber-Weiss reactions with superoxide anions. The production of these radicals may lead to lipid peroxidation, protein modification and DNA damage. Chelating agents may not activate metal ions and potentially inhibit the metal-dependent processes [33]. Also, the production of highly active ROS such as $O_2^{\cdot-}$, H_2O_2 and $OH^{\cdot}$ is also catalyzed by free iron though Haber-Weiss reactions:

$$O^{\cdot}_2 + H_2O_2 \rightarrow O_2 + OH^- + OH^{\cdot}$$

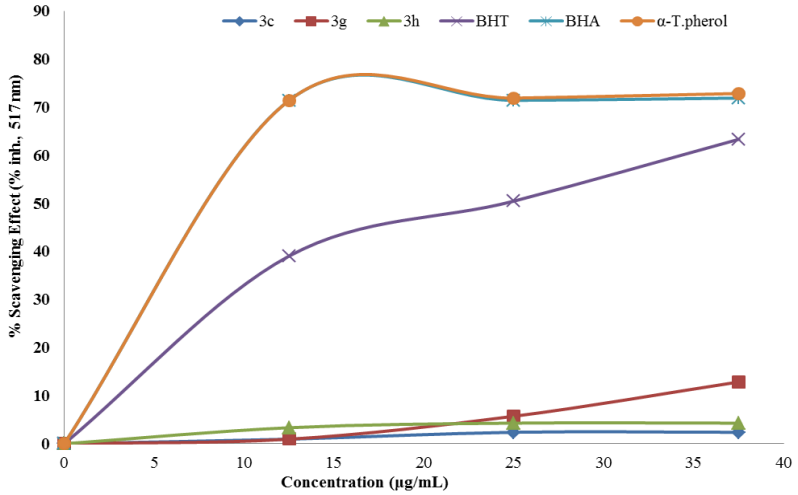

Fig. 1. Scavenging effect of compounds **3**, BHT, BHA and α-tocopherol at different concentrations (12,5-25-37.5 µg/mL)

Among the transition metals, iron is known as the most important lipid oxidation pro-oxidant due to its high reactivity. The ferrous state of iron accelerates lipid oxidation by breaking down the hydrogen and lipid peroxides to reactive free radicals via the Fenton reactions:

$$Fe^{2+} + H_2O_2 \rightarrow Fe^{3+} + OH^- + OH^{\cdot}$$

Fe^{3+} ion also produces radicals from peroxides, even though the rate is tenfold less than that of Fe^{2+} ion, which is the most powerful pro-oxidant among the various types of metal ions [34]. It was reported that chelating agents that form σ-bonds with a metal are effective as secondary antioxidants because they reduce the redox potential thereby stabilizing the oxidized form of metal ion [35].

Low absorbance at 562 nm indicates high metal chelating activity. In the study, chelating activities of compounds and standard antioxidants such as BHA, BHT and α-tocopherol were determined. The data obtained from Fig. 2 reveal that the metal chelating effects of the compounds **3,** except **3i,** were not concentration-dependent. The chelating effect of the compounds, except **3i**, is high at low concentrations.

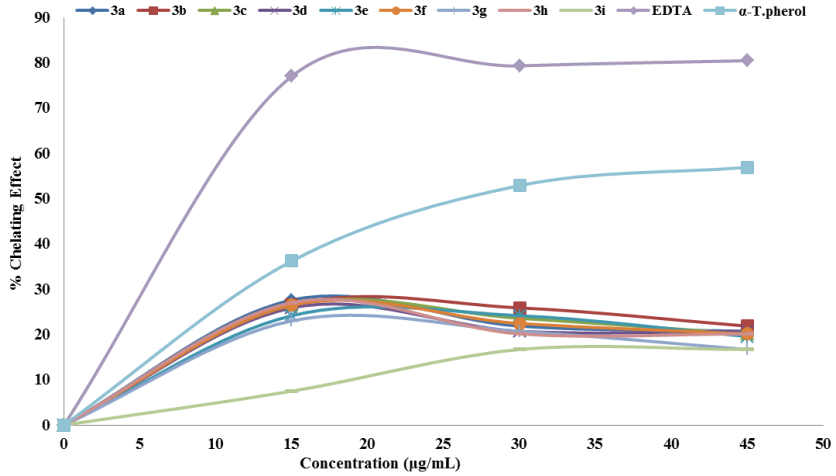

Fig. 2. Metal chelating effect of different amount of the compounds **3**, BHT, BHA and α-tocopherol on ferrous ions

Antimicrobial activity

Results were interpreted in terms of the diameter of inhibition zone:
(-): < 5.5 mm (No activity)
(+): 5.5-10 mm (Low level of activity)
(++): 11-16 mm (Moderate activity)
(+++): ≥ 17 mm (High level of activity)

Ampicillin, neomycin and streptomycin were standard antibacterial and antifungal agents. DMSO was used as solvent control. The observed data for the antimicrobial activity of **3** type compounds were given in Table 1. All of the compounds did not display any antimicrobial activity against Bacillus subtilis. The data reveal that, the highest zone diameter was obtained from compound **3d** against Bacillus cereus and **3h** against Pseudomonas aeruginosa.

Table 1. Antimicrobial activity of the compounds **3**

Comp.	Microorganisms and zone of inhibition (mm)					
	Bs	Bc	Pa	Kp	Sa	Ec
3a	-	8	8	8	9	-
3b	-	**14**	8	**12**	8	-
3c	-	9	12	7	7	8
3d	-	**16**	10	8	8	-
3e	-	8	**13**	8	7	9
3f	-	7	**13**	8	7	10
3g	-	8	10	9	9	**12**
3h	-	-	**16**	8	8	8
3i	-	9	**11**	**11**	**14**	-
Amp.	33	36	36	35	37	34
Neom.	17	17	17	16	13	16
Strep.	12	12	12	11	21	10

Bs: *Bacillus subtilis* (ATCC-11774), Bc: *Bacillus cereus* (ATCC-11778), Pa: *Pseudomonas aeruginosa* (ATCC-27853), Kp: *Klebsiella pneumoniae* (ATCC-4352), Sa: *Staphylococcus aureus* (ATCC-6538), Ec: *Escherichia coli* (ATCC-25922), Amp.: Ampicillin (3261), Neo.: Neomycin 3360, Str.: Streptomycin 3385 (-): no activite.

Table 2. The half-neutralization potential (HNP) and the corresponding pK_a values of new compounds **3a-i** in four non-aqueous solvents at 25°C.

Compd.	**Isopropyl alcohol**		***tert*-Butyl alcohol**		**DMF**		**Acetone**	
No	**HNP (mV)**	**pK_a**	**HNP (mV)**	**pK_a**	**HNP (mV)**	**pK_a**	**HNP(mV)**	**pK_a**
3a	-	-	-	-	-	-	-166	10.51
3b	-	-	-	-	-	-	-451	15.49
3c	-	-	-	-	-	-	-460	12.50
3d	-	-	-60	8.59	-124	9.72	-297	12.79
3e	-	-	-	-	-	-	-442	15.38
3f	-	-	-	-	-240	11.69	-274	12.22
3g	-	-	-	-	-59	8.37	-407	14.64
3h	-	-	-	-	-309	12.85	-	-
3i	-	-	-138	9.98	-	-	-239	11.80

Potentiometric titrations

Newly synthesized **3** type compounds were titrated potentiometrically with TBAH in non-aqueous solvents, the mV values from each titration were plotted against TBAH volumes used (mL) and the potentiometric titration curves were obtained for all the cases. From the titration curves, the HNP values and the corresponding pK_a values were calculated. As an example, the potentiometric titrations curves for 0.001 M solutions of 3-ethyl-4-[3-(4-methoxy-benzenesulfonyloxy)-4-methoxybenzylideneamino]-4,5-dihydro-1*H*-1,2,4-triazol-5-one (**3b**) titrated with 0.05 M TBAH in DMF, acetone, *tert*- butyl alcohol, isopropyl alcohol are shown in Fig. 3.

The half-neutralization potential (HNP) values and the corresponding pK_a values for new compounds **3a-i**, obtained from the potentiometric titrations with 0.05 M TBAH in isopropyl alcohol, *tert*-butyl alcohol, acetone and *N*,*N*-dimethyl formamide are presented in Table 2.

When the dielectric permittivity of solvents is taken into consideration, the acidity order can be given as follows: *N*,*N*-dimethylformamide (ε=37.0)

> acetone (ε=20.7)> isopropyl alcohol (ε=19.4) > *tert*-butyl alcohol (ε=12.0). As seen in Table 1, the acidity order for compound **3d** is *tert*-butyl alcohol > DMF > acetone, for compounds **3f** and **3g** it is: DMF > acetone, for compound **3i** it is: *tert*-butyl alcohol > acetone > DMF. Moreover, as seen in Table 1, for compounds **3a-i** in isopropyl alcohol, for compounds **3a-c**, **3e-h** in tert-butyl alcohol, for compounds **3a-c**, **3e**, **3i** in DMF and for compound **3h** in acetone, the HNP values and the corresponding pK_a values were not obtained.

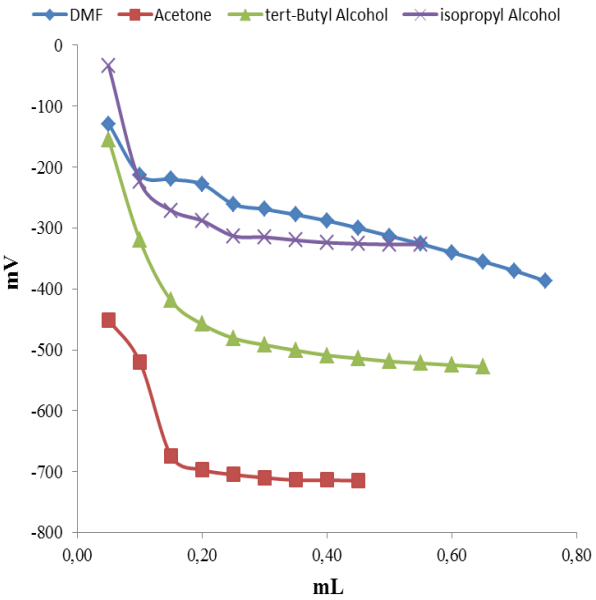

Fig. 3. Potentiometric titration curves of 0.001 M solutions of compound **3b** titrated with 0.05 M TBAH in isopropyl alcohol, tertbutyl alcohol, DMF, acetone at 25°C.

As it is well known, the acitidy of a compound depends on some factors. The two most important factors are the solvent effect and moleculer structure [36]. Table 2 shows that the HNP values and corresponding pK_a values obtained from the potentiometric titrations rely on the non-aqueous solvents used and the substituens at C-3 in 4,5-dihydro-1*H*-1,2,4-triazole-5-one ring.

CONCLUSIONS

The synthesis and in vitro antioxidant and antimicrobial evaluation also acidic properties of new 4,5-dihydro-1*H*-1,2,4-triazol-5-one derivatives are described in the study. Design and synthesis of novel small molecules can play specifically a protective role in biological systems and in modern medicinal chemistry. The results on the investigation of their biological activities might be helpful in the future drug development process.

REFERENCES

1. P. Karegoudar, D. J. Prasad, M. Ashok, M. Mahalinga, B. Poojary, B. S. Holla, *Eur. J. Med. Chem.*, **43**, 808 (2008).
2. H. Yuksek, A. Demirbas, A. Ikizler, C. B. Johansson, C. Celik, A. Ikizler, *Arzneim.-Forsch*, **47**, 405 (1997).
3. M. Pitucha, A. Olender, M. Wujec, P. Borowski, M. Mardarowicz, *J. Chin. Chem. Soc.*, **57**, 260 (2010).
4. O. Gursoy-Kol, H. Yuksek, F. Islamoglu, *J. Chem. Soc. Pak.*, **35,** 1179 (2013).
5. H. Yuksek, O. Akyildirim, M. L. Yola, O. Gursoy-Kol, M. Celebier, D. Kart, *Arch. Pharm.*, **346**, 470 (2013).
6. B. Kahveci, M. Ozil, E. Mentese, O. Bekircan, K. Buruk, *Russ. J. Org. Chem* **44**, 1816 (2008).
7. A. A. Kaczor, M. Pitucha, Z. Karczmarzyk, W. Wysocki, J. Rzymowska, D. Matosiuk, *Med. Chem.*, **9**, 313 (2013).
8. A. M. Vijesh, A. M. Isloor, P. Shetty , S. Sundersan, H. K. Fun, *Eur. J. Med. Chem.*, **62**, 410 (2013).
9. C. B. Zhang, C. W. Yang, X. Q. Deng, Z. S. Quan, *Med. Chem. Res.*, **21**, 3294 (2012).
10. H. A. Saadeh, I. M. Mosleh, A. G. Al-Bakri, M. S. Mubarak, *Monatsh Chem.*, **141**, 471 (2010).
11. M. A. Henen, S. A. A. El Bialy, F. E. Goda, M. N. A. Nasr, H. M. Eisa, *Med. Chem. Res.*, **21**, 2368 (2012).
12. Z. Y. Li, Y. Cao, P. Zhan, C. Pannecouque, J. Balzarini, E. De Clercq, X. Y. Liu, *Lett. Drug Des. Discov.*, **10**, 27 (2013).
13. K. A. Ali, E. A. Ragap, T. A. Fargly, M. M. Abdalla, *Acta. Pol. Pharm.*, **68**, 237 (2011).
14. H. Yuksek, E. Koca, Ö. Gursoy-Kol,. Akyildirim, M. Çelebiler, *J. Molecular Liquids*, **206**, 359 (2015).
15. Ö. Aktaş-Yokuş, H. Yuksek, Ö. Gursoy-Kol, Ş. Alpay-Karaoğlu, *Med. Chem. Res.*, **24**, 2813 (2015).
16. H. Yuksek, S. Kolaylı, M. Küçük, M. Ö. Yüksek, U. Ocak, E. Şahinbaş, E. Sivrikaya, M. Ocak, *Indian J. Chem.*, **45B**, 715 (2006).

17. Ş. Bahçeci, H. Yuksek, Z. Ocak, İ. Azaklı, M. Alkan, M. Özdemir, *Collect Czech Chem. Commun*, **67**, 1215 (2002).
18. Ş. Bahçeci, H. Yuksek, Z. Ocak, C. Köksal, M. Özdemir, *Acta. Chemica Slovenica*, 49, 783 (2002).
19. A.A. Ikizler, H. Yüksek, *Org. Prep. Proceed. Int.*, 1993, 25, 99.
20. A.A. Ikizler, R. Un, *Chim. Acta Turc.*, 1979, 7, 269, [*Chem. Abstr.*, 1991, 94, 15645d].
21. M. Oyaizu, *Jpn. J. Nutr.*, **44**,307 (1986).
22. M. S. Blois, *Nature*, **181**,1199 (1958).
23. T. C. P. Dinis, V. M. C. Madeira, L. M. Almeida, *Arch. Biochem Biophys*, **315**, 161 (1994).
24. C. Perez, M. Pauli, P. Bazerque, *Acta. Biol. Med. Exp*., 15, 113 (1990).
25. I. Ahmad, Z. Mehmood, F. Mohammed, *Ethnopharmacol*, **62**, 183 (1998).
26. S. Meir, J. Kanner, B. Akiri, S. Philosophhadas, *J. Agric. Food Chem.*, **43**,1813 (1995).
27. A. Yildirim, A. Mavi, A. A. Kara, *J. Agric. Food Chem.*, **49**, 4083 (2001).
28. J. Baumann, G. Wurn, F. V. Bruchlausen, *N-S Arch. Pharmacol*, **308**:R27 (1979).
29. J. R. Soares, T. C. P. Dinis, A. P. Cunha, L. M. Almeida, *Free Radical Res*., **26**, 469 (1997).
30. P. D. Duh, Y. Y. Tu, G. C. Yen, *Food Sci Technol-Leb*, **32**, 269 (1999).
31. F. Yamaguchi, T. Ariga, Y. Yoshimura, H. Nakazawa, *J. Agric. Food Chem.*, **48,** 180 (2000).
32. M. Strlic, T. Radovic, J. Kolar, B. Pihlar, *J. Agric. Food Chem.*, **50**, 6313 (2002).
33. A. E. Finefrock, A. I. Bush, P. M. Doraiswamy, *J. Am. Geriatr. Soc.*, **51**, 1143 (2003).
34. I. Calis, M. Hosny, T. Khalifa, S. Nishibe, *Phytochemistry*, **33**, 1453 (1993).
35. M. H. Gordon, Elsevier, London.
36. T. Gündüz, Susuz Ortam Reaksiyonları (Gazi Büro Kitabevi Tic. Ltd. Şti., Ankara, Turkey) (1998).

Bulgarian Chemical Communications, Volume 49, Issue I (pp. 107– 114) 2017

Synthesis, acetylcholinesterase, butyrylcholinesterase and tyrosinase ınhibition, and antioxidant studies of 2-[2-(substituted-benzyl)-4(7)-phenyl-1*H*-benzimidazol-1-yl]acetohydrazides and methyl 2-[2-(substituted-benzyl)-4(7)-phenyl-1*H*-benzimidazol-1-yl]acetates

M.K. Gümüş[1]*, İ.S. Doğan[2]*, B. Barut[3], A. Özel[3], B. Kahveci[4]

[1] *Artvin Coruh University, Faculty of Education, Department of Science and Mathematics Teaching, Artvin, Turkey*
[2] *Faculty of Pharmacy, Department of Pharmaceutical Chemistry, Karadeniz Technical University, Trabzon, Turkey*
[3] *Faculty of Pharmacy, Department of Biochemistry, Karadeniz Technical University, Trabzon, Turkey*
[4] *Faculty of Health Sciences, Department of Nutrition and Dietetics, Karadeniz Technical University, Trabzon, Turkey*

Submitted May 22, 2017; Revised September 1, 2017

In this research study we intend to synthesize six new 2-[2-(substituted-benzyl)-4(7)-phenyl-1*H*-benzimidazol-1-yl]acetohydrazides (**8a-f**) and six new methyl 2-[2-(substituted-benzyl)-4(7)-phenyl-1*H*-benzimidazol-1-yl]acetates (**7a-f**) with potency inhibiting acetylcholinesterase, butyrylcholinesterase and tyrosinase enzymes and antioxidant activities.

The chemical structures of synthesized compounds were identified by IR, ^{1}H-NMR, ^{13}C-NMR, and elemental analysis. All these compounds were evaluated for their acetylcholinesterase, butyrylcholinesterase and tyrosinase enzymes inhibitory potentials and antioxidant activities.

Biological activity results revealed that compounds **8f** and **7c** showed the highest tyrosinase inhibition with 52.46 ± 2.67% and 52.32 ± 0.70%, respectively. Compound **8f** had the highest radical scavenging activities with 24.83 ± 1.28% among the compounds whilst compound **8c** showed the lowest activities with 9.62 ± 0.85%. Compound **8f** gave the highest PRAP and FRAP absorbance values with 0.180 ± 0.013 and 0.358 ± 0.009 at 100 μM, respectively.

Key words: benzimidazoles, tyrosinase, acetylcholinesterase, butyrylcholinesterase, antioxidant activity

INTRODUCTION

Today, most of the drugs used in the treatment of diseases are obtained by organic synthesis. The fact that they are more economical than those obtained naturally leads to the rapid development of new compounds through synthesis. In this scope, benzimidazole synthesis, which is an important member of heterocyclic compounds, has become an important area of interest [1]. Some drugs (albendazole, mebendazole, omeprazole, etc.), which bear the benzimidazole ring and have been taken up by the World Health Organization (WHO), are listed in the literature [2-6]. Compounds containing the benzimidazole skeleton also show important pharmacological activities such as antimicrobial [7], antibacterial [8-10], antifungal [11,12], antiviral [13,15], antioxidant [16,17] activities.

Alzheimer Disease (AD) is recognized to impaired cognitive functions such as loss of memory and abnormal social behaviors [18]. AD has become a major health issue in the developing countries due to its rapid growth among elderly people [19]. Even though the pathogenesis of AD has not been established so far, the cholinergic hypothesis is the most accepted theory for this disease due to a deficit in acetylcholine level in the brain of patients. Therefore, treatment of this disease is to increase the acetylcholine level in the brain using acetylcholinesterase (AChE) inhibitor [20]. Tyrosinase is a copper-containing polyphenol oxidase enzyme, which may play an important role in the generation of neuromelanin. Inhibition of tyrosinase is an important target in finding new drugs against Parkinson Disease (PD) [21]. Therefore, the researchers have aimed to find new tyrosinase and cholinesterase enzyme inhibitors against these diseases (AD and PD).

For all the above reasons, in this study, we synthesized a new series of benzimidazole derivatives and evaluate the biological properties (enzyme inhibition and antioxidant) of these compounds for the first time.

EXPERIMENTAL

Measurements

Melting points were determined on a WRS-1B Digital Melting-Point Apparatus and were not corrected. FT-IR spectrums were recorded on a Shimadzu IR-Prestige-21 spectrometer fitted with an Attenuated Total Reflectance (ATR) sampling accessory as neat films. ^{1}H- and ^{13}C-NMR spectrum was acquired on a Varian Inova 400 MR spectrometer. All microwave experiments were

*) To whom all correspondence should be sent:
E-mail: isdogan@ktu.edu.tr

carried out using a monomode Anton Paar Mowave 300 microwave reactor. Elemental analyses were performed on a vario MACRO cube CHNS element analyzer. All reagents and solvents were purchased from commercial suppliers and used without further purification.

Synthesis

Compound **3** and compound **4**, which were used in the synthesis, were prepared by known literature methods [22]. Compound **4** and iminoester hydrochloride derivatives (**5a-f**) reacted in methanol under suitable conditions and benzimidazole derivative compounds (**6a-f**) were synthesized [23]. Esterification of benzimidazole derivative compounds (**7a-f**) was carried out according to the methods described in the literature [24]. The acetohydrazide derivative compounds (**8a-f**) were synthesized by treatment of these ester derivatives (**7a-f**) with hydrazine monohydrate by irradiation at a ceiling temperature of 120 °C and a maximum power of 850W for 60 min. The complete synthesis of the compounds is given in Scheme 1.

Structures of the novel compounds **7a-f** and **8a-f** were elucidated and confirmed by IR, ^{1}H-NMR, ^{13}C-NMR, elemental analysis techniques.

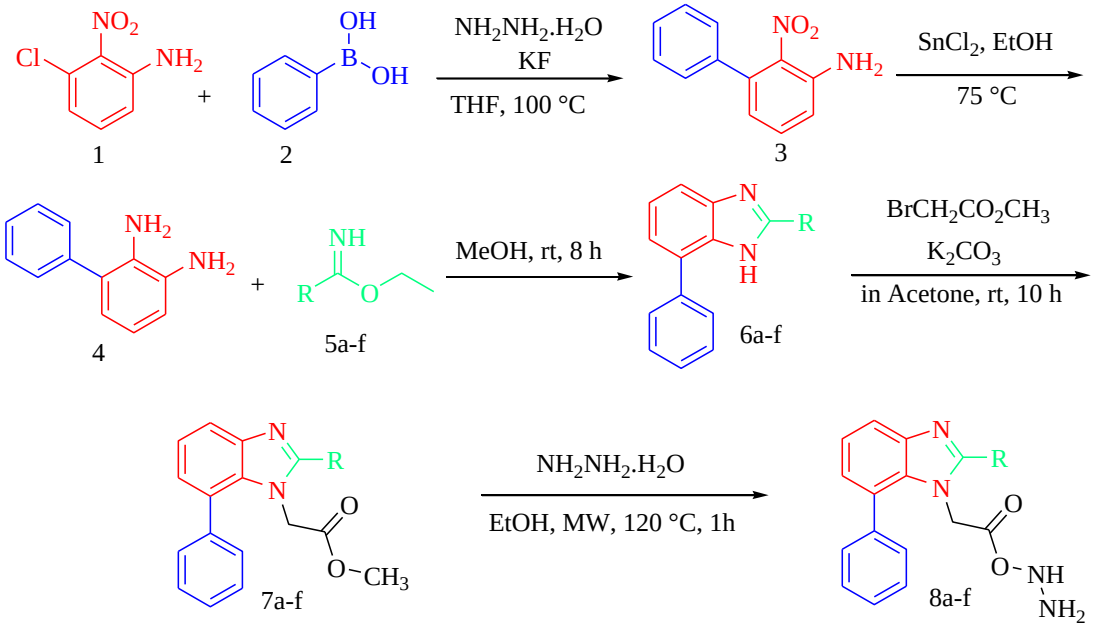

Scheme 1. Synthesis of the compounds, a: 4-chlorobenzyl; b: 3-chlorobenzyl; c: 4-methylbenzyl; d: 3-methylbenzyl; e: benzyl; f: phenyl.

Synthesis of compounds 7a-f: Compounds **7a-f** were synthesized from methyl bromoacetate and compounds **6a-f** in acetone with dry K_2CO_3 under basic conditions at room temperature [24].

Methyl 2-[2-(4-Chlorobenzyl)-4(7)-phenyl-1*H*-benzimidazol-1-yl]acetate (7a). Yield 92%, white powder, mp 142-144 °C. IR (ATR, ν_{max}, cm^{-1}): 3047 (aromatic C-H), 2993, 2954, 2931 (aliphatic C-H), 1736 (C=O) 1519, 1489, 1435 (C=C and C=N), 1226, 1010, 748 (C-C, C-N, C-O). ^{1}H NMR spectrum (DMSO-d$_6$, 400 MHz), δ, ppm: 3.49 (3H, s, OCH_3); 4.32 (2H, s, CH_2); 5.20 (2H, s, NCH_2), 7.25-7.38 (6H, m, H Ar); 7.42-7.50 (4H, m, H Ar); 8.04-8.10 (2H, m, H Ar). ^{13}C NMR spectrum (DMSO-d$_6$, 100 MHz, δ (ppm): 32.6 (CH_2); 45.0 (NCH_2); 52.6 (OCH_3); 110.0; 121.3; 123.0; 127.6; 128.7 (2C); 128.8 (2C); 129.4 (2C); 131.0 (3C); 131.7; 135.9; 136.9; 138.5; 140.1 (18C Ar); 153.8 (C=N); 168.6 (C=O). Found, %: C 72.80; H 4.522; N 7.61. $C_{23}H_{19}ClN_2O_2$. Calculated, %: C 70.68; H 4.90; N 7.17.

Methyl 2-[2-(3-Chlorobenzyl)-4(7)-phenyl-1*H*-benzimidazol-1-yl]acetate (7b). Yield 95%, dark cream powder, mp 129-131 °C. IR (ATR, ν_{max}, cm^{-1}): 3055 (aromatic C-H), 2993, 2954 (aliphatic C-H), 1736 (C=O) 1597, 1512, 1435 (C=C and C=N), 1211, 1157, 748 (C-C, C-N, C-O). ^{1}H NMR spectrum (DMSO-d$_6$, 400 MHz), δ, ppm: 3.49 (3H, s, OCH_3); 4.34 (2H, s, CH_2); 5.23 (2H, s, NCH_2), 7.20-7.38 (6H, m, H Ar); 7.41-7.50 (4H, m, H Ar); 8.04-8.10 (2H, m, H Ar). ^{13}C NMR spectrum (DMSO-d$_6$, 100 MHz, δ (ppm): 32.7 (CH_2); 45.0 (NCH_2); 52.6 (OCH_3); 110.0; 121.2; 123.0; 127,0 127.6; 127.9; 128.7 (2C); 129.0; 129.4 (2C); 130.7; 131.0; 133.4; 136.9; 138.5; 139.4; 140.1 (18C Ar); 153.6 (C=N); 168.6 (C=O). Found, %: C 71.64; H 4.669; N 7.42. $C_{23}H_{19}ClN_2O_2$. Calculated, %: C 70.68; H 4.90; N 7.17.

Methyl 2-[2-(3-Methylbenzyl)-4(7)-phenyl-1*H*-benzimidazol-1-yl]acetate (7c). Yield 88%, light cream powder, mp 143-145 °C. IR (ATR, ν_{max}, cm^{-1}): 3055 (aromatic C-H), 2931 (aliphatic C-H),

1751 (C=O) 1597, 1520, 1427 (C=C and C=N), 1265, 1165, 750 (C-C, C-N, C-O). ^{1}H NMR spectrum (DMSO-d_6, 400 MHz), δ, ppm: 2.22 (3H; s; –CH_3); 3.46 (3H, s, OCH_3); 4.27 (2H, s, CH_2); 5.15 (2H, s, NCH_2), 6.97-7.30 (5H, m, H Ar); 7.33-7.53 (5H, m, H Ar); 8.05-8.10 (2H, m, H Ar). ^{13}C NMR spectrum (DMSO-d_6, 100 MHz, δ (ppm): 21.41 (CH_3); 33.35 (CH_2); 45.05 (NCH_2); 52.54 (OCH_3); 110.98; 121.18; 122.90; 126,20 127.61; 127.66; 128.73 (2C); 128.81; 129.36 (2C); 129.66; 130.95; 136.64; 136.97; 137.99; 138.56; 140.10 (18C Ar); 154.15 (C=N); 168.51 (C=O). Found, %: C 76.27; H 5.435; N 7.47. $C_{24}H_{22}N_2O_2$. Calculated, %: C 77.81; H 5.99; N 7.56.

Methyl 2-[2-(4-Methylbenzyl)-4(7)-phenyl-1*H*-benzimidazol-1-yl]acetate (7d). Yield 86%, cream powder, mp 131-133 °C. IR (ATR, ν_{max}, cm^{-1}): 3032 (aromatic C-H), 2924 (aliphatic C-H), 1735 (C=O) 1597, 1512, 1435 (C=C and C=N), 1226, 1011, 750 (C-C, C-N, C-O). ^{1}H NMR spectrum (DMSO-d_6, 400 MHz), δ, ppm: 2.23 (3H; s; –CH_3); 3.48 (3H, s, OCH_3); 4.27 (2H, s, CH_2); 5.14 (2H, s, NCH_2), 7.04-7.16 (4H, m, H Ar); 7.26-7.53 (6H, m, H Ar); 8.06-8.10 (2H, m, H Ar). ^{13}C NMR spectrum (DMSO-d_6, 100 MHz, δ (ppm): 21.04 (CH_3); 33.02 (CH_2); 45.00 (NCH_2); 52.57 (OCH_3); 109.92; 121.15; 122.86; 127,57; 128.71 (2C); 128.96 (2C); 129.37 (2C); 129.44 (2C); 130.95; 133.69; 136.05; 136.96; 138.59; 140.14 (18C Ar); 154.28 (C=N); 168.51 (C=O). Found, %: C 76.74; H 5.580; N 7.47. $C_{24}H_{22}N_2O_2$. Calculated, %: C 77.81; H 5.99; N 7.56.

Methyl 2-[2-(Benzyl)-4(7)-phenyl-1*H*-benzimidazol-1-yl]acetate (7e). Yield 92%, white powder, mp 96-98 °C. IR (ATR, ν_{max}, cm^{-1}): 3032 (aromatic C-H), 2924 (aliphatic C-H), 1736 (C=O) 1512, 1427 (C=C and C=N), 1211, 1165, 763 (C-C, C-N, C-O). ^{1}H NMR spectrum (DMSO-d_6, 400 MHz), δ, ppm: 3.46 (3H, s, OCH_3); 4.31 (2H, s, CH_2); 5.17 (2H, s, NCH_2), 7.15-7.30 (6H, m, H Ar); 7.32-7.52 (5H, m, H Ar); 8.04-8.10 (2H, m, H Ar). ^{13}C NMR spectrum (DMSO-d_6, 100 MHz, δ (ppm): 33.32 (CH_2); 45.01 (NCH_2); 52.58 (OCH_3); 109.97; 121.18; 122.90; 127.02; 127,60; 128.72 (2C); 128.89 (2C); 129.09 (2C); 129.37 (2C); 130.96; 136.81; 136.94; 138.56; 140.12 (18C Ar); 154.28 (C=N); 168.51 (C=O). Found, %: C 76.64; H 5.369; N 7.32. $C_{23}H_{20}N_2O_2$. Calculated, %: C 77.51; H 5.66; N 7.86.

Methyl 2-[2-(Phenyl)-4(7)-phenyl-1*H*-benzimidazol-1-yl]acetate (7f). Yield 85%, cream powder, mp 130-131 °C. IR (ATR, ν_{max}, cm^{-1}): 3032 (aromatic C-H), 2924 (aliphatic C-H), 1751 (C=O) 1473, 1442 (C=C and C=N), 1211, 987, 694 (C-C, C-N, C-O). ^{1}H NMR spectrum (DMSO-d_6, 400 MHz), δ, ppm: 3.66 (3H, s, OCH_3); 5.24 (2H, s, NCH_2), 7.32-7.50 (5H, m, H Ar); 7.52-7.73 (6H, m, H Ar); 8.08-8.14 (2H, m, H Ar). ^{13}C NMR spectrum (DMSO-d_6, 100 MHz, δ (ppm): 46.42 (NCH_2); 52.99 (OCH_3); 110.44; 121.75; 123.66; 127.72; 128.76 (2C); 129.32 (2C); 128.40 (2C); 129.53 (2C); 130.26; 130.42; 131.55; 137.40; 138.40; 140.43 (18C Ar); 154.28 (C=N); 168.51 (C=O). Found, %: C 76.01; H 5.445; N 7.41. $C_{22}H_{18}N_2O_2$. Calculated, %: C 77.17; H 5.30; N 8.18.

Synthesis of compounds 8a-f: A mixture of compounds **7a-f** (0.01 mol) and hydrazine monohydrate (0.025 mol) in ethanol (4 ml) in a microwave process vial was added. The mixture was irradiated at a ceiling temperature of 120 °C and a maximum power of 850W for 60 min. The reaction mixture was cooled, the mixture was kept overnight in the refrigerator and precipitated. The crude product was filtered off, dried, and recrystallized from EtOH.

2-[2-(4-Chlorobenzyl)-4(7)-phenyl-1*H*-benzimidazol-1-yl]acetohydrazide (8a). Yield 88%, white powder, mp 198-200 °C. IR (ATR, ν_{max}, cm^{-1}): 3309, 3171 (N-H); 3047 (aromatic C-H), 2993 (aliphatic C-H), 1658 (C=O) 1512, 1489, 1442 (C=C and C=N), 1242, 1018, 748 (C-C, C-N, C-O). ^{1}H NMR spectrum (DMSO-d_6, 400 MHz), δ, ppm: 4.30 (2H, s, CH_2); 4.36 (2H, s, NH_2, exchanged with D_2O); 4.80 (2H, s, NCH_2); 7.22-7.50 (10H, m, H Ar); 8.00-8.06 (2H, m, H Ar); 9.50 (1H, s, NH, exchange, D_2O). ^{13}C NMR spectrum (DMSO-d_6, 100 MHz, δ, ppm: 32.59 (CH_2); 45.05 (NCH_2); 109.89; 121.08; 122.76; 127.56; 128.69 (2C); 128.80 (2C); 129.30 (2C); 130.91; 130.98 (2C); 131.64; 136.32; 136.79; 138.57; 140.19 (18 C Ar); 154.05 (C=N); 166.25 (C=O). Found, %: C 67.05; H 4.340; N 14.16. $C_{22}H_{19}N_4O$. Calculated, %: C 67.60; H 4.90; N 14.33.

2-[2-(3-Chlorobenzyl)-4(7)-phenyl-1*H*-benzimidazol-1-yl]acetohydrazide (8b). Yield 83%, white powder, mp 179-182 °C. IR (ATR, ν_{max}, cm^{-1}): 3356, 3286, 3178 (N-H); 3047 (aromatic C-H), 2993 (aliphatic C-H), 1712, 1674 (C=O) 1504, 1427, 1396 (C=C and C=N), 1226, 1157, 1010, 748 (C-C, C-N, C-O). ^{1}H NMR spectrum (DMSO-d_6, 400 MHz), δ, ppm: 4.25 (2H, s, NH_2, exchanged with D_2O); 4.33 (2H, s, CH_2); 4.84 (2H, s, NCH_2); 7.22-7.50 (10H, m, H Ar); 8.00-8.06 (2H, m, H Ar); 9.52 (1H, s, NH, exchange, D_2O). ^{13}C NMR spectrum (DMSO-d_6, 100 MHz, δ, ppm: 32.73 (CH_2); 45.10 (NCH_2); 109.96; 121.08; 122.78; 126.99; 127.57; 127.90; 128.68 (2C); 129.05; 129.29 (2C); 130.66; 130.88; 133.40; 136.75; 138.56; 139.85; 140.20 (18 C Ar); 153.85 (C=N); 166.27 (C=O). Found, %: C 66.38; H 4.052; N 13.74.

$C_{22}H_{19}N_4O$. Calculated, %: C 67.60; H 4.90; N 14.33.

2-[2-(3-Methylbenzyl)-4(7)-phenyl-1*H*-benzimidazol-1-yl]acetohydrazide (8c). Yield 81%, white powder, mp 152-154 °C. IR (ATR, ν_{max}, cm^{-1}): 3302, 3232 (N-H); 3047 (aromatic C-H), 2993 (aliphatic C-H), 1651, 1604 (C=O) 1512, 1435, 1396 (C=C and C=N), 1234, 1165, 1010, 756 (C-C, C-N, C-O). ^{1}H NMR spectrum (DMSO-d_6, 400 MHz), δ, ppm: 2.23 (3H; s; $–CH_3$); 4.26 (2H, s, CH_2); 4.31 (2H, s, NH_2, exchanged with D_2O); 4.77 (2H, s, NCH_2); 6.98-7.50 (10H, m, H Ar); 8.00-8.08 (2H, m, H Ar); 9.49 (1H, s, NH, exchange, D_2O). ^{13}C NMR spectrum (DMSO-d_6, 100 MHz, δ, ppm: 21.44 (CH_3); 33.38 (CH_2); 45.04 (NCH_2); 109.88; 121.00; 122.67; 126.08; 127.55; 127.68; 128.69 (2C); 128.85; 129.32 (2C); 129.61; 130.87; 136.87; 137.07; 138.05; 138.63; 140.21 (18 C Ar); 154.41 (C=N); 166.29 (C=O). Found, %: C 74.08; H 5.729; N 14.87. $C_{23}H_{22}N_4O$. Calculated, %: C 74.57; H 5.99; N 15.12.

2-[2-(4-Methylbenzyl)-4(7)-phenyl-1*H*-benzimidazol-1-yl]acetohydrazide (8d). Yield 91%, white powder, mp 183-184 °C. IR (ATR, ν_{max}, cm^{-1}): 3317, 3163 (N-H); 3032 (aromatic C-H), 2978, 2916 (aliphatic C-H), 1658 (C=O) 1512, 1442, 1396 (C=C and C=N), 1219, 1157, 972, 748 (C-C, C-N, C-O). ^{1}H NMR spectrum (DMSO-d_6, 400 MHz), δ, ppm: 2.23 (3H; s; $–CH_3$); 4.25 (2H, s, CH_2); 4.31 (2H, s, NH_2, exchanged with D_2O); 4.75 (2H, s, NCH_2); 7.05-7.50 (10H, m, H Ar); 8.02-8.08 (2H, m, H Ar); 9.48 (1H, s, NH, exchange, D_2O). ^{13}C NMR spectrum (DMSO-d_6, 100 MHz, δ, ppm: 21.06 (CH_3); 33.04 (CH_2); 45.01 (NCH_2); 109.84; 120.99; 122.65; 126.08; 127.53; 128.69 (2C); 128.87 (2C); 129.32 (2C); 129.52 (2C); 130.87; 134.11; 136.03; 136.86; 138.64; 140.22 (18 C Ar); 154.56 (C=N); 166.29 (C=O). Found, %: C 73.95; H 5.458; N 14.94. $C_{23}H_{22}N_4O$. Calculated, %: C 74.57; H 5.99; N 15.12.

2-[2-(Benzyl)-4(7)-phenyl-1*H*-benzimidazol-1-yl]acetohydrazide (8e). Yield 82%, white powder, mp 150-151 °C. IR (ATR, ν_{max}, cm^{-1}): 3294, 3271 (N-H); 3055 (aromatic C-H), 2939 (aliphatic C-H), 1651 (C=O) 1512, 1472, 1388 (C=C and C=N), 1242, 1165, 918, 694 (C-C, C-N, C-O). ^{1}H NMR spectrum (DMSO-d_6, 400 MHz), δ, ppm: 4.21 (2H, s, NH_2, exchanged with D_2O); 4.30 (2H, s, CH_2); 4.78 (2H, s, NCH_2); 7.15-7.50 (11H, m, H Ar); 8.02-8.06 (2H, m, H Ar); 9.49 (1H, s, NH, exchange, D_2O). ^{13}C NMR spectrum (DMSO-d_6, 100 MHz, δ, ppm: 33.37 (CH_2); 45.02 (NCH_2); 109.87; 121.03; 122.70; 127.01; 127.55; 128.69 (2C); 128.94 (2C); 129.02 (2C); 129.31 (2C); 130.88; 136.83; 137.22; 138.61; 140.20 (18 C Ar); 154.41 (C=N); 166.28 (C=O). Found, %: C 73.02; H 5.246; N 15.42. $C_{22}H_{20}N_4O$. Calculated, %: C 74.14; H 5.66; N 15.72.

2-[2-(Phenyl)-4(7)-phenyl-1*H*-benzimidazol-1-yl]acetohydrazide (8f). Yield 80%, white powder, mp 250-251 °C. IR (ATR, ν_{max}, cm^{-1}): 3302, 3263 (N-H); 3032 (aromatic C-H), 2931 (aliphatic C-H), 1658 (C=O) 1527, 1419, 1388 (C=C and C=N), 1242, 1157, 972, 748 (C-C, C-N, C-O). ^{1}H NMR spectrum (DMSO-d_6, 400 MHz), δ, ppm: 4.40 (2H, s, NH_2, exchanged with D_2O); 4.88 (2H, s, NCH_2); 7.30-7.86 (11H, m, H Ar); 8.08-8.14 (2H, m, H Ar); 9.62 (1H, s, NH, exchange, D_2O). ^{13}C NMR spectrum (DMSO-d_6, 100 MHz, δ, ppm: 46.30 (NCH_2); 110.33; 121.52; 123.36; 127.66; 128.74 (2C); 129.12 (2C); 129.37 (2C); 129.89 (2C); 130.27, 130.47; 131.44; 137.43; 138.50; 140.51 (18 C Ar); 154.15 (C=N); 166.68 (C=O). Found, %: C 74.77; H 5.321; N 16.21. $C_{21}H_{18}N_4O$. Calculated, %: C 73.67; H 5.30; N 16.36.

Enzym assay

Acetylcholinesterase enzyme (AChE) from electric eel, acetylthiocholine iodide (AChI), ascorbic acid (AA), butyrylcholinesterase enzyme (BuChE), butyrylthiocholine iodide (BTCI), 5,5-dithio-bis(2-nitrobenzoic)acid (DTNB), 2,2-diphenyl-1-picrylhydrazyl (DPPH), ethanol, galantamine, kojic acid, $_L$-DOPA, methanol, tyrosinase from mushroom, Trisma-base, phoshomolybdic acid, and quercetin (QE) were purchased from Sigma-Aldrich (St. Louis, MO). Experiments of biological activities were performed by Multikan^{Tm} Go Microplate Spectrophotometer.

ENZYME INHIBITION

AChE/BuChE inhibition assays

AChE/BuChE inhibition was examined using the method described by Ingkaninan et al. [25]. All of the compounds were prepared as stock solutions in 20% DMSO. 50 mM Tris-HCl buffer (pH 8.00), 3 mM DTNB (in buffer), 0.2 U/mL AChE/BuChE and compounds at 100 µM were added in a 96-well microplate. The mixtures were incubated for 15 min at 25 °C. After incubation, 15 mM AChI/BTCI was added in a microplate and incubated for 5 min at room temperature. The absorbance was measured at 412 nm using a 96-well microplate reader. Galantamine was used as the positive control. AChE/BuChE inhibition percentage was calculated at 100 µM using the Formula 1. Where $A_{control}$ is the activity of enzyme without compound and $A_{compound}$ is the activity of enzyme with compound at different concentrations. The experiments were carried out in

triplicate and results were expressed as the mean ± standard deviation (SD).

Formula 1. Formula for both enzyme inhibition and scavenging percentage:

$$Inhibition\ \% = \frac{(Acontrol - Acompound)}{Acontrol} \times 100$$

Tyr inhibition assay

The Tyr inhibitions of compounds were investigated using the method described by Masuda et al. [26]. The compounds at 100 µM, 250 U/mL tyrosinase and 100 mM pH 6.8 phosphate buffer solutions were added in a 96-well microplate. The mixtures were incubated for 10 min at room temperature. Then, 3 mM L-DOPA was added and the microplate was further incubated at room temperature for 20 min. Subsequently, the absorbance of dopachrome was measured at 475 nm using a 96-well microplate reader. Kojic acid was used as the positive control. Tyr inhibitions percentage was calculated at 100 µM using Formula 1.

DPPH radical scavenging assay

The DPPH radical scavenging activities were examined using the method described by Blois compared to ascorbic acid as the reference compound [27]. The total volume of assay mixture was 1 mL containing methanolic DPPH solution (0.4 mM) and at 100 µM of compounds. The mixtures were incubated for 30 min at room temperature in the dark. After incubation, the mixtures were measured at 517 nm and scavenging percentage was calculated using Formula 1.

Phosphomolybdenum-reducing antioxidant power (PRAP) assay

PRAP of compounds were examined using phosphomolybdic acid [28]. The total volume of assay mixture was 1 mL containing 10% phoshomolybdic acid solution in ethanol (w/v) and at 100 µM of compounds. The mixtures were incubated for 30 min at 80 ºC. After incubation, the absorbance was measured at 600 nm. PRAP of compounds was expressed absorbance at 100 µM and compared with quercetine as reference compound.

Ferric-Reducing Antioxidant Power (FRAP) Assay

FRAP of compounds was examined using the method described by Oyaizu [29]. 1 mL of various concentrations of the extracts and BHA as the reference compound were added to 1 mL of phosphate buffer (pH 6.6) and 1 mL of 10% (w/v) potassium ferricyanide. The mixtures were incubated at 50 °C for 20 min and then 1 mL of 10% trichloroacetic acid was added. After vigorous shaking, the solutions were mixed with 1 mL distilled water and 150 µL of 0.15% $FeCl_3$. The mixtures were incubated for 30 min at room temperature in the dark. After incubation, the absorbance was measured at 700 nm. FRAP of compounds was expressed absorbance at 100 µM and compared with BHA as reference compound.

RESULTS AND DISCUSSION

Chemistry

Since both the ester derivatives (**7a-f**) and the hydrazide derivatives (**8a-f**) are new, spectral analysis of each compound were made. The spectral data (IR, ^{1}H-NMR, ^{13}C-NMR) results of these new compounds were consistent with the literatures [30-33].

The IR spectra of compounds **7a-f** showed the characteristic bands at 1735-1751 cm^{-1} for ester C=O groups, at 3055-3032 cm^{-1} for aromatic C-H groups. IR absorption band appeared at 1597- 1427 cm^{-1} and 1265-1010 cm^{-1} were assigned to C=C, C=N and C-C, C-N functions in the benzimidazole structure, respectively. In the final compounds, **8a-f**, the hydrazide group is in place of the ester group. So, IR absorption band appeared at 3356-3171 cm^{-1} was assigned to NH atoms.

In case of ^{1}H-NMR spectral analysis of compounds **7a-f**, the methyl and methylene groups have a chemical shift because of their *neighboring protons and have been* appeared as a singlet. The methyl protons (-COOC$\underline{H}_3$) which next to the presence of ester carbonyl, oxygen groups, giving peak in 3.46-3.66 ppm range; the methylene protons (-ArC$\underline{H}_2$-Ph) which next to the presence of substitute phenyl ring and benzimidazole groups, giving peak in 4.27-4.34 ppm range and the methylene protons (-NC$\underline{H}_2$-COO) which next to the presence of ester carbonyl and benzimidazole groups, giving peak in 5.14-5.24 ppm range. Aromatic protons were seen where expected (δ = 6-8 ppm regions). In the compounds **8a-f**, the positions of the protons in the hydrazide group were determined by exchange of deutero-solvent. The ^{1}H-NMR spectra of compounds **8a-f** showed the presence of a singlet at δ = 4.21-4.40 ppm for the hydrazide-NH_2 proton, and hydrazide-NH protons appeared at δ = 9.48–9.62 ppm.

^{13}C-NMR spectrum of compounds **7a-f** and **8a-f**, gives signal at 153.85-154.56 (C=N) and 166.25-166.68 (C=O) ppm and the aromatic field were observed at 109.84–140.51 ppm. All peaks were

observed at expected locations in accordance with literature data [30-33].

The elemental analysis results confirm the carbon, nitrogen, hydrogen and oxygen fractions of the compounds.

Enzyme activity. Enzyme Inhibition

The AChE/BuChE inhibition of compounds was measured by Ingkaninan's assay with galantamine as a standard drug. AChE/BuChE inhibition results of compounds were expressed as inhibition (%) values were presented in Table 1. The solubility of benzimidazole derivative compounds decreases at basic pH. No activity was detected in the solutions prepared for the AChE/BuChE enzyme since the substances precipitated in the pH 8 buffer. The results showed that tested compounds did not inhibit against AChE/BuChE. However, inhibition of compounds and standard drug on tyrosinase enzyme were illustrated in Table 1. The inhibition ratios of tyrosinase by the compounds were measured at the concentrations of 100 µM, as shown in Table 1. **8f** and **7c** exhibited the highest tyrosinase inhibition with 52.46 ± 2.67% and 52.32 ± 0.70%, respectively. In addition, **7a**, **7b**, **7d** and **8d** demonstrated tyrosinase inhibition more than 45.00 % at 100 µM. These results showed that, these compounds have promising candidates for tyrosinase inhibitors.

Table 1. AChE, BuChE and Tyr enzyme inhibition of compounds at 100 µM.

Compounds	AChE at 100 µM (%)	BuChE at 100 µM (%)	Tyr at 100 µM (%) ± SD
7a	Nd	Nd	45.22 ± 0.39
7b	Nd	Nd	49.43 ± 2.04
7c	Nd	Nd	52.32 ± 0.70
7d	Nd	Nd	47.00 ± 0.36
7e	Nd	Nd	43.68 ± 2.63
7f	Nd	Nd	39.63 ± 1.84
8a	Nd	Nd	40.27 ± 1.32
8b	Nd	Nd	35.59 ± 1.68
8c	Nd	Nd	39.36 ± 1.24
8d	Nd	Nd	46.31 ± 1.05
8e	Nd	Nd	41.03 ± 3.87
8f	Nd	Nd	52.46 ± 2.67
Galantamine	88.03 ± 0.31	79.30 ± 0.26	-
Kojic Acid	-	-	85.48 ± 0.40

*nd: no data ** SD: Standart deviation

Table 2. DPPH, PRAP and FRAP activities of compounds **7a-f** and **8a-f** at 100 µM.

Compounds	DPPH at 100 µM (%) ± SD	PRAP at 100 µM (Absorbance) ± SD	FRAP at 100 µM (Absorbance) ± SD
7a	11.25 ± 0.11	0.132 ± 0.002	0.236 ± 0.004
7b	14.50 ± 0.24	0.142 ± 0.007	0.263 ± 0.007
7c	21.42 ± 0.71	0.169 ± 0.010	0.326 ± 0.010
7d	13.50 ± 0.41	0.141 ± 0.004	0.247 ± 0.007
7e	14.71 ± 0.83	0.135 ± 0.010	0.269 ± 0.006
7f	9.26 ± 0.28	0.125 ± 0.006	0.194 ± 0.002
8a	13.48 ± 0.44	0.121 ± 0.003	0.227 ± 0.002
8b	12.26 ± 0.36	0.128 ± 0.005	0.217 ± 0.001
8c	9.62 ± 0.85	0.121 ± 0.001	0.179 ± 0.002
8d	16.05 ± 0.57	0.127 ± 0.004	0.294 ± 0.011
8e	17.27 ± 0.69	0.157 ± 0.009	0.271 ± 0.003
8f	24.83 ± 1.28	0.180 ± 0.013	0.358 ± 0.009
AA	84.02 ± 0.09	-	-
QE	-	0.849 ± 0.022	-
BHA	-	-	1.426 ± 0.014

*SD: Standard deviation

Antioxidant activities

In this work, DPPH radical scavenging activities, PRAP and FRAP reducing antioxidant power assay of compounds have been investigated spectrophotometrically method and their results were presented in Table 2. All the compounds

displayed moderate DPPH radical scavenging activities when compared to AA. **8f** had the highest radical scavenging activities with 24.83 ± 1.28% among the compounds whilst **8c** showed the lowest activities with 9.62 ± 0.85%. PRAP assay was based on the reduction of Mo(VI) to Mo(V) by the compounds. The highest absorbance values of the compounds at 600 nm exhibited a higher reducing antioxidant power. All of the compounds showed the lowest values at 100 μM when compared to quercetin as standard compound. **8f** and **7c** gave the highest absorbance values with 0.180 ± 0.013 and 0.169 ± 0.010 at 100 μg/mL, respectively. The ferric reducing antioxidant power (FRAP) assay was a fast method to determine the antioxidant potential of compounds. . The compounds capacity to reduce Fe^{3+} to Fe^{2+} was determined and the results were shown in Table 2. The results of this study demonstrated that compounds have a moderate ferric reducing power. **8f** has the highest absorbance values with 0.358 ± 0.009 at 100 μM. All of these results showed that, the newly synthesized compounds have moderate antioxidant activities when compared to standard compounds.

CONCLUSION

All the synthesized molecules were achieved in excellent yields using a simple method. The projected structures of synthesized compounds were well supported by the spectral characterization data by IR, ^{1}H-NMR, ^{13}C-NMR and elemental analysis.

The antioxidant, AChE/BuChE and tyrosinase inhibition properties of all compounds were evaluated. The tested compounds did not inhibit against AChE/BuChE. The phenyl substituted hydrazide derivative compound **8f** and the 4-methylbenzyl substituted ester derivative compound **7c** showed the highest tyrosinase inhibition with 52.46 ± 2.67% and 52.32 ± 0.70%, respectively. **8f** had the highest radical scavenging activities with 24.83 ± 1.28% among the compounds whilst **8c** showed the lowest activities with 9.62 ± 0.85%. **8f** gave the highest PRAP and FRAP absorbance values with 0.180 ± 0.013 and 0.358 ± 0.009 at 100 μM, respectively. All of these results demonstrated that the newly synthesized compounds have moderate antioxidant and tyrosinase inhibition activities when compared to standard compounds.

In our previous work [23], we have synthesized benzimidazole derivatives **6a-f** compounds, when we evaluated the tyrosine inhibition activity, 4-chlorobenzylsubstitued benzimidazole derivative **6a**, 3-chlorobenzylsubstituted benzimidazole derivative **6b** and 3-methylbenzylsubstitued benzimidazole derivative **6d**, were found to be the most active derivatives. In this study, we evaluated tyrosine inhibition activity of compounds **7a-f** obtained from the esterification of **6a-f** derivatives. The compounds **7a-d** (4-chloro/3-chloro/4-methyl/3-methylbenzylsubstituted compounds) were found to be active. It can be said that the ester derivatives do not show much difference in activity compared to the benzimidazole derivatives. According to the activity results of the hydrazide derivatives **8a-f** compounds, the tyrosine inhibition activity was quite good in the phenyl derivative **8f** compound. The 4-methylbenzyl derivative **8c** showed very low activity. The high activity of the phenyl substituted derivative, compound **8f**, suggested that activity may be high in the aryl derivatives, with reduced activity in the arylalkyl derivative **8a-8e** compounds. Activity evaluation can be done by testing different aryl, heteroaryl derivatives.

Acknowledgments. *This research was financially supported by Artvin Coruh University Scientific Research Projects Fund (BAP-2016.F34.02.01).*

REFERENCES

1. B. Kahveci and E. Menteşe, *Curr. Microwave Chem.*, **4**, 73 (2017).
2. J. Asteinza, R. Camacho-Carranza, R. E. Reyes-Reyes, V. D. Gonzales, J. J. Espinosa-Aguirre, *Env. Tox. and Pharm.*, **9**, 31 (2000).
3. J. D. Baggot, Q. A. McKellar, *J. of Vet. Pharm. and Therap*., **17**, 409 (1994).
4. S. Jiang, J. Meadows, S. A. Anderson, A. Mukkada, *Antimicrob. Agents Chemother*., **46**, 2569 (2002).
5. N. Dzeletovic, J. McGuire, M. Daujat, J. Tholander, M. Ema, Y. Fujii-Kuriyama, J. Bergman, P. Maurel., L. Podlinger, *Journal of Biological Chem*., **272**, 12705 (1997).
6. J. Pérez-Villanueva, A. Romo-Mancillas, A. Hernández-Campos, L. Yépez-Mulia, F. Hernández-Luis, R.Castillo, *Bioorg Med. Chem. Lett*., **21**, 7351 (2011).
7. D. J. Brown, W. C. Dunlap, G. W. Grigg, L. Danckwerts, *Aust. J. Chem.*, **31**, 447 (1978).
8. H. Abou-Shadı, G. El-Taliawi, I. Nabih, M. M. Kamel, A. Zayed, L. M. Faddah, *Pharmazie*, **34**, 576 (1979).
9. E. S. Charles, V. K. Agrawal, S. Sharma R. N. Iyer, O. P. Srivastava, *Eur. J. Med. Chem.-Chim. Therap.*, **14**, 435 (1979).
10. S. Özden, T. Özden, F. Gümüş, S. Akın, *Ankara Ecz. Fak. Der.*, **16**, 37 (1986).
11. P. R. Naik, N. S. Pandeya, A. Pandey, *Acta Pharm. Turcica*, **38**, 37 (1996).
12. T. Hisano, M. Ichikawa, K. Tsumoto, M. Tasaki, *Chem. Pharm. Bull*., **30**, 2996 (1982).
13. C. J. Pfau, K. P. Camyre, *Virology,* **35,** 375 (1968).

14. I. Tamm, H. J. Eggers, R. Bablanian, A. F. Wagner, K. Folkers, *Nature*, **223,** 785 (1969).
15. F. Gualtiere, G. Brody, A. H. Fieldsteel, W.A. Skinner, *J. Med. Chem.*, **15**, 420 (1972).
16. I. Kerimov, *Ankara University Institute of Health Sciences*, PhD. Thesis, pp. 34–39 (2011).
17. C. Kuş, *Ankara University Institute of Health Sciences*, PhD. Thesis, p. 68 (1998).
18. K. Ingkaninan, P. Temkitthawon, K. Chuenchom, T. Yuyaem, W. Thongnoi, *J. of Ethnopharmacology*, **89**, 261 (2003).
19. M. Mohammadi-Khanaposhtani, M. Saeedi, N. S. Zafarghandi, M. Mahdavi, R. Sabourian, E. K. Razkenari, H. Alinezhad, M. Khanavi, A. Foroumadi, A. Shafiee, T. Akbarzadeh, *Eur. J. of Med. Chem.*, **92**, 799 (2015).
20. F. S. Senol, I. E. Orhan, M. Kurkcuoglu, M. T. H. Khan, A. Altintas, B. Sener, K. H. C. Baser, *Food Research International*, **53**, 502 (2013).
21. E. Neagu, G. Paun, C. Albu, G. L. Radu, *J. of the Taiwan Institute of Chem. Engineers*., **52**, 1 (2015).
22. K. K. Nanda, D. A. Henze, K. D. Penna, R. Desai, M. Leitl, W. Lemaire, M. T. Bilodeau, B. W. Trotte, *Bioorg. & Med. Chem. Lett.*, **24**, 1218 (2014).
23. İ. S. Doğan, A. Özel, Z. Birinci, B. Barut, H. E. Sellitepe and B. Kahveci, *Archiv der Pharmazie*, **349**, 881 (2016).
24. E. Menteşe, S. Ülker and B. Kahveci *Chemistry of Heterocyclic Compounds*, **50**, 1671 (2015).
25. K. Ingkaninan, D. Best, V. D. Heijden, A. J. P. Hofte, B. Karabatak, H. Irth, U. R. Tjaden, V. D. Greef, R. Verpoorte, *J. Chromatogr. A*, **872**, 61 (2000).
26. T. Masuda, D. Yamashita, Y. Takeda, S. Yonemori, *Bioschi. Biotechnol. Biochem.*, **69**, 197 (2005).
27. M. S. Blois, *Nature*, **181**,1199 (1958).
28. G. Falcioni, D. Fedeli, L. Diano, I. Calzuola, L. Mancinelli, V. Marsili, G. Gianfranceschi, *J. Food Sci.*, **67**, 2918 (2002).
29. M. Oyaizu, *Jpn. J. Nutr*., **44**, 307 (1986).
30. D.J. Rabiger, M.M. Joullié, *J. Org. Chem.*, **29**, 476 (1964).
31. R. M. Silverstein, F.X. Webster, (6th edn.), *Spectrometric Identification of Organic Compounds*, John Wiley & Sons Inc., New York (1998).
32. E. Pretsch, T. Clerk, J. Seibl, W. Simon, *Tables of Spectral Data for Structure Determination of Organic Compounds*, Springer-Verlag, Berlin (1983).
33. R. W. Layer, *Chem. Rev.*, **63**, 489 (1963).

Bulgarian Chemical Communications, Volume 49, Issue I (pp.115 – 121) 2017

Metal complexes of perimidine and Schiff base ligands bearing both naphthalene and chromone moieties: synthesis and catalytic activity

N. Beyazit*, S. Çobanoğlu, C. Demetgül

Mustafa Kemal University, Chemistry Department, Faculty of Arts and Sciences, 31060 Hatay/Turkey

Submitted May 22, 2017; Revised September 1, 2017

A new perimidine and a new Schiff base compounds were prepared by the condensation of visnagin derivative containing a carbonyl group with 1,8-diaminonaphthalene (1,8-DAN) and 2,3-diaminonaphthalene (2,3-DAN), respectively. Metal complexes of these chromone type ligands were also isolated by using the Cu(II) and Fe(II) ions. The synthesized compounds were characterized by UV-Vis, FT-IR, ^{1}H&^{13}C NMR, mass spectrometry, elemental and AAS analyses and also magnetic susceptibility and molar conductivity measurements. Catecholase activity of the complexes was investigated in methanol medium using 3,5-di-*tert*-butylcatechol (3,5-DTBC) as model substrate and the results showed that all complexes are active for catalyzing the oxidation of 3,5-DTBC to the corresponding quinone with first order reaction kinetics. Fe(II) complex of Schiff base ligand has been found to exhibit the best catecholase activity with a turnover number value of 890.1 h^{-1}.

Keywords: Schiff base, perimidine, metal complexes, catecholase activity

1.INTRODUCTION

Coordination chemistry has received a great deal of attention for a long time of period with the synthesis and characterization of a large number of transition metal complexes with various ligand systems containing nitrogen and oxygen donor atoms owing to their wide applications in various fields such as biological [1], analytical [2], material science [3] and catalysis [4]. Among these ligand systems, while Schiff bases have been studied extensively for decades [5,6], in recent years considerable attention has been drawn to perimidines as they have electron affinity, reduction potential and also exhibit diverse range of biological activities [7]. Synthetic method for the preparation of perimidines is the condensation reaction of 1,8-diaminonaphthalene (1,8-DAN) with various carbonyl groups, which requires a special reagent or force reaction conditions. Usually the product of this condensation is Schiff base, however when 1,8-DAN is used as primer diamine it can be obtained perimidine or its derivatives [8]. Although it is well-documented that metal complexes of salen type Schiff bases can be easily prepared [9], only a few studies dealt with metal complexes of perimidine derivatives in which the metal is bound to one nitrogen and to another donor atom introduced on a ring present on C-2 [10-14].

In this paper, we present the synthesis of a Schiff base and a 2,3-dihydro-1*H*-perimidine derivative obtained from the condensation of visnagin based carbonyl compound with 2,3-diaminonaphthalene (2,3-DAN) and 1,8-diaminonaphthalene (1,8-DAN), respectively. The synthesis, characterization and catecholase-like activity investigations of their mononuclear copper (II) and iron(II) complexes were also reported. Catecholase-like activity of metal complexes via oxidation of 3,5-di-*tert*-buthylcatechol (3,5-DTBC) to 3,5-di-*tert*-buthylquinone (3,5-DTBQ) was performed.

2.EXPERIMENTAL

2.1. Material

2,3-diaminonaphthalene, 1,8-diaminonaphthalene, copper(II) chloride ($CuCl_2$), iron(II) chloride tetrahydrate ($FeCl_2.4H_2O$), hydrogen peroxide (H_2O_2) solution (30 wt. % in H_2O), 3,5-di-*tert*-butylcatechol (3,5-DTBC) were purchased from Sigma-Aldrich and used without further purification. Solvents for the synthesis and analysis were commercially available and used as received.

2.2. Physical measurements

Melting points were determined on a Thermo Scientific 9100 apparatus using open capillary and the reported values are uncorrected. Elemental analyses (carbon, hydrogen and nitrogen) were carried out using a THERMO SCIENTIFIC Flash 2000 CHNS/O Analyzer, and the results agree with the calculated values. The FT-IR spectra of the samples were recorded on a Perkin Elmer Spectrum Two with U-ATR FTIR spectrometer in the wavenumber range of 4000–400 cm^{-1}. Electronic spectra were recorded in a OPTIZENα UV-Vis Spectrometer. ^{1}H NMR (600 MHz) and ^{13}C NMR (600 MHz) spectra were recorded in $CDCl_3$ on a Bruker Advance III HD spectrometer using TMS as

*) To whom all correspondence should be sent:
E-mail:nbeyazit@mku.edu.tr;
beyazitneslihan@gmail.com

an internal standard. Molar ionic conductance of the complexes were determined in dimethyl sulphoxide using a solution of about 10^{-3} M concentration on a Jenway Model 4070 conductivity meter. The magnetic susceptibilitiy measurements on powder form of the complexes were carried out with a Sherwood magnetic susceptibility balance (Model MK1) using $MnCl_2.4H_2O$ as calibrant at room temperature. Mass spectra were obtained either on an Agilent LC/MSD spectrometer using the ESI technique or on a Thermo Finnigan LCQ Advantage MAX using the ESI technique. Thin-layer chromatography (TLC) was performed on Merck silicagel plates ($60F_{254}$), and detection was carried out with ultraviolet light (254 and 366 nm).

2.3. Synthesis of free ligands, L^1 and L^2

Visnagin derivative starting material, *6-formyl-7-hydroxy-5-methoxy-2-methylbenzopyran-4-one* **(1)**, was prepared according to the reported method by our group [15]. For the synthesis of **L^1**, a mixture of **1** (0.47 g, 2 mmol) and 2,3-DAN (0.16 g, 1 mmol) in 95% ethanol (50 mL) was refluxed for 2h. For preparing of **L^2**, 0.23 g (1mmol) of **1** and 0.16 g (1 mmol) of 1,8-DAN was refluxed for 2h in 95% ethanol (50mL). The precipitates were filtered off, recrystallized from hot ethanol and dried.

L^1. (Yellow solid) Yield 81%; M.p.: 296-297ºC. Calculated for $C_{33}H_{26}N_2O_8$ (590.17): C, 69.15; H, 4.44; N, 4.74. Found C, 68.97; H, 4.72; N, 4.91. Selected IR data (ATR, cm^{-1}): 3045 (Aromatic C-H), 2843 (Aliphatic C-H), 1660 (C=O), 1605 (C=N). UV-Vis in DMSO (nm): 280, 350, 480. ^{1}H NMR (600 MHz, $CDCl_3$): δ, ppm 2.32 (s, 6H, Chromone-CH_3), 4.03 (s, 6H, Chromone-OCH_3), 6.00 (s, 2H, H-3 and H-3'), 6.75 (s, 2H, H-8 and H-8'), 7.54 (*dd*, 2H, Naph-H), 7.66 (s, 2H, Naph-H), 7.92 (*dd*, 2H, Naph-H), 9.23 (s, 2H, CH=N), 14.53 (s, 2H, Ar-OH). ^{13}C NMR (600 MHz, APT, $CDCl_3$): δ, ppm 19.95(CH_3), 64.27(OCH_3), 101.00 (CH), 110.45 (C), 111.44 (CH), 111.79 (C), 117.24 (CH), 126.86 (CH), 127.91 (CH), 132.88 (C), 142.00 (C), 159.74 (CH=N), 161.63 (C), 162.85 (C), 163.90 (C), 165.76 (C), 176.43 (C=O). MS (+ESI): *m/z* 591.3 $[M+H]^+$.

L^2. 6-(2,3-dihydro-*1H*-perimidin-2-yl)-7-hydroxy-5-methoxy-2-methyl-4H-chromen-4-one. (Gray solid) Yield 68%; M.p.: 170-171ºC. Calculated for $C_{22}H_{18}N_2O_4$ (374.13): C, 70.58; H, 4.85; N, 7.48. Found C, 70.07; H, 4.97; N, 7.63. Selected IR data (ATR, cm^{-1}): 3329 (N-H), 3251(N-H), 3048 (Aromatic C-H), 2925 (Aliphatic C-H), 1650 (C=O). UV-Vis in DMSO (nm): 290, 330, 350. ^{1}H NMR (600 MHz, $CDCl_3$): δ, ppm 2.32 (s, 3H, Chromone-CH_3), 3.89 (s, 3H, Chromone-OCH_3), 5.07(s, 2H, N-H), 5.98(s, 1H), 6.06 (s,1H), 6.51 (s, 1H, H-8), 6.75-7.35 (m, 6H, Naph-H), 10.33 (s, 1H, Ar-OH). ^{13}C NMR (600 MHz, APT, $CDCl_3$): δ, ppm 19.95(CH_3), 61.74(CH), 63.86(OCH_3), 101.05(CH), 107.79(CH), 110.44(C), 111.36(CH), 114.14(C), 115.42(C), 119.20(C), 126.84 (CH), 134.66(C), 141.12(C), 158.47(C), 159.47 (C), 162.73(C), 164.01(C), 176.78 (C=O). MS (+ESI): *m/z* 375.1 $[M+H]^+$.

2.4. Synthesis of the metal complexes

A hot solution of MCl_2 (M = Fe or Cu) (1 mmol) in ethanol (30 mL) was added dropwise to a refluxing solution of **L^1** (0.59 g, 1 mmol) or **L^2** (0.37 g, 1 mmol) in chloroform (50 mL). The synthesis process of Fe(II) complexes was performed under nitrogen atmosphere. After refluxing for 2 hours, the resulting solution was concentrated to 10 mL. In case of no precipitation, pure water was added into the final solution dropwisely until precipitation occurs. The precipitates were collected by filtration and dried in vacuum under pressure to obtain metal complexes.

$[CuL^1(H_2O)_2]$. The product isolated as light brown powder was obtained after recrystallization from DMSO. Yield 63%. Calculated for $C_{34}H_{28}CuN_2O_{10}$ (687.1): C, 59.34; H, 4.10; N, 4.07; Cu, 9.23. Found C, 59.01; H, 4.32; N, 4.19; Cu, 9.07. Selected IR data (ATR, cm^{-1}): 2828 (Aliphatic C-H), 1650 (C=O), 1600 (C=N), 567-466 (M-O and M-N). UV-Vis in DMSO (nm): 280, 300, 350, 520. MS (+ESI): *m/z* 711.2 $[M+H+Na]^+$. Λ(DMSO) 7.3 Ω^{-1} cm^2 mol^{-1}; μ_{eff} : 1.79 B.M.

$[FeL^1(H_2O)_2]$. The product isolated as dark brown powder was obtained after recrystallization from DMSO. Yield 70%. Calculated for $C_{34}H_{28}FeN_2O_{10}$ (680.11): C, 60.01; H, 4.15; N, 4.12; Fe, 8.21. Found C, 59.87; H, 4.39; N, 4.32; Fe, 8.55. (Selected IR data (ATR, cm^{-1}): 2840 (Aliphatic C-H), 1650 (C=O), 1598 (C=N), 567-447 (M-O and M-N). UV-Vis in DMSO (nm): 280, 300, 350, 520. MS (+ESI): *m/z* 681.4 $[M+H]^+$. Λ(DMSO) 7.8 Ω^{-1} cm^2 mol^{-1}; μ_{eff} : 4.77 B.M.

$[CuL^2(H_2O)_4]$. The product isolated as light brown powder was obtained after recrystallization from DMSO. Yield 55%. Calculated for $C_{22}H_{24}CuN_2O_8$ (507.08): C, 52.02; H, 4.76; N, 5.51; Cu, 12.51. Found C, 51.86; H, 4.92; N, 5.69; Cu, 12.09. Selected IR data (ATR, cm^{-1}): 3272 (N-H), 3056 (Aromatic C-H), 2923 (Aliphatic C-H), 1653 (C=O), 564-400 (M-O and M-N). UV-Vis in DMSO (nm): 270, 290, 350, 410, 450, 680. MS (+ESI): *m/z* 529.54

$[M+Na]^+$. Λ(DMSO) 5.6 Ω^{-1} cm^2 mol^{-1}; μ_{eff} : 1.89 B.M.

$[FeL^2(H_2O)_4]$. The product isolated as dark brown powder was obtained after recrystallization from DMSO. Yield 72%. Calculated for $C_{22}H_{24}FeN_2O_8$ (500.9): C, 52.82; H, 4.84; N, 5.60; Fe,11.16. Found C, 52.22; H, 5.1; N, 5.72; Fe, 11.01. Selected IR data (ATR, cm^{-1}): 3299 (N-H), 3063 (Aromatic C-H), 2924 (Aliphatic C-H), 1655 (C=O), 561-460 (M-O and M-N). UV-Vis in DMSO (nm): 270, 340, 360, 600. MS (+ESI): *m/z* 501.39 $[M+H]^+$. Λ(DMSO) 5.1 Ω^{-1} cm^2 mol^{-1}; μ_{eff} : 4.83 B.M.

2.5. Catecholase activity

The catecholase activity of the prepared metal complexes was evaluated by using 3,5-DTBC as the substrate. The reactions were monitored spetrophotometrically by following the absorption increase at c.a. 400 nm of the corresponding quinone (3,5-DTBQ). To measure the ability of complexes to oxidize 3,5-DTBC, 2.10^{-5} M methanolic solution of complexes were treated with 2.10^{-3} M of 3,5-DTBC at room temperature in the presence of H_2O_2 (as an oxygen source). Absorbance *vs* wavelength plots were recorded for the resultant reaction mixture at a regular time interval of 2 min in the range 300–500 nm. To determine the dependence of the rates and kinetic parameters such as V_{max}, K_m and k_{cat}, the kinetics measurements were performed by using the initial rate method at 25°C for all complexes.

3. RESULTS AND DISCUSSION

3.1. Syntheses

A new 2,3-dihydro-1*H*-perimidine derivative, a new Schiff base ligand and their Cu(II) and Fe(II) complexes were prepared and the structures have been confirmed by studying their physical and spectral properties. The synthetic routes for ligands are given in Scheme 1. The obtained results of micro-analysis, molar conductivity and magnetic susceptibility measurements for the synthesized compounds are consistent with the calculated results from empirical formula of all molecules. The lower molar conductance values (5.1-7.8 Ω^{-1} cm^2 mol^{-1}) in DMSO support the non-electrolytic nature of all the metal complexes, indicating that there are no counter ions in the proposed structures [16]. Magnetic measurements were recorded at room temperature and they were in the range of 1.79-1.89 and 4.77-4.83 B.M. for Cu(II) and Fe(II) complexes, respectively, suggesting octahedral geometry [17]. The proposed structures of the complexes are given in Figure 1.

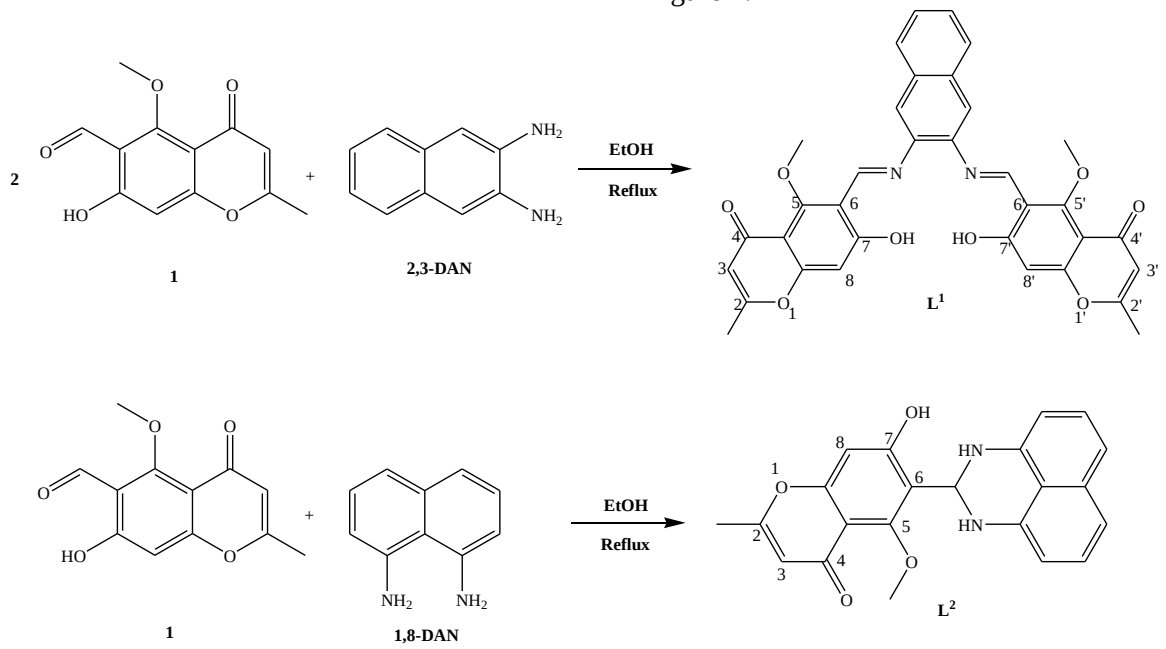

Scheme 1. Synthesis of free ligands.

3.2. Electronic spectra

The electronic absorption spectra in the UV-Visible region of the ligands and their metal complexes were measured using freshly prepared 10^{-4} M solutions in DMSO. In the 270-350 nm region, the spectra exhibit the strong broad absorption bands for both perimidine and Schiff base ligands, indicating π-π* and n-π* transitions of azomethine groups and aromatic rings. In the spectra of all metal complexes, the weak bands at longer wavelengths (450-680 nm) might be attributed to d-d transitions of metal ions [18].

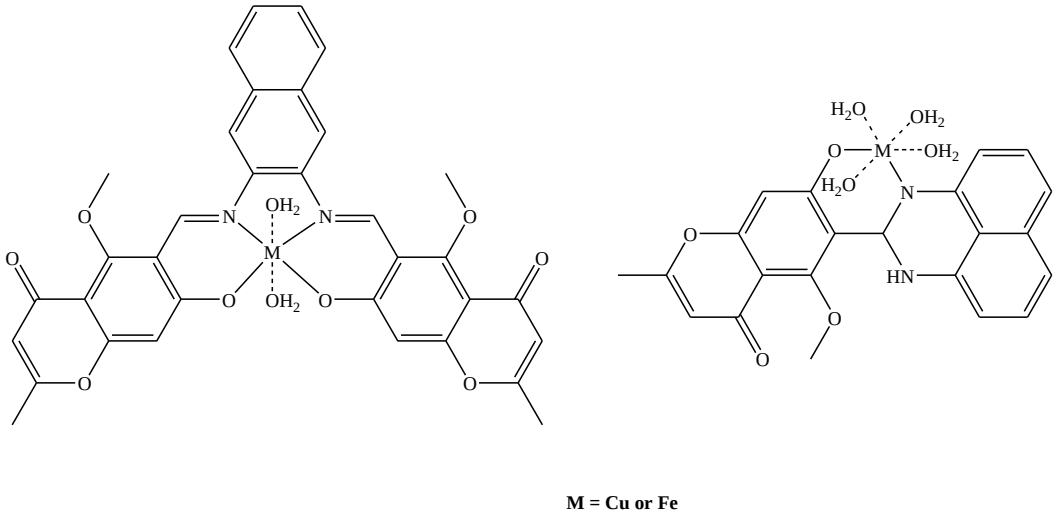

Figure 1. The proposed structures of Schiff base and perimidine metal complexes.

3.3. FT-IR spectra

In the FT-IR spectrum of **L²**, two bands with medium intensity were observed at 3329 and 3251 cm^{-1} attributing to two N-H stretching vibrations of perimidine ring. The strong bands appeared at 1650 and 1594 cm^{-1} can assigned to carbonyl absorption of chromone ring and C=C stretching vibrations, respectively. The FT-IR spectra of perimidine Cu(II) and Fe(II) complexes revealed a medium, broad band at 3272 and 3299 cm^{-1}, respectively, attributing to a N-H stretching vibration and this indicates that one of the N-H groups of perimidine ring is not coordinated to the metal ion. Furthermore, the coordination of perimidine ring to the metal ion is supported by the existence of medium intensity bands in the region 460-564 cm^{-1} due to M-N and M-O stretching vibrations [10]. In the FT-IR spectrum of **L¹**, two sharp peaks observed at 1660 and 1605 cm^{-1} are due to carbonyl and azomethine groups, respectively. The absorption bands of carbonyl and azomethine groups have been shifted to lower frequencies in Cu(II) and Fe(II) complexes of Schiff base, indicating the involvement of oxygen and nitrogen atoms in complexation with the metal ions. This is further confirmed by appearance of the new bands in the region 466-567 cm^{-1} attributing to M-N and M-O stretching vibrations [19].

3.4. NMR spectra

The ^{1}H NMR spectrum of **L¹** in $CDCl_3$ showed two significant singlets at 9.23 and 14.53 ppm, corresponding to the azomethine (CH=N) and phenolic protons (Ar-OH), respectively. The signals in the range of 6.00-7.92 ppm were assigned to the aromatic protons on the naphthalene and chromone rings. Two sharp singlets were observed at 2.32 and 4.03 ppm due to methyl and methoxy protons, respectively. In the ^{13}C APT NMR spectrum of **L¹**, the total count of the carbon peaks matched well with the composition of the compound. The positive signal at 159.74 ppm clearly indicates the presence of methine carbon at imine (CH=N) group. The negative signal at 176.43 ppm was attributed to the quaternary carbon of carbonyl group in the chromone ring. The quaternary carbon atoms belong to the chromone ring and adjacent to the oxygen atoms were appeared as four negative signals in the region 161.63-165.76 ppm in the APT spectrum of **L¹**. In the ^{1}H NMR spectrum of **L²**, the singlets appear at 2.32, 3.89 and 10.33 ppm were attributed to $–CH_3$, $-OCH_3$ and Ar-OH groups in the chromone ring, respectively. The aromatic protons were observed in the range of 6.75-7.35 ppm. The singlet observed at 5.07 ppm were assigned to –NH protons of perimidine structure. The signals corresponding to Ar-OH and –NH protons were disappeared after addition of D_2O (Figure 2).

The ^{13}C NMR spectrum (with the aid of APT and DEPT techniques) in $CDCl_3$, were found to agree with the proposed structure of **L²**. The negative signal at 176.78 ppm clearly indicates the presence of quaternary carbonyl carbon. The positive peaks observed at 19.95 and 63.86 ppm were assigned to methyl and methoxy carbons of chromone ring, respectively. Another positive signal appeared at 61.74 ppm was likely to be assigned to the aliphatic methine carbon in the perimidine ring.

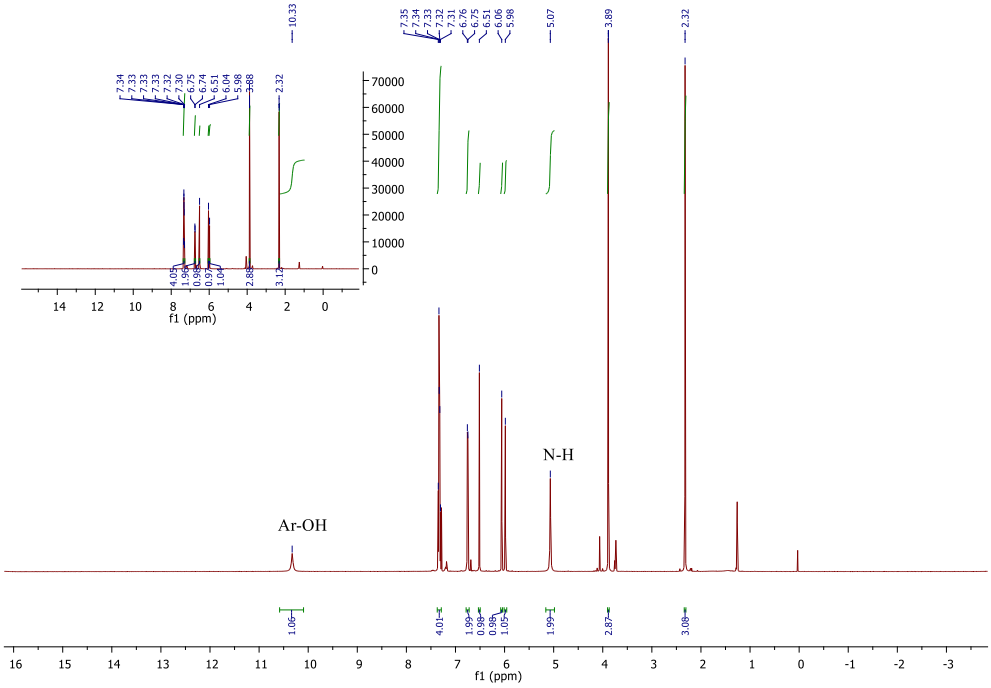

Figure 2. ^{1}H-NMR Spectrum of $\mathbf{L^2}$ ligand in $CDCl_3$ (Inset shows D_2O exchange spectrum of $\mathbf{L^2}$)

3.5. Mass spectra

In the mass spectra of the ligands, the molecular ion peaks for $\mathbf{L^1}$ and $\mathbf{L^2}$ can be seen at m/z = 591.3 and at m/z = 375.1 corresponds to $[M+H]^+$, respectively. Also, the formation of complexes was further confirmed by mass spectroscopy. The mass spectra for mononuclear complexes, $[CuL^1(H_2O)_2]$, $[FeL^1(H_2O)_2]$, $[CuL^2(H_2O)_4]$, $[FeL^2(H_2O)_4]$, show peaks at m/z = 711.2, 681.4, 529.54, 501.39 related to fragments of $[M+H+Na]^+$, $[M+H]^+$, $[M+Na]^+$ and $[M+H]^+$, respectively.

3.6. Catecholase activiy

2.11.1. Spectrophotometric study. In order to investigate the catecholase activity of all prepared complexes, 3,5-DTBC with low quinone-catechol reduction potential has been chosen as substrate. The oxidised product, 3,5-DTBQ is remarkably stable and shows a maximum absorption around 400 nm [20]. Methanol solution of the complexes was added in 100 equivalents of 3,5-DTBC in the presence of H_2O_2 and the repetitive UV-Vis spectral scan was recorded at a regular time interval of 2 min in the range 300-500 nm. After addition of 3,5-DTBC and H_2O_2, the time dependent spectral scan shows very smooth growing band at 400 nm (Figure 3) for all complexes, indicating the formation of the corresponding quinone (3,5-DTBQ).

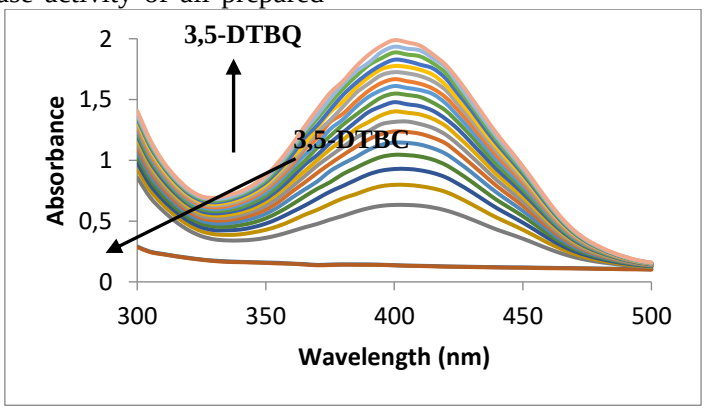

Figure 3. UV–Vis spectral changes of $[CuL^2(H_2O)_4]$ complex in methanol upon addition of 100-fold excess of 3,5-DTBC, observed at two minute intervals of time.

2.11.2. Enzyme kinetics study. Enzymatic kinetic experiments were performed by using UV–Vis spectrophotometry thermostated at 25 °C. To understand the kinetic aspects of catalysis, the rate

constant for a catalyst complex was determined by traditional initial rate methods. The pseudo-first-order condition was maintained by using substrate solutions ranging between 10 times and 100 times larger than that of the synthesized complexes. The Michaelis-Menten approach of enzyme kinetics was applied to analyze the rate versus concentration of the substrate data. In all cases, a first-order kinetic dependence was observed at low concentrations of 3,5-DTBC, whereas a saturation kinetics was observed at higher concentration (Figure 4).

Linearization by using Lineweaver–Burk plot of 1/V versus 1/[S], provided the Michaelis–Menten constant (K_M), maximum initial rate (V_{max}) and turnover number (k_{cat}). The calculated kinetic parameters are listed in Table 2. According to their calculated turnover number values (k_{cat} values), the overall comparison of the complexes based on catecholase activity suggests that Fe(II) complex of Schiff base ligand has the best activity in catalyzing the oxidation of 3,5-DTBC to 3,5-DTBQ in methanol solution, with a turnover number (k_{cat}) of 890.1 h^{-1}. Also Fe(II) complexes have been found to show better catalytic acitivity than those of Cu(II) complexes for any ligand.

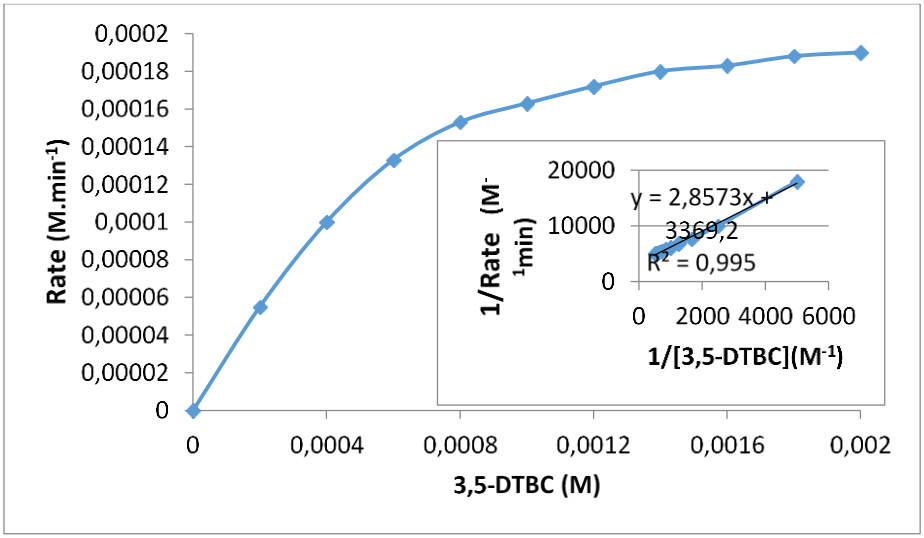

Figure 4. Michaelis–Menten and (inset) Lineweaver–Burk plots for $[FeL^1(H_2O)_2]$ with 3,5-DTBC in methanol.

Table 2. Kinetic parameters for the oxidation of 3,5-DTBC catalyzed by the prepared complexes.

Complex	*V*max (M min^{-1})	K_M (M)	k_{cat}(h^{-1})
$[CuL^1(H_2O)_2]$	$5.02x10^{-5}$	$7.6x10^{-4}$	151.4
$[FeL^1(H_2O)_2]$	$2.97x10^{-4}$	$8.5x10^{-4}$	890.1
$[CuL^2(H_2O)_4]$	$3.51x10^{-5}$	$5.4x10^{-4}$	66.9
$[FeL^2(H_2O)_4]$	$6.82x10^{-5}$	$9.1x10^{-4}$	106.5

4. CONCLUSION

In this paper, we have described the synthesis and characterization of four new mononuclear metal complexes with a perimidine derivative and a Schiff base derivative ligand and their application in catalytic field. All prepared complexes have been evaluated for their catecholase activity potential and they have been observed to exhibit moderate catecholase activity with turnover number values ranging from 66.9 to 890.1 h^{-1}. To the best of our knowledge, metal complexes of perimidine ligand in this study are the first compounds which have been found to show catecholase acitivity. However, in comparison to metal complexes of perimidine ligand, Schiff base metal complexes have better catecholase activity towards the oxidation of 3,5-DTBC to the corresponding quinone.

Acknowledgement. *This study was financially supported by Mustafa Kemal University Scientific Research Projects (MKU BAP) through project no: 15102.*

REFERENCES

1. S. Sharma, M. Chauhan, A. Jamsheera, S. Tabassum, F. Arjmand, *Inorg. Chim. Acta*, **458**, 8 (2017).
2. M. Biesaga, K. Pyrzynska, M. Trojanowicz, *Talanta,* **51**, 209 (2000)
3. Y. Sun, W. Xu, C. Di, D. Zhu, *Synthetic Met.*, **225**, 22 (2017).
4. M. Hoarau, C. Hureau, E. Gras, P. Faller, *Coordin. Chem. Rev.*, **308, Part 2,** 445 (2016).
5. S. Kumar, D.N. Dhar, P.N. Saxena, *J. Sci. Ind. Res. India,* **68**, 181 (2009).
6. A.M. Abu-Dief, I.M.A. Mohamed, *Beni-Suef Univ. J. Appl. Sci.,* **4**, 119 (2015).
7. B. Kolodziej, M. Morawiak, B. Kamienski, W. Schilf, *J. Mol. Struct.*, **112**, 81 (2016).
8. V.V. Patil, G.S. Shankarling, *Catal. Commun.*, **57**, 138 (2014).
9. K.C. Gupta, A.K. Sutar, *Coordin. Chem. Rev.*, **252**, 1420 (2008).
10. M. Azam, I. Warad, S. Al-Resayes, M. Zahin, I. Ahmad, M. Shakir, *Z. Anorg. Allg. Chem.* **638**, 881 (2012).
11. P. Bazinet, T. Ong, J. S. O'Brien, N. Lavoie, E. Bell, G.P.A. Yap, I. Korobkov, D.S. Richeson, *Organometallics,* **26**, 2885 (2007).
12. I.G. Jung, S.U. Son, K.H. Park, K. Chung, J.W. Lee, Y.K. Chung, *Organometallics* **22**, 4715 (2003).
13. M.E. Cucciolito, B. Panunzi, F. Ruffo, A. Tuzi, *Tetrahedron Lett.*, **54**, 1503 (2013).
14. A.K. Mahapatra, R. Maji, K. Maiti, S.K. Manna, S. Mondal, C.D. Mukhopadhyay, S. Goswami, D. Sarkar, T.K. Mondal, C.K. Quah, H.K. Fun, *Sensor. Actuat. B-Chem.,* **207**, 878 (2015).
15. N. Beyazit, B. Çatıkkaş, Ş. Bayraktar, C. Demetgül, *J. Mol. Struct.* **119,** 124 (2016).
16. D. Deletioğlu, S. Yalçınkaya, C. Demetgül, M. Timur, S. Serin, *Mater. Chem. Phys.*, **128**, 500 (2011).
17. A. Sharma and M. Shah, *IOSR Journal of Applied Chemistry (IOSR-JAC)*, **3**, 62 (2013).
18. A. Hasan, A.A. Ameer, A. Ahmed, E. Yousif, *J. Chem. Pharm. Res.*, **7**, 531 (2015).
19. C. Demetgül, D. Deletioğlu, F. Karaca, S. Yalçınkaya, M. Timur, S. Serin, *J. Coord. Chem.*, **63**, 2181 (2010).
20. A.K. Maji, S. Khan, A.K. Ghosh, C.H. Lin, B.K. Ghosh, R. Ghosh, *J. Mol. Struct.,* **1143**, 489 (2017).

Bulgarian Chemical Communications, Volume 49, Issue I (pp. 122 – 127) 2017

Investigation of hydroxyapatite morphology at different experimental conditions

Ö. Dogan*, B. Bodur

Yildiz Technical University, Chemical Engineering Department, Davutpasa Campus, 34210 Istanbul, Turkiye

Submitted: June 1, 2017; Accepted: September 1, 2017

The effects of experimental conditions and polymeric additives on hydroxyapatite (HAP) crystallization were investigated by wet chemical synthesis. Polyacrylic acid homopolymer and styrene-acrylic copolymer were used as additive. The obtained HAP powders were characterized by X-Ray Powder Diffraction (XRD), Scanning Electron Microscopy (SEM), Fourier Transform Infrared Spectroscopy (FTIR) and BET method. Thermal analysis (TG–DTA) was carried out to investigate the thermal stability of the powders. The result showed that the properties of HAP powders changed depending on the experimental conditions.

Keywords: Hydroxyapatite; polymeric additives; crystallization; chemical synthesis.

INTRODUCTION

Controlled synthesis of inorganic crystals is important on material fabrication which requires particles of specific size, shape and morphology. Experimental conditions and both organic and inorganic additives play an important role in crystallization process. They alter the surface properties of the crystals which have major effects on nucleation and growth which leads to change the shape and properties of the crystal [1].

The calcium phosphate salts is of particular interest because of its importance in various fields such as industrial water systems, wastewater treatment processes, agriculture fertilizers, biological calcification processes and drug delivery systems [2-5]. The thermodynamically most stable phase of calcium phosphate salt is hydroxyapatite (HAP, $Ca_5(PO_4)_3OH$). HAP properties depend on its stoichiometry and morphological characteristics especially its crystal size distribution, crystallinity, porosity and shape. Therefore recently, the study of controlling these parameters has gained great scientific and industrial interest. It was reported that small changes in these properties have significant effects on the mechanical properties of HAP crystals which are further processed to produce ceramics or incorporated with other materials to produce biocomposites [6-11].

In this study, the effects of temperature and polymeric additives on HAP crystallization were investigated by wet chemical synthesis. Polyacrylic acid homopolymer (PAA) and styrene-acrylic copolymer (SAA) were used as additive.

EXPERIMENTAL

Hydroxyapatite powders were prepared from calcium chloride and potassium dihydrogen phosphate solution at specified temperature. During the crystallization process, the pH was kept constant in the range of 9-9.5 with additions of 0.1 M KOH solution. Nitrogen gas was introduced into the solution to ensure a CO_2 free atmosphere. In experiments where additives used, a similar procedure was followed and the polymer solutions were added to the reactant solutions. After the experiment was terminated, the precipitate was separated and then refluxed for twenty four hours in its supersaturated solution. At the end of this period, the powders were filtered, dried and stored in a desiccator.

Hydroxyapatite powders were sintered by thermal treatment with a heating rate of 10°C/min for 3 hours at 650°C, 800°C and 1000°C. The obtained powders were characterized by X-Ray diffraction analysis (Phillips Panalytical X'ert Pro), FTIR spectral analysis (Bruker Alpha P), BET method (Quantachrome Instruments Autosorb 1), Scanning Electron Microscopy (JEOL-FEG-SEM) and thermal analysis (Perkin Elmer Pyris Diamond).

RESULTS AND DISCUSSION

X-ray diffraction analysis of the HAP powders was carried out by Phillips Panalytical X'ert Pro powder diffractometer. The data were collected in the 2θ range from 20 to 70° at scan rate of 0.020° $step^{-1}$. XRD pattern of the powders which synthesized at different temperature are shown in Figure 1. The grown main phase was identified as hydroxyapatite by XRD and compared with that of the JCPDS (01-073-0293) standards. As it can be seen from Figure 1, that the crystallinity of powders increases with the increase of synthesis temperature.

The specific surface area of the synthesized powders samples was determined by nitrogen

*) To whom all correspondence should be sent:
E-mail: dogano@yildiz.edu.tr

sorption/desorption isotherms according to multiple point BET method. The powders were outgassed for 4 h at 40°C. The obtained specific surface areas and micropore volumes for non-sintered and sintered HAP powders are summarized in Table 1. As it can be clearly seen from Table 1, a decrease in synthesis temperature results in an increase of the specific surface area, however reactant concentration does not effect the specific surface area. In addition, the increase in sintering temperature reduces the specific surface area.

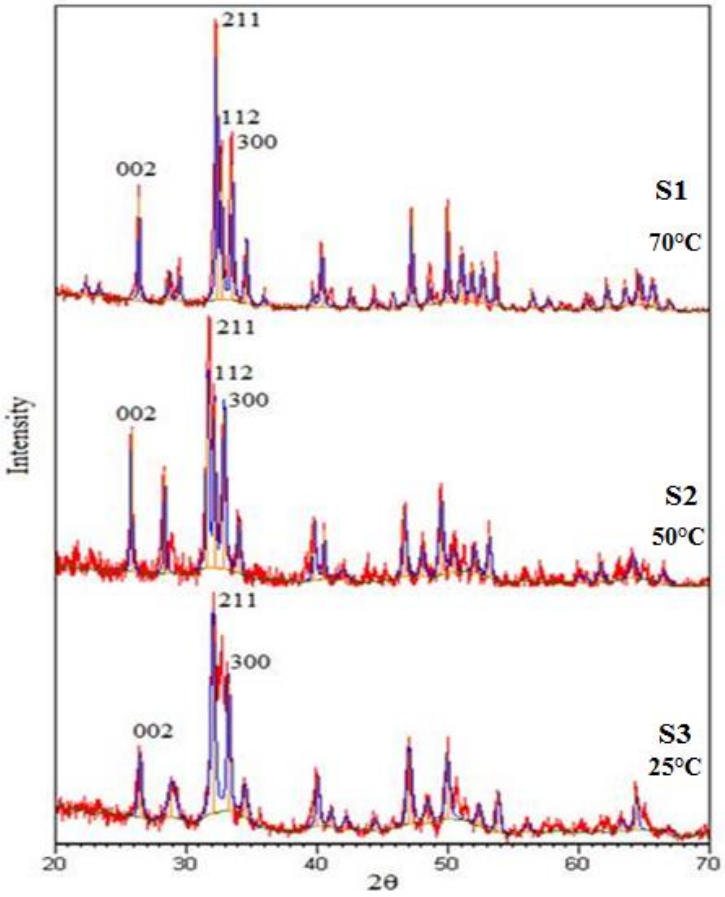

Figure 1. X-ray diffraction patterns of HAP powders synthesized at different temperatures.

Table 1. Effect of experimental conditions on the specific surface area of HAP powders.

Samples	T_{Ca} (mole/L)	Synthesis Temperature (°C)	Sintering Temperature (°C)	Specific Surface Area (m^2/g)	Micropore Volume (mm^3/g)
S1	0.5	70	0	34.19	3.39
	0.5	70	650	23.04	1.42
	0.5	70	800	8.91	0.44
S2	0.5	50	0	62.25	4.49
	0.5	50	650	23.78	2.79
S3	0.5	25	0	80.30	7.75
	0.5	25	650	19.16	2.03
S4	1	70	0	36.18	2.54
	1	70	650	20.12	1.69
S5	0.25	70	0	32.11	1.55
	0.25	70	650	20.57	1.87

Purity of the samples was also tested by FTIR spectral analysis (Figure 2). FTIR spectra of the powders synthesized at 70°C showed that they consisted of HAP (S1). But FTIR spectra of the powders synthesized at 50°C (S2) and 25°C (S3), showed a weak band at around 2300-2400 cm^{-1}, which was indicating that the dicalcium phosphate dihydrate ($CaHPO_4.2H_2O$) and the dicalcium phosphate anyhdrate ($CaHPO_4$) are formed in the structure [12].

FTIR spectra of the powders synthesized at different reactant concentration are given in Figure 2. It showed a weak band at around 2300-2400 cm^{-1} for S3, S4 and S5 samples, which was indicating that the dicalcium phosphate dihydrate ($CaHPO_4.2H_2O$) and the dicalcium phosphate anyhdrate ($CaHPO_4$) are formed in the structure [12].

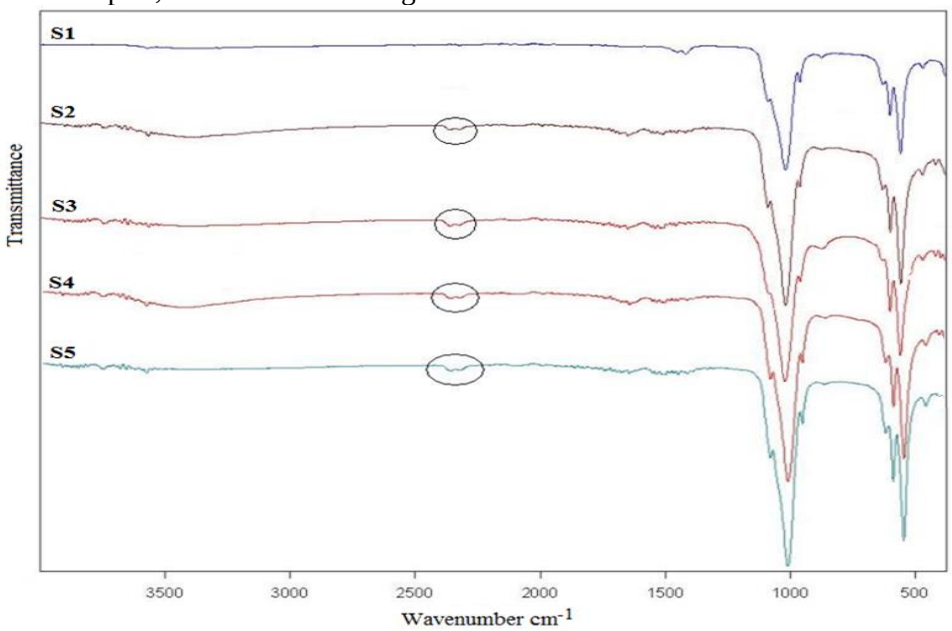

Figure 2. FTIR spectrums of HAP powders.

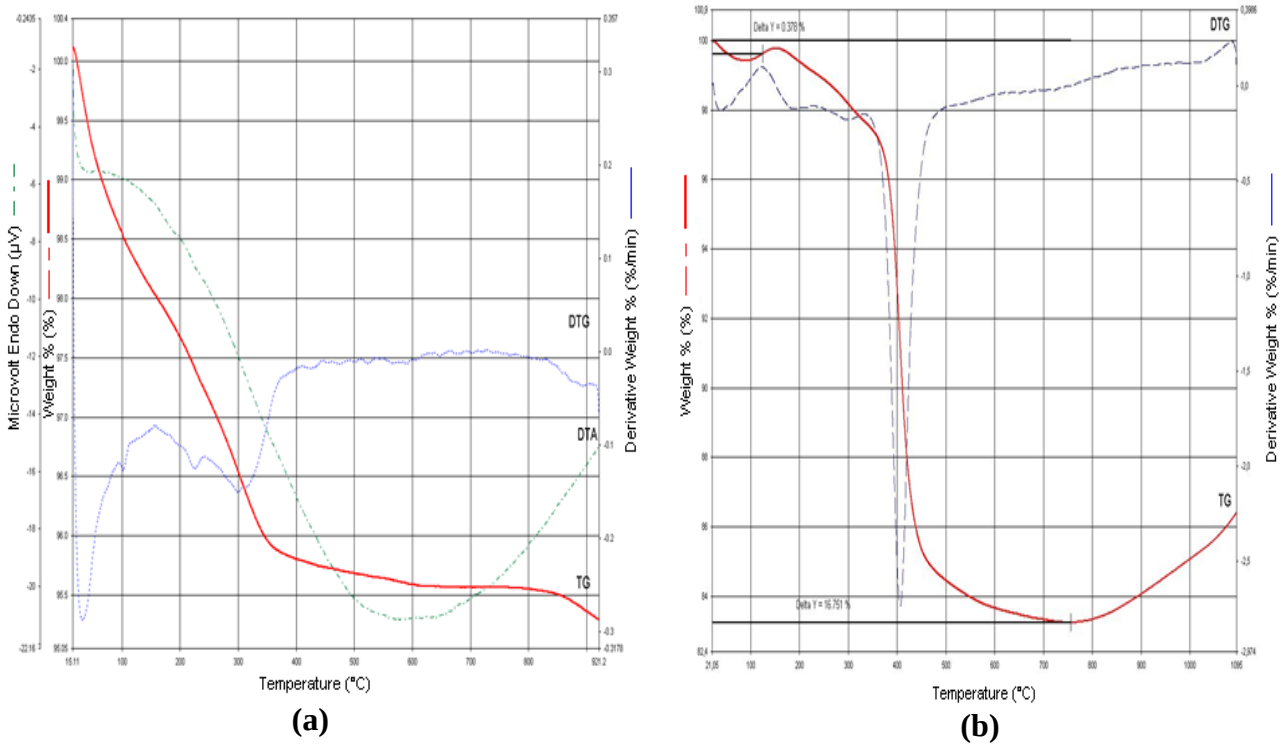

Figure 3. (a) TG, DTA and DTG curves for HAP powders synthesized without polymer addition **(b)** TG and DTG curves for HAP powders synthesized with polymer addition.

CO_3^{-2} ions were detected in the precipitate from the peaks around 1400 cm^{-1}. The presence of CO_3^{-2} ions indicates that the HAP formed during reaction includes some carbonate substituted apatite [7,13].

The stability phase composition of powders was analyzed by thermal treatment under nitrogen atmosphere (Figure 3a). Initially, 2% weight loss was observed in sample due to moisture. TG analysis showed a two stage weight loss. The weight loss of about 1.1% was observed up to temperature 400°C, which is due to the evaporation of absorbed water from the surface and lattice water from the surface

and pores. Removal of the crystalline water may also take place in this temperature range. A continuous weight loss over 800°C is attributed to the loss of water from dehydroxylation of HAP [14,15]. The weight loss of 16.8% in the range of 120˚C to 710˚C temperature that can be seen from Figure 3b shows that the polymer is removed from the structure.

The obtained specific surface areas and micropore volumes for non-sintered and sintered HAP powders which are synthesized in the presence of varying concentrations of polyacrylic acid homopolymer and styrene-acrylic copolymer are summarized in Table 2. It can be seen from Table 2, in the presence of styrene-acrylic copolymer, the specific surface area of powders does not change with increasing polymer concentration. However, in the presence of polyacrylic acid homopolymer, an increase in polymer concentration results in an increase of the specific surface area of the crystals.

Table 2. Effect of experimental conditions on the specific surface area of HAP powders in the presence of polymeric additives.

Samples	T_{Ca} (mole/L)	Polymer	Polymer Concentration (ppm)	Sintering Temperature (°C)	Specific Surface Area (m^2/g)	Micropore Volume (mm^3/g)
S6	0.5	SAA	5000	0	30.31	…
	0.5	SAA	5000	650	17.43	1.52
	0.5	SAA	5000	800	11.68	1.46
S7	0.5	SAA	7500	0	31.32	….
	0.5	SAA	7500	650	23.81	2.63
S8	0.5	SAA	10000	0	29.93	…
	0.5	SAA	10000	650	22.79	2.39
	0.5	SAA	10000	800	13.53	1.15
	0.5	SAA	10000	1000	8.35	0.34
S9	0.5	SAA	15000	0	30.03	…
	0.5	SAA	15000	650	11.44	1.39
S10	0.5	PAA	2000	0	47.47	…
	0.5	PAA	2000	800	8.94	0.84
S11	0.5	PAA	5000	0	71.84	…
	0.5	PAA	5000	800	7.81	0.32
S12	0.5	PAA	10000	0	108.04	…

The crystal materials are usually sintered at high temperature to improve their mechanical properties, crystallinity and catalytic activity. Because of this understanding the sintering behavior of crystals that allows designing ceramics with controlled grain growth, microstructure and mechanical properties is important [16,17]. The FTIR spectrums of non-sintered and sintered powders synthesized in the presence 15000 ppm styrene-acrylic copolymer (S9) at different temperatures are given ин Figure 4. The FTIR spectrum of the non-sintered powders showed the characteristic bands of HAP and styrene-acrylic copolymer. The FTIR spectrum of the powders sintered at 650°C showed that the peaks for styrene-acrylic copolymer around 760 cm^{-1} disappears [18]. CO_3^{-2} ions were detected in the precipitate from the peaks around 1400 cm^{-1}. At 1000°C sintering, the mode of the CO_3^{-2} at 1400 cm^{-1} group disappears in all samples, which indicates an increase in crystallinity during sintering processes.

The morphologies of the HAP powders was analyzed by using SEM. The HAP powders synthesized at 70°C and sintered at 650°C are formed agglomerated particles of a needle-like morphology (Figure 5a). Figure 5b shows the SEM images of the HAP powders synthesized in the presence of 15000 ppm styrene-acrylic copolymer and sintered at 650°C. Significant changes in morphology were not observed in the presence of polymers. The precipitated crystals show similar need-like shape. The powders precipitated at 70°C have average length of around 171 nm and width 55 nm. For the powders sintered at 650°C, the average length and width increased to 194 nm and 66 nm respectively. In the presence of 15000 ppm styrene-acrylic copolymer, the lengths and width of the crystals increased to 262 nm and 80 nm respectively.

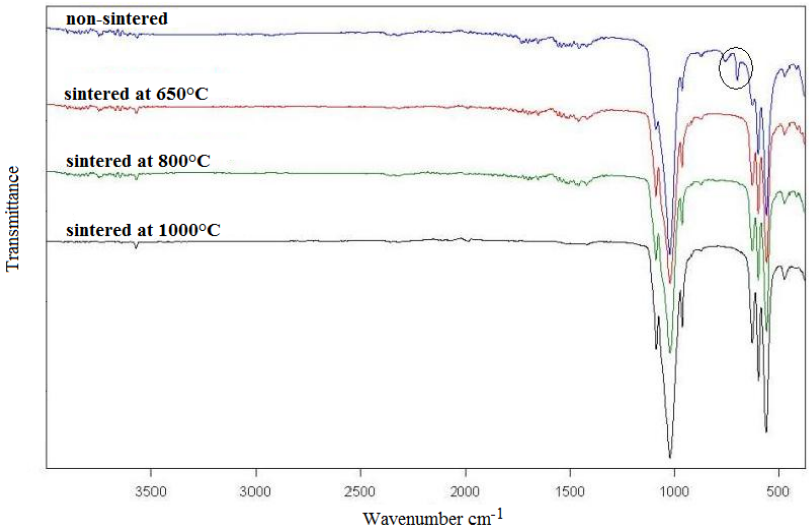

Figure 4. FTIR spectrums of HAP powders synthesized in the presence of polymers.

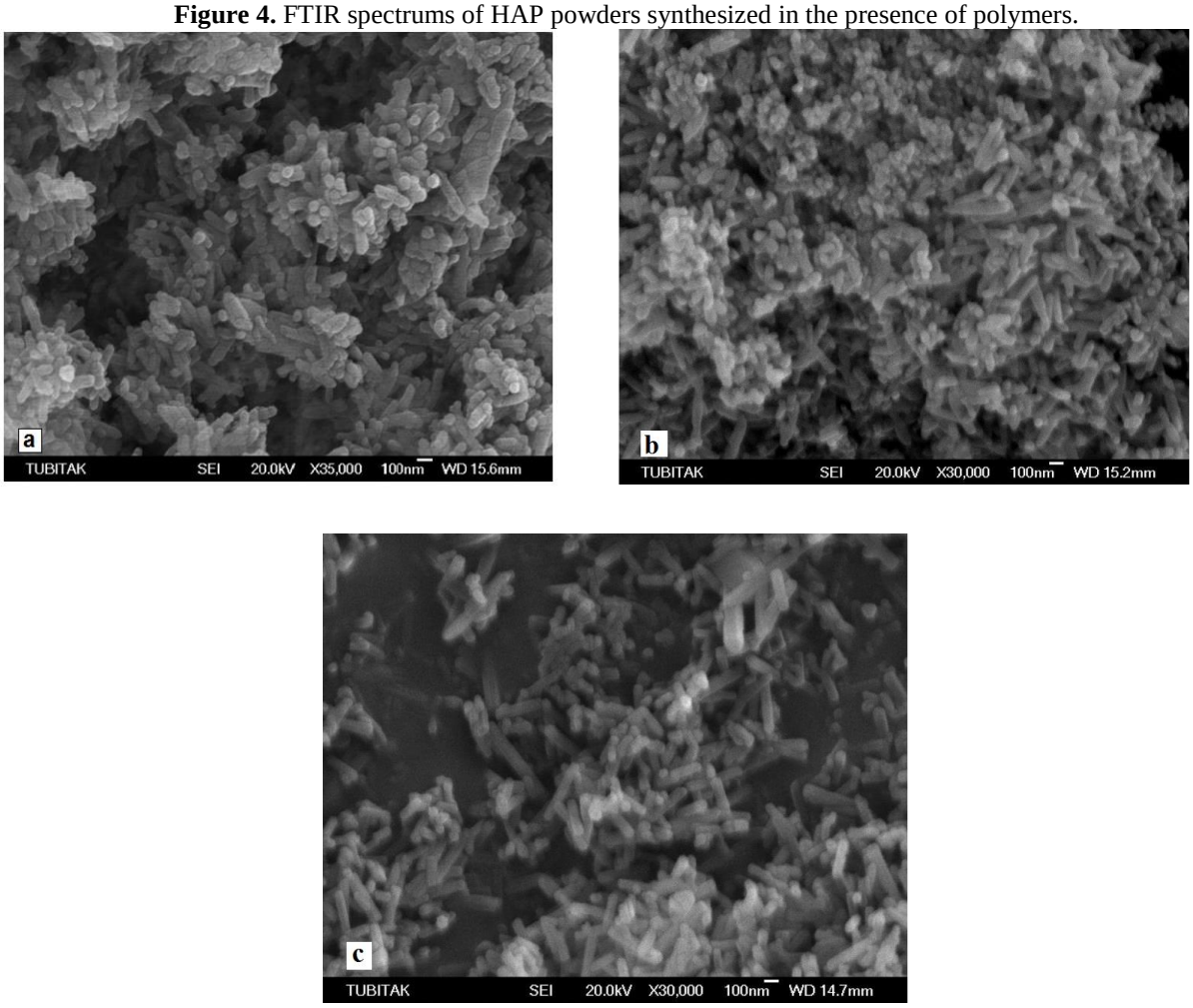

Figure 5. SEM of the HAP powders synthesized **(a)** without polymer addition and non-sintered **(b)** without polymer addition and sintered at 650°C **(c)** with polymer addition and sintered at 650°C.

CONCLUSIONS

The HAP powders were synthesized at different experimental conditions. Results show that the crystallinity, specific surface area, micropore volume and crystal size of the obtained powders changed depending on the experimental conditions. The specific surface area and the micropore volume of powders increased with decreasing synthesis temperature while the crystallinity of crystals decreased. Sintering caused a decrease of the specific surface area and the micropore volume and an increase of the particle size and crystallinity. The particle size increased with addition of polymeric additives.

Acknowledgements. *This study was supported by Yildiz Technical University Scientific Projects Coordination (project no: 2011-07-01-yulap02).*

REFERENCES

1. M. Oner, O. Dogan, *Progress in Crystal Growth & Characterization of Materials*, **50**, 39 (2005).
2. B. Sandrine, N. Ange, B.A. Didier, C. Eric, S. Patrick, *J. Hazard. Mater. A*, **139**, 443 (2007).
3. H. H. Pham, P. Luo, F. Genin, A. K. Dash., *AAPS Pharm. Sci. Tech*., **3**, 1 (2002).
4. H.-W. Kim, J. C. Knowles, H.-E. Kim, *Biomaterials*, **25**, 1279 (2004).
5. O. Dogan, M. Oner, *Langmuir*, **22,** 9671 (2006).
6. D. K. Son, Y. J. Kim, *Materials Sci. Eng. C*, **33**, 499 (2013).
7. P. Wang, C. Li, H. Gong, X. Jiang, H. Wang, K. Li, *Powder Technol.*, **203**, 315 (2010).
8. O. Dogan, M. Oner, *J. Nanosci. Nanotechnol*.**, 8**, 667 (2008).
9. Y. X. Pang, X. Bao, *J. Eur. Ceramic Soc.*, **23**, 1697 (2003).
10. V.P. Orlovskii, V.S. Komlev, S.M. Barinov, *Inorganic Materials*, **38**, 973 (2002).
11. R. I. Martin, P. W. Brown, *J. Materials Science: Materials in Medicine*, 6, 138 (1995).
12. S. Koutsopoulos, *J. Biomedical Mater. Res., Part A*, **62**, 600 (2002).
13. K. Agrawal, G. Singh, D. Puri, S. Prakash, *J. Minerals&Materials Character. Eng.*, **10**, 727 (2011).
14. Y. Chen, X. Miao, *Biomaterials*, **26**, 1205 (2005).
15. D. Malina, K. Biernat, A. Sobczak-Kupiec, *Acta. Biochim. Pol.*, **60**, 851 (2013).
16. N. Monmaturapoj, C. Yatongchai, *J. Metals, Materials & Minerals*, **20**, 53 (2010).
17. Y. C. Teh, C.Y. Tan, S. Ramesh, J. Purbolaksono, Y. M. Tan, H. Chandran, W. D. Teng, B. K. Yap, *Ceramics-Silikaty*, **58**, 320 (2014).
18. M.W. Urban, J.L. Koenig, L.B. Shih, J.R. Allaway, *Applied Spectroscopy*, **41**, 590 (1987).

Bulgarian Chemical Communications, Volume 49, Issue I (pp.128 – 132) 2017

A fibrous solid electrolyte for lithium-ion batteries

S. Erol

Department of Chemical Engineering, Eskisehir Osmangazi University, Eskişehir 26040, Turkey

Received May 26, 2017, Revised September 5, 2017

The new methodology proposed in this work uses oxide filaments/fibers instead of a dense thin film electrolyte, allowing: (i) straightforward fabrication without the use of costly thin film production techniques, (ii) minor changes in the existing Li-ion battery production lines, and (iii) better mechanical stability and electrochemical performance. $Li_7La_3Zr_2O_{12}$ (LLZO) fibers as an electrolyte were prepared using the electrospinning technique. The crystallographic phase and morphology of the products was studied X-ray diffraction (XRD) patterns and scanning electron microscopy (SEM), respectively. The results indicated that the produced electrolyte would be a good alternative of all-solid-state batteries for electric vehicles in terms of battery safety and performance.

Key words: All-solid-state Li-ion battery; fiber electrolyte; LLZO, battery safety; battery performance

INTRODUCTION

Lithium-ion batteries are currently the dominant power source for portable electronic devices because of their high energy density and efficiency. Recently, there is a strong growing interest to develop large-scale Li-ion batteries, particularly for electric vehicles. Developing batteries with high energy density, safe operation, low cost, and long life is vital for successful implementation of Li-ion batteries in automotive industry. All-solid-state Li-ion batteries have been shown to significantly improve volumetric energy density, safety, and cycle life; however, their real-world applications are hindered by the complex and costly manufacturing processes. Recognizing this important need, the main objective of this study is to examine a new scalable and inexpensive technique for fabrication of an electrolyte for all-solid-state batteries.

Conventional Li-ion batteries typically consist of a positive electrode (cathode), a negative electrode (anode), and a liquid organic electrolyte. During charge/discharge cycles Li ions migrate through the liquid electrolyte between the two electrodes. Large-scale Li-ion batteries face many challenges in terms of safety, cost, and cycle life. Many of these challenges are associated with the use flammable liquid organic electrolytes. The liquid electrolyte can leak through the containment walls of the battery and catch on fire. The liquid electrolyte cannot provide a separation between the cathode and anode; therefor, polymeric separators need to be used in order to prevent the battery from a potential short-circuit. The use of flammable organic liquid electrolytes and polymeric separators induce serious safety problems including the risk of fire and explosion. Besides these safety concerns, the complex packaging remarkably increases the manufacturing cost, and lowers the energy density by increasing the weight and volume of the battery packs. In addition, side reactions and poor thermal stability of the liquid electrolyte result in a capacity fade, which shortens the battery cycle life [1].

In all-solid-state Li-ion batteries, the components are all made up of solid phase. The non-flammability of the solid electrolyte overcomes the safety problem of the conventional Li-ion batteries. Since solid electrolytes neither leak nor vaporize easily, all of the cell components can be directly stacked in one container, instead of multiple containers as in the liquid-containing cells. Therefore, as shown in Fig. 1a, the battery size reduces, and thus the volumetric energy density significantly improves up to 3 times. Moreover, solid electrolytes physically separate the cathode from the anode, eliminating the need for separators. In addition, solid electrolytes have a wider range of operating potentials (over 5 V) and operating temperatures. They can be paired with certain high-voltage and high-capacity electrodes that are generally difficult to combine with liquid electrolytes. The good examples of these electrodes are lithium metal anodes and sulfur cathodes. Another feature of solid electrolytes is their single-ion conduction that suppresses side reactions and leads to a long battery life. As a result of unity transference number indicating that Li ions are the sole charge carriers, there is no concentration gradient inside the operating cells; thus, the cell over-potential is negligible. Furthermore, the capacity fade caused by the continuous decomposition of the electrode surface in contact with liquid is avoided [2-4].

*) To whom all correspondence should be sent:
E-mail: esalim@ogu.edu.tr

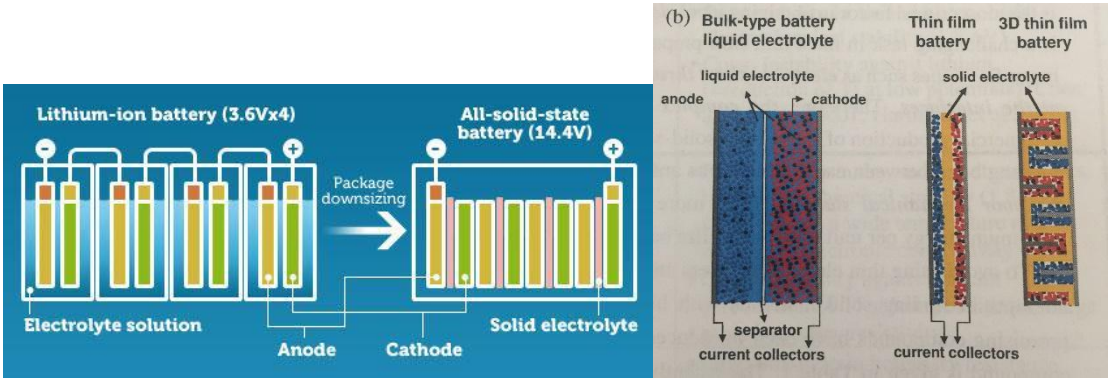

(a) (b)

Fig. 1. (a) Improved packaging efficiency by direct stacking of the all-solid-state cells instead of using multiple containers in liquid-containing cells, (b) A comparison between the Li-ion accessibility in bulk-type liquid-containing cells, and 2D and 3D all-solid-state thin film batteries.

In summary, solid electrolytes improve safety, offer higher volumetric and gravimetric energy densities, and potentially lower the cost of the battery by increasing the battery life, decreasing the dead-space in battery packs, and simplifying the packaging.

Li-ion batteries are the preferred system for large-scale energy storage, particularly in automobiles. Most common rechargeable Li-ion batteries are made using organic liquid electrolytes, which is currently the major constraint for design and production of these batteries for large-scale applications. The liquid electrolyte can leak through the containment walls of the battery and can catch fire or cause an explosion due to the flammability of lithium exposing to air. The replacement of the organic liquid electrolyte with a more reliable inorganic solid electrolyte in all-solid-state Li-ion batteries simplifies the design of these batteries and improves their durability. Compared to liquid electrolytes, nonflammable solid electrolytes significantly improve the safety of the batteries. Moreover, direct stacking of all-solid-state cells in one package yields a high operating voltage in a smaller volume and provides higher energy density. In order to achieve the potential advantages of solid-state batteries and to commercialize this class of batteries, thin films of the solid electrolytes were developed to provide low resistance for Li-ion transfer. Current vacuum-based deposition techniques such as pulsed-laser deposition, atomic layer deposition, and magnetron sputtering that are used in laboratory environments and electronics industry are too costly and therefore do not allow for scale-up of the process and commercial production of large-scale batteries. Furthermore, a good contact between the solid electrolyte and electrode materials cannot be readily obtained, making it difficult to fabricate an all-solid-state battery.

The solid electrolyte is the most critical component in all-solid-state batteries. It should exhibit a high Li-ion conductivity to facilitate shuttling of the Li ions between the two electrodes. Moreover, it should have a low electronic conductivity to electronically separate the electrodes and to lower the self-discharge. The chemical stability in contact with other cell components and under the operating potential and temperature is another important property that a solid electrolyte should possess.

Inorganic solids, particularly oxides, usually have a low ionic conductivity. The Li-ion conductivity of lithium phosphorus oxynitride (LIPON), which is 10^{-6} S cm^{-1} with a transference number of 1 [5,6], known as a good Li-ion conductor, is still 4 orders of magnitude lower than the commercial liquid electrolytes, which have 10^{-2} S cm^{-1} conductivity with a transference number of <0.5 [7]. Therefore, thin films (<200 nm) of the solid electrolytes were developed to provide low resistance for Li-ion transfer [5]. In addition to the low ionic conductivity, the solid electrolyte, unlike liquids, cannot penetrate through the pores inside the porous electrodes. Thus, the contact area between the electrodes and the solid electrolyte is very limited to, as demonstrated in Fig. 1b. The small contact area limits the accessibility of ions to the electrode active sites, resulting in low utilization of the electrode materials. Various designs of 3D thin film batteries (Fig. 1b), by providing a larger macroscopic contact area, could partly address this issue [8-12]. Currently, the thin film batteries are fabricated using costly vacuum-based techniques, such as pulsed-layer deposition, atomic layer deposition, and magnetron sputtering [6,13-16]. The concentration of chemicals and point defects is the most critical factor in obtaining ideal electrical properties, while an exact stoichiometric control is a challenging task in most thin film preparation

techniques. Scaling down the film thickness also magnifies issues such as electrical short through pinholes in the film and poor electrical conductivity at the interfaces. Therefore, the complex design of thin film batteries limits the scale-up and commercial production of large-scale solid-state batteries. As film thickness is increased, maintaining a strong bond between each of the films and the supporting substrate becomes more difficult. Thus, the poor mechanical stability, even more than the electrical resistance, dictates the design and maximum energy per unit area of the film batteries [17].

There have been extensive attempts in finding solid materials with Li-ion conductivity to avoid using thin electrolyte layers and costly vacuum technologies. As a result, a number of promising compounds have been introduced. A summary of advantages and disadvantages of each compound is depicted in Table 1. The recently reported sulfide compounds [3] exhibit significantly a high Li-ion conductivity (10^{-2} S cm^{-1}) that is comparable to that of liquid electrolytes. However, the instability of the sulfide glasses in direct contact with lithium and the hygroscopic feature of sulfide compounds can constraint their application.

Table 1. Examples of Li-ion conducting inorganic compounds considered as electrolyte material in all-solid-state Li-ion batteries.

Groups of materials		Example(s): Li-ion conductivity	Advantages & Disadvantages
Sulfides	Sulfide glasses	LiI-Li_2S-X (X: P_2S_5, B_2S_3, SiS_2): 2×10^{-3} S cm^{-1} [18-20]	Pros: high ionic conductivity in the absence of transition metal oxide (wide electrochemical window), low grain boundary resistance even in a cold-pressed pellet (convenient for the bulk-type batteries). Cons: low chemical stability in air, synthesis under controlled atmosphere, instability against Li metal, high resistance at the $LiCoO_2$/sulfide interface
	Crystalline sulfides	$Li_{10}GeP_2S_{12}$ (Thio-LISICON): 1.2×10^{-2} S cm^{-1} [21]	
	Glass-ceramic sulfides	Li_2S-P_2S_5: 3.2×10^{-3} S.cm^{-1} [22,23]	
Oxysalts	NASICON-type	Al-doped $LiTi_2(PO_4)_3$ (LTP): 3×10^{-3} S cm^{-1} [5]	Pros: stability in air and water, high electrochemical stability (1.8-6 V); Cons: instability against Li (reduction of Ti at low potentials) [24,25]
	γ-Li_3PO_4-type	Amorphous lithium phosphorus oxynitride (LIPON): 2×10^{-6} S cm^{-1} [26]	Pros: wide electrochemical potential window (0-5.5 V). Cons: sufficient conductance and mechanical stability only when thinner than 2 μm [6,27]
Oxides	Perovskite-type	$Li_{3x}La_{(2/3)-x}TiO_3$ (LLTO) with modified grain boundaries: 1×10^{-4} S cm^{-1} [28,29]	Pros: stability in dry and wet atmosphere, high electrochemical stability (1.8-8 V), stability over a wide temperature range, negligible electronic conductivity. Cons: instability against Li (reduction of Ti at low potentials), high grain boundary resistance
	Garnet-type	$Li_7La_3Zr_2O_{12}$ (LLZO): 8.7×10^{-4} S cm^{-1} [30]	Pros: low grain boundary resistance, excellent chemical stability (stability against Li), wide electrochemical potential window (0-9 V) [31]

EXPERIMENTAL

Fabrication of the electrolyte in the form of fiber, whisker, and/or filament was performed using the electrospinning technique. This technique is widely used for fabricating fibers from a wide range of materials, including oxysalts, oxides, and sulfides, with diameters ranging from several nanometers to micrometers and lengths up to several millimeters. The process is based on the unidirectional elongation of a spinnable viscoelastic solution by considering various parameters involved in the electrospinning process [32]. For the experiments, a solution containing the stoichiometric amount of oxide precursors (lithium acetate, zirconium, and lanthanum nitrate hexahydrate), acetic acid, and granular polyvinylpyrrolidone (PVP) dissolved in ethanol were drawn into a 15-gauge syringe with a blunt-tip stainless steel needle that was placed 15 cm from the collector. The ceramic precursor to PVP ratio was 1:2. During electrospinning, a positive voltage of 20 kV was applied to the needle, and the solution feed rate of 0.1 mL h^{-1} was maintained using a syringe pump. The schematics of the electrospinning process are illustrated in Fig. 2.

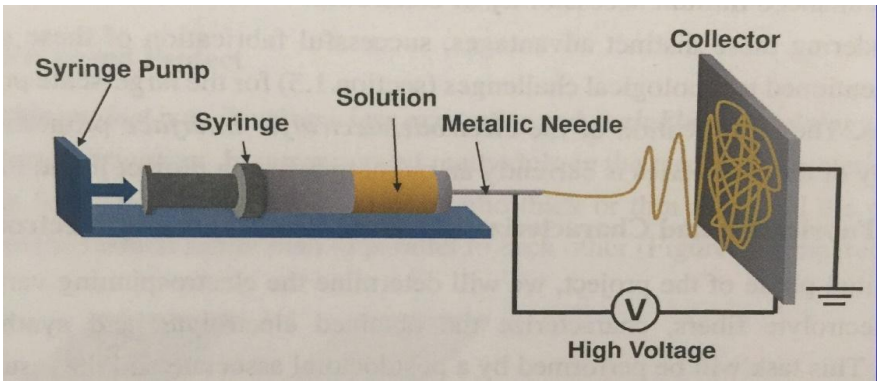

Fig. 2. Schematic representation of electrospinning process.

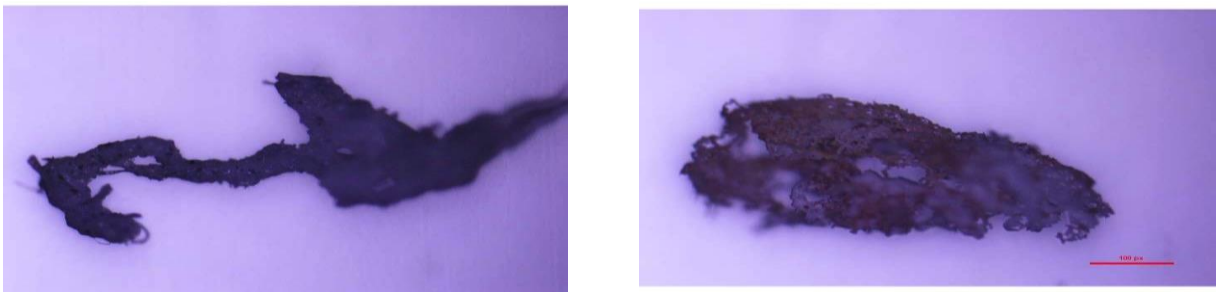

(a) (b)

Fig. 3. Microscopic images of spun LLZO fibers (a) before calcination and (b) after calcination. The scale bar in (b) is 100 px (40 μm), and the scaling is same for both images.

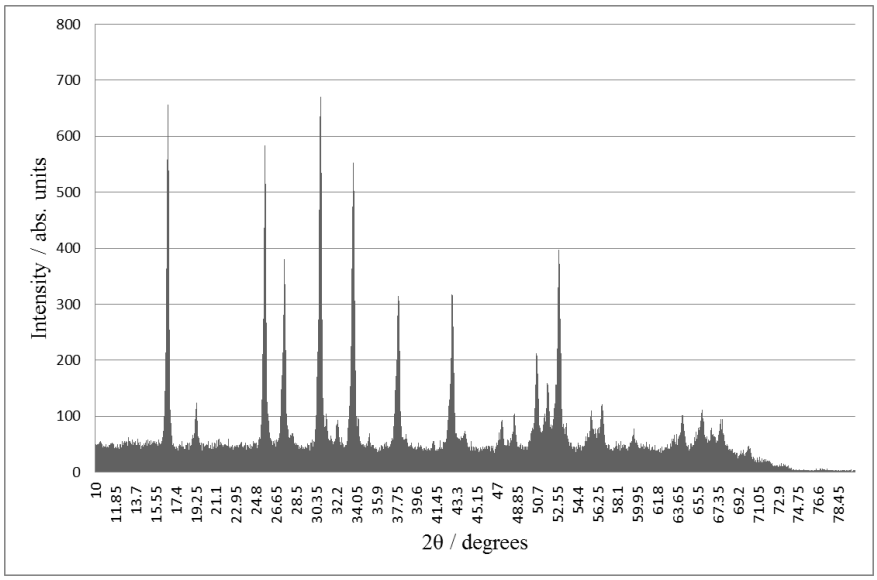

Fig. 4. X-ray diffraction patterns for LLZO sample.

The obtained inorganic-organic composite fibers were collected on an ash-less filter paper. The paper was placed on the metal collector, which was an aluminum foil. The fibers and the ash-less paper removed from the collector after the electrospinning process and dried at 80 ºC for 12 h. Then, the spun fiber was calcined at 900 ºC to obtain the final oxide fiber. The crystallographic phase and morphology of the calcined fibers was studied X-ray diffraction (XRD) patterns and microscopic images. Various parameters that can heavily influence the morphology of the fibers, including processing parameters (the applied electric potential, the solution rate, the diameter of the syringe and the needle, the syringe tip-to-collector distance, and the calcination temperature) and solution parameters (viscosity, pH, and the precursor to PVP ratio) were all investigated by repeating the experiments several times, and the parameter values were optimized as mentioned above.

RESULTS AND DISCUSSION

Microscopic images of spun LLZO fibers before calcination and after calcination are shown in Fig. 3. The images reveal that the fibrous structure was maintained an even improved after the calcination process.

The XRD patterns of the calcined LLZO sample is demonstrated in Fig. 4. This specific pattern shows that the LLZO obtained in this study is in cubic structure. The cubic LLZO has higher conductivity than that of tetragonal.

The microscopic images and XRD results suggest that the fabricated LLZO fibers are ready to be used as an electrolyte for all-solid-state Li-ion batteries.

CONCLUSION AND FUTURE WORK

Electrospinning is an easy and inexpensive method to form electrolyte fibers, filaments, or whiskers. The fibrous LLZO electrolyte fabricated using the electrospinning technique might be an appropriate electrolyte of all-solid-state battery for electric vehicles in terms of battery safety and performance.

A high capacity all-solid-state Li-ion battery using this type electrolyte is proposed to present in a subsequent paper. In this proposed cell configuration, the fibrous electrolyte will be placed on an insulating layer; then a very narrow insulating glue will be applied in the center. The prepared electrode slurries will be spread on the both sides of the insulating glue, and current collectors (foil or mesh) will be attached.

REFERENCES

1. J.B. Bates, G.R. Gruzalski, N.J. Dudney, C.F. Luck, X.H. Yu, S.D. Jones, *Solid State Technol.*, **36**, 59 (1993).
2. K. Takada, *Acta Mater.*, **61**, 759 (2013).
3. M. Tatsumisago, M. Nagao, A. Hayashi, *J. Asian Ceram. Soc.*, **1**, 17 (2013).
4. C. Cao, Z.B. Li, X.L. Wang, X.B. Zhao, W.Q. Han, *Front. Energy Res.*, **2**, 25, (2014).
5. J.B. Bates, N.J. Dudney, G.R. Gruzalski, R.A. Zuhr, A. Choudhury, C.F. Luck, *J. Power Sources*, **43**, 103 (1993).
6. J.B. Bates, N.J. Dudney, D.C. Lubben, G.R. Gruzalski, B.S. Kwak, X. Yu, R.A. Zuhr, *J. Power Sources*, 5**4**, 58 (1995).
7. C. Capiglia, Y. Saito, H. Kageyama, P. Mustarelli, T. Iwamoto, T. Tabuchi, H. Tukamoto, *J. Power Sources*, **81**, 859 (1999).
8. S. Leopold, I.U. Schuchert, J. Lu, M.E. Toimil-Molares, M. Herranen, J.O. Carlsson, *Electrochim. Acta*, **47**, 4393 (2002).
9. R.W. Hart, H.S. White, B. Dunn, D.R. Rolison, *Electrochem. Commun.*, **5**, 120 (2003).
10. C. Wang, G. Jia, L.H. Taherabadi, M.J. Madou, *J. Microelectromech. S.*, **14**, 348 (2005).
11. P.L. Taberna, S. Mitra, P. Poizot, P. Simon, J.M. Tarascon, *Nat. Mater.*, **5**, 567 (2006).
12. E. Perre, L. Nyholm, T. Gustafsson, P.L. Taberna, P. Simon, K. Edström, *Electrochem. Commun.*, **10**, 1467 (2008).
13. J.B. Bates, N.J. Dudney, B. Neudecker, A. Ueda, C.D. Evans, *Solid State Ionics*, **135**, 33 (2000).
14. E.J. Jeon, Y.W. Shin, S.C. Nam, W.I. Cho, Y.S. Yoon, *J. Electrochem. Soc.*, **148**, A318 (2001).
15. H. Ohtsuka, Y. Sakurai, *Solid State Ionics*, **144**, 59 (2001).
16. S. Zhao, Q. Qin, *J. Power Sources*, **122**, 174 (2003).
17. F. Vereda, N. Clay, A. Gerouki, R.B. Goldner, T Haas, P. Zerigian, *J. Power Sources*, **89**, 201 (2000).
18. R. Mercier, J.P. Malugani, B. Fahys, G. Robert, *Solid State Ionics*, **5**, 663 (1981).
19. H. Wada, M. Menetrier, A. Levasseur, P. Hagenmuller, *Mater. Res. Bull.*, **18**, 189 (1983).
20. J.H. Kennedy, Y. Yang, *J. Electrochem. Soc.*, **133**, 2437 (1986).
21. N. Kamaya, K. Homma, Y. Yamakawa, M. Hirayama, R. Kanno, M. Yonemura, T. Kamiyama, Y. Kato, S. Hama, K. Kawamoto, A. Mitsui, *Nat. Mater.*, **10**, 682 (2011).
22. F. Mizuno, A. Hayashi, K. Tadanaga, M. Tatsumisago, *Adv. Mater.*, **17**, 918 (2005).
23. Y. Seino, T. Ota, K. Takada, A. Hayashi, M. Tatsumisago, *Energy Environ. Sci.*, **7**, 627 (2014).
24. C.H. Chen, K. Amine, *Solid State Ionics*, **144**, 51 (2001).
25. P. Hartmann, T. Leichtweiss, M.R. Busche, M. Schneider, M. Reich, J. Sann, P. Adelhelm, J. Janek, *J. Phys. Chem. C*, **117**, 21064 (2013).
26. H. Aono, E. Sugimoto, Y. Sadaoka, N. Imanaka, G. Y. Adachi, *J. Electrochem. Soc.*, **137**, 1023 (1990).
27. N.J. Dudney, *Mater. Sci. Eng. B*, **116**, 245 (2005).
28. Y. Inaguma, C. Liquan, M. Itoh, T. Nakamura, T. Uchida, H. Ikuta, M. Wakihara, *Solid State Commun.*, **86**, 689 (1993).
29. A. Mei, X.L. Wang, J.L. Lan, Y.C. Feng, H.X. Geng, Y.H. Lin, C.W. Nan, *Electrochim. Acta*, **55**, 2958 (2010).
30. J.L. Allen, J. Wolfenstine, E. Rangasamy, J. Sakamoto, *J. Power Sources*, **206**, 315 (2012).
31. L. Cheng, H. Hou, S. Lux, R. Kostecki, R. Davis, V. Zorba, A. Mehta, M. Doeff, *J. Electroceram.*, (2017). https://doi.org/10.1007/s10832-017-0080-3
32. S. Kalluri, K.H. Seng, Z.P. Guo, H.K. Liu, S.X. Dou, *RSC Adv.*, **3**, 25576 (2013).

Bulgarian Chemical Communications, Volume 49, Issue I (pp. 133 – 139) 2017

Molecules of benidipine: experimental and theoretical investigation

A. Karasakal, G. Dogan, Y. Yalcin Gurkan*

Namik Kemal University, Department of Chemistry, Tekirdag, Turkey

In the search for a plausible mechanism for the photocatalytic degradation reaction of BEN, DFT reactivity descriptors were employed to have information about the most susceptible sites for hydroxyl radical attack. Subsequently, the lowest energy status was found out through geometric optimization via Gaussian 09 programme. This study aims to determine the most probable path for the product distribution of transition state complexes and OH radical interaction in gas phase and aqueous media. With the aim to determine the intermediates occurring at the reaction of transition state complexes degradation, geometric optimization of the reactant and transition status complexes were realized through semiempirical AM1 and PM3, ab initio Hartree-Fock HF/3-21G, HF/6-31G* and Density Functional Theory (DFT) methods. Based on the Quantum mechanical calculation, all probable rate constants of reaction paths were calculated by using Transition State Theory (TST). The impact of water solvent was investigated by using COSMO as the solvation model.

Keywords: benidipine; DFT; COSMO; Gaussian 09; hydroxyl radical.

1. INTRODUCTION

Benidipine HCl (BEN), (±)-(R')-3-[(R')-1-benzyl-3-piperidyl] methyl 1,4 dihydro-2,6-dimethyl-4-(m-nitrophenyl)-3,5-pyridenecarboxylate hydrochloride is a dihydropyridine-derived calcium channel blocker with general properties similar to those of nifedipine. It has relatively high vascular selectivity and is expected to show protective effects on vascular endothelial cells. It is used orally in the management of hypertension and angina pectoris [1,2]. In this Benidipine molecule. Various analytical procedures have been reported for the determination of BEN. They include cyclic voltammetry, liquid chromatography [3], tandem mass spectrometry, capillary column gas chromatography [4], negative ion chemical ionization mass spectrometry [5] and spectrophotometric methods [6]. Tipre and Vavia developed validated stability indicating HPLC (A), HPTLC (B) and spectrophotometric (C) method for the estimation of nitrendipine and the stability indicating capability of the assays were proved using forced degradation, by exposing drug solution to sunlight, acidic and alkaline medium [7]. Canavesi et al., were examined validation and development of a stability-indicating LC–UV method for the determination of pantethine (PAN) and its degradation product based on a forced degradation study. The method showed linearity for PAN (0.4–1.2 mg mL^{-1}), methyl-p-hydroxybenzoate (MHB), propyl-p-hydroxybenzoate (PHB) (0.4–1.2 μg mL^{-1}) and in the this work the chemical stability of PAN was for the first time established through a forced degradation study followed by liquid chromatography tandem mass spectrometry investigation showing the formation of three degradation products of PAN (PD1, PD2 and POx) arising from hydrolytic, thermal and oxidative stresses. PD1 (2.5–100 μg mL^{-1}); the precision, determined in terms of intra-day and inter-day precision, expressed as RSDs, were in the ranges 0.4–1.2 and 0.7–1.4, respectively. The method demonstrated to be accurate and robust; indeed the average recoveries were 100.2, 99.9, and 100.0% for PAN, MHB and PHB, respectively, and 99.9% for PD1 [8]. A rapid and gradient high-performance liquid chromatography combined with quadrupole time-of-flight electrospray ionization tandem mass spectrometry (LC/Q-TOF–ESI-MS/MS) method has been developed for the identification and structural characterization of stressed degradation products of tamsulosin. The drug was degraded significantly under hydrolytic (base and neutral), thermal, oxidative and photolytic conditions, while it was stable to acid hydrolytic stress conditions by Namdev et al. [9] Kamila et al were examined a simple, sensitive and accurate UV spectrophotometric method was developed for the assay of nebivolol hydrochloride in raw material and tablets. The absorbance was measured at 282 nm for nebivolol hydrochloride tablet solution. The linearity range was found to be 5–50 μg/mL for the drug [10]. The International Conference on Harmonization (ICH) guideline entitled 'stability testing of new drug substances and products' requires that stress testing be carried out to elucidate the inherent stability characteristics of the active substance [11]. In the present analytical work, we have developed and compared new, simple and reproducible stability indicating spectrophotometric

*) To whom all correspondence should be sent:
E-mail: yyalcin@nku.edu.tr

methods for the estimation of BEN. The stability indicating capability of the assays is proved using forced degradation, by exposing drug solution to acidic, alkaline and oxidative medium. The aim of this work was to develop stability methods for estimation of percentage degradation of BEN. Therefore in the present investigation, an attempt has been made to develop an accurate, simple and an economic UV method for the estimation of BEN in tablet formulation and validated for accuracy, linearity and stability to forced degradation studies according to the prescribed procedures mentioned in ICH guidelines. Modern pharmaceuticals consist of small organic molecules that are moderately water soluble as well as lipophilic to be biologically active. Among the groups of pharmaceutical compounds of greatest environmental interest are antibiotics due to their extensive use for the treatment of bacterial infections in the whole world. The most dangerous effect of antibiotics is the development of multi-resistant bacterial strains that can no longer be treated with the presently known drugs [12]. After the administration, antibiotics are absorbed, metabolized and finally excreted from the body as unchanged or as metabolites. Metabolism reactions introduce functional groups that are attached to drug molecules to yield polar and hydrophilic molecules that can be readily excreted in urine and feces [13,14]. Thus, they subsequently enter into sewage treatment plants. However, polar antibiotics are not completely removed in sewage treatment plants. As a result, they are often present in effluents from sewage treatment plants as well as in surface and groundwater, where they have to be removed.

2. EXPERIMENTAL

2.1. Instrument and materials

The instruments used were Shimadzu 2600 double-beam UV/Visible spectrophotometer. All chemicals and reagents used were of analytical grade. BENwas kindly provided by Deva (Istanbul, Turkey). Coniel tablets (4 mg) (Deva, Tekirdag, TR) was purchased from a local pharmacy.

2.2. Methods

2.2.1. UV Spectrophotometric method of BEN. In our previous studies, we have developed and validated the UV spectrophotometric method of BEN. This method was used to study the stress degraded behavior of BEN.

2.2.2. Preparation of standard stock solution. A stock solution of BEN was prepared in methanol at 1 mg mL^{-1}. This stock solution was further diluted with methanol to obtain working solutions of 100 µg mL^{-1}.

2.2.3. Preparation of calibration curve. Aliquots of 1-3.5 mL portion of stock solutions were transferred to series of 10 mL volumetric flasks, and the volume made up to mark with methanol. Solutions were scanned in the range of 200- 800 nm against blank. The absorption maxima values were found at 357 nm against blank. The calibration curve was plotted.

Forced degradation studies

A stock solution containing 1 mg BEN in 10 mL methanol was prepared. This solution was used for forced degradation to provide an indication of the stability-indicating property and specificity of the proposed method. In all degradation studies, the absorbance of the drug was measured at 357 nm and the amount of degraded drug was calculated.

2.2.4. Acid and base induced degradation. Acid decomposition studies were performed by using 0.1 mol L^{-1}, 0.5 mol L^{-1}, and 2 mol L^{-1} HCl, and basic decomposition studies were performed by using 0.1 mol L^{-1}, 0.5 mol L^{-1} and 2 mol L^{-1} NaOH. The concentration of BEN was 10 µg mL^{-1} for both acid and base degradation studies. The studies were carried out at 70ºC in water bath within 2, 4, and 6 h.

2.2.5. Oxidative degradation. To study hydrogen peroxide-induced degradation, initial studies were performed in 30% hydrogen peroxide at room temperature for 22 h. For the spectroscopic studies, the resultant solutions were scanned between 800 and 200 nm and the absorbance was taken. The studies were carried out at room temperature within 2, 4, and 6 h in dark.

2.2.6. Neutral hydrolysis. To study the degradation behavior of BEN under neutral conditions, it was dissolved in distilled water and the solution was kept for 2, 4 and 6 h.

2.2.7. Procedure for tablets. Ten tablets of BEN were accurately weighed and the average weight of tablet was calculated. The tablets were crushed well to a fine powder. A portion of the powder equivalent to 100 mg BEN was transferred into a 100 mL calibrated flask and dissolved in 50 mL of methanol. The contents of the flask were sonicated for 30 minutes and then completed to volume methanol. The contents were mixed well and filtered; the first portion of the filtrate was rejected. An aliquot was used for the determination of each drug according to the procedure mentioned above. This solution was prepared three times and the absorbance of each solution was determined at 357 nm. All determinations were conducted in triplicate.

2.2.8. Method validation. The accuracy and precision of the assay, as well linearity of the calibration curve, were determined. The absorbance

of each solution was determined at 357 nm. The standard graph was plotted by taking concentration of drug on x-axis and absorbance on y-axis. All determinations were conducted in triplicate.

3. COMPUTATIONAL SET-UP

Geometry optimization of the reactants, the product radicals, pre-reactive and transition state complexes were performed with the DFT method within the Gaussian 09 package [15]. DFT methods use the exact electron density to calculate molecular properties and energies, taking electron correlation into account. They do not suffer from spin contamination and this feature makes them suitable for calculations involving open-shell systems. The DFT calculations were carried out by the hybrid B3LYP functional, which combines HF and Becke exchange termswith the Lee–Yang–Parr correlation functional.

Choice of the basis set is very important in such calculations. Based on these results, optimizations in the present study were performed at the B3LYP/6-31G(d) level. The forming C–O bonds in the addition paths and the H–O bond in the abstraction path were chosen as the reaction coordinates in the determination of the transition states. Ground-state and transition-state structures were confirmed by frequency analyses at the same level. Transition structures were characterized by having one imaginary frequency that belonged to the reaction coordinate, corresponding to a first-order saddle point. Zero-point vibrational energies (ZPEs) were calculated at the B3LYP/6-31G(d) level [16].

4. RESULTS AND DISCUSSION

The overlay graph of 10 µg mL^{-1} BEN is shown in Fig.1.

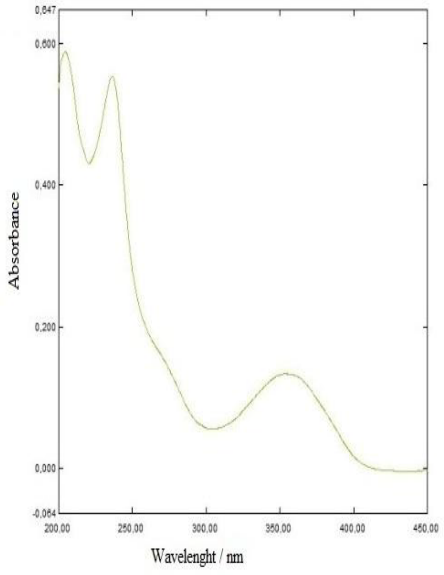

Fig 1. The overlay graph of 10 µg/mL BEN.

4.1. Linearity and calibration curve

The linearity range was found to be 10-35 µg mL^{-1}. The absorbance of each solution was determined at 357 nm. The calibration curve is shown in Fig. 2 and Table 1. The equations of the calibration curves are as in the following:

$$y = 0.0165x\text{-}0.0053 \ (r^2 = 0.999)$$

where y is absorbance intensity and x is BEN concentration (µg mL^{-1}).

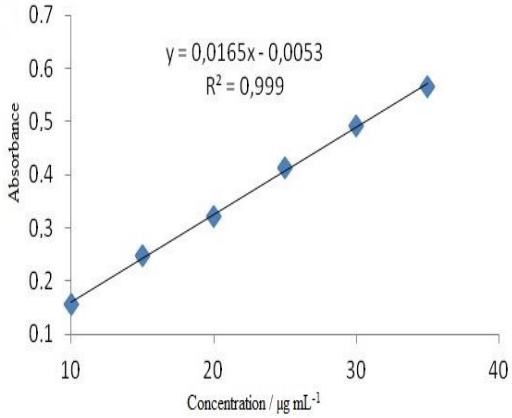

Fig.2. Calibration graph of BEN hydrochloride.

Table 1. Optical characteristics and statistical data.

Parameters	Value
Linearity (µg mL^{-1})	10-35
Regression equation	y = 0.0165x – 0.0053
Slope	0.0165
Slope ± SD	0.0165 ± 0.00092
Intercept	0.0053
Intercept ± SD	0.0053± 0.00743
LOD (µg mL^{-1})	1.56
LOQ (µg mL^{-1})	4.69

4.2 .Limit of detection and limit of quantification

The limit of detection (LOD) and limit of quantification (LOQ) were calculated according to the current ICH guidelines [17]. LOD and LOQ were calculated. Linearity range, regression equation, correlation coefficient, LOD and LOQ (n=3) from the equation of (standard deviation of intercept)/(slope of regression equation) by multiplying 3.3 and 10, respectively. LOD and LOQ values were calculated as 1.56 and 4.69 µg mL^{-1}, respectively.

4.3. Precision and accuracy

Accuracy and precision of the assay was determined by intra-day and inter-day for 3 consecutive days. Three different concentrations of BEN were analyzed in six independent series in the same day (intra-day precision) and 3 consecutive days (inter-day precision). The accuracy and precision of the method was expressed by relative mean error (RME %) and by relative standard deviation (RSD %), respectively. Intra- and inter-day precision and accuracy were calculated by measuring the amount of BEN in three times of 30 µg mL^{-1} concentration levels. The intra-day accuracy ranged from 1.42 % and the inter-day accuracy ranged from 2.62%. The intra-day precision ranged from 0.7, and the inter-day precision ranged from 1.4%.

4.4. Pharmaceutical application

The proposed method was successfully applied to pharmaceutical preparation (Table 2). The determination of BEN tablets, Coniel 4 mg were analyzed at 357 nm against blank. From the calibration curve, concentration of drug in percentage was calculated. The recovery was found to be 100±0.05 %.

Table 2. Analysis of benidipin hydrochloride in tablets.

Tablet	Labeled claim (mg)	Amount found (mg)	Assay ± SD%	RSD %
	4.00	4.00	100 ± 0.05	0.88

4.5. Forced degradation studies

4.5.1. Acid degradation. The acid degradation was performed using 0.1 mol L^{-1}, 0.5 mol L^{-1}, and 2 mol L^{-1} HCl. The overlay graph of 10 µg mL^{-1} acid-degraded BEN is shown in Fig.3. BEN is degraded within 2, 4 and 6 h. The percentage of degraded drug was calculated. The results are shown in Tables 3-5.

4.5.2. Alkaline degradation. The alkaline degradation was performed using 0.1 N, 0.5 N, and 2 N NaOH. The overlay graph of 10 µg/mL alkaline-degraded BEN is shown in Fig.3. BEN is degraded within 2, 4 and 6 h. The percentage of degraded drug was calculated. The results are shown in Table 6-8.

4.5.3. Neutral degradation. The neutral degradation was performed. The overlay graph of neutral-degraded BEN is shown in Fig. 3. BEN is degraded within 2, 4 and 6 h. The percentage of degraded drug was calculated. The results are shown in Table 9.

Table 3. Acid degradation (0.1 mol L^{-1} HCl) of Benidipine hydrochloride

Name	Absorbance	Concentration mg	Degradation %
Analyte at 2 h	0.168	10.5	0
Analyte at 4 h	0.154	9.65	3.5
Analyte at 6 h	0.150	9.41	5.9

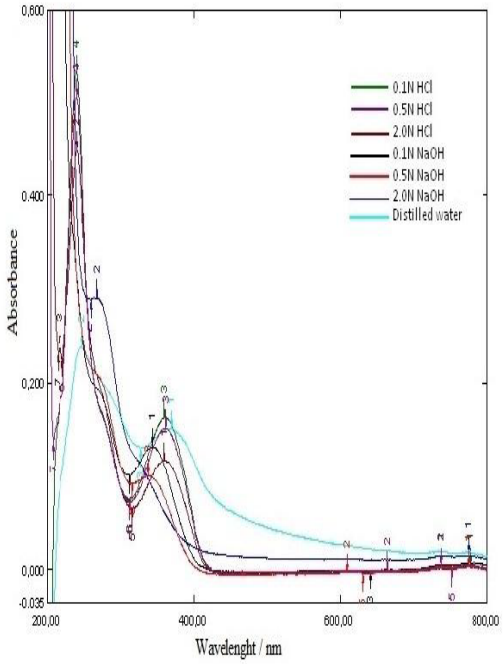

Fig.3. Overlay graphs of BEN hydrochloride degraded (acidic, alkaline degradation) within 6 h.

Table 4. Acid degradation (0.5 mol L^{-1} HCl) of Benidipine hydrochloride

Name	Absorbance	Concentration mg	Degradation %
Analyte at 2 h	0.159	9.96	0.4
Analyte at 4 h	0.152	9.53	4.7
Analyte at 6 h	0.145	9.11	8.9

This proved that there is degradation of BEN under heat conditions. The proposed method has good reproducibility, accuracy and revealed that the commonly used excipients and additives in formulation were not interfering and the drug is stable to acid and oxidative treatments. The method can be adopted for routine quality control.

Table 5. Acid degradation (2 mol L^{-1} HCl) of Benidipine hydrochloride

Name	Absorbance	Concentration mg	Degradation %
Analyte at 2 h	0.137	8.62	13.8
Analyte at 4 h	0.122	7.72	22.8
Analyte at 6 h	0.099	6.32	36.8

4.5.4. Oxidative degradation. Oxidative degradation was performed by using 30% hydrogen peroxide. BEN is degraded within 22 h. The percentage of degraded drug was calculated. The results are shown in Table 10. Fig 4 shows overlay graph of BEN degraded (oxidative) within 22 h at room temperature in dark. This proved that there is degradation of BEN under heat conditions. The proposed method has good reproducibility, accuracy and revealed that the commonly used excipients and additives in formulation were not interfering and the drug is stable to acid and oxidative treatments. The method can be adopted for routine quality control.

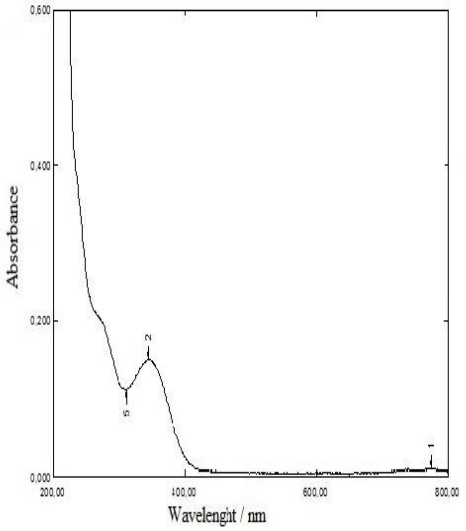

Fig.4. Overlay graph of BEN hydrochloride degraded (oxidative) within 22 h at room temperature.

Table 6. Alkaline degradation (0.1 mol L^{-1} NaOH) of Benidipine hydrochloride

Name	Absorbance	Concentration mg	Degradation %
Analyte at 2 h	0.147	9.23	7.7
Analyte at 4 h	0.141	8.87	11.3
nalyte at 6 h	0.130	8.20	18.0

4.6. Theoretical prediction of the degradation mechanism

In the search for a plausible mechanism for the photocatalytic degradation reaction of BEN, DFT reactivity descriptors were employed to have information about the most susceptible sites for hydroxyl radical attack. Fig. 5 shows the optimized structure of BEN molecule and the numbering system that is used throughout the calculations. Three main competing reaction pathways shown in Fig. 6 were determined by selecting the specific sites of BEN molecule, on the basis of their softness values being close to that of the •OH radical. The predicted mechanism was confirmed by comparison with the experimental results on simple structures reported in the literature, as explained below. The lowest-energy structure is the most stable structure. Statements in this fragmentation took place both experimental and theoretical, as seen from the Gibbs free energy values of Table 11 and support it.

Table 7. Alkaline degradation (0.5 mol L^{-1} NaOH) of Benidipine hydrochloride

Name	Absorbance	Concentration mg	Degradation %
Analyte at 2 h	0.133	8.38	16.2
Analyte at 4 h	0.113	7.17	28.3
Analyte at 6 h	0.095	6.02	39.2

Table 8. Alkaline degradation (2 mol L^{-1} NaOH) of Benidipine hydrochloride

Name	Absorbance	Concentration mg	Degradation %
Analyte at 2 h	0.114	7.23	27.7
Analyte at 4 h	0.082	5.29	47.1
nalyte at 6 h	0.057	3.78	62.2

Table 9. Neutral degradation of Benidipine hydrochloride

Name	Absorbance	Concentration mg	Degradation %
Analyte at 2 h	0.114	10.5	0
Analyte at 4 h	0.082	10.3	0
Analyte at 6 h	0.057	9.84	1.6

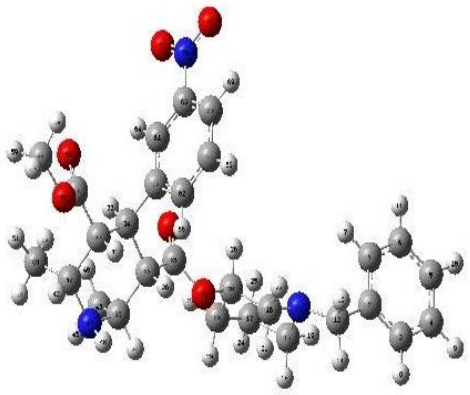

Fig. 5. Optimized structure of BEN and the numbering system (gray, carbon;red, oxygen; blue, nitrogen; white, hydrogen).

Table 10. Oxidative degradation (30% hydrogen peroxide) of Benidipine hydrochloride

Name	Absorbance	Concentration mg	Degradation %
Analyte at 22 h	0.144	9.05	9.5

Three main competing reaction pathways shown in Fig. 6 were determined by selecting the specific sites of BEN molecule, on the basis of their softness values being close to that of the •OH radical. The predicted mechanism was confirmed by comparison with the experimental results on simple structures reported in the literature, as explained below. The lowest-energy structure is the most stable structure. Statements in this fragmentation took place both experimental and theoretical, as seen from the Gibbs free energy values of Table 11 and support it.

Table 11. Constant energy, enthalpy and Gibbs free energy values according to the DFT method.

Molecules	Energy (kcal mol^{-1})	Enthalpy (kcal mol^{-1})	Gibbs free energy (kcal mol^{-1})
Benidipine	-1069012.515	-1068609.154	-1068676.829
F1	-926021.799	-925648.345	-925709.257
F2	-742038.567	-741798.939	-741847.870
F3	-327727.700	-327551.055	-327582.649
F4	-72611.831	-72692.532	-72709.473

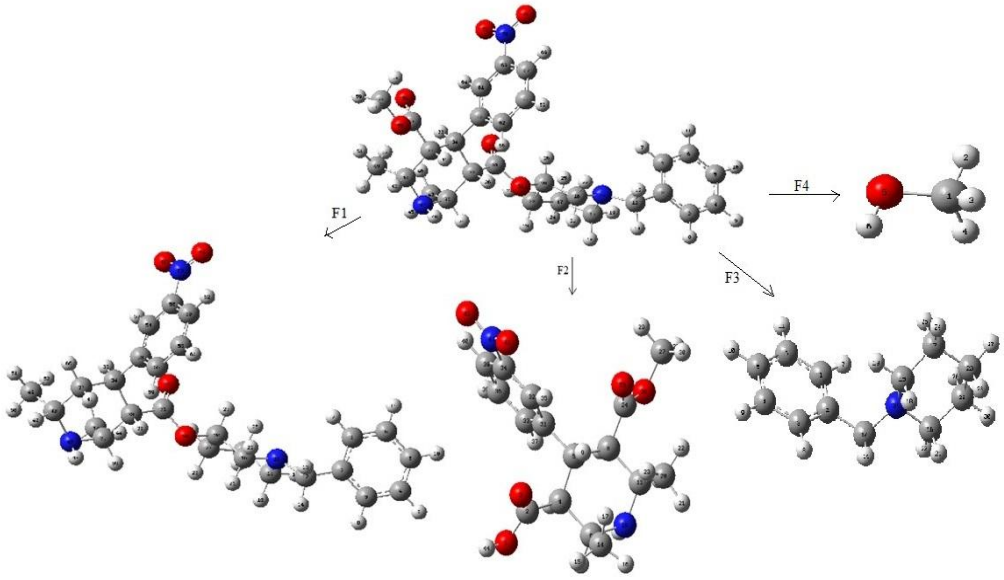

Fig. 6. Possible pathways for the photocatalytic degradation of BEN.

5. CONCLUSIONS

Stress degradation study of BEN was done using UV spectrophotometric method. The method was found to be simple and cost effective. It was found that BEN was degraded in acidic, alkaline and oxidative conditions. This method also provides quantification of BEN in presence of degraded products. Degradation of BEN was predicted to occur through intramolecular F1, F2, F3 and F4 ring cleavages followed by subsequent reactions with •OH radicals transforming the fragments into smaller species such as NO_3^- and NH_4^+.

Acknowledgments. *This work was supported by the Research Fund of the University of Namik Kemal (Project no: NKUBAP.00.24.AR.13.08)*

REFERENCES

1. S.C. Sweetman Martindale, The Extra Pharmacopoeia, thirty five ed. in: Pharm Press, 2007..
2. K.D. Sanborn, Physicians Desk Reference, sixty one ed. in: Med. Eco. Co., Montvale, 2007.
3. N. Karadas, S. Sanli, M. Gumustas, S.A. Ozkan, *J. Pharm. Biomed. Anal*., **66,** 116 (2012).
4. W. Kang, H.Y. Yun, K.H. Liu, K.I. Kwon, J.G. Shin, *J. Chromatogr.* B., **805,** 311 (2004).
5. H. Magara, H. Kobayashi, S.J. Kobayashi, *J. Chromatogr.*, **617,** 59 (1993).
6. I. Singhvi, S.C. Chaturvedi, *Ind. J. Pharm. Sci*.,**61,** 190 (1999).
7. D.N. Tipre, P.R.Vavia, *J. Pharm. Biomed. Anal*., **24,** 705 (2001).
8. R. Canavesi, S. Aprile, E. Varese, G. Grosa, *J. Pharm. Biomed. Anal*., **97,** 14 (2014).
9. D. Namdev, R.M. Borkar, B. Raju, P.D. Kalariya, V.T. Rahangdale, S. Gananadhamu, R. Srinivas, *J. Pharm. Biomed. Anal*., **88,** 245 (2014).
10. M.M. Kamila, N. Mondal, L.K. Ghosh, B.K. Gupta, *Pharmazie.*, **62,** 486 (2007).
11. ICH, Stability Testing of New Drug Substances and Products, in: International Conference on Harmonization, 1993.
12. M. Addamo, V. Augugliaro, A.D. Paola, E. Garcia-Lopez, V. Loddo, G. Marci, L. Palmisano, *J. Appl. Electrochem.,* **765,** 35 (2005).
13. M. Rabiet, A. Togola, F. Brissaud, J.L. Seidel, H. Budzinski, F. Elbaz-Poulichet, *Environ. Sci.Technol.*, **40,** 5282 (2006).
14. K. Ikehata, N.J. Naghashkar, M.G. El-Din, *Ozone: Sci. Eng*., **28,** 353 (2006).
15. Gaussian 09, Revision B.04, in: *Gaussian, Inc.*, 2009.
16. A. Hatipoglu, D. Vione, Y. Yalçın, C. Minero, Z. Çınar, *J. Photochem.Photobiol. A: Chemistry*, **215,** 59 (2010).
17. International Conference on Harmonization, ICH Guideline, Q2R1, in: Validation of Analytical Procedure: Text and Methodology, 2005.

Bulgarian Chemical Communications, Volume 49, Issue I (pp. 140 – 145) 2017

Synthesis of SiC from poly(silyne-*co*-hydridocarbyne) under CO_2 atmosphere

Y. Nur*, G.E. Bayol

Department of Chemistry, Faculty of Arts and Sciences, Mustafa Kemal University, 31070, Hatay, Turkey

Submitted: June 1, 2017; Accepted: September 1, 2017

It is well known that advanced ceramics from polymer precursor have been producing upon heating under an ambient and inert atmosphere, like argon or nitrogen gases over 40 years. However, the effect of these gases on the production and on the crystal form of ceramic obtained are not well understood during thermal treatments. Here, we report to demonstrate a novel, simple and a common method for the production of crystalline SiC ceramic species using a polymeric precursor, which is poly(silyne-co-hydridocarbyne) (PSC), upon heating under an ambient and CO_2 atmosphere. The Raman and X-ray analysis showed that polycrystalline SiC production was successfully achieved at 1000 and 750°C under CO_2 atmosphere. Amorphous ceramic material was obtained at 500°C under CO_2 atmosphere. Also, the results showed that SiC powder produced under CO_2 has not crucial differences in crystal forms that is produced under argon atmosphere. SiC produced at 1000°C is mostly Moissanite-5H, at which temperature there is also a small amount of Moissanite-8H and Moissanite-84R. SiC produced at 750°C is mostly Moissanite-5H. There is also the trace of Moganite and Coesite, which are crystal forms of SiO_2. As a result, the type of produced SiC depends on process temperature and production atmosphere.

Keywords: Electropolymerization; pre-ceramic polymer; silicon carbide; ceramic

1. INTRODUCTION

Organo-silicon compounds have been widely recognized over 40 years as polymeric precursors for the production of advanced ceramics. Unlike the conventional synthesis procedures, they can be adopted to plastic-forming techniques such as fiber spinning, foaming, extrusion, injection molding or resin transfer molding to generate some special components in desired shape, or advanced ceramics known as polymer-derived ceramics or PDCs by pyrolysis above 750°C, especially under a non-oxidative atmosphere like nitrogen or argon atmosphere [1–12]. Pre-ceramic polymers are an important class of polymers since they stand as the interface between polymers and ceramics [2, 3, 10]. They easily produce ceramic materials upon moderate heating. Generally, the most crucial properties of these types of polymers are to form tough, hard-wearing ceramic materials with high thermal stabilities. A many kinds of ceramics that is not achievable by other techniques can be produced by using polymeric precursors. The composition of ceramic strictly depends on the nature and chemistry of polymeric precursors [1-12]. For example, an amorphous SiCO residue is produced from silicones upon heating in a non-oxidative atmosphere, which is considered as a silica glass [5-8]. Polysilazanes, another well investigated class of preceramic polymers, yield a SiCN ceramic at low pyrolysis temperature and after further heating to higher temperatures a similar microstructural evolution in materials will take place to form Si_3N_4 and SiC nano-sized regions [9]. Moreover, PMSi forms silicon carbide (SiC) [10,11], or PHC easily yields diamond and diamond-like carbon (DLC) [12] via pyrolysis under argon atmosphere. Likewise, since it already contains silicon and organic carbon atoms on its backbone, poly(silyne-co-hydridocarbyne) (PSC) can be transformed into silicon carbide without requiring additional carbon source and a catalyst [2].

Silicon carbide (SiC) is a wide band gap semi-conducting material and exhibits many excellent properties for high temperature, high frequency and high power applications. SiC has extensive usage such as in field emission display, nanosensors and nanoscale electro-devices [7]. Besides, SiC is used an abrasive and a wear resistant material in the form of powder or protective coatings, and also widely used in high temperature and high power electronic devices. In addition, amorphous SiC thin film has been recently used as a functional material for micro-electro-mechanical systems (MEMS) to prevent corrosion [8, 9].

The synthesis of silicon carbide (SiC) is accomplished with methods such as carbon nanotubes-confined growth [13], chemical vapor deposition (CVD) [14] and carbon-thermal reduction with catalyst [15] or without catalyst [16] etc. However, the most of these synthetic approaches comprise of complicated processes and manipulations. For example, it is quite difficult to get rid of the resident metal catalyst from the vapor–liquid–solid growth process, or CVD needs some complex equipment with well-controlled

*) To whom all correspondence should be sent:
E-mail: ynur2005@gmail.com

atmosphere. The method for the production of ceramics via pyrolysis using polymeric precursors has been applying since 1970's [17]. The advantages of this method are to be low impurity level and low cost production, to yield homogeneous element distribution, and to need low processing temperatures [2, 3, 10-12]. SiC can also be formed as a film upon heating on a surface because polymeric precursors are soluble in common organic solvents like, THF or chloroform etc [2, 3, 10-12].

In this research project, PSC was synthesized and characterized as reported in references 2 and 3 and its structure is presented in Figure 1. Advanced ceramic, like SiC, is mostly produced via thermal process of polymeric precursor under an inert media i.e. argon (Ar) or nitrogen (N_2) gas during thermal process [1-12]. In this article, it is aimed to investigate the type of SiC produced from PSC upon heating under CO_2 atmosphere. There is no such a work to demonstrate the production of SiC under CO_2 atmosphere.

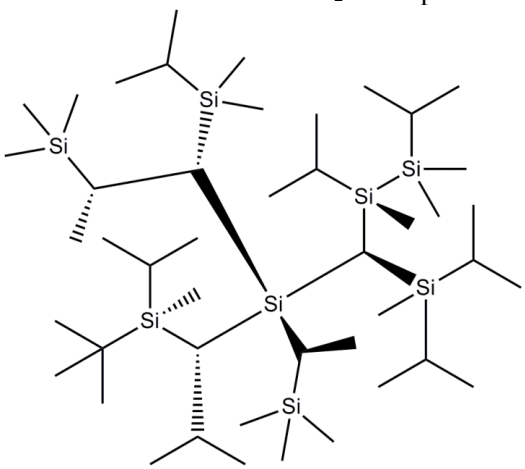

Fig. 1. Schematic representation of structure of poly(silyne-co-hydridocarbyne).

2. EXPERIMENTAL

2.1 Materials and methods

The reagents were bought from Sigma-Aldrich and used without further purification. The chemicals and materials used are trichloro(dichloromethyl) silane (96%), dimethoxy ethane (DME, anhydrous, 99.5%), tetrabutylammonium tetrafluoroborate (TBAFB, 99%), lithium aluminum hydrate (LAH, powder, 95%), methyl lithium (MeLi, 3.1 M in diethoxymethane), 430 stainless steel and copper electrode.

2.2. Equipment

The electrolysis of monomer was done via a DC power supply. ^{1}H Nuclear Magnetic Resonance (^{1}H-NMR) spectra were obtained using a Bruker-Spectrospin Avance DPX 400 Ultra-Shield (400 MHz, $CDCl_3$ solvent). Attenuated Total Reflectance-Fourier Transform Infrared (FTIR) spectra were collected using a Bruker Vertex 70 spectrophotometer by an Attenuated Total Reflectance (ATR) module. UV/visible spectra were taken using an HP8453A UV/visible spectrometer (Hexane as solvent). Gel Permeation Chromatography (GPC) was performed by a Perkin-Elmer Series 200 apparatus with a refractive index (RI) detector using TSKgel AM GPC Gel column and N,N-dimethyl form amide (DMF) eluent at a flow rate of 1.0 ml/min and calibrated via polystyrene standards. Heat treatment of the polymer was carried out in an alumina ceramic boat using Protherm brand PTF12/50/450 model a tube furnace fitted with an alumina tube under a constant flow of carbon dioxide (CO_2). FEI Quanta 250 FEG instrument was run for Scanning electron microscopy (SEM). Raman spectroscopy was carried out using a Bruker FRA 106/S spectrograph fitted with a He-Ne laser (wavelength 532 nm) as the excitation source. X-ray diffraction (XRD) patterns were taken with a Rigaku Miniflex Diffractometer and CuKα (30 kV, 15 mA, λ=1.54051 Å) radiation. Scanning was done between $5^\circ<2\theta<100^\circ$. All measurements were made with 0.05 degree steps and 2 degree/minute rate. The divergence slit was variable, and the scattering and receiving slits were 4.2 degrees and 0.3 mm, respectively.

2.3. Synthesis of poly(silyne-co-hydridocarbyne)

The synthesis and characterization of PSC was performed as reported in references 2 and 3. Shortly, electrochemical synthesis of PSC was accomplished in 250 ml of an undivided cell. A 2 ml of trichloro(dichloro methyl) silane (0.007 M, in 60 ml DME) and 200 mg of TBAFB (0.01 M, in 60 ml DME) was mixed in 60 ml of DME to prepare electrolyte solution while it was purged with Ar. The cell was equipped with a 430 stainless steel as the cathode (10 cm × 5 cm × 0.5 mm) and copper as the

anode (10 cm × 5 cm × 0.5 mm). −8.0 V potential was applied to achieve the electrolysis for 8 h at room temperature and under Ar atmosphere. Once the electrolysis was finished, 150 mg of LAH was added to the solution and refluxed for 12 h. After evaporation of solvent and then re-dissolving the residue in DME, 4 ml of MeLi (3.0 M in DME) was added dropwise into this solution to replace chlorine atoms with methyl substituents, which makes PSC resistant against moisture being in the air by increasing hydrophobicity of the polymer backbone. The polymer formed was a light-brown powder and about 70% yields as reported in references 2 and 3.

2.4. Synthesis of SiC

SiC was synthesized and characterized as reported in previous works [2,3, 10-12]. Shortly, PSC was put into alumina ceramic boats and then heated at 1000◦C, at 750◦C and at 500◦C in a tube furnace under CO_2, at a ramp rate of 10◦C/min, held for 24 h to produce SiC and then cooled to room temperature. The crystalline SiC obtained was about 25% yields. All SiC samples were characterized by Raman, X-ray spectroscopy and SEM.

3. RESULTS AND DISCUSSION

3.1 Poly(silyne-co-hydridocarbyne)

The network structure of PSC with tetrahedral bounded carbon and silicon atoms is presented in Fig. 1. Like polycarbynes and polysilynes, PSC can be easily converted to SiC ceramic unless it has any functional groups like double bound which gives an intense absorption band in the visible region [2, 3, 10, 11]. UV/Vis spectroscopy, hence, was used to figure out whether the polymer has or not a functional group on its backbone. The characteristic structure of PSC results in a unique electronic spectrum with broad absorption starting in the ultraviolet (UV) region (at ~200 nm) tailing off the visible region (Fig. 2a) [2,3]. A small amount of aliphatic SiHx (1–3) and CHx (x: 2–3) groups on the backbone cause some weak absorptions appearing in the visible region (Fig. 1a), which may explain the dissolution of PSC in common solvents. FTIR spectrum of PSC (Fig. 2b) showed the usual broad Si-C absorption (δSi-C) at ~750 cm^{-1}, which is the combination of the peaks at 770 (antisym), 688 (sym) and 650 cm^{-1} [2,3]. A peak at ~1450 cm^{-1} is due to Si-CH_3 and Si-CH_2- absorptions [2, 3, 10, 11]. FTIR of PSC (Fig. 2b) is consistent with a primarily network backbone structure of the formula (SiCH)n. All characterization data for PSC shown here is consistent with the product being poly(silyne-co-hydridocarbyne), [(SiCH)n]. The ^{1}H-NMR of PSC is shown in Fig. 2c.

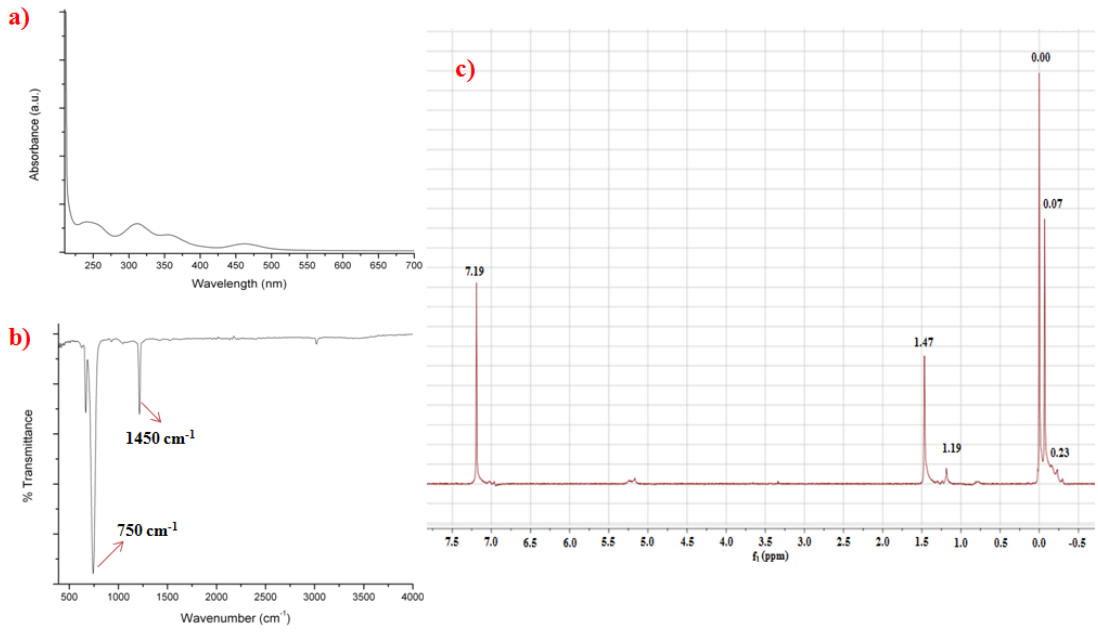

Fig. 2. a) UV/Vis; b) FTIR and c) ^{1}H NMR spectrum of poly(silyne-co-hydridocarbyne).

Fig. 2c shows the broad ^{1}H-NMR resonances, which is common spectrum for this type of polymer [2, 3, 18, 19]. The peaks between -0.1 and 0.10 ppm correspond to the protons of methyl (CH_3) and methine (CH) attached to silicon (νCH_3-Si: 0.02 and ν CH-Si: 0.08), other peaks at 1.19 and 1.47 ppm correspond to aliphatic -CH-, -CH_2-and -CH_3 protons [2, 3, 13–19]. Average molecular weight of PSC was determined by GPC (GPC of PSC: Mn = 4589, Mw = 6404, PD = 1.40). This low molecular

weight result of PSC is due to the calibration of GPC instrument with linear polystyrene [2, 3, 10–19].

3.2 Polymer derived ceramic, SiC

Heat treatment of PSC produces a hard crystalline substance in high yield; typically in the range of 20–50%, depending on pyrolysis conditions. Pyrolysis at 1000 and 750◦C nearly resulted with 25% yield ceramic, while the material at 500◦C was obtained in approximately 42% yield.

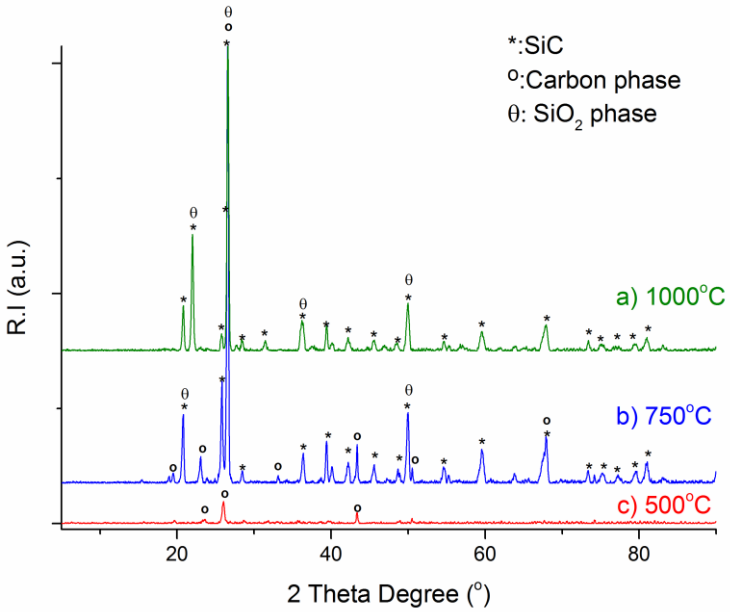

Fig. 3. X-ray powder diffraction patterns of SiC ceramics produced at **a)** 1000ºC, **b**) 750ºC and **c**) 500ºC.

The X-ray diffraction pattern of the SiC specimens is shown in Fig. 3. Wide angle X-ray powder diffraction patterns showed that SiC ceramics were successfully produced from PSC under CO_2 and ambient atmosphere. While SiC produced at 500ºC (Fig. 3c) was X-ray amorphous, the samples produced at higher temperature, at 750 and 1000ºC (Fig. 3a and 3b) , were crystalline, and their reflections were consistent with the mixture of Moissanite-5H, Moissanite-8H and Moissanite-84R, reflections of which were assigned according to "The International Center for Diffraction Data (ICDD))" (PDF- 42-1360", "PDF-72-1625", "PDF-73-2082" and "PDF-73-2086, PDF-14-0654, PDF-38-0360 and PDF-42-1360). These crystalline samples are mostly composed of Moissanite-5H, which results are consistent with ICDD [2,3]. There are also some small reflections in Fig. 3a that cannot be assigned to Moissanite-5H or any other SiC phase [3]. Pyrolysis of the sample was carried out in an alumina crucible and an alumina tube and thus, it is believed that these peaks probably arose from Al_2O_3 contamination or SiO_2 formation during heat process [2].

The polycrystalline SiC has several overtone peaks in the range of 1000–2000 cm^{-1} (Fig. 4) [20–23]. SiC has a weak peak about 1620 cm^{-1} [21, 23]. The Raman spectrum of the samples (Fig. 4) showed very broad peaks in the vicinity of 1340 and 1600 cm^{-1}. The peaks around 1300 cm^{-1} are the so-called defect-induced D band, the peaks around 1600 cm^{-1} are the in-plane vibrational G band, which are respectively related with a strong sp^3-like resonant contribution and a sp^2-like doublet as observed in carbonous materials [21, 23]. Raman signals (Fig. 4) related to carbon and SiC interfered with each other since they appeared at the same Raman shift region and were very broad shifts. The weak peaks of SiC corresponding to the transversal optic at 796 cm^{-1} and the longitudinal optic at 972 cm^{-1} phonon modes were not clearly observed since D and G band in the spectra were significantly intense in Fig. 4. D and G bands emerging in Fig. 4a are nearly at same heights; however these are obviously different for SiC produced at 750 and 500ºC. Also, SiC formed at 500ºC (Fig. 4c) might be attributed to be crystalline SiC material from its Raman analysis; however, it revealed that the X-ray diffraction pattern obtained is more likely for an amorphous material. It can be concluded that the composition of SiC produced at 500ºC is mainly graphitic carbonous material. Thus, this is the reason why D and G band in the Raman analysis strongly appeared. Moreover, D band clearly appeared with lower intensity than that of G-band (Fig. 4c) which is another evidence for it to be amorphous. This result is also very consistent with X-ray and SEM (Fig. 3c and 5c) analyses.

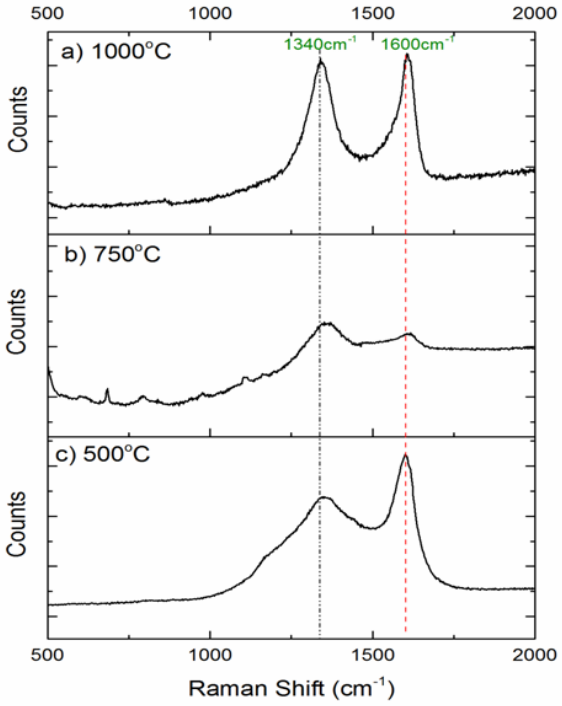

Fig. 4. Raman spectrum of SiC ceramics produced at **a)** 1000°C, **b)** 750°C and **c)** 500°C.

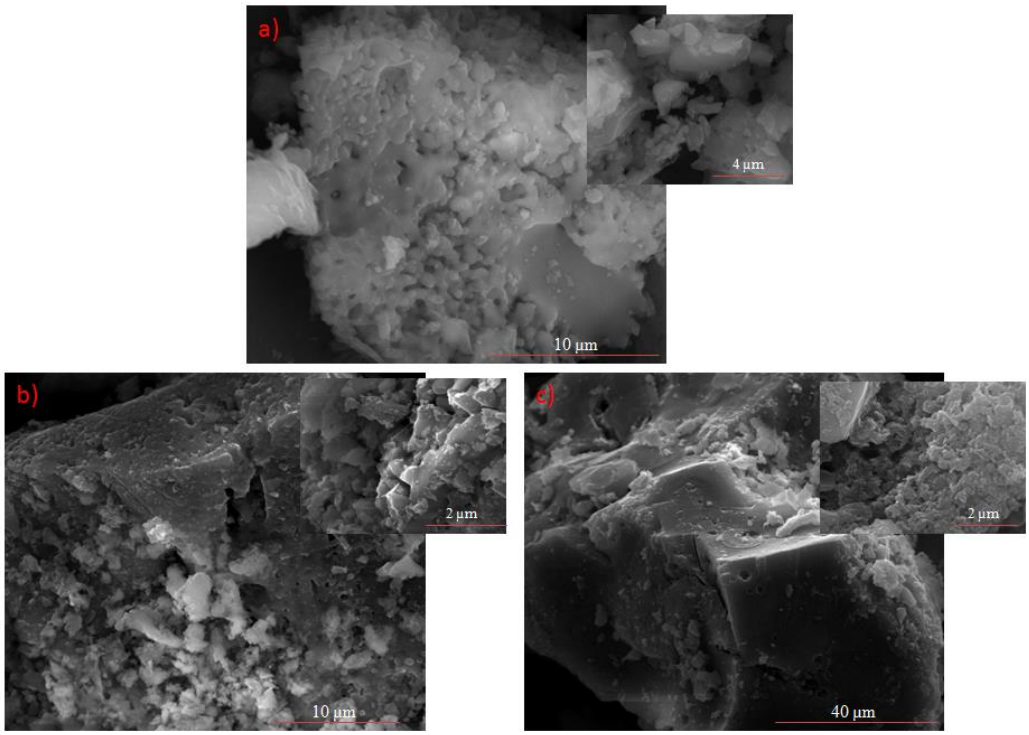

Fig. 5. SEM images of SiC ceramics produced at **a)** 1000°C, **b)** 750°C and **c)** 500°C.

The SEM micrographs of SiC produced at different temperatures are shown in Fig. 5. In terms of morphology, it can be seen from Fig. 5 that ceramics are made up of particles which are irregular in shape and form as agglomerates. The size of the crystals is also mostly in the micrometer scale as seen clearly in SEM images in Fig. 5. At the moment, we have no significant means to control the crystal size and shape. It is obviously seen that SiC produced at 500°C is amorphous (Fig. 5c) which is very consistent with other analyses (Fig. 3c).

4. CONCLUSIONS

The results showed that the synthesis of both the polymer and the resulting ceramic is relatively straightforward and simple. In the production of advanced ceramic, argon or nitrogen gas is used to create an inert media during thermal process, however, there is no such a work to demonstrate the production of SiC under CO_2 atmosphere. The Raman and X-ray analysis showed that polycrystalline SiC production was successfully achieved at 1000 and 750◦C under CO_2 atmosphere. The material produced at 500◦C was amorphous and the X-ray analysis showed it clearly. XRD results seem to indicate that the SiC was not a single Moissanite-5H, but the mixture of Moissanite-5H, Moissanite-8H and Moissanite-84R.

Acknowledgments. *We especially thank to TUBITAK for financial support (project number:211T108).*

REFERENCES

1. P. Colombo, G. Mera, R. Riedel, G. D. Sorarù, *J. Am. Ceram. Soc.,* **93,** 1805 (2010).
2. Y. Nur, L. Toppare, *J. of Macromol. Sci. Part A: Pure and Appl. Chem*., **50**, 923 (2013).
3. Y. Nur, G. E. Bayol, *J. Sol-Gel Sci. Tech*., **83**, 223 (2017).
4. P. Greil, *Adv.* Eng. *Mater*., **2**, 339 (2000).
5. T. Rouxel, G. Massouras, G. D. Soraru, *J*. Sol-Gel *Sci. Tech.*, **14**, 87 (1999).
6. A. Scarmi, G. D. Sorarù, R., *J. Non-Cryst. Solids*, **351**, 2238 (2005).
7. H. Brequel, J. Parmentier, G. D. Soraru, L. D. Schiffini, S. Enzo, *NanoStruct. Mater*., **11**, 721 (1999).
8. G. D. Soraru, S. Modena, E. Guadagnino, P. Colombo, J. Egan, C. Pantano, *J. Am. Ceram. Soc*., **85**, 1529 (2002).
9. G. D. Soraru, D. Suttor, *J. Sol-Gel* Sci. *Techn.*, **14**,69 (1999).
10. G. Mera, A. Navrotsky, S. Sen, H. J. Kleebe, R., *J. Mater. Chem. A*, **1**, 3826 (2013).
11. M.W. Pitcher, S J. Joray, P.A. Bianconi, *Adv. Mater*., **16**, 706 (2004).
12. L.A. Vermeulen, K. Smith, J. Wang, *Electrochim. Acta*, **45**,1007 (1999).
13. Y. Nur, M. W. Pitcher, S. Seyyidoglu, L. Toppare, *J. Macromol. Sci. A*, **45**,358 (2008).
14. Z. L. Wang, Z. R. Dai, R. P. Gao, Z. G. Bai, J. L. Gole, *Appl. Phys. Lett*., **77**, 3349 (2000).
15. M.S. Al-Ruqeishi, R. M. Nor, Y. M. Amin, K. Al-Azri, *J. Alloy. Compd*., **497**, 272 (2010).
16. S. Yajima, K. Okamura, J. Hayashi, M. Omori, *J. Am. Ceram. Soc.*, **59**, 324 (1976).
17. R.W. Rice, *Am. Ceram. Soc. Bull*., **62**, 889 (1983).
18. A.I. Kharlamov, N.V. Kirillova, S. N. Kaverina, Theor. Exp. Chem., 38, 237 (2002).
19. R. D. Rieke, T.A. Chen, *Chem. Mater*., **6**, 576 (1994).
20. E. Corro, M. Taravillo, J. Gonzalez, V. G. Baonza, *Carbon,* **49**, 973(2011).
21. S. Urbonaite, L. Halldahl, , G. Svensson, *Carbon*, **46**, 1942 (2008).
22. Y. Xu, X. Wu, C. Ye, Y. Deng, T.Chen, S. Ge, *Thin Solid Films*, **527**, 65 (2013).
23. Z. H. Ni, W. Chen, X. F. Fan, J. L. Kuo, T. Yu, A. T. S.Wee, Z. X. Shen, *Phys. Rev. B*., **77**, 1 (2008).

Bulgarian Chemical Communications, Volume 49, Issue I (pp. 146 – 150) 2017

Application of artificial neural networks for Zeta potential of copolymer

F. Noyan Tekeli*

Yildiz Technical University, Faculty of Arts and Sciences, Department of Statistics 34220 Esenler, Istanbul, Turkey

Submitted: June 1, 2017; Accepted: September 1, 2017

One of the measure of stability of the colloidal system is Zeta potential. In this study, artificial neural networks based prediction of the zeta potential of the copolymer was investigated. Multilayered perceptron and generalized regression neural networks were developed for zeta potential measurements of the copolymer as a function of pHs. Performance indices were demonstrate that structured generalized regression neural networks can predict the zeta potential of the copolymer quite efficiently than multilayer perceptron neural networks. The results showed that generalized regression neural networks could be useful to predict the zeta potential of the copolymer at different pH values.

Keywords: zeta potential, artificial neural networks, multilayer perceptron, generalized regression neural network

1. INTRODUCTION

Artificial neural networks (ANNs) can be summarized as an information processing system consisting of many neurons in the human brain that connected to one another in parallel with different levels of effect. Artificial neural network is an artificial simulation of the biological structure of the human nervous system and the working system of the human brain. Artificial neural networks are algorithmic systems that can grasp nonlinear relationships between different parameters, can order large quantities of input data and transform them into a graphical pattern of the output data. In chemistry, several problems are composed of complex systems and and artificial neural networks (ANNs) are tools that provides accurate results for complex and nonlinear problems requiring high computational costs [1-2].

In addition to fast computation superiority, the basic advantages of ANNs are learning, generalization ability of data, fault tolerance and inherent contextual information processing [3].

Drug carriers that succeed several goals like anhancement of biovailability,satability, preventing the drug interactions are the most important ways among new drug delivery systems. These carrier systems which include, cellular carriers, particulate carriers, lipoidal carriers, etc. were developed for different aims depending on the requirements [4]. The aim of this article is to estimate the zeta potential at different pHs of the copolymer

as an alternative drug carrier system using algorithms and methodologies based on the ways in which the human brain solves the problems. For this purpose, we developed two type of neural network: multilayer perceptron neural network (MLPNN) and generalized regression neural network (GRNN). The neural networks were

compared in order to the prediction capacity of the zeta potential of copolymer at different pH values.

2. ARTIFICIAL NEURAL NETWORKS

Recently there has been a growing interest on the applications of neural networks in biomedical research [5]. Artificial neural networks are designed to simulate some of the functions of the human brain using different learning algorithms. ANNs, have notable information working properties of human brain such as nonlinearity, high parallelism, robustness, fault and failure tolerance, learning, to handle imprecise and fuzzy information and their ability to generalize [6]. Using this feature, ANN can be used to solve complex real-life problems such as classification, clustering, function approximation and optimization[7].

Depending on the nature of the problem, different neural network modeling arrangements are made. These schemes are called artificial neural network architecture and define the number of hidden layers, the number of hidden nodes, the number of nodes in the input and output layers,the nature of activation functions and the learning algorithm [8].

The two main categories can be divided into ANN architectures, feed forward neural networks and feedback neural networks. In the feed forward neural networks, learning is a very important. Supervised and unsupervised are the two type of learning. Supervised learning occurs presenting input and output data to the network [9].

The measurement types used to measure the accuracy of the prediction are based on comparisons between the predicted output and the actual values in

* To whom all correspondence should be sent.
E-mail: fnoyan@yildiz.edu.tr

supervised neural network. Coefficient of determination (R^2) and mean square error (MSE) are the most common network performance measurements [9].

Unsupervised neural network uses only the input data to expose models in the characteristics of the data. Unsupervised learning is to make the computer learn how to do something we do not say how to do it. Classification, data mining, and self-organizing maps are most common unsupervised neural networks. Supervised feed forward neural networks has two different types: feed forward neural networks trained with backpropagation algorithm and statistical neural networks [9]. In this article, we used the multilayer perceptron neural network and generalized regression neural network. MLPNN is the most common and successful supervised learning architecture with multilayer backpropagation algorithm. GRNN is the type of neural networks that mainly depend on statistical methods and probability theory.

2.1. Multilayer perceptron neural network

With multilayer perceptron the data information only flows forward, which means that the output of a layer is used only as the input of the next layer [10]. These algorithms are organized by several neurons of different layers and are thus called multilayered. Each connection between the input and hidden layers (or more hidden layers) is like a synapse, and the input data is replaced with a certain weight.

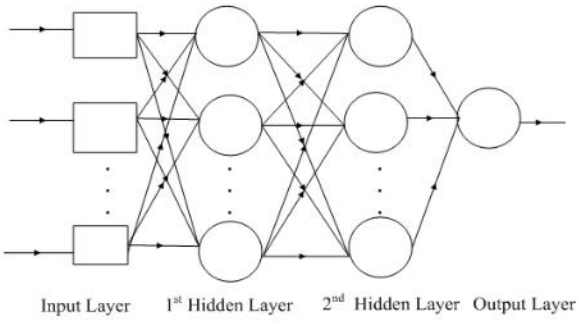

Figure 1. General structure of MLP NN.

A three layer feed-forward network is composed by an input layer, two hidden layers and the output layer as shown in Fig. 1[11].

The value coming out of an input unit is labeled x_j. Each hidden node computes the weighted sum of its inputs and applies a threshold value function to determine the output of the hidden node [12]. The weighted sum of inputs for hidden node z_h is calculated as follows:

$$\sum_{j=0}^{d} w_{hj} x_j \qquad (1)$$

Where w_{hj} a weight going to hidden unit z_h from input unit x_j would be labeled w_{hj} .

Step or sigmoid functions are generally chosen as threshold functions performed in the hidden node. In the hidden node, using the sigmoid function, z_h becomes as follows

$$z_h = sigmoid\left(\sum_{j=0}^{d} w_{hj} x_j\right) = \frac{1}{1+e^{-\sum_{j=0}^{d} w_{hj} x_j}} \qquad (2)$$

for h=1,2,…,H, where H is the number of hidden nodes. Output is computed by the weighted sum of inputs such that

$$o_i = \sum_{h=0}^{H} v_{ih} z_h \qquad (3)$$

to produce the output. We can apply several functions on each of the output nodes, such as Sigmoid [12]. If we apply the "softmax" function to the weighted sum

$$y_i = softmax(o_i) = \frac{e^{o_i}}{\sum_{i=1}^{K} e^{o_i}}$$

$$= \frac{e \sum_{h=0}^{H} v_{ih} z_h}{\sum_{i=1}^{K} e \sum_{h=0}^{H} v_{ih} z_h} \qquad (4)$$

2.2. Generalized regression neural network

The generalized regression neural network proposed by Specht (1991) does not require a recurrent training procedure, such as the back propagation method. GRNN predicts the function between input and output vectors using training data. GRRN has a rapid training capability on sparse data sets such as probabilistic neural networks.As the training set expands, the prediction error is reduced. GRNN use just for the estimation of continuous variables as standard regression techniques. GRNN, which is similar to radial-based functions, is based on standard regression. When a training set is given, GRNN predicts the joint probability density function of x and y [9].

If the joint probability density function f (x, y) is known;

$$E[y/X] = \frac{\int_{-\infty}^{+\infty} y f(X,y) dy}{f(X,y) dy} \qquad (5)$$

If the probability density function is not known

$$\hat{f}(X,Y) = \frac{1}{2\pi^{\frac{(p+1)}{2}} s^{(p+1)}} *$$

$$\frac{1}{n} \sum_{i=1}^{n} exp\left[-\frac{\left(X-X^i\right)^T \left(X-X^i\right)}{2s^2}\right] *$$

$$exp\left[-\frac{(Y-Y^i)^2}{2s^2}\right] \quad (6)$$

In this equation, p is the size of the x vector, n is the number of observations, s is the correction parameter. As D_i^2 is a scalar function,

$$D_i^2 = \left(X - X^i\right)^T (X - X^i) \quad (7)$$

regression of dependent variable y according to independent variable x is

$$\hat{Y}(X) = \frac{\sum_{i=1}^{n} Y^i \exp\left(-\frac{D_i^2}{2s^2}\right)}{\sum_{i=1}^{n} \exp\left(-\frac{D_i^2}{2s^2}\right)} \quad (8)$$

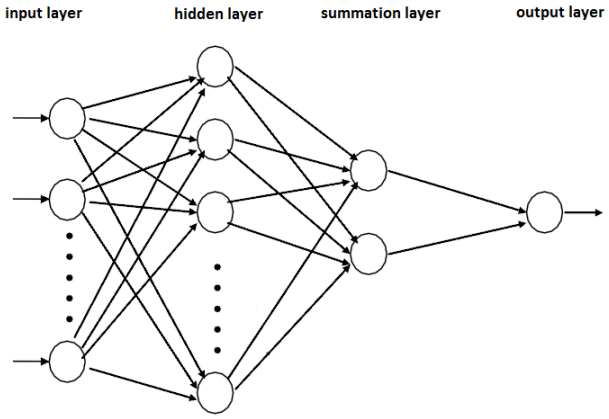

Figure 2. General structure of GRNN

A four layer generalized regression neural network is shown in Fig.2 [9].

3. EXPERIMENTAL STUDY

3.1. Instrument and materials

The particle size of copolymer in water was measured via Brookhaven 90 Plus/BI-MAS (Multi Angle Particle Sizing) and zeta potential measurements of copolymer were also determined by Brookhaven Zeta Potential Analyzer in water as a function of pH at physiological temperature 37ºC. [13].

Zeta potential is the measurement of the push or pull value between the particles. Zeta potential measurement gives detailed information about the distribution mechanisms and is the key to the electrostatic distribution control. A certain overhead grain pulls counter-load ions in the suspension resulting in a strong bond surface on the surface of the loaded grain. And then form an outwardly spread surface from the loaded grain. Within this diffused surface there is a boundary called "sliding surface". Loaded grain and its surrounding the portion of the ions up to the sliding surface boundary acts as a single piece. Potential on this slip surface is called zeta potential and is affected both by the surface texture of the grain and by the content of the liquid it contains. The behavior of granules in polar liquids determines the potential values of zeta, not the electric charge on their surface [14].

The most important reason for determining the zeta potential is to determine the size of the diffuse double layer around the particle. Zeta potential provides an understanding of many important properties of the colloidal systems and allows them to be controlled and to determine the electrical charge or potential on the particles. It is also very important for the understanding of dispersion and aggregate processes. The size of the zeta potential stabilizes the colloidal suspensions by preventing aggregate formation [14].When all the particles have a very large negative or positive zeta potential, the particles push each other and the dispersion becomes stable. When the particles have low zeta potential, there is no force to prevent the particles from accumulating, so dispersion imbalance (aggregation and sedimentation) occurs.

Zeta potential is dependent on surface charge density and double layer thickness. The surface charge density depends on the concentration of the potential determining ions. Since the H^+ ion is the potential determinant ion in many systems, the zeta potential is dependent on pH [14]. In this study, the particle size and zeta potential of the copolymer in the water was measured at different pHs [13].

Nano Particles with a zeta potential value that is more positive than +30 mV and negative than -30 mV are considered stable and particles with a zeta potential value of +30 mV to -30 mV are considered unstable [15].

One of the most important factors that affect the Zeta potential is pH. In this study, the effects of different pHs and particle sizes of copolymer on the zeta potential were investigated by using GRNN and MLPNN. And estimation results are compared by mean squared error and coefficient of determination.

4. RESULTS AND DISCUSSION

Model included two input variables (the particle size (nm), the pH) and one output variable (the zeta potential (mV)). The pH was measured at 17 different values, the lowest being 2.5 and the highest being 11.7. The particle size was measured 5 times

for each pH value and the zeta potential was calculated for each value [13].
Figure 3 shows the relationship between input and output variables.

In the MLPNN and GRNN models, 70% (60 zeta potential measurements) of the data were randomly selected for the training and 30% (25 zeta potential measurements) were used for testing. After preparing the data, code for GRNN was implemented and then the code was processed.

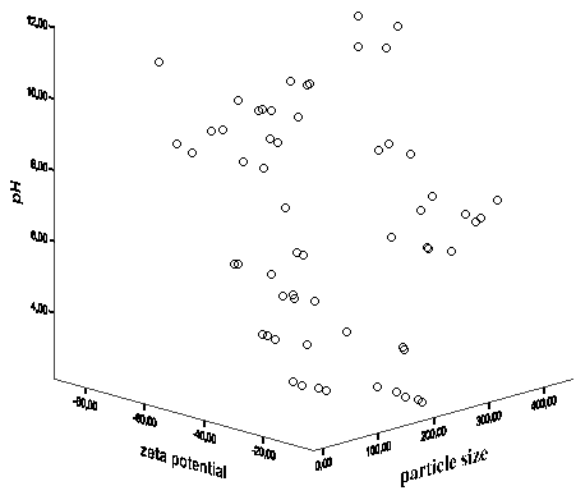

Figure 3. The relationship between input and output data of experimental measurements [13]

Using Weka software 3.8.1, the MLPNN model is developed using ANN fitting tool. In the MLPNN, a hidden layer was used in the network. To find the optimal number of neurons in hidden layers of the model, the size was expanded by adding 1 neuron at each step starting from 1. The maximum number of hidden layer neurons, which l is the number of input variables, should be at most 2l+1 as discussed by Caudill (1988). MPNNs having one to five hidden neurons were trained and one hidden neurons were used for optimal network. Different transfer functions were investigated and sigmoid transfer function was used to achieve the best performance in model. Learning rate and momentum were equal to 0.1 and 0.01, respectively. The initial weight matrices were randomly selected and the learning process continued until a sufficiently low mean square error was obtained. Training started with a small number of epochs (50) and the maximum number of epochs to train was chosen as 500 [16].

Table 1. Result comparison of MLP and GRNN Model

Model	Training set results		Testing set results	
	MSE	R^2	MSE	R^2
*MLP*NN	15.68	0.8692	12.87	0.7437
GRNN	6.23	0.8943	10.65	0.8371

As shown in Table 2, GRNN gives better result than MLPNN both training and testing sets to predict the zeta potential of copolymer solution. The regression plot for training and testing data of GRNN is shown in Fig.4 and Fig.5, respectively.

The GRNN results of training and test data were good fit with the experimental results as shown in Fig. 4 and Fig.5.

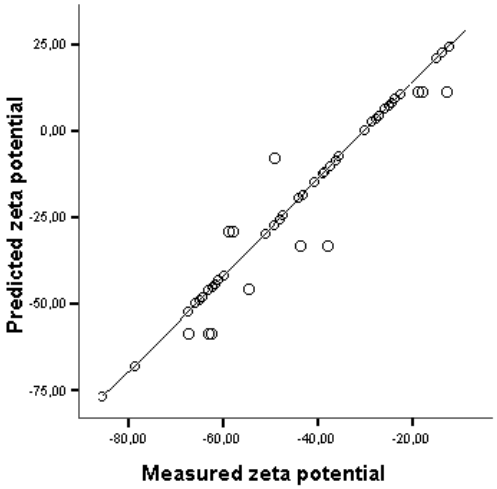

Figure 4. Regression plot of training data of the GRNN model

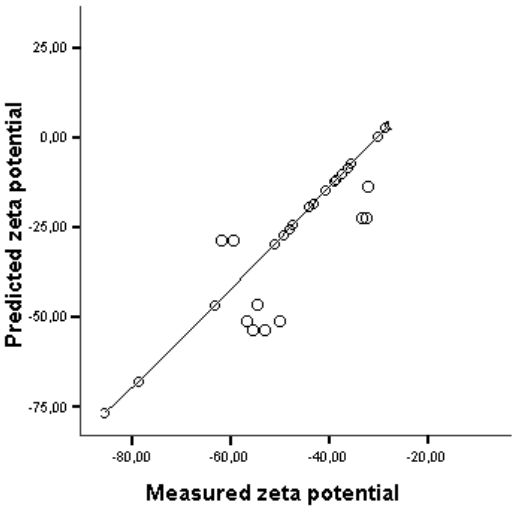

Figure 5. Regression plot of testing data of the GRNN model

5. CONCLUSIONS

In this article, the two artificial neural network algorithms, MLPNN and GRNN, were used to predict the zeta potential of the copolymer and the performance of these were compared. In order to determine the stability of the copolymer, the particle size and zeta potential in water were measured as a function of pHs. The zeta potential behavior of the copolymer solution is complex and important at different pHs. The experimental data [13] were

randomly divided into two groups as sets of training and test. The models of MLPNN and GRNN were built separately for these sets. In this study, coefficient of determination (R^2) and mean square errors (MSE) for both models are considered to compare prediction prerformance of the models. The experimental data were compared to the predicted values of zeta potential of copolymer based on both models for training and test sets. The GRNN model that has higher R^2 values and lower MSE values than MLPNN model showed better performance in terms of prediction accuracy. As a result, GRNN model of pH on the zeta potential of the copolymer can be preferred to MLPNN models in prediction with articifical neural network.

REFERENCES

1. V. Gonçalves Maltarollo, K. Maria Honório, A. Borges Ferreira da Silva, in: Artificial Neural Networks - Architectures and Applications, K.Suzuki (ed.),Chapter 10, 2013, p.1.
2. V. Kvasnička, *Chem. Papers*, **44**, 775 (1990).
3. A.S. Luna, E.R.A. Lima, K.P.F. Alberton, *Int. Computer Res.*, **23**, 19 (2016).
4. K. Srikanth,V. Rama Mohan Gupta, S. Raj Manvi, N. Devanna, *Int. Res. J. Pharmacy*, **3**,22 (2012).
5. M. Rafienia, M. Amiri , M. Janmaleki & A.Sadeghian, *Appl. Art. Intell.*, **24**,807 (2010).
6. I.A. Basheer, M. Hajmeer, *J. Microbiol Methods*, **43**, 3 (2000).
7. Y. Sun, Y. Peng, Y. Chen , AJ. Shukla, *Adv. Drug Deliv. Rev.*, **55**,1204 (2003).
8. J. Gasteiger, J Zupan, *Angew. Chem. Int.*, **32**, 506 (1993).
9. M.D.R. Martinez-Blanco, V. Hugo Castañeda-Miranda, G. Ornelas-Vargas, H.A. Guerrero-Osuna, L.O. Solis-Sanchez, R. Castañeda-Miranda, J.M. Celaya-Padilla, C.E. Galvan-Tejada, J.I. Galvan-Tejada, H.N. Vega-Carrillo, M. Martínez-Fierro, I. Garza- Velo, J.M., in: Artificial Neural Networks - Models and Applications, L. G. Rosa (ed.), Chapter3, 2016, pp.6,7,14,16.
10. F.A Marini, *Anal. Chim. Acta*, **635**, 123 (2009).
11. G. Kumar,,H. Malik, *Procedia Computer Sci.*, **93**, 28 (2016).
12. L.E. Parker, CS494/594: Projects in Machine Learning, 2-4 (2006).
13. D. Sakar Dasdan, A. Dizdar, G. Karakus, *Bul. Chem. Commun.*, **49,** Issue I, 43 (2017).
14. http://www.iksa.com.tr/pdf/zeta.pdf
15. https://cms.inonu.edu.tr/uploads/contentfile/642/files/Colloids_Surface_Zeta%20Potential_M_Erdemoglu.pdf
16. Y. Erzin , Y. Yukselen, *Math. Geosci.* ,**41**,788 (2009).

CONTENTS

NOTES TO CONTRIBUTORS

The journal BULGARIAN CHEMICAL COMMUNICATIONS publishes research papers and invited reviews in all branches of Chemistry: General and Inorganic, Analytical, Physical, Organic, Polymer, Theoretical, Chemical Engineering, and Biochemistry.

Manuscripts are submitted by e-mail or mail. They should be in a concise and clear style. The text must be typed double-spaced, on A4 format paper using Times New Roman font size 12, normal character spacing and should not exceed 15 pages (about 3500 words), including photographs, tables, drawings, formulae, *etc*. Authors are requested to use margins of 3 cm on all sides. Hard copies should be submitted in duplicate and reproduced by a clearly legible duplication process.

Manuscripts are published in English. All papers should be supplied with a summary. It has to be self-explanatory and clear, without reference to the text, and should not exceed 250 words.

Key words (up to 6) should be indicated on a separate line after the summary.

The first and the middle name of the authors are to be indicated by initials, the family name(s) of the authors(s) are to be given in full. The name of the author to whom correspondence should be addressed is to be marked by an asterisk. The affiliation of the author(s) should be listed in detail (no abbreviations!).

References, quoted in the manuscript by Arabic numerals in square brackets set on the line, should be typed on a separate sheet. The names of all authors of a certain publication should be given. The use of "*et al*." in the list of references is not acceptable. Titles of journals must be abbreviated according to Chemical Abstracts.

Figure captions and tables should be appended to the manuscript in separate files (sheets). Special attention is drawn to conciseness of captions. Author(s) name(s), title of the paper, number of drawings, photographs, diagrams, *etc*., should be written on the back of the illustrative material in accordance with the list enclosed. Avoid using more than 6 (12 for reviews, respectively) figures in the manuscript.

The final text should be submitted by e-mail or on a 3.5'' diskette (CD). The main text, list of references, tables and figure captions should be saved in separate files as *.rtf or *.doc of Word processor with clearly identifiable file names. Pictures should be presented in *.tif, *.jpg, *.cdr or *.bmp format, the chemical reaction schemes should be written using ISIS Draw or ChemDraw programme.

The authors are required to list three individuals and their e-mail addresses that can be considered by the Editors as potential reviewers. Please, note that the reviewers should be outside the authors' own institution or organization. The Editorial Board of the journal is not obliged to accept these proposals.

Instructions about Preparation of Manuscripts can be found at:
http://www.bcc.bas.bg/BCC_Guide_for_Authors.html

Manuscripts and enclosures should be sent to:

Prof. V. Beschkov
Editor-in-Chief
Bulgarian Chemical Communications
Institute of Chemical Engineering
Bulgarian Academy of Sciences
Acad. G. Bonchev St., Block 103
1113 Sofia
Bulgaria
E-mail: bioreac@bas.bg or vbeschkov@yahoo.com

or

Prof. D. Yankov
Editor
Bulgarian Chemical Communications
Institute of Chemical Engineering
Bulgarian Academy of Sciences
Acad. G. Bonchev St., Block 103
1113 Sofia
Bulgaria
E-mail:yanpe@bas.bg

ISSN 0861-9808